Department for Engineering
Study Program Renewable Energy Systems

Shekh Mojamil

Simulation and Validation of Small to Large-Scale Hydrogen Liquefaction Cycles using Mixed and Normal-Hydrogen Refrigerant in MATLAB/Simscape Fluids

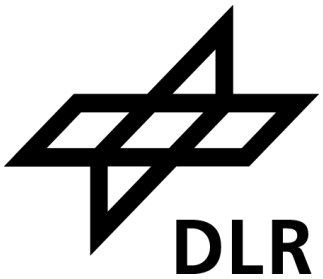

Master thesis for obtaining the
academic degree:
Master of Engineering (M. Eng.)
Submission date: 19.03.2026
Matriculation Number: 45198

First reviewer: Dr.-Ing. Pascal Leibbrandt
University of Applied Sciences, Nordhausen

Second reviewer: Dr.-Ing. Jan Haemisch, Dipl. Phys. Philipp Johannes Kallina
Deutsches Zentrum für Luft- und Raumfahrt

ABSTRACT

Hydrogen is emerging as one of the most promising energy carriers for a clean global energy system. It can address the issues facing the energy and transportation sectors with air pollution and climate change. Liquid hydrogen has sparked widespread interest due to its high energy storage density and potential for long-distance transportation. Delivering and storing hydrogen in its cryogenic liquid form is an economical method. The key factor for obtaining liquid hydrogen is an effective hydrogen liquefaction procedure, which cools down feed hydrogen gas at 300 K to liquid hydrogen at 20 K. However, compared to the straightforward compression-storage approach, hydrogen liquefaction requires a greater infrastructure investment. Therefore, investigating energy-saving techniques for hydrogen liquefaction is crucial.

This thesis work employed a physical modeling tool, **Simscape Fluids,** within the MATLAB/Simulink environment, which is used to model and simulate the energy-efficient hydrogen liquefaction process. This study evaluated the dynamic features of the hydrogen liquefaction process by creating a model of the unit module and performing simulation optimization based on the steady-state process and process parameters. In this study, hydrogen liquefaction systems are simulated at small, medium, and large-scale capacities of 5 TPD, 50 TPD, and 120 TPD, respectively. Each configuration employs different refrigerant arrangements with the objective of reducing the specific energy consumption (SEC) and improving overall thermodynamic performance.

For the small-scale 5 TPD plant, a dual-pressure pre-cooling hydrogen liquefaction system is implemented. Normal hydrogen is used as the primary refrigerant, while liquid nitrogen provides the pre-cooling stage. The system achieves a specific energy consumption of 9.69 $\mathrm{kWh/kg_{LH_2}}$, an exergy efficiency of 0.542, and a coefficient of performance (COP) of 0.118.

In the medium-scale 50 TPD configuration, a Joule-Brayton cycle is adopted for the main liquefaction process. Helium serves as the refrigerant, and liquid nitrogen is utilized for pre-cooling. This configuration demonstrates improved thermodynamic performance, with an SEC of 5.75 $\mathrm{kWh/kg_{LH_2}}$, an exergy efficiency of 0.574, and a COP of 0.193.

For the large-scale 120 TPD plant, the system is integrated with a liquefied natural gas (LNG)-based hydrogen production facility. The cold energy released during LNG regasification is effectively recovered to pre-cool the feed hydrogen from 300 K to 114 K, thereby significantly reducing the refrigeration load. A helium Brayton cycle is then employed for deep cryogenic

cooling, with helium as the working refrigerant. This large-scale configuration achieves a reduced SEC of 7.56 $\mathrm{kWh/kg_{LH_2}}$, an exergy efficiency of 0.432, and a COP of 0.144.

KURZFASSUNG

Wasserstoff entwickelt sich zu einem der vielversprechendsten Energieträger für ein klimaneutrales, sauberes globales Energiesystem. Durch seine emissionsfreie Verbrennung kann er die drängenden Probleme des Energie- und Verkehrssektors hinsichtlich Luftreinhaltung und Klimawandel wirksam mildern. Insbesondere flüssiger Wasserstoff hat aufgrund seiner hohen Energiespeicherdichte und seiner Eignung für den Ferntransport großes Interesse geweckt. Die Bereitstellung und Speicherung von Wasserstoff in seiner flüssigen, tiefkalten Form sind wirtschaftliche Optionen. Der Schlüsselfaktor zur Gewinnung von flüssigem Wasserstoff ist ein hocheffizientes Wasserstoffverflüssigungsverfahren, das gasförmigen Wasserstoff von ca. 300 K auf 20 K abkühlt. Obwohl die Verflüssigung im Vergleich zu rein druckbasierten Speicherlösungen mit höheren Investitionskosten verbunden ist, eröffnet sie langfristig ökonomisch attraktive Speicher- und Transportoptionen. Daher sind die Untersuchung und Entwicklung energiesparender Wasserstoffverflüssigungsprozesse von entscheidender Bedeutung.

In der vorliegenden Arbeit wird ein physikalisch fundiertes Modellierungs- und Simulationswerkzeug, (***Simscape Fluids*** innerhalb der MATLAB/Simulink-Umgebung) eingesetzt, das zur Modellierung und Simulation der energieeffizienten Wasserstoffverflüssigungsprozesse verwendet wird. Diese Studie untersucht die dynamischen Eigenschaften des Wasserstoffverflüssigungsprozesses, indem ein dynamisches Modell der einzelnen Anlagenmodule erstellt und eine Simulationsoptimierung auf Grundlage des stationären Prozesses und der Prozessparameter durchgeführt wird. In dieser Studie werden Wasserstoffverflüssigungssysteme in kleinen, mittleren und großen Maßstäben mit Kapazitäten von 5 t/d, 50 t/d und 120 t/d simuliert. Jede Konfiguration verwendet eine unterschiedliche Zusammenstellung von Kältemittel mit dem Ziel, den spezifischen Energieverbrauch (SEC) zu reduzieren und die gesamte thermodynamische Leistung zu verbessern.

Für die Kleinanlage mit 5 t/d wird ein Wasserstoffverflüssigungssystem mit zweistufiger Vorkühlung und unterschiedlichen Druckniveaus implementiert. Normaler Wasserstoff wird als primäres Kältemittel verwendet, während flüssiger Stickstoff die Vorkühlstufe bereitstellt. Das System erreicht einen spezifischen Energieverbrauch von 9,69 $\mathrm{kWh/kg_{LH_2}}$, einen Exergie-Wirkungsgrad von 0,542 und eine Leistungszahl (COP) von 0,118.

In der mittleren 50-t/d-Konfiguration wird ein Joule-Brayton-Kreisprozess für den Hauptverflüssigungsprozess eingesetzt. Helium dient als Kältemittel, und flüssiger Stickstoff wird zur Vorkühlung verwendet. Diese Konfiguration zeigt eine verbesserte thermodynamische

Leistung mit einem SEC von 5,75 $\mathrm{kWh/kg_{LH_2}}$, einem Exergie-Wirkungsgrad von 0,574 und einem COP von 0,193.

Für die Großanlage mit 120 t/d wird das System in eine auf verflüssigtem Erdgas (LNG) basierende Wasserstoffproduktionsanlage integriert. Die während der LNG-Regasifizierung freigesetzte Kälteenergie wird effektiv zurückgewonnen, um den zugeführten gasförmigen Wasserstoff von 300 K auf 114 K vorzukühlen, wodurch die Kälteleistung erheblich reduziert wird. Anschließend wird ein Helium-Brayton-Kreisprozess für die tiefe kryogene Kühlung eingesetzt, wobei Helium als Arbeitskältemittel dient. Diese Großkonfiguration erreicht einen reduzierten SEC von 7,56 $\mathrm{kWh/kg_{LH_2}}$, einen Exergie-Wirkungsgrad von 0,432 und einen COP von 0,144.

ACKNOWLEDMENT

This dissertation is the result of my research conducted within the framework of the EXACT2; HAP5 project at the German Aerospace Center (DLR). I would like to express my sincere gratitude to the Institute of Renewable Energy Technology (in.RET) and to my esteemed supervisor, Dr.-Ing. Pascal Leibbrandt from Hochschule Nordhausen, for their valuable guidance and continuous support throughout my academic study.

In particular, I want to express my heartfelt gratitude to my thesis supervisors, Dr.-Ing. Jan Haemisch and Dipl. Phys. Philipp Johannes Kallina from DLR, for the exceptional support and dedication during the past 9 months, and their effort in my academic endeavors has been truly admirable. I appreciate them taking the time to attend our weekly meetings, where they have provided me with insightful feedback and guidance. I am grateful for the constant encouragement for my thesis work, which has motivated me to expand my investigation. In the future, I hope to have a second chance to work with them.

I would also like to express my sincere gratitude to the RA-AWT LA- Applied Hydrogen Technologies department in DLR for offering me an opportunity to conduct my research in such an innovative and fascinating environment. My academic experience has been tremendously enhanced by being a part of this department, which has also enabled me to expand my knowledge of hydrogen technology.

I am particularly grateful to the team leader, Ms. Daniela Lindner, for her insightful remarks and helpful recommendations over the course of my research. Her advice and unwavering support have greatly enhanced the caliber of my thesis. Additionally, I would like to thank the IT team for their excellent technical assistance. In particular, I am deeply grateful to Ms. Marina Schmidt and Mr. Alexander Funck for their assistance with software licensing and system updates, which allowed me to work effectively.

Last but not least, my parents, I will never forget the love and support received from them from the beginning of my journey.

Lampoldshausen, 19th March 2026 Shekh Mojamil

Contents

List of Figures

List of Tables

List of Symbols

Symbol	Unit	Meaning
a	$\frac{m^6 \cdot Pa}{mol^2}$	Repulsive Constant
b	$\frac{m^3}{mol}$	Volume Occupied by hydrogen molecules
€	-	Euro
R	$\frac{J}{K \cdot mol}$	Gas Constant
P	MPa	Pressure
T	K	Temperature
n	-	Number of Moles
V	m^3	Volume
$\mathbf{C_p}$	$\frac{J}{kg \cdot K}$	Specific heat at constant pressure
$\boldsymbol{\Delta H}$	$\frac{kJ}{kg}$	Change in Specific Enthalpy
$\boldsymbol{\Delta G}$	$\frac{kJ}{mol}$	Gibb's Free Energy
Q	kW	Thermal Energy
$\boldsymbol{\Delta S}$	$\frac{kJ}{kg \cdot K}$	Change in Specific Entropy
ρ	$\frac{kg}{m^3}$	Density
ṁ	$\frac{kg}{s}$	Mass Flow Rate
Q̇	kW	Heat Transfer Rate
Ẇ	kW	Total Power Consumption

$\boldsymbol{\varepsilon}$	%	Exergy Efficiency
$\boldsymbol{\Delta E}$	kW	Exergy Loss
$\boldsymbol{e}$	kW	Mass Exergy
$\boldsymbol{\omega}$	$\frac{\text{m}}{\text{s}}$	Angular Velocity
$\boldsymbol{\eta}$	%	Efficiency
C	-	Clearance Volume Fraction
$\boldsymbol{n}$	-	Polytropic Exponent
Φ	kW	Energy Flow
y	-	Equilibrium Molar Fraction
h	J s	Planck Constant
k	$\frac{\text{J}}{\text{K}}$	Boltzmann Constant
$\Delta\boldsymbol{h}$	$\frac{\text{kJ}}{\text{kg}}$	Heat of Conversion

List of Abbreviations

Nomenclature

ADP	Adenosine Diphosphate
AEMs	Alkaline Anion Exchange Membranes
AP	Acidification Potential
ASU	Air Separation Unit
ATP	Adenosine Triphosphate
ATR	Autothermal Reforming
AWE	Alkaline Water Electrolysis
BOG	Boil-off Gas
CAPEX	Capital Expenditure
CCS	Carbon Capture system
CFD	Computational Fluid Dynamics
CGH_2	Compressed Gaseous Hydrogen
CMM	Coal Mine Methane
COMP	Compressor
COP	Coefficient of Performance
DBT	Dibenzyl-Toluene

DMR	Dual-Mixed Refrigerant
DNEC	Dodecahydro-N-ethylcarbazole
DVB	Divinylbenzene
EX	Expander
EXE	Exergy Efficiency
FCEVs	Fuel Cell Electric Vehicles
Fd	Ferredoxin
FOM	Figure of Merit
GA	Genetic Algorithm
GH_2	Gaseous Hydrogen
GHG	Greenhouse Gas
GHR	Gas Heated Reformer
GWP	Global Warming Potential
HER	Hydrogen Evolution Reaction
H_2	Hydrogen Molecule
HXs	Heat Exchangers
IDEALHY	Integrated Design for Demonstration of Efficient Liquefaction of Hydrogen
J-B	Joule Brayton
J-T	Joule-Thompson
LCOH	Levelized cost of hydrogen
LHV	Lower Heating Value
LH_2	Liquid Hydrogen
LNG	Liquefied Natural Gas
LN_2	Liquid Nitrogen
LOHCs	Liquid Organic Hydrogen Carriers
MA	Moist Air
MCH	Methylcyclohexane
MOFs	Metal Organic Frameworks
MR	Mixed Refrigerant
MSW	Municipal Solid Waste
NA	Not Available
$NADP^+$	Nicotinamide Adenine Dinucleotide Phosphate (Oxidized Form)

$NADPH_2$	Nicotinamide Adenine Dinucleotide Phosphate (Reduced Form)
NASA	National Aeronautics and Space Administration
NEC	N-ethylcarbazole
NG	Natural Gas
NMHCs	Non-Methane Hydrocarbons
OER	Oxygen Evolution Reaction
OPC	Ortho-Para Conversion
Pc	Plastocyanin
PDBT	Perhydro-Dibenzyl-Toluene
PEMs	Proton Exchange Membranes
PFSA	Perflurosulfonated Acid
POX	Partial Oxidation
PPM	Parts per million
PPS	Polyphenyl Sulfide
pqH_2	Plastoquinone
PSA	Pressure Swing Adsorption
PTP	Power-to-Power
PV	Photovoltaics
RE	Renewable Energy
REFPROP	Reference Fluid Thermodynamic and Transport Properties Database
RONs	Research Octane Numbers
SEC	Specific Energy Consumption
SMR	Steam Methane Reforming
SOE	Solid Oxide Water Electrolysis
TOL	Toluene
TPD	Tons Per Day
UNFCC	United Nations Framework Convention on Climate Change
WGS	Water-Gas Shift
YSZ	Yttria-Stabilized Zirconia
2P	Two-phase

Subscripts

in	Inlet Stream
out	Outlet Stream
c	Compressor
i	Number of Components
E	Expander
HX	Heat Exchanger
h	Hot Stream
c	Cold Stream
inc	Increased
re	Reduced
c	Critical
0	Standard Condition
rev	Reversible Liquefaction
act	Actual Liquefaction
dis	Displacement
v	Volumetric
$2P1,2$	Two-Phase Fluid 1 & 2
Seg	Segment
N	Number of Segments
L	Sub-Cooled Liquid
u	Internal Energy
M	Liquid-Vapor Mixture
V	Superheated Vapor
$Corr$	Corrected Flow Parameter

Chemical Species

H_2O	Water
CO	Carbon Monoxide
CH_4	Methane
C	Carbon
H	Hydrogen
n, m	Number of Carbon and Hydrogen atoms, respectively

N_2	Nitrogen Gas
CHs	Hydrocarbons
tar	Condensable Hydrocarbon
$char$	Solid Carbon Residue
$C_6H_{12}O_6$	Glucose
CH_3COOH	Acetic Acid
$CH_3CH_2CH_2COOH$	Butyric Acid
Ir	Iridium
Ru	Ruthenium
KoH	Potassium Hydroxide
$NaHCO_3$	Sodium Bicarbonate
NiO	Nickel oxide
ZrO_2	Zirconium Dioxide
CO_3O_4	Cobalt Oxide
SO_2	Sulfur Dioxide
H_2S	Hydrogen Sulfide
NH_3	Ammonia
O_2	Oxygen
N_2O	Nitrous Oxide

1. Introduction

Over the past 200 years, the worldwide population has increased dramatically, and at the same time, industrialization has increased the risks of air pollution and global warming from greenhouse gas emissions like carbon dioxide (CO_2). National governments and international organizations have recently implemented more stringent environmental laws and established goals for lowering greenhouse gas emissions in an effort to mitigate the effects of climate change. One such example is the UNFCC 2015 Paris Climate Agreement (Cardella, Decker, & Klein, 2017). The rising global energy demand as a result of the world's population growth necessitates a sustainable source of energy with a lower environmental impact than traditional energy supplies. Energy produced from renewable resources, such as wind and solar energy, must be stored using a storage medium. Hydrogen is considered in certain quarters as the ultimate, non-polluting fuel and energy storage medium for future centuries. It can be generated from water using a primary energy source and then combusted back to water in a closed chemical cycle that does not emit carbonaceous pollutants (Dell & Bridger, 1975).

Hydrogen is an abundant source of energy around the world and can be used in a variety of ways. It can be manufactured using a variety of fuel processing methods, including hydrocarbon and ammonia reforming, desulfurization, and pyrolysis, among others. These techniques obtain hydrogen by transforming hydrogen-containing fuels. It can also be extracted from water using electrolysis or thermolysis technologies that use electricity to split hydrogen and oxygen within a wide temperature range (Nikolaidis & Poullikkas, 2017).

Hydrogen is an interesting energy carrier that may be stored and delivered in a variety of ways. It can be compressed and stored in high-pressure containers or liquefied and kept at specific temperatures and pressures. It can be adsorbed in carbonic structures or disseminated in metallic structures, resulting in metal hydrides (Andersson & Grönkvist, 2019). There are significant drawbacks to storing hydrogen through adsorption in carbon materials, such as the formation of hydrides in metals like iron and magnesium, and the formation of complicated metal hydrides, such as those containing boron and nitrogen. The storage and release of hydrogen in the majority of hydrides are highly endothermic or exothermic reactions that occur at high temperatures and necessitate extensive cooling and heating. Furthermore, metal hydrides have low gravimetric capacity (wt. %) and volumetric capacity (g L^{-1}) (Umegaki et al., 2009), making them undesirable for large-scale industrial applications. The transportation of gaseous hydrogen requires a large volume and a high-pressure storage tank. On the other hand, gaseous hydrogen has a very low energy content per unit volume. Therefore, hydrogen liquefaction is proposed to

address this problem. Compared to gaseous hydrogen, liquid hydrogen (LH_2) has an 800-times higher bulk density and a 6 to 8-fold higher transport efficiency (Muhammad Aziz, 2021). Due to the higher density of liquid hydrogen LH_2, up to 3600 kg LH_2 can be transported in one LH_2 trailer compared to a maximum of about 900 kg GH_2 in one CGH_2 trailer (Ball & Wietschel, 2009). Liquefied hydrogen offers certain advantages over alternative hydrogen storage options. Liquefying hydrogen is recognized as the most cost-effective method of distributing and storing hydrogen in huge volumes across long distances, such as in road trailers or ship carriers (Umberto Federico Cardella, 2018). In a case study, liquid hydrogen and ammonia are transported to Europe and Japan, and the levelized cost of hydrogen delivered to these regions is 5 €/kg H_2 for liquid hydrogen and 5.9 €/kg H_2 for ammonia, indicating that liquid hydrogen is comparatively more cost-effective and highlighting its importance as a carrier over other alternatives.

The major limiting factor in hydrogen liquefaction is the considerable amount of work required. Furthermore, the boiling temperature of hydrogen is approximately -253 °C, and liquefying at such a low temperature can be highly energy-consuming. A hydrogen source gas stream is cooled and liquefied from room temperature to around 20 K to produce liquid hydrogen LH_2. The state-of-the-art hydrogen liquefaction process is designed with a hydrogen feed gas pre-cooling carried out with a liquid nitrogen (LN_2) stream or a nitrogen refrigeration cycle, followed by further cooling and liquefaction in a cryogenic refrigeration cycle with a hydrogen Claude cycle or a helium Brayton cycle (S. Zhang & Liu, 2022).

The primary disadvantage of hydrogen liquefaction is the small size of the hydrogen liquefiers that are currently in operation and have relatively high specific energy consumption. The thermodynamic efficiency of the hydrogen liquefaction process was only a secondary consideration in the design of built industrial hydrogen liquefiers, which were often developed to reduce their initial capital expenses (Quack, 2002). Existing hydrogen liquefiers have a specific energy consumption (SEC) of about 11.9-15 kWh/kg_{LH_2}(Drnevich & Praxair, 2003; Rezaie et al., 2016a).

This dissertation proposes a systematic approach for implementing small to large-scale hydrogen liquefaction technology to develop a more energy-efficient system. It explores the evolution from the most advanced liquefaction plants already in operation to recently developed liquefaction processes, emphasizing opportunities for both technological advancement and performance enhancement.

1.1 Background and Motivation

Dewar was the first to liquefy hydrogen in 1898 (Dewar, 1898). Larger industrial hydrogen liquefaction plants were later established in the USA during the 20th century, for space programs and nuclear weapons development. An estimated 400 TPD of LH_2 can be produced globally with installed liquid hydrogen production capacity. The biggest hydrogen liquefaction facilities were constructed in the United States between the 1960s and 1980s, with a maximum capacity of 55 TPD. The largest hydrogen liquefiers in operation today are located in the USA, with a maximum liquefaction capacity ranging from 20 to 35 TPD (Krasae-in et al., 2010a). The brief summarization of the early development of the hydrogen liquefaction plant based on various cycle configurations is described in the section **6.1**.

Linde commissioned a hydrogen liquefaction facility in Leuna in 2008, using a pre-cooled Claude cycle with a specific energy consumption of 11.9 kWh/kg_{LH_2} (Rezaie et al., 2016a). In this study, the Leuna facility is used as a reference case, with its process flow configuration serving as the simulation baseline for 5 TPD. The suggested small-scale design is based on the same fundamental cycle model, but with changes to the component arrangement and operating conditions to achieve a lower overall SEC. Moreover, adjusting the refrigerant mass flow rate within the cycle is given particular attention to improve overall efficiency and reduce compression work. A detailed thermodynamic analysis is conducted to improve the overall exergy efficiency and enhance the energy efficiency of the system.

For the 50 TPD baseline model for the simulation, a study made by Song et. al. on Simulation and Analysis of a Novel Hydrogen Liquefaction Process Based on the Liquid Nitrogen and Helium Joule-Brayton Cycle is taken as a reference model (Song et al., 2025). The thermodynamic behavior, component interactions, and irreversibility distribution identified in commercial-scale operations are not sufficiently modeled by such a small-scale configuration, even though the previously developed and validated MATLAB-based simulation model showed dependable performance for a 0.5 TPD system. Scaling hydrogen liquefaction capacity to 50 TPD results in much greater mass flow rates, altered heat transfer properties, modified compressor and turbine performance, and possibly variable exergy destruction patterns across system components. This scale-up analysis aims to bridge the gap between pilot-scale modeling and real-world commercial implementation, thereby contributing to the development of more energy-efficient and economically viable large-capacity hydrogen liquefaction systems.

The boundary conditions and operating parameters suggested by Jiang et al. in their study on the thermodynamic and economic analysis of a novel hydrogen liquefaction process with LNG

pre-cooling and a dual-pressure Brayton cycle serve as the basis for simulating and optimizing a 120 TPD hydrogen liquefaction process. The operating circumstances described in their research were taken into consideration when designing and simulating the process flow diagram (PFD). The goal of this research is to replicate the suggested system and enhance its functionality by reducing the specific energy consumption (SEC) through process parameter optimization.

In Europe, achieving climate-neutral aviation by 2050 prioritizes hydrogen as a key enabling technology, given its potential to achieve zero in-flight CO_2 emissions. The EXACT2 project seeks to model future energy systems under this framework. Large-scale hydrogen liquefaction is an essential part of this shift since aviation requires liquid fuels with high energy density, and to precisely evaluate system performance, energy usage, and economic viability, hydrogen liquefaction systems must be simulated and analyzed under realistic, high-capacity operational conditions. The current study contributes to EXACT2 and HAP5 by providing extensive thermodynamic and exergy-based models of hydrogen liquefaction, which aid in infrastructure development, system optimization, and overall feasibility assessments of hydrogen-powered aviation.

1.2 Research Objectives

One of the most serious problems of our time is to drastically reduce anthropogenic climate impacts, with the aviation sector playing a particularly important role due to its expected long-term growth and restricted decarbonization options. As other industries gradually lower their emissions, aviation risks becoming the leading contributor to global greenhouse gas emissions unless transformative technical solutions are developed. Given these challenges and the limitations, liquid hydrogen fuels are preferred as an aviation fuel due to their zero emission of GHG into our environment. Therefore, deep-dive research is required to further optimize the liquefaction cycle in terms of SEC, exergy, and overall efficiency. One of the existing plants in Germany is in Leuna, which employs a pre-cooled Claude cycle configuration, and modifications to the liquid nitrogen mass flow rate for pre-cooling and to the refrigerant mass flow rates were developed to optimize the specific energy consumption and improve the overall cycle efficiency. This thesis presents a simulation and comparative study of both existing and conceptual cycles proposed by various authors. The selected cycle was simulated for three different production capacities: 5, 50, and 120 tons per day (TPD).

The purpose of this study is to evaluate and examine an advanced hydrogen liquefaction system and its performance. This will involve energy and exergy assessments. These particular goals can be enumerated more precisely as follows:

1. To develop and design an advanced hydrogen liquefaction system for 5 TPD capacity based on the system developed by Linde in Ref. (Krasae-in et al., 2010a).
2. To develop and upscale the design of an advanced hydrogen liquefaction system for 50 TPD capacity based on the system developed in Ref. (Song et al., 2025).
3. To develop and design an advanced hydrogen liquefaction system for 120 TPD capacity based on the system developed in Ref. (Bian et al., 2021a).
4. To carry out a thorough exergy analysis of the developed hydrogen liquefaction systems by assessing the energy efficiency and destruction of the main parts, such as compressors, expanders, and heat exchangers.
5. To estimate important indicators of performance, including the coefficient of performance (COP) and specific energy consumption (SEC), to assess the thermodynamic performance of the proposed liquefaction systems.
6. To evaluate the comparative study between the proposed simulated design and the reference model.

1.3 Thesis Framework

This section serves as the framework of the thesis.

Section **1** introduces the topic, explains the research motivation, identifies gaps, states objectives, discusses solutions, and provides an overview.

Section **1** presents the major hydrogen production methods based on hydrocarbon reforming processes. It comprises common methods including hydrocarbon pyrolysis, partial oxidation (POX), autothermal reforming (ATR), and steam methane reforming (SMR). The basic concepts, reaction mechanisms, and operating conditions are explained in this section.

Section **3** provides information on hydrogen production from renewable sources. This section discusses various sustainable methods for producing hydrogen, including biomass conversion processes, thermochemical processes, biological production routes, and water-splitting methods.

Section **4** illustrates the different environmental impacts due to the production of hydrogen via conventional and renewable sources.

Section **5** provides information on hydrogen as a clean energy carrier and discusses various hydrogen storage methods, including compressed gas, liquid hydrogen, liquid organic hydrogen carriers (LOHC), and adsorption. This section also highlights the advantages of using liquid hydrogen compared to other storage methods, particularly in terms of energy-efficient transportation and storage.

Section **6** examines a detailed study of hydrogen liquefaction cycles. It includes information on the early development of hydrogen liquefaction, the basic liquefaction processes along with their schematic diagrams, and an overview of existing and conceptual hydrogen liquefaction plants.

Section **7** discusses the simulation study, in which detailed research is conducted on extracting fluid properties from different property tables using MATLAB. It also provides the process flow diagram of the proposed 5 TPD design model, along with its process description and thermodynamic analysis.

Section **8** analyzes the main components of the system, including the compressor, heat exchanger, expander, and ortho-para converters, which are modeled and parameterized to achieve an energy-efficient system**.**

Section **9** presents a process flow diagram of a 50 TPD hydrogen liquefaction cycle, which employs a pre-cooled Joule-Brayton cycle, along with its process description.

Section **10** illustrates a process flow diagram of 120 TPD of hydrogen liquefaction, which utilizes LNG cold energy as a pre-cooling, and further Cascade Joule-Brayton cycle for cryogenic cooling, along with its process description.

Section **11** outlines the results and discussion of the study conducted in this thesis

1.4 Theoretical Background on Hydrogen

Hydrogen is a colorless, tasteless, odorless, flammable gaseous substance that is the simplest member of the family of chemical elements. The nucleus of the hydrogen atom contains a proton and an electron, with the proton having a positive electric charge and the electron a negative electric charge. Although hydrogen is the most abundant element in the world, it constitutes only about 0.14 % of the Earth's crust by weight. Nevertheless, it exists in large amounts as a component of atmospheric water (Hydrogen | Properties, Uses, & Facts | Britannica, 2025). The energy per mass content of hydrogen is 143 MJ/kg, which is up to three times higher than that of fuels based on liquid hydrocarbons (Mazloomi & Gomes, 2012).

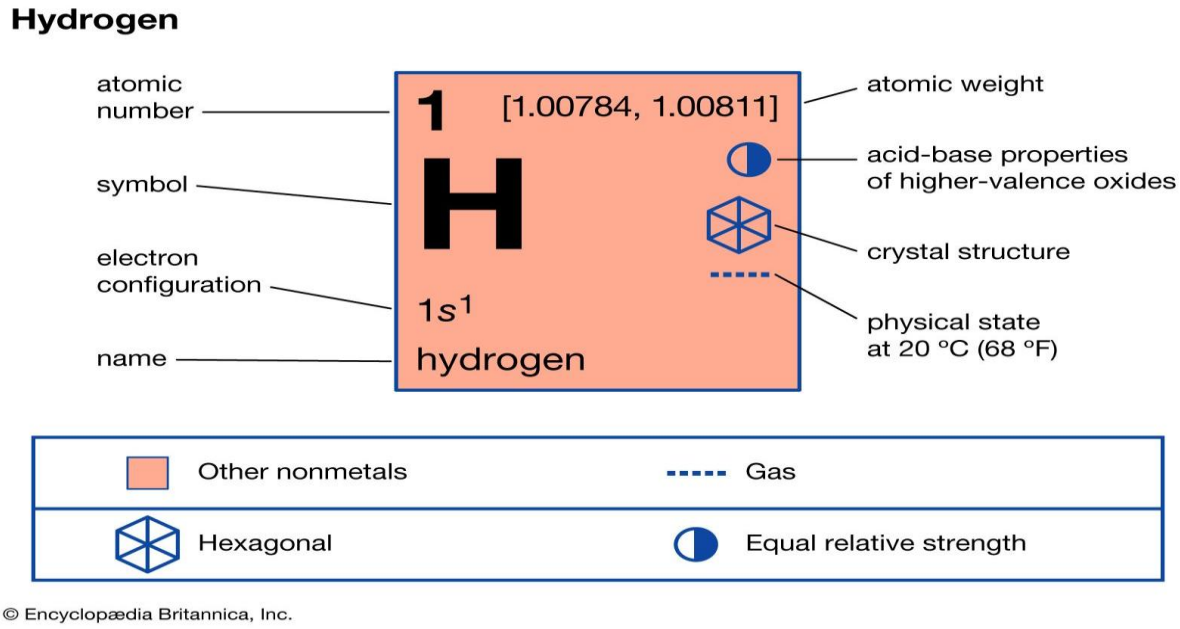

Figure 1. Fundamental atomic properties of hydrogen (adapted from Ref. (Hydrogen | Properties, Uses, & Facts | Britannica, 2026)).

The diagram in **Figure 1** provides a clear and visually organized summary of identity, structure, classification, and physical state of hydrogen. Hydrogen is represented by the letter H, and the top-left atomic number 1 indicates it has one proton in its nucleus. The atomic weight appears as a small range (1.00784, 1.00811), reflecting minor variations caused by the natural

abundances of hydrogen isotopes. The hydrogen sole electron is shown occupying the lowest-energy orbital, described by the electron configuration $1s^1$. The background color classifies hydrogen as a non-metal, and the dotted line symbol indicates that it is a gas at room temperature. A hexagon illustrates the hydrogen crystal structure when solidified under extreme conditions, while another symbol depicts its acid-base behavior in relation to other substances. The anti-knock ability of hydrocarbon fuels is measured by octane rating, which ranges from 0 to 100. Higher octane levels indicate an additional factor that helps prevent undesired auto-ignitions in the combustion chamber.

Table 1. Research octane number of comparable fuels (adapted from Ref. (Verhelst & Wallner, 2009)).

Fuel	Octane number
Hydrogen	>130
Methane	125
Ethane	108
Propane	105
Octane	100
Gasoline	87
Diesel	300

Fuel is run through a chamber at various compression settings to obtain this data in **Table 1**, which shows the Research Octane Numbers (RONs) of some similar fuels (Verhelst & Wallner, 2009).

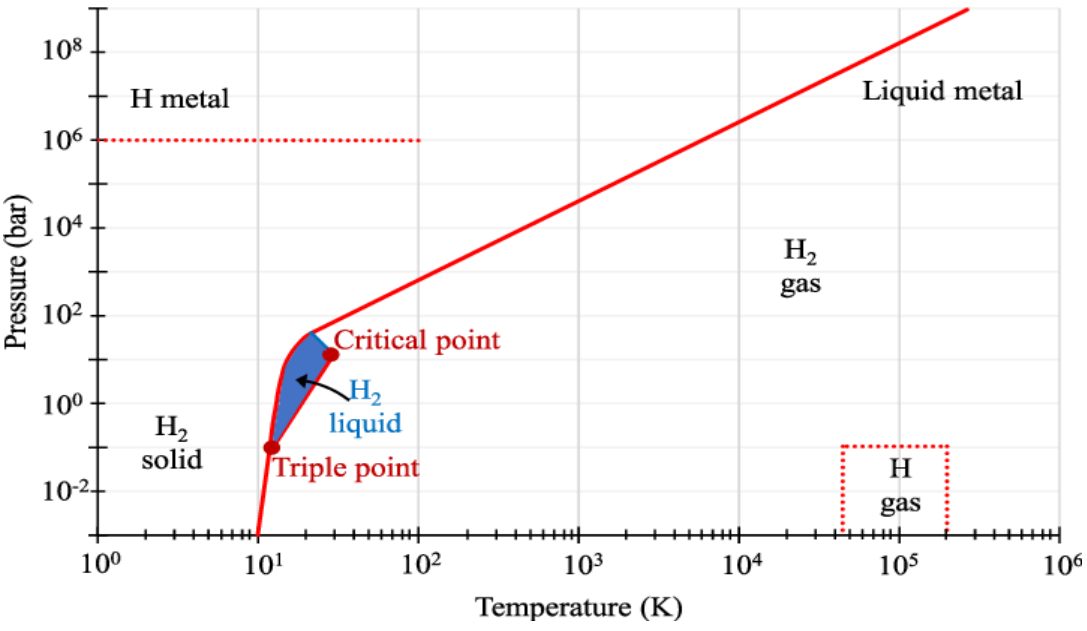

Figure 2. Hydrogen phase diagram (adapted from Ref. (Züttel, 2004)).

The hydrogen phase diagram illustrates the different physical states, such as solid, liquid, and gas. However, it shows the phase change behavior with different temperatures and pressures. Hydrogen shows a gaseous state at standard conditions (Hydrogen - Thermophysical Properties, 2025). The phase diagram in **Figure 2,** which illustrates that different forms of the hydrogen molecule exist based on temperature and pressure. At low temperature, hydrogen is a solid with a density of 70.6 kg/m^3 at -262 ℃. At higher temperatures, it is a gas with a density of 0.089886 kg/m^3 at 0 ℃ and a pressure of 1 bar. At -253 ℃, liquid hydrogen has a density of 70.8 kg/m^3 and is visible in a small zone that begins at the triple point and ends at the critical point in the above figure. Hydrogen is a gas at room temperature (298.15 K) (Züttel, 2004). At ambient temperature (298.15 K), hydrogen is a gas and can be described by the van der Waals equation:

$$p(v) = \frac{nRT}{v-nb} - a\frac{n^2}{v^2} \qquad (1.1)$$

Where p is the gas pressure, v is the volume, T the absolute temperature, n is the number of moles, R the gas constant (R = 8.314 J K^{-1} mol^{-1}), a is the dipole interaction or repulsion constant (a = 2.476×10^{-2} m^6 Pa mol^{-2}), and b is the volume occupied by the hydrogen molecules (b = 2.661×10^{-5} m^3 mol^{-1}).

Table 2. Shows the physical, chemical, and thermal properties of hydrogen at 25 ℃ (298.15 K) and atmospheric pressure (0.101325 MPa) (adapted from Ref. (Hydrogen - Thermophysical Properties, 2025)).

Properties	Units	Value
Molecular Weight		2.016
Specific Gravity		0.070
Specific Volume	m^3/kg	12.1
Density of liquid at atmospheric pressure	m^3/kg	71.0
Absolute viscosity	centipoises	0.009
Sound velocity in gas	m/s	1315
Specific heat (C_p)	J/kg-K	14310
Specific heat ratio (C_p/C_v)	-	1.405
Gas constant (R)	J/kg ℃	4126
Thermal conductivity	W/m ℃	0.182
Boiling point	℃K	20.4
Freezing or melting point at 1 atm	℃	-259.1

Properties	Units	Value
Latent heat of evaporation at boiling point	J/kg	447000
Latent heat of fusion	J/kg	58000
Critical temperature	°C	-240.0
Critical pressure	MPa	1.30
Critical volume	m^3/kg	0.033
Flammable		Yes
Heat of combustion	J/kg	$144x10^6$

The primary thermodynamic and physical characteristics of hydrogen at 25 °C and atmospheric pressure are given in **Table 2**. In addition to having a high specific volume and low density, hydrogen also has a high specific heat and thermal conductivity. It has exceptionally low boiling and critical temperatures. liquefaction requires cryogenic conditions and a lot of energy due to its high latent heat. Furthermore, hydrogen has a very high heat of combustion and is extremely combustible, emphasizing both its great energy potential and the importance of careful handling.

2. Hydrogen Production

The reason for shifting toward hydrogen technology is that it offers a clean, adaptable way to power the future. Hydrogen has a high energy density per kilogram and can be integrated with existing gas infrastructure, serving as both a climate solution and an economic opportunity. This promotes the development of new technologies and jobs, while supporting the global shift to net-zero emissions. Fossil fuels are readily available in nature, but hydrogen is produced from any primary energy source and used as fuel for direct combustion in an internal combustion engine or fuel cell, generating only water as a byproduct (Nikolaidis & Poullikkas, 2017). There are various methods for hydrogen production from (conventional) fossil fuels and renewable sources of energy, and to attain carbon neutrality, the sources must be renewable by necessity, and the production processes must utilize renewable energy sources (Martino et al., 2021).

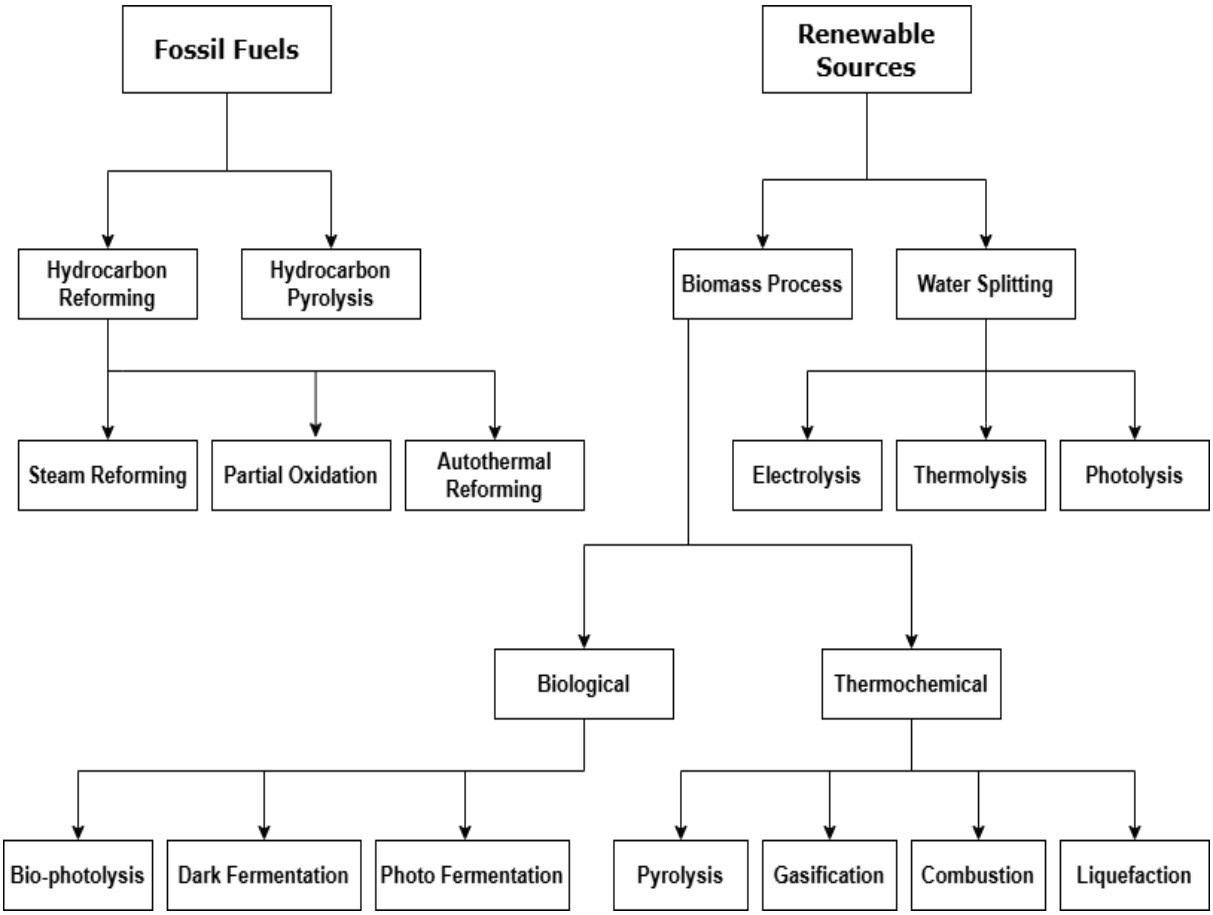

Figure 3. Hydrogen production methods (adapted from Ref. (Nikolaidis & Poullikkas, 2017)).

Approximately 98 % of global hydrogen production consists of gray and blue hydrogen (Usman & Yamada, 2025). Hydrogen produced from fossil fuels such as natural gas or coal without any carbon capture system (CCS) is known as gray hydrogen. In contrast, blue hydrogen is produced

with CCS technology to reduce its environmental impact. Green hydrogen is considered the cleanest option because it is produced via electrolysis using renewable energy sources. Pink hydrogen is generated by utilizing nuclear energy to power the electrolysis process (Usman & Yamada, 2025). The flow chart in **Figure 3** demonstrates the different processes of producing hydrogen, which include both conventional and non-conventional energy sources such as natural gas, coal, nuclear, biomass, solar, and wind.

2.1 Hydrocarbon Reforming Methods

The chemical process in which hydrogen-rich fuels (such as natural gas, methane, or other hydrocarbons) are converted into hydrogen gas using heat, a catalyst, and reactants like steam or oxygen. The reactants for the reforming process can be steam, resulting in the endothermic reaction known as steam reforming, or an oxygen reactant can lead to an exothermic reaction known as partial oxidation. The combination of these two reactions is referred to as the autothermal reaction (Chen et al., 2008).

2.1.1 Steam Reforming Method

Steam reforming is a catalytic conversion of hydrocarbons and steam into hydrogen and carbon dioxide. It includes various steps such as reforming, water-gas shift (WGS) reaction, and methanation or gas purification. Methane and natural gas, as well as various combinations of light hydrocarbons such as ethane, propane, butane, pentane, and both light and heavy naphtha, can be used as raw materials for the SMR process in the feedstock (Nikolaidis & Poullikkas, 2017).

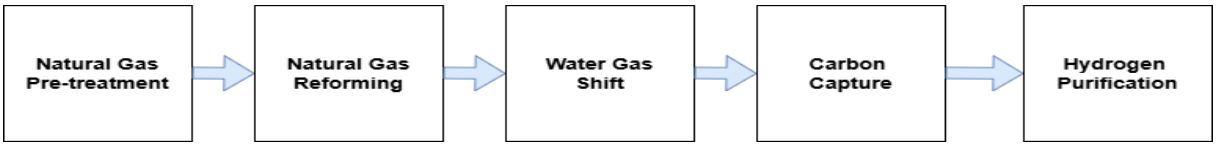

Pre-treatment is required for desulphurization because SMR is a catalytic conversion and catalysts are poisoned by a small amount of Sulphur. The Sulphur absorbed in the catalyst surface significantly reduces catalytic activity and plant efficiency (Chen et al., 2008). The mixture of raw material and steam enters a reformer, where it converts the raw materials into hydrogen and carbon dioxide in the presence of a catalyst bed at a lower temperature ranging from 350-550 °C (Jakobsen & Åtland, 2016). After passing through the reformer, the gas mixture undergoes a heat recovery step and enters a WGS reactor, where CO reacts with steam to produce additional hydrogen. Afterward, the mixture either goes through a CO_2-removal and methanation process or undergoes pressure swing adsorption (PSA), resulting in H_2 with a higher purity of nearly 100 % (Nikolaidis & Poullikkas, 2017).

The chemical reactions that take place in the steam reforming method are given in Equations 2.1 - 2.3.

Reformer: $$C_nH_m + nH_2O \rightarrow nCO + \left(n + \frac{1}{2}m\right)H_2 \quad (2.1)$$

WGS reactor: $$CO + H_2O \rightarrow CO_2 + H_2 \quad (2.2)$$

Methanation: $$CO + 3H_2 \rightarrow CH_4 + H_2O \quad (2.3)$$

The representation of n & m in the equation is based on choosing suitable raw materials; for instance, steam reforming of methane can be achieved by applying n = 1 and m = 4 to Equation 2.1. (Chen et al., 2008) evaluated that SMR is the most established and widely used technique for producing hydrogen on a large scale, which has a conversion efficiency of 74-85 %. Natural gas and steam are combined using a nickel-based catalyst to generate syngas at higher temperatures around 850-900 °C. The higher quality of hydrogen can be achieved through PSA, which separates it from other components. It is estimated that the process emits 0.3-0.4 m^3 CO_2 per cubic meter volume of hydrogen produced.

2.1.2 Partial Oxidation Method

Partial oxidation (POX) is a thermal process where a hydrocarbon reacts with a controlled, small amount of oxygen to produce syngas (H_2 + CO). Most large-scale systems incorporate an air separation plant to provide clean oxygen. POX consists of catalytic and non-catalytic processes. The catalytic process occurs at about 950 °C with methane to naphtha, and the non-catalytic process occurs at about 1150-1315 °C with methane, heavy oil, and coal (Nikolaidis & Poullikkas, 2017).

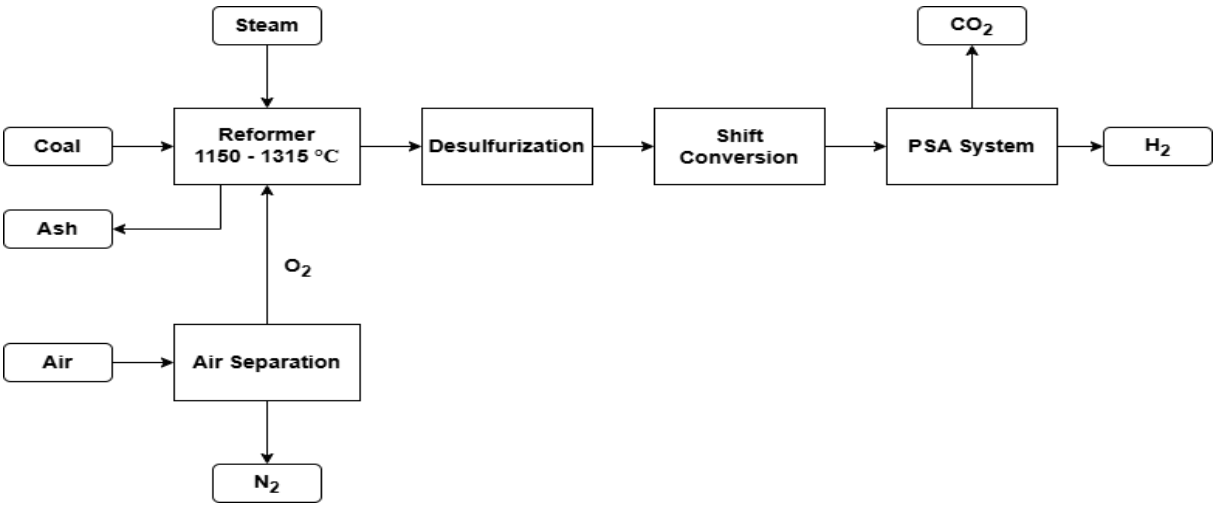

Figure 4. Flow diagram of the partial oxidation method (adapted from Ref. (Nikolaidis & Poullikkas, 2017)).

Reformer: $$C_nH_m + \frac{1}{2}nO_2 \rightarrow nCO + \frac{1}{2}mH_2 \text{ (Catalytic)} \quad (2.4)$$

$$C_nH_m + nH_2O \rightarrow nCO + \left(n + \frac{1}{2}m\right)H_2 \text{ (non-catalytic)} \quad (2.5)$$

WGS reactor: $$CO + H_2O \rightarrow CO_2 + H_2 \quad (2.6)$$

Methanation: $$CO + 3H_2 \rightarrow CH_4 + H_2O \quad (2.7)$$

The reforming processes, both catalytic and non-catalytic, are detailed in Eqs. 2.4 and 2.5, while the chemical reactions for WGS and methanation are illustrated in Eqs. 2.6 and 2.7.

2.1.3 Autothermal Reforming Method

Autothermal reforming (ATR) is a method of producing hydrogen and syngas by combining steam reforming and partial oxidation in a single reactor. The energy generated by the heat released from the POX reaction is sufficient to drive the steam reforming reaction, thereby rendering the process self-sustaining. ATR does not need an external furnace due to this internal heat balance. Hence, both SMR and POX reactions occur simultaneously (Jakobsen & Åtland, 2016). The reactors typically operate at temperatures ranging from 900 to 1150 °C, with pressure levels in the range of 0.1 to 8 MPa.

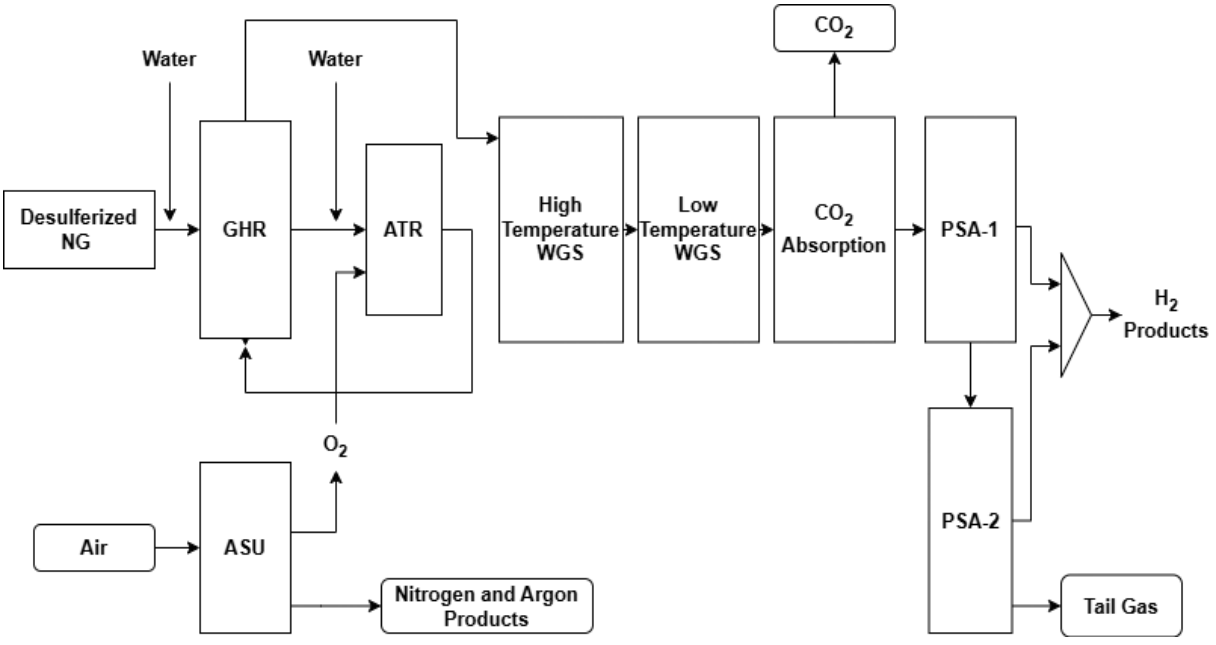

Figure 5. Flow diagram of Autothermal reforming method (adapted from Ref. (Jakobsen & Åtland, 2016)).

Figure 5 shows a process flow diagram of ATR, and the mechanism is explained in Eq. 2.8.

$$C_nH_m + \frac{1}{2}nH_2O + \frac{1}{4}nO_2 \rightarrow nCO + \left(\frac{1}{2}n + \frac{1}{2}m\right)H_2 \quad (2.8)$$

2.2 Hydrocarbon Pyrolysis

By definition, the process of thermal decomposition of hydrocarbons at high temperatures without the presence of oxygen is known as hydrocarbon pyrolysis. It is the method for producing low-cost and low-emission hydrogen. (Patlolla et al., 2023) has evaluated that hydrogen produced from the SMR method costs less than 1.452 €/kg. However, it emits 9-12 kg CO_2 eq. per kilogram of hydrogen and has a 48 % global market share

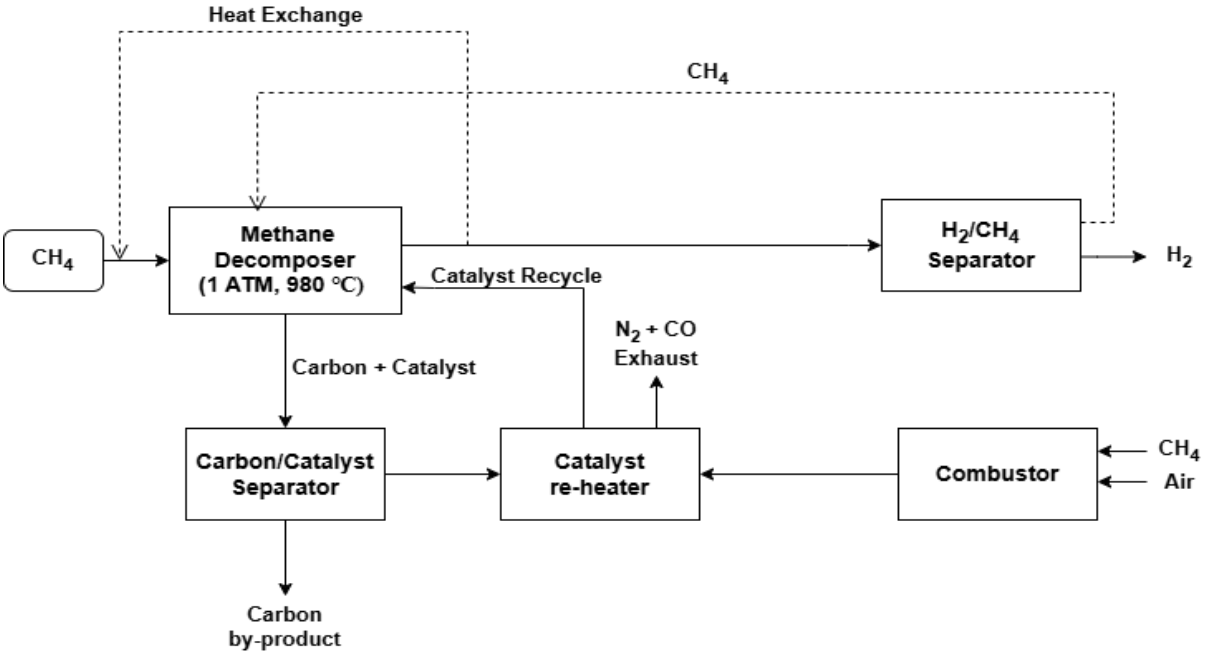

Figure 6. Flow diagram of methane pyrolysis method (adapted from Ref. (Nikolaidis & Poullikkas, 2017)).

Methane pyrolysis is an endothermic process that requires temperatures above 900 °C. Catalysts and pressure are two variables that can affect this process. According to Le Chatelier's principle, increasing the pressure of the methane pyrolysis reaction at the thermodynamic equilibrium state reduces the methane conversion and hydrogen generation. A higher reaction pressure reduces the rate of methane conversion under actual operating conditions that deviate from equilibrium, but it also increases the number of reactants in the reactor, which results in the production of additional hydrogen (Patlolla et al., 2023).

$$C_nH_m \rightarrow nC + \tfrac{1}{2}\, mH_2 \qquad (2.9)$$

The thermal decomposition follows the reaction outlined in Eq. 2.9. The end products of this process are solid carbon and hydrogen. The solid carbon byproducts can take various forms, ranging from highly specialized carbon nanotubes and fibers to ordered graphitic solids and amorphous carbon black. The water-gas shift and CO_2-removal stages, which are typically needed in conventional hydrogen production methods like SMR, gasification, and partial

oxidation, are not required here because this process does not produce CO or CO_2 gas as byproducts (Abbas & Wan Daud, 2010).

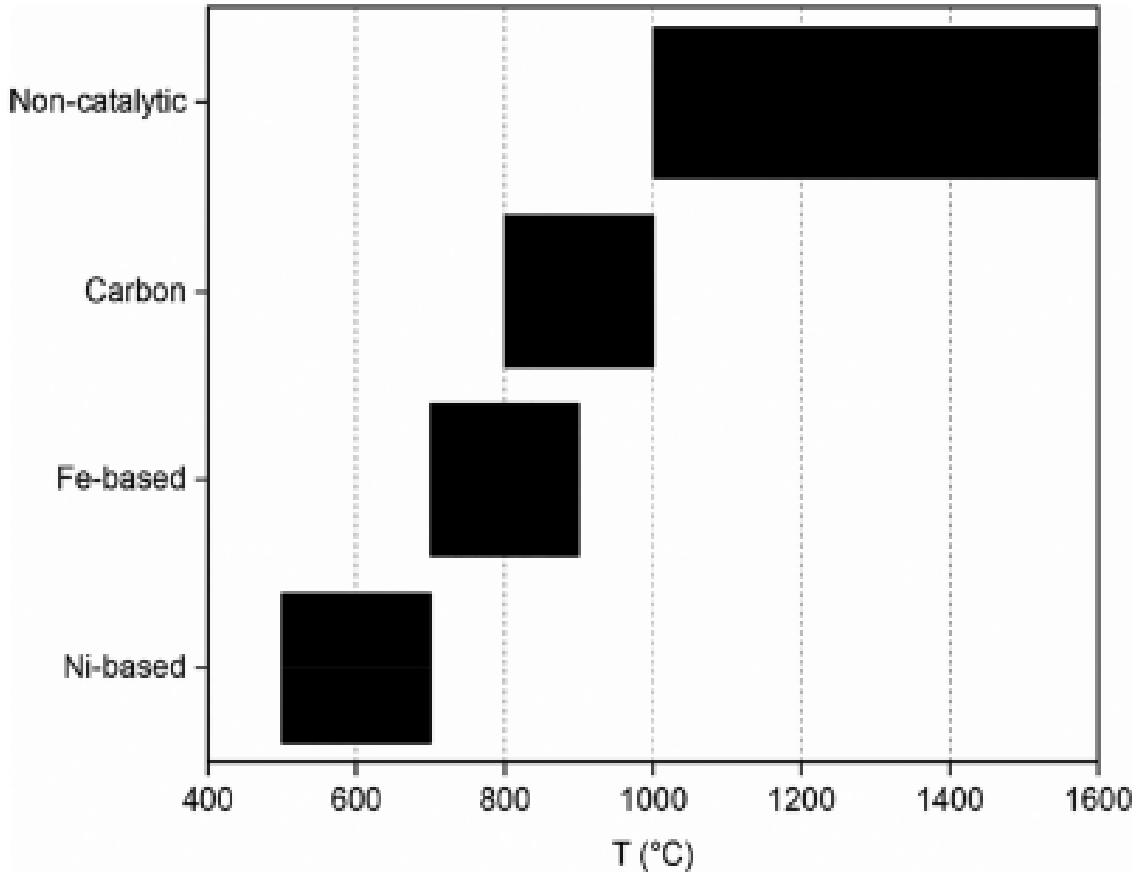

Figure 7. Temperature range of applicability of different catalysts for methane pyrolysis (adapted from Ref. (Patlolla et al., 2023)).

Rapid loss of catalytic activity is promoted by any factor that accelerates methane breakdown without proportionally increasing the rate of carbon transfer. Carbon materials require higher operating temperatures, typically between 800 and 1000°C, and are less active than metal catalysts, as shown in **Figure 7**. The ideal working temperature varies depending on the type of metal catalyst. Nickel-based catalysts are more active at high temperatures than iron-based catalysts, but deactivate more quickly (Sánchez-Bastardo et al., 2021). Due to these differences, studies involving nickel materials are conducted at a lower temperature range (500-700 °C) than those involving iron catalysts (700-900 °C). Temperatures between 1000 and 1600 °C are necessary for non-catalytic hydrocarbon pyrolysis, which is entirely powered by thermal energy.

3. Renewable Sources

Currently, 85 % of the world's energy needs are met by carbon-based fuels. Annually, over 36 billion tons of CO_2 are released into the atmosphere to fulfill energy demands (Worku et al., 2024). Fossil fuels account for more than 90 % of these emissions, and this percentage is expected to increase in the future. Due to the depletion of fossil fuels and the impacts of climate change, transitioning to renewable energy has become essential. It offers a sustainable alternative to hydrogen derived from fossil fuels, allows for the storage of intermittent renewable electricity, and encourages the decarbonization of transportation and heavy industries. Various methods for producing hydrogen from renewable resources are outlined here.

3.1 Biomass Source

Biomass is derived from organic materials that absorbed carbon from the atmosphere; it is a significant renewable source of hydrogen production. Agricultural waste, wood residues, algae, food waste, and other plant-based materials are forms of biomass. Depending on the type of biomass and the technique utilized, it can be processed in several ways when used to produce hydrogen (Demirbaş, 2001a). There are two ways to produce hydrogen from biomass: thermochemical and biological. Biological processes produce modest rates and yields (mol H_2/mol feedstock) of hydrogen, depending on the raw materials utilized, despite being less energy-intensive and more ecologically friendly due to their mild operating conditions (Kalinci et al., 2009). Wood and wood waste account for 64 % of biomass energy production on average, followed by municipal solid waste (MSW) 24 %, agricultural waste 5%, and landfill gases 5 % (Demirbaş, 2001a). About 60-90 % less trash is placed in landfills when it is burned for energy. Additionally, this lowers land costs. Cellulose, lignin, and hemicellulose constitute 43 %, 36 %, and 22 % of wood, respectively. Dry wood normally produces 52 % of carbon, 6.3 % of hydrogen, and 0.4 % of nitrogen (Demirbaş, 2001b).

3.2 Thermochemical Process

The thermochemical process of biomass involves producing hydrogen through heat, often combined with pressure, catalysts, or controlled oxygen, to convert solid biomass such as wood, agricultural waste, algae, or other biomass into a hydrogen-rich gas. This conversion, which converts biomass and greenhouse gases into hydrogen, has gained significant attention as scientists develop environmentally friendly, cost-effective, and highly efficient thermochemical techniques. New technologies are being explored for thermochemical hydrogen production with minimal or net-zero carbon emissions. Catalysts fasten the hydrogen production process while

reducing the formation of tar and other byproducts. Additionally, catalysts allow the process to be carried out at lower temperatures, decreasing the reliance on high-energy inputs.

Thermochemical conversion processes can be subdivided into gasification, pyrolysis, combustion, and liquefaction (Nikolaidis & Poullikkas, 2017). Gasification and pyrolysis are the two primary processes in thermochemical technology. Among other gaseous products, both conversion methods yield CO and CH_4, which can be further processed for additional hydrogen production using the WGS reaction and SMR. In addition to these methods, liquefaction and direct combustion are two more undesirable approaches because they both produce limited hydrogen, with the latter requiring challenging operating conditions of 5-20 MPa in the absence of oxygen and the formation of hazardous byproducts (Ni et al., 2006).

3.2.1 Hydrogen from Biomass Pyrolysis

Biomass pyrolysis is a thermochemical process that produces gases, liquids, and char by heating biomass without oxygen. The biomass decomposes into volatile molecules during this process, which then crack and reform to produce syngas that is rich in hydrogen. Pyrolysis is the thermal conversion of biomass at 650-800 K and 0.1-0.5 MPa in the absence of air/oxygen. It produces gaseous products such as H_2, CH_4, CO, CO_2, and other gases, depending on the organic composition of the biomass (Ni et al., 2006).

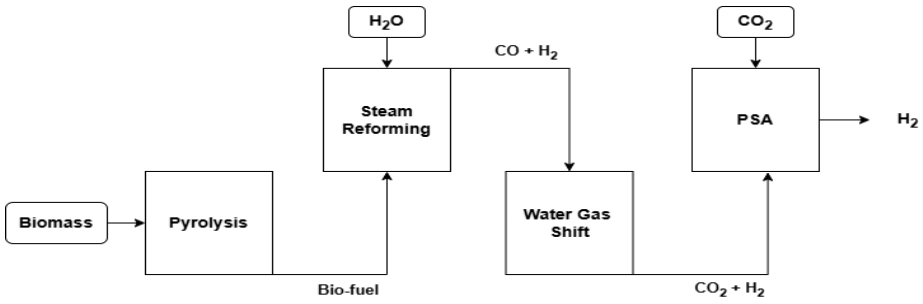

Figure 8. Process flow diagram of hydrogen production from Biomass pyrolysis (adapted from Ref. (Das & Datta Peu, 2022)).

The liquid products mainly consist of tar and oils that remain in the liquid form at room temperature, including compounds like acetone and acetic acid. The solid products are primarily char, which is mostly pure carbon along with other inert materials. Overall, pyrolysis converts biomass into gas, liquid, and solid fractions through thermal decomposition without oxygen. Steam reforming can be performed for methane and hydrocarbon gases, and the WGS reaction is used to produce even more hydrogen. Following the conversion of CO into CO_2 and H_2, PSA releases the desired purified hydrogen (Iribarren et al., 2014). The different steps of biomass pyrolysis are given in equations below:

Biomass pyrolysis: $H_2 + CO + CO_2 + hydrocarbon\ gases + tar + char$ (3.1)

$$C_nH_m + nH_2O \rightarrow nCO + \left(n + \frac{1}{2}m\right)H_2 \quad (3.2)$$

WGS reactor: $$CO + H_2O \rightarrow CO_2 + H_2 \quad (3.3)$$

3.2.2 Hydrogen from Biomass Gasification

The thermochemical transformation of biomass into a gaseous fuel (syngas) in a gasification medium, such as air, oxygen, or steam, is known as biomass gasification. It occurs at temperatures between 500 °C and 1400 °C, with operating pressures ranging from ambient to 3.3 MPa, depending on the size of the plant and the size of the plant and the intended use of the syngas produced. The types of reactors are differentiated based on the flow and velocity (Nikolaidis & Poullikkas, 2017). Gasification is carried out at high temperature to maximize gas output. The resultant gas, referred to as producer gas, has a blend of carbon dioxide, nitrogen, hydrogen, methane, and carbon monoxide (Demirbaş, 2001a). Fixed-bed and fluidized-bed reactors are types of gasifiers. When compared to fluidized bed reactors, fixed bed reactors often create lower concentrations of dust and particles in the product gas, and they are also more economical (Megía et al., 2021). Cracking reaction and lowering the activation energy, using a catalyst during the gasification process will lower the energy consumption. Noble metal, mineral, or alkali metal catalysts are among the various types of catalysts used for this process. These catalysts stand out from all Ni-based catalysts due to their high activity and low cost, which is why they are widely employed for biomass catalytic gasification. Equations 3.4 and 3.5 depict the conversion of biomass into syngas when it reacts with air or steam, respectively (Nikolaidis & Poullikkas, 2017).

$$Biomass + Air \rightarrow H_2 + CO_2 + Co + N_2 + CH_4 + other\ CHs + tar + H_2O + char \quad (3.4)$$

$$Biomass + Steam \rightarrow H_2 + CO_2 + Co + N_2 + CH_4 + other\ CHs + tar + H_2O + char \quad (3.5)$$

3.3 Biological Process

Under mild conditions, microorganisms are used in biological processes to produce hydrogen from biomass. The majority of biological processes consume less energy since they function at room temperature and pressure. Additionally, they capitalize on limitless renewable energy sources and aid in trash recycling by using a variety of waste products as feedstock (Nikolaidis & Poullikkas, 2017). The primary bioprocess technologies used to produce hydrogen are

photolytic hydrogen production from water by cyanobacteria or green algae (also called direct photolysis), dark fermentative hydrogen production during the acidogenic phase of anaerobic digestion of organic material, photo fermentative processes, two-stage dark fermentative, and hydrogen production by WGS (Holladay et al., 2009). Water for photolysis processes, where hydrogen is produced by some bacteria or algae directly, and biomass for fermentative processes, where the carbohydrate-containing materials are converted to organic acids and then to hydrogen gas by using bio-processing technologies, serve as the feeds for biological hydrogen.

3.3.1 Bio-Photolysis Process

Photosynthetic bacteria split water and produce hydrogen using sunlight, which is known as bio-photolysis. By utilizing their photosystems to collect light energy, organisms like cyanobacteria and green algae produce electrons that are directed toward the hydrogenase. Protons (H^+) are then reduced by these enzymes to create molecular hydrogen (Hallenbeck, 2002). There are two types of bio-photolysis: direct bio-photolysis, in which water is directly split into H_2 and O_2, and indirect bio-photolysis, in which organisms initially generate biomass or carbohydrates under certain circumstances and convert them into hydrogen.

3.3.1.1 Direct Bio-Photolysis

Green algae use photosynthesis to split water molecules into hydrogen and oxygen ions during direct bio-photolysis (Nikolaidis & Poullikkas, 2017). The hydrogenase enzyme then transforms the produced hydrogen ions into hydrogen. Because of the enzyme's extreme sensitivity to oxygen, the oxygen content must be kept below 0.1 %. The hydrogen in this reaction is bound in the plastoquinone (pqH_2) molecule (Sorensen 30-35).

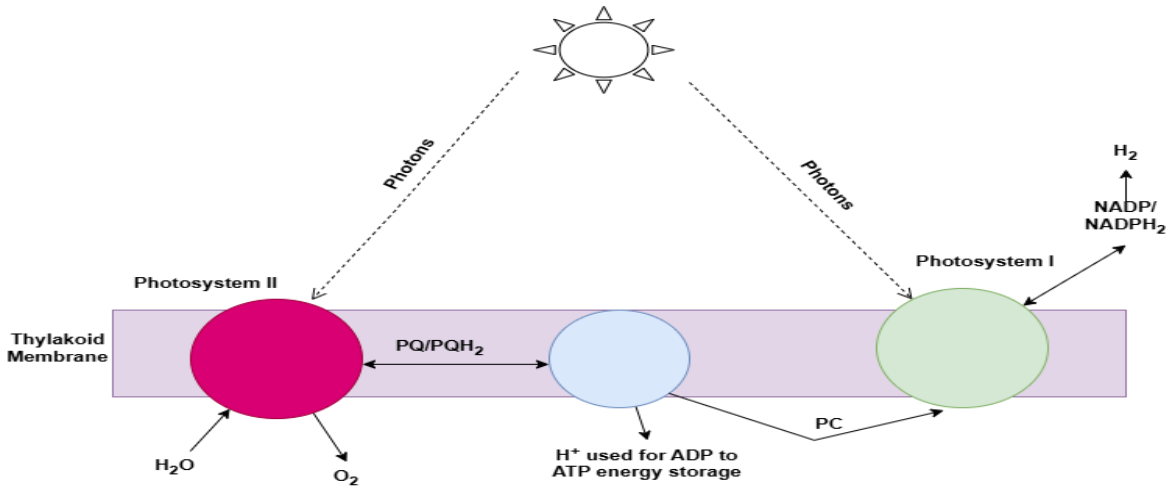

Figure 9. Schematic diagram of direct bio-photolysis (adapted from Ref. (Holladay et al., 2009))

The stored energy from pqH2 is transferred to plastocyanin (Pc) via cytochrome b6f, which receives pqH_2 across the membrane. Photosystem II reuses the recycled pqH_2, as shown in **Figure 9**. Photosystem I absorb additional sunlight and uses it to transfer the chemical energy in Pc to ferredoxin (Fd), where NADP+ is converted into $NADPH_2$ using Fd. The conversion of CO2 into carbohydrates occurs through $NADPH_2$ via the Benson-Bass-Calvin cycle. However, under anaerobic conditions, some organisms use the enzyme hydrogenase to release extra electrons by converting hydrogen ions in Fd into hydrogen gas (Hallenbeck, 2002; Holladay et al., 2009). The following generic reaction can be used to illustrate hydrogen production through direct bio-photolysis (Nikolaidis & Poullikkas, 2017).

$$2H_2O + light\ energy \rightarrow 2H_2 + O_2 \qquad (3.6)$$

3.3.1.2 Indirect bio-photolysis

The indirect bio-photolysis process includes a two-stage biological process, where photosynthetic microorganisms such as algae or cyanobacteria absorb sunlight and CO_2 to initially produce biomass, which is subsequently converted into hydrogen under specific circumstances. When separating the evolution of hydrogen and oxygen in space and/or time, issues with the sensitivity of the hydrogen evolving process in indirect bio-photolysis can potentially be avoided, as shown in **Figure 10** (Hallenbeck, 2002). The following reactions, 3.7 and 3.8, can be used to illustrate the overall process by which cyanobacteria or blue-green algae produce hydrogen from water (Nikolaidis & Poullikkas, 2017).

$$12H_2O + 6CO_2 + light\ energy \rightarrow C_6H_{12}O_6 + 6O_2 \qquad (3.7)$$

$$C_6H_{12}O_6 + 12H_2O + light\ energy \rightarrow 12H_2 + 6CO_2 \qquad (3.8)$$

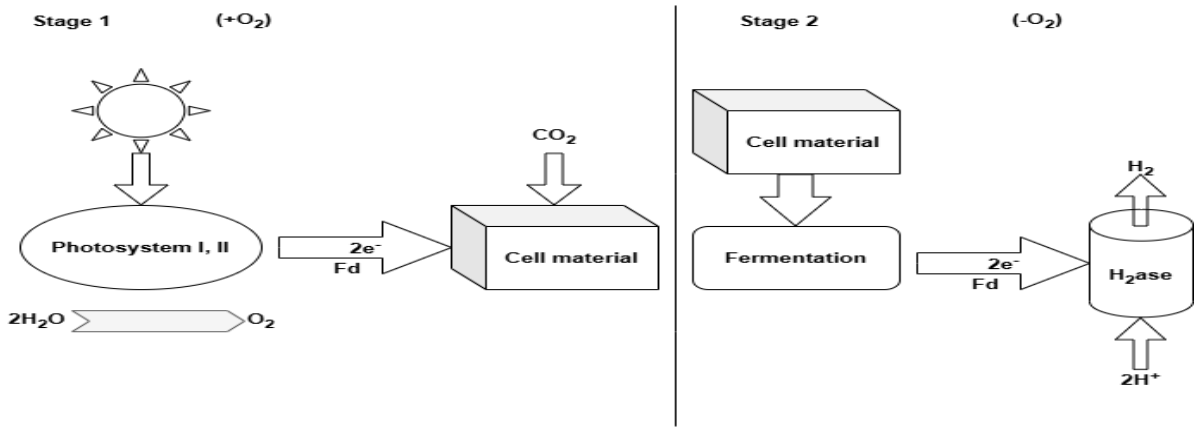

Figure 10. Two-stage indirect bio-photolysis process (adapted from Ref. (Hallenbeck, 2002)).

In terms of utilizing water as a renewable resource and CO_2 consumption as one of the air pollutants, algal H_2 production could be regarded as a cost-effective and sustainable solution.

However, the primary disadvantages of this bio-hydrogen generation technology are its low hydrogen production potential, large surface area to absorb enough light, and no waste utilization (Kapdan & Kargi, 2006).

3.3.2 Dark Fermentation

Fermentations are biochemical processes that occur with or without oxygen and carry out microbial transformations of organic feed materials to produce CO_2, alcohols, acetone, and H_2 in trace amounts. These techniques employ waste materials to produce energy at a low cost while simultaneously handling waste, making them an appealing way to produce bio-hydrogen (Balthasar, 1984).

Dark fermentation involves growing carbohydrate-rich substrates in the dark, mainly with anaerobic bacteria. However, some algae are also used in this conversion process. The biomass used in fermentative processes must be affordable, widely available, biodegradable, and high in carbohydrates. Although pure, simple sugars like lactose and glucose, which are quickly biodegradable, are preferred, they are either expensive or difficult to produce in large quantities (Holladay et al., 2009).

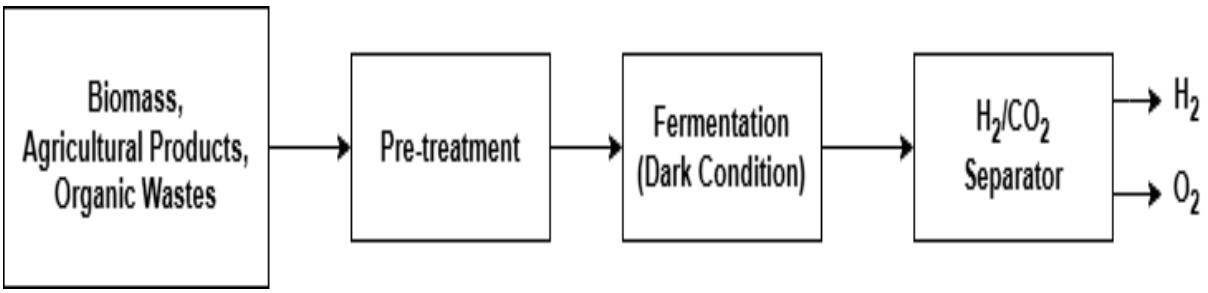

Figure 11. Process flow diagram of dark fermentation (adapted from Ref. (Nikolaidis & Poullikkas, 2017)).

Considering glucose as the model substrate, acetic and butyric acids account for more than 80 % of all end products, as shown in Eqs. 3.9 and 3.10. Theoretically, the yields of H_2 in acetate and butyrate type fermentation are 4 and 2 mol per mole of glucose, respectively (Nikolaidis & Poullikkas, 2017).

$$C_6H_{12}O_6 + 2H_2O \rightarrow 2CH_3COOH + 4H_2 + 2CO_2 \text{(Acetate fermentation)} \quad (3.9)$$

$$C_6H_{12}O_6 + 2H_2O \rightarrow CH_3CH_2CH_2COOH + 2H_2 + 2CO_2 \text{(Butyrate fermentation)} \quad (3.10)$$

3.3.3 Photo Fermentation

In the biological process of photo fermentation, photosynthetic bacteria use sunlight energy to produce hydrogen from organic substrates (Hallenbeck, 2002). In contrast to bio-photolysis, photo fermentation does not directly split water; instead, bacteria like *Rhodobacter* and *Rhodospirillum* use light to generate energy for enzymes, mainly nitrogenase, that degrade butyric acid or organic acids (Kapdan & Kargi, 2006). Water is transformed into protons, electrons, and O_2 by sunlight. When protons and electrons react with nitrogen and ATP (Adenosine Triphosphate) in the presence of nitrogenase catalyst results in ammonia, hydrogen, and ADP (Adenosine Diphosphate) (Holladay et al., 2009).

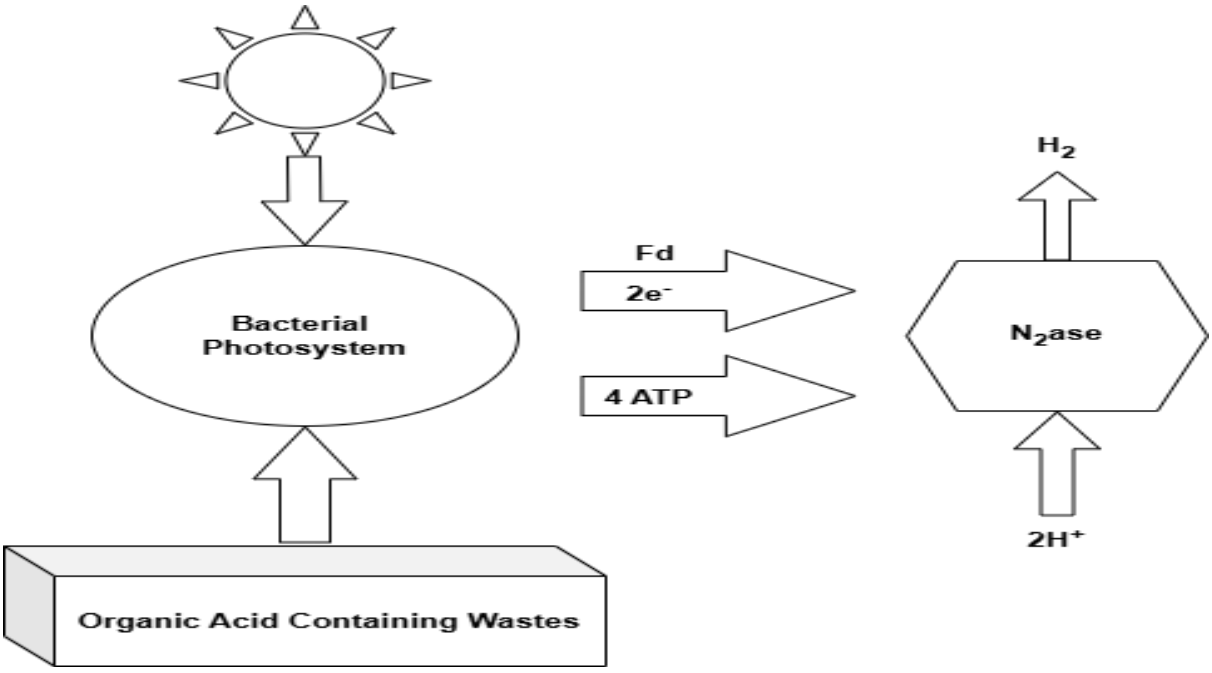

Figure 12. Schematic diagram of photo fermentation (adapted from Ref. (Hallenbeck, 2002)).

The complete conversion into hydrogen using acetic acid as the reactant is shown below (Nikolaidis & Poullikkas, 2017):

$$CH_3COOH + 2H_2O + light\ energy \rightarrow 4H_2 + 2CO_2 \qquad (3.11)$$

The nitrogenase enzyme's slowness, the process's comparatively high energy requirements, hydrogen re-oxidation, and the scarcity of organic acids are the drawbacks of this process. Maintaining the right ratio of carbon to nitrogen nutrients is necessary to boost nitrogenase activity and lower energy requirements (Holladay et al., 2009).

3.4 Water Splitting

Water is one of the most abundant and affordable resources on Earth and can serve as a clean, environmentally friendly source. Researchers have considered water splitting to be the most

promising technique for hydrogen production. Furthermore, the water splitting mechanism is an advanced method for increasing water splitting efficiency and consequently producing a higher yield of hydrogen (Rafique et al., 2020). Hydrogen can become one of the most environmentally friendly energy sources available to humanity, provided that the energy required to produce it is supplied by renewable sources. The various water splitting methods or techniques are described below:

3.4.1 Electrolysis

Electrolysis mainly refers to the process of applying an electric current to split water (H_2O) into hydrogen (H_2) and oxygen (O_2). The process is carried out in an electrolyzer, which has two electrodes: the anode, which releases O_2, and the cathode, which produces H_2. The bonds that hold hydrogen and oxygen atoms together are broken when electricity flows through water. Electrolytes, such as acids, bases, or salts, are frequently added to pure water to increase conductivity because pure water does not conduct electricity well. The purity of hydrogen from this method is around 99.999 vol. %. Such purity levels have a significant advantage over both fossil fuels and biomass-based methods since electrolytic hydrogen can potentially be used directly in low-temperature fuel cells. The processing cost per kilogram of hydrogen varies from 3 to 15 €, depending on the size of the electrolysis system. The biggest electrolytic hydrogen production facilities in the world have historically been situated near hydroelectric facilities to capitalize on the supply of power during cheap hours (Ursua et al., 2012).

The process enthalpy change ΔH determines the energy needed for the water electrolysis reaction while an electrolytic cell operates at constant temperature and pressure. A portion of the energy must be electric. This part relates to the shift in Gibbs' free energy, ΔG. The remaining amount is thermal energy Q, which is equal to the product of the entropy change, ΔS, and the process temperature, T. The relationship between these thermodynamic magnitudes is expressed as follows (Ursua et al., 2012):

$$\Delta G = \Delta H - Q = \Delta H - T\Delta S \tag{3.12}$$

Water is the reactant in the electrolysis process, and direct current allows it to split into hydrogen and oxygen.

Anode: $$H_2O \rightarrow \frac{1}{2}O_2 + 2H^+ + 2e^- \tag{3.13}$$

Cathode: $$2H^+ + 2e^- \rightarrow H_2 \tag{3.14}$$

Overall: $$H_2O \rightarrow H_2 + \frac{1}{2}O_2 \tag{3.15}$$

Alkaline water electrolysis (AWE), solid oxide water electrolysis (SOE), alkaline anion exchange membranes (AEMs), and proton exchange membranes (PEMs) are the various electrolyte systems designed for water electrolysis. These systems employ various materials and operating circumstances, but the underlying concepts remain the same. Low and high-temperature water electrolysis are also feasible based on varying operating temperatures (Chi & Yu, 2018).

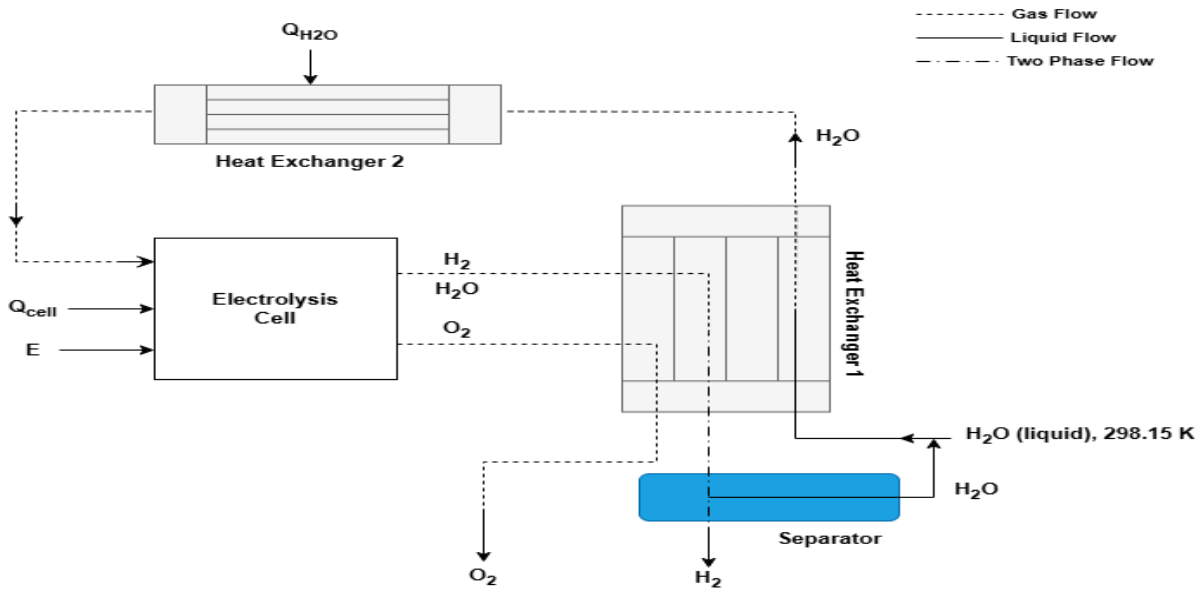

Figure 13. The schematic diagram of the electrolysis system for hydrogen production (adapted from Ref. (H. Zhang et al., 2010)).

The diagram illustrated in **Figure 13** shows a typical water electrolysis system used to produce hydrogen. An electrolysis cell, a separator, and two heat exchangers constitute the majority of the system. It can be connected to any power generation system and effectively utilizes the waste heat contained in the products. The model developed here is more rational and broader. In order to drive the water splitting reaction, the electrolysis cell is supplied with water, energy, and heat. The generated hydrogen and residual water flow out at the cathode of the electrolysis cell, while the generated oxygen flows out at the anode. It is preferable to recover the waste from the products using heat exchanger 1 since a significant portion of the heat delivered to the feed water remains in the products at the outlet. Oxygen can be utilized as a byproduct once it has cooled down to reference conditions (298.15 K and 101.325 kPa) after exiting heat exchanger 1. H_2 and H_2O enter the separator, where the hot water is circulated at reference conditions for the subsequent hydrogen production cycle. The water supply is further heated through heat exchanger 2 before reaching the temperature of the electrolysis cell because of the inefficiency of exchanger 1 and the different thermodynamic characteristics of the reactant and products (H. Zhang et al., 2010).

Table 3. Comparison of different types of electrolyzer technologies (adapted from Ref. (El-Shafie, 2023)).

Specification	AWE	PEM	SOEC	AEM
Technology maturity	Mature	Commercial	R&D	R&D
Cell temperature, °C	65-100	70-90	900-1000	50-70
Cell pressure, bar	25-30	30-80	<30	-30
Current density, mA/cm^2	200-500	800-2500	300-1000	200-500
Cell voltage, V	1.8-2.4	1.8-2.2	0.95-1.3	1.8-2.2
Voltage efficiency, %	50-70.8	48.5-65.5	81-86	39.7
Specific system energy consumption, kWh/Nm^3	4.5-7.5	5.8-7.5	2.5-3.5	4.8-5.2
Hydrogen production, Nm^3/hr	<760	0.265-30	-	0.25-1
Stack lifetime, hr	10000	<20000	<40000	NA
Electrolyte	20-30 % KOH	Perflurosulfonated acid (PFSA)	Yttria-stabilized Zirconia (YSZ)	DVB polymer support with KOH or $NAHCO_3$
Separator	Asbestos, Nio, ZrO_2, stabilized with PPS mesh	PFSA (e.g., Nafion)	Solid electrolyte	Quaternary ammonia
Charge carrier	OH^-	H^+	O_2^-	OH^-
OER catalyst	Ni-coated perforated stainless steel	Ir/Ru oxide	Perovskite-type	CO_3O_4
HER catalyst	Ni	Platinum	Ni/YSZ	Ni
Hydrogen purity, vol. %	99.3-99.9	99.999	-	99.99
Capital cost, €/kW	1000-1200	1860-2320	>2000	NA

The values illustrated in **Table 3** offers a comparative summary of the primary water electrolysis technologies, such as AWE, PEM, SOEC, and AEM, which emphasize their operating conditions, performance attributes, materials used, and costs. It provides information on the variations in technological maturity, efficiency, energy use, operating temperature and pressure, catalyst used, and hydrogen purity. This helps to identify the trade-offs among the cost, efficiency, operating complexity, and technological readiness from this comparison, as well as how each technology is appropriate for various applications and development phases.

4. Environmental Impact of Hydrogen Production Methods

The increased use of fossil fuels in recent decades has raised concerns among international researchers about their negative effects on the environment and human health. This is mainly caused by the emission of toxic greenhouse gases such as CO_2, SO_2, and H_2S. Several harmful effects, including respiratory issues, climate change, global warming, and reduced crop yields, are becoming more common due to unusual greenhouse gas emissions into the atmosphere. The Earth's average temperature is expected to rise by 1.25, 2.2, 3.5, and 5.4 degrees Celsius by the end of 2025, 2050, 2075, and 2100, respectively, driven by the increase in atmospheric carbon dioxide levels (Nnabuife et al., 2023).

The impacts of hydrogen production methods on the environment vary greatly. The SMR process, which produces gray hydrogen from natural gas, releases a large amount of carbon dioxide and significantly contributes to climate change. Although methane leakage during gas extraction remains a concern, blue hydrogen is made using SMR with CCS, which reduces some emissions. Green hydrogen is considered the most environmentally friendly option because it is produced using renewable energy and results in very few emissions. However, green hydrogen requires large amounts of clean electricity and water, which can strain local resources if not managed carefully.

(Osman et al., 2022) evaluated that the color coding is inaccurate because it assumes green hydrogen has lower carbon emissions than blue or gray hydrogen. For example, the thermochemical conversion of bioenergy feedstock like biomass emits greenhouse gases such as CH_4, SOx, NOx, and CO_2. Additionally, CCS methods reduce carbon emissions when producing blue hydrogen. There are mainly two impacts characterized based on the assessment. The impact of human emissions on the radiative forcing of the atmosphere is known as the global warming potential (GWP), and it results in climate change that may have an impact on ecosystems and human health. GHG emissions affect the Earth’s surface temperature via intensifying radiative forcing, often known as the “greenhouse effect”. The unit of measurement for GWP is kg CO_2-eq. The natural environment, the anthropogenic environment, human health, and natural resources are all impacted by acidification potential (AP), which is associated with the deposition of acidifying pollutants on surface waters, groundwater, soil, ecosystems, materials, and biological organisms. The main causes of AP are SO_X, NO_x, and NH_X, which are expressed in kg SO_2-eq. Depending on the sources and processing stages involved, emissions from the materials utilized in various hydrogen production techniques vary significantly. Natural gas is necessary for SMR, and both the extraction process and the

reforming process itself produce enormous quantities of carbon dioxide and methane emissions. Electrolysis powered by renewable energy sources may significantly reduce emissions. Water used in electrolysis contributes less in terms of direct emissions, but depending on the energy source, water treatment and purification can increase the footprint.

(Spath & Mann, 2000) evaluated that CO_2 emissions constitute 99 % by weight of all air emissions, which is the largest amount. The system GWP is 89.3 %, which is the sum of CO_2, CH_4, and N_2O emissions expressed as CO_2-equivalency over 100 years. Methane accounts for 10.6 % of the GWP from the total system GWP, i.e., 11,888 g CO_2-equivalent/kg of the hydrogen produced.

Table 4. Breakdown GHG emissions by different sources of the system involved in the SMR plant (adapted from Ref. (Spath & Mann, 2000)).

	Total (g/kg of H_2)	% from construction & decommissions (a)	% from natural gas production & transport	% from electricity generation	% from H_2 plant operation	% from avoided operation (b)
Greenhouse gas emissions (CO_2-eq)	11888	0.4	25	2.3	74.8	-2.5

(a) Construction and decommissioning include plant construction and decommissioning as well as construction of the natural gas pipeline.

(b) Avoided operations are those that do not occur because excess steam is exported to another facility.

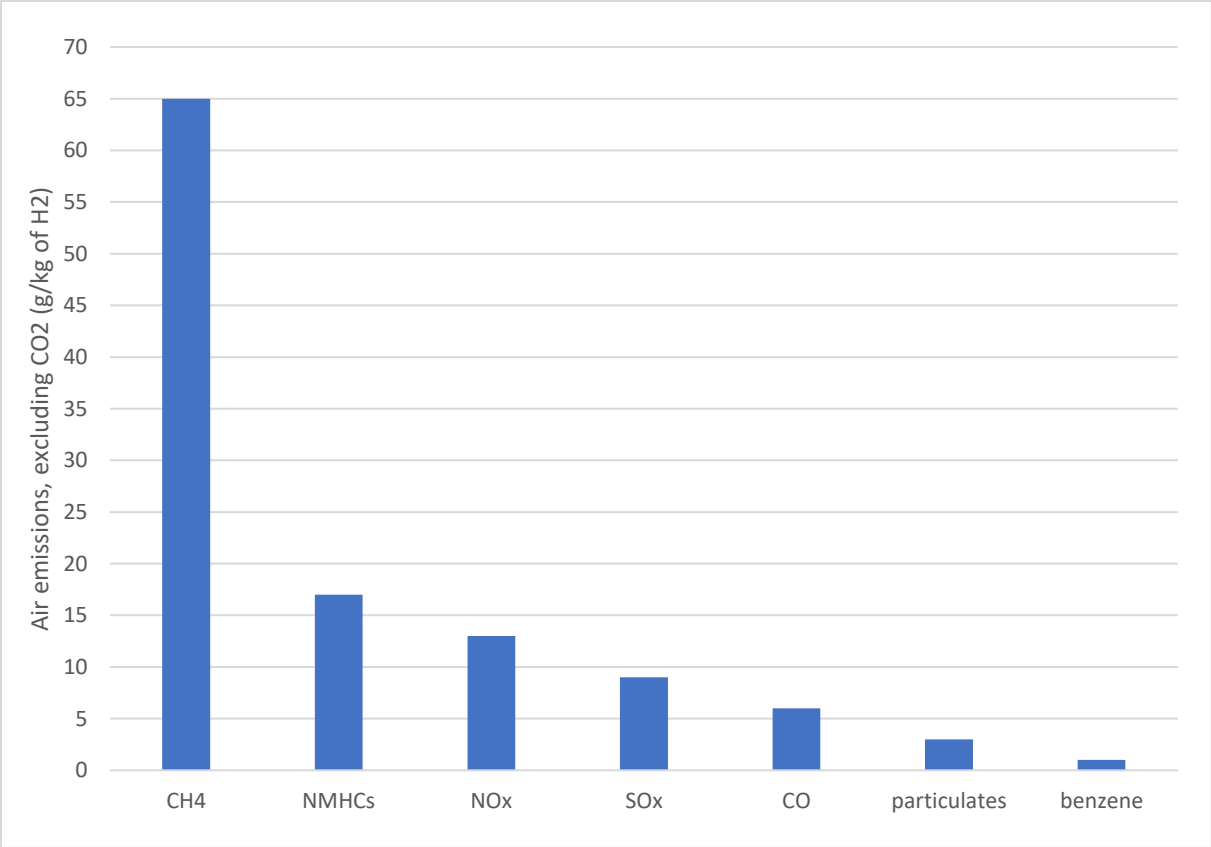

Figure 14. Various GHG emissions excluding carbon dioxide (adapted from Ref. (Spath & Mann, 2000)).

Methane is released in the second-highest amount after CO_2, followed by non-methane hydrocarbons (NMHCs), NO_x, SO_x, Co, particulates, and benzene, as shown in **Figure 14**. The production and distribution of natural gas are the main causes of these air pollutants. The most-consumed resource is natural gas, followed by coal, iron, limestone, and oil. Additionally, there is a significant amount of water consumption because of the requirement of steam and the shift conversion reaction in SMR (Spath & Mann, 2000).

(Mann & Spath, 2004) presented that water is used in upstream procedures alongside the electrolysis processes. It uses 26.7 liters of water to produce 1 kilogram of hydrogen. The electrolyzer uses about 45 % of it, whilst wind turbines and hydrogen storage tanks utilize 38 % and 17 %, respectively. The production of steel and concrete for the wind turbines and hydrogen storage accounts for 77 % of the CO_2 in the system. Particulates are the next most common air pollutant after CO_2. These are mostly obtained from the quarrying of the limestone and sand required to make concrete, and 85 % of the particle emissions come from the manufacture of concrete for the wind turbines. SO_X accounts for 26 % of the total air emissions during the electrolysis process, whereas NO_x accounts for 47 %.

Table 5. Average air emissions emitted from the electrolysis system (adapted from Ref. (Mann & Spath, 2004)).

Air emission	System total (g/kg of H_2)	from wind turbines	from electrolysis	from storage
CO_2	950	78.1	4.4	17.5
CO	0.9	80.3	3.5	16.2
CH_4	0.3	92.4	2.8	4.8
N_2O	4.7	45.9	47.1	7.0
NO_x	0.05	67.1	5.6	27.3
NMHCs	4.4	62.5	7.3	30.1
Particulates	28.7	94.2	0.7	5.0
SO_x	6.1	61.8	26.1	12.1

(Wulf & Kaltschmitt, 2012) evaluated the entire life cycle of hydrogen production at a German hydrogen refueling station. At least half of the hydrogen produced in this station comes from on-site water electrolysis using renewable resources like wind. The remaining 50 % of the hydrogen is provided by trucks from a large-scale production facility that produces hydrogen from glycerol as a byproduct of producing diesel. Up to 99.8 % of the emissions from hydrogen produced by electrolysis derive from the German grid, and up to 96.8 % derive from green electricity. The manufacturing of the electrolyzer and hydroxide is responsible for the insignificant amount. As anticipated, electrolysis using green electricity and wood biomass can produce the lowest emissions. The GWP values are 32, 4.1, 4.1, and 12.9 kg CO_2 eq./kg H_2 for grid electricity electrolysis, green electrolysis, wood gasification, and steam methane reforming, respectively. However, environmental effects, such as changes in land usage if biomass wood gasification is employed, might need to be examined. Despite using a renewable resource, the emissions from pyro-reforming glycerol are surprisingly large, compared to those from coal gasification (approximately 23 kg CO_2 eq./kg H_2).

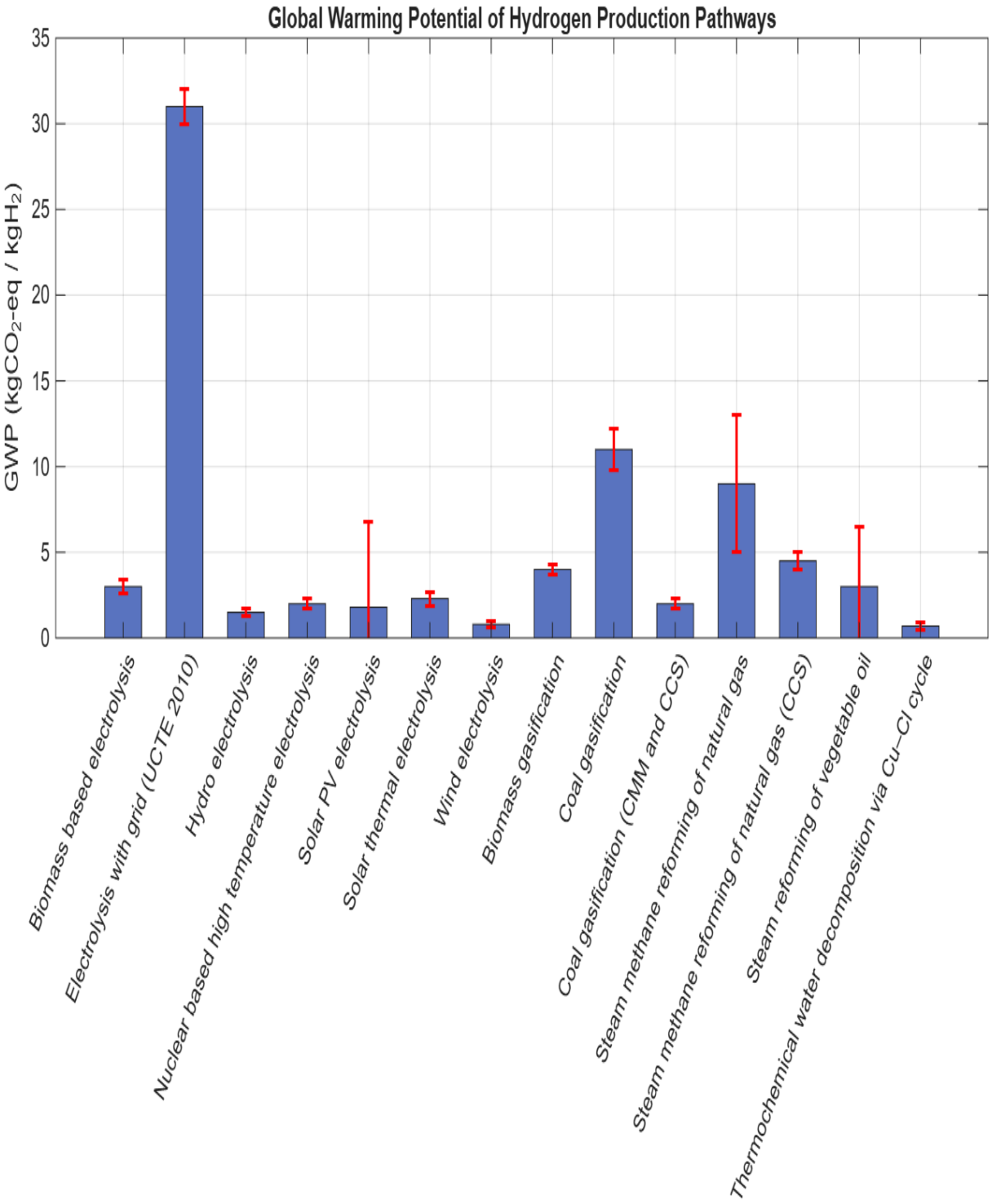

Figure 15. Average GWP emissions by different production methods (adapted from Ref. (Bhandari et al., 2014)).

The graphical comparison illustrated in **Figure 15** compares the GWP values of several electrolytic and non-electrolytic systems. The extended lines on the bar tips show the diverse values from other research (for instance, the value for steam methane reforming of natural gas varies from 8.9 to 12.9 kg CO_2 eq./kg H_2) (Bhandari et al., 2014).

5. Clean Energy Carrier

Global interest in hydrogen as a flexible and clean energy carrier has grown due to the shift toward sustainable energy systems. Over 75 % of the world's primary energy is produced by fossil fuels (coal and hydrocarbons), with the remaining 6 % generated from nuclear power (fission), 7 % from hydropower, and 12 % from biomass. The significance of hydrocarbons derives from their high energy density, ease of storage, and abundance a century ago (Züttel et al., 2010). Hydrogen produces water as a byproduct when it burns or is used in a fuel cell, unlike traditional fossil fuels that release carbon dioxide.

This unique trait of hydrogen makes it a key part of decarbonization plans for the transportation, energy, and industrial sectors. Hydrogen offers a promising route to achieve carbon neutrality. Hydrogen is regarded as a viable secondary energy source (energy carrier) that can be transformed, stored, and utilized efficiently, leading to a large range of possibilities for future applications. Furthermore, hydrogen and electricity are mutually converted, resulting in high energy security and several business opportunities for high energy resilience. Hydrogen can be stored in various ways, including compressed gas, liquid hydrogen, hydrides, absorbed hydrogen, and reformed fuel (Muhammad Aziz, 2021). Since hydrogen may be converted into and out of various secondary energy sources like heat and electricity, these secondary energy sources could have the ability to convert each other. The consumption of hydrogen encompasses a wide range of oxidation methods, such as fuel cells, fuel mixing with internal combustion engines, and turbine combustion (Juste, 2006).

Hydrogen is expected to play a crucial role as an energy carrier in the future energy system. Currently, fossil fuels are the primary energy source and energy carriers worldwide. However, the supply of fossil fuels is finite, and their use causes environmental impacts. Moreover, using present technology, these sources are capable of producing, for the most part, one energy carrier: electricity (Rosen & Koohi-Fayegh, 2016). Hydrogen is produced with a low carbon footprint in the atmosphere. The major steps are to be considered while storing and transporting hydrogen from one destination to another. Hydrogen storage involves reducing the volume of the gas. For example, storing 1 kg of hydrogen gas at 20 °C and 1 bar pressure requires 11 m^3 (Züttel et al., 2010).

Therefore, to optimize the volume of gas for the same quantity, there are various methods for storage, for instance, physical and chemical storage methods, as described in the section **5.1**.

5.1 Hydrogen Storage

There are different storage options, such as compression, liquefaction, hydrides, and adsorption, as shown in **Figure 16**. In physical storage, hydrogen can be stored through compressed and liquefaction in forms of compressed, liquid, cryo-compressed, and slush hydrogen. In addition, chemical storage causes a wide variety of compounds to bind or react with hydrogen. These include hydride (metal, interstitial metal, complex, and chemical hydrides), liquid organic hydrogen carriers (LOHC), reformed organic fuels, and hydrolysis.

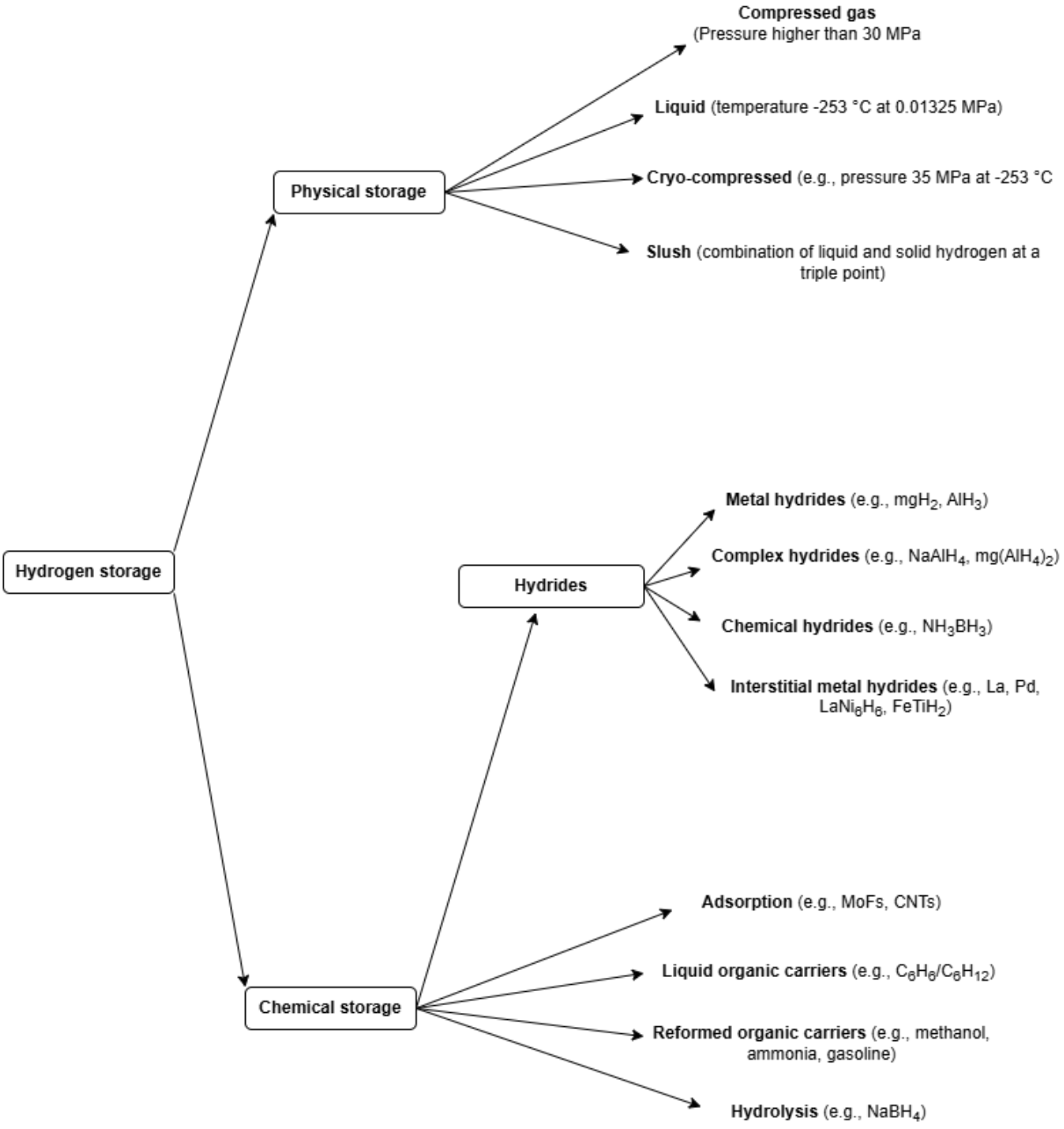

Figure 16. Various hydrogen storage options (adapted from Ref. (Muhammad Aziz, 2021)).

Compression and metal hydrides are among the most efficient methods for storing hydrogen on a small to medium scale (Muhammad Aziz, 2021). Larger-scale hydrogen storage research is

being conducted to develop materials that are safe, dependable, affordable, and suitable for fuel cell technology. Hydrogen needs to be packaged, transported, stored, and transferred to get from production to its intended use, just like any other product. The storage of hydrogen is the primary technological obstacle to a sustainable hydrogen economy, and discovering an affordable way to store hydrogen is still a formidable task. Researchers are looking into novel approaches to hydrogen storage.

To evaluate hydrogen storage solutions for mobility, it is important to identify the properties of each system. Mobile applications require high energy density at volumetric and gravimetric ranges. Gasoline and diesel are widely utilized fuels for surface transportation and can serve as a benchmark. The energy density of various fuels varies due to the variety of blends available in the market. However, around 38 wt. % and 35 MJ/L are normal. At ambient temperature and pressure, pure hydrogen has a high gravimetric energy density of 120 MJ/kg (100 wt. %) but a low volumetric energy density of 0.01 MJ/L (Rivard et al., 2019). Safety is critical in an optimal storage solution, particularly for general public use. Toxicity, flammability, the risk of explosion or projections, and so on are undesirable but difficult to assess. Avoid using materials that require resource-intensive extraction, as well as designs that make recycling difficult or impossible.

5.1.1 Present Industry Choice: Compressed Gas

The most commonly used storage systems are high-pressure gas cylinders with a maximum pressure of 20 MPa. The hydrogen reaches a volumetric density of 36 kg/m³, which is almost half that of its liquid form at the standard boiling point, owing to the development of new lightweight composite cylinders that can withstand pressures up to 80 MPa. Hydrogen volumetric density rises with pressure and reaches a maximum of 100 MPa, depending on the material's tensile strength (Züttel et al., 2010). But when pressure rises, the gravimetric density falls; therefore, zero overpressure yields the highest gravimetric density. Thus, in a compressed gas system, the decrease in gravimetric density occurs at the expense of the rise in volumetric storage density. Compressed hydrogen is utilized in various applications, including automobiles, hydrogen filling stations, and industrial processes. Toyota Mirai and Hyundai Clarity both rely on pressure vessels to store hydrogen on board (Rivard et al., 2019).

Hydrogen has low energy density. However, it has significantly higher energy mass compared to other fuel types. Fuel cell electric vehicles (FCEVs) require 5 kg of hydrogen to get a driving range of 300 miles (DOE/EE-1552, 2017). At 70 MPa, a storage system would have a volume of around 200 liters, which is three to four times larger than conventional gasoline tanks in cars.

Table 6. Pressure vessel materials according to their type.

Type	Materials	Typical pressure (MPa)	Gravimetric density (wt.%)
I	All-metal construction	30	1.7
II	Mostly metal, composite overwrap in hoop direction	20	2.1
III	Metal liner, full composite overwrap	70	4.2
IV	All-composite construction	70	5.7 (Toyota Mirai)

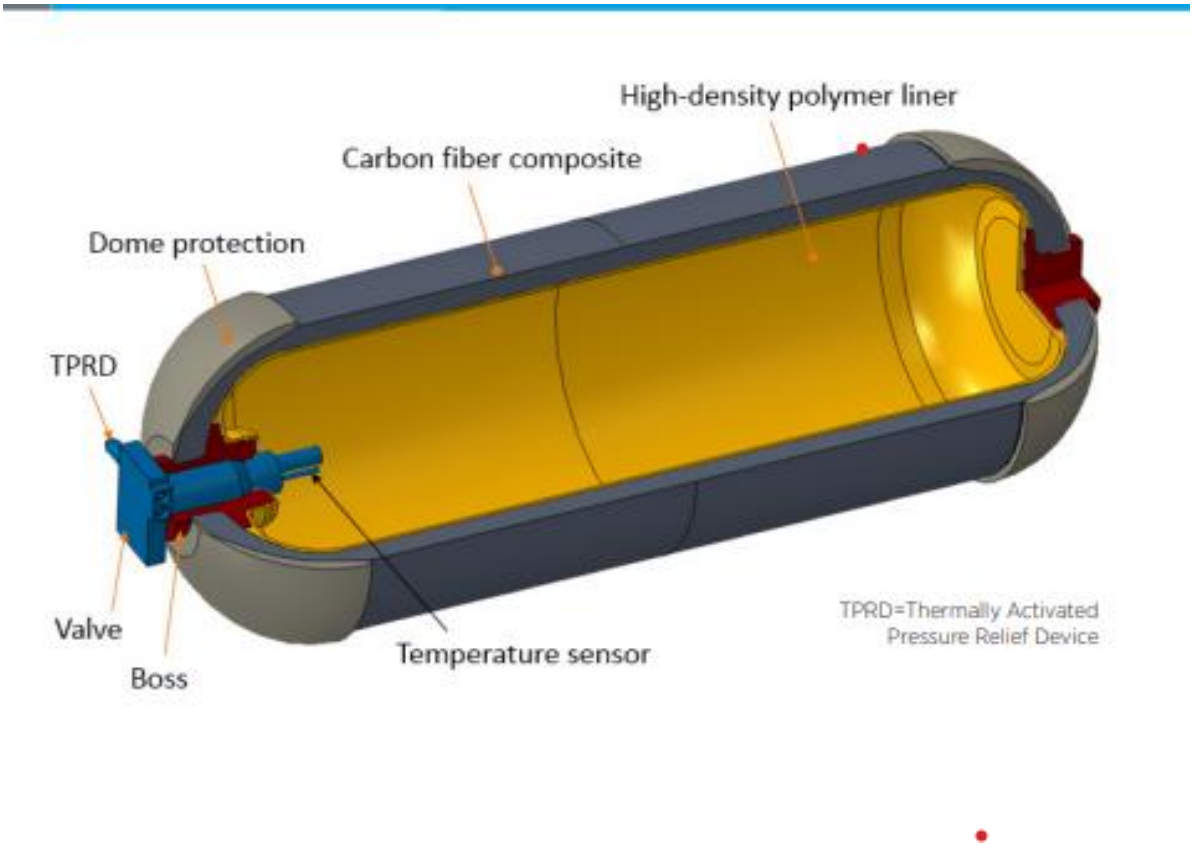

Figure 17. Type IV composite overwrapped hydrogen pressure vessel (adapted from Ref. (DOE/EE-1552, 2017)).

Hydrogen is stored in 70 MPa, Type IV pressure tanks in the first generation of FCEVs, as seen in **Figure 17**. Type IV pressure vessels contain a plastic lining that is strengthened by costly carbon-fiber composites, which is substantially less than that of all metal pressure vessels. However, the use of Type IV pressure vessels raises the cost of hydrogen storage in FCEVs, mostly because the carbon-fiber composite material is expensive.

5.1.2 Metal Hydrides

Metal, complex, chemical, and interstitial metal hydrides are among the hydrides used to store hydrogen. Stable and unstable hydride-forming elements combine to generate metal hydrides, which are intermetallic complexes. $MgH_2, AlH_2, LaNi_5, Mn_2Zn$ are examples of common metal hydrides (Shafiee & McCay, 2016). The advantages of metal hydrides include stability and safety during storage (possibility of long-term storage), absorption and desorption under constant pressure, and functioning at a moderate temperature (Sakintuna et al., 2007). The extremely high volumetric density of hydrogen atoms in the host lattice is a unique characteristic of metallic hydrides. Mg_2Fe_6 and $Al(BH)_4$ have the greatest known volumetric hydrogen density of 150 kg/m^3 (Andreas Züttel et al., 2010). Compounds with the generic formula $M(XH_n)_m$, where M and X stand for metal cations and metal or non-metal elements that have covalent or iono-covalent bonds with hydrogen, are commonly referred to as complex hydrides (He et al., 2019). Alanates (e.g., $LiAlH_4$ (10.4 wt. %) and $Mg(AlH_4)_2$ (9.7 wt. %)), amide–hydride composites (e.g., $LiNH_2 \cdot 2LiH$ (11.5 wt. %)), metal B-based complex hydrides (e.g., $LiBH_4(NH_3BH_3)$ (18.9 wt. %), $Mn(BH_4) \cdot 6NH_3$ (14.0 wt. %)), and metal-organic hydrides are examples of complex hydrides. Chemical hydrides are another promising choice. Chemical hydrides have higher hydrogen densities and are lighter than metal hydrides. Promising chemical hydrides include LiH (25.2 wt. %), $LiAlH$ (21.1 wt. %), $NaBH$ (21.3 wt. %), and NH_3BH_3 (19.6 wt. %) (He et al., 2019). Despite having a high hydrogen density, these complex and chemical hydrides nevertheless have a number of issues, such as limited reversibility, sluggish kinetics during hydrogenation and dehydrogenation, thermodynamic constraints during dehydrogenation, and the possibility of another product evolving.

5.1.3 Adsorption, LOHC, and Slush Hydrogen

Adsorption uses the physical van der Waals bonding between molecular hydrogen and a substance with a high specific surface area to store hydrogen. To achieve considerable hydrogen storage densities through adsorption, low temperatures and high pressures are typically required due to the fragility of the van der Waals bond. Liquid nitrogen (Boiling point: -196 °C) is the most widely used refrigerant for hydrogen adsorption. Depending on the adsorbent and the intended use, the applied hydrogen pressure can vary from 1 to 10 MPa (Andersson & Grönkvist, 2019). Beyond a certain point, using higher pressures is not beneficial, as the adsorbents presence may no longer increase the hydrogen storage capacity compared to storing compressed gas in the same vessel. This is because the adsorbent consumes up space. Hydrogen adsorption faces several obstacles, including low adsorbent density, the need for additives to

improve heat conductivity, low volumetric hydrogen density, and the need for heat management. Adsorption is exothermic; hence, heat removal is essential to provide a sufficient amount of absorption.

A molecule of hydrogen is nonpolar. Therefore, when hydrogen is physically absorbed, the energy of its interaction with the absorbent is limited to 10 kJ/mol. Even excellent absorbents like metal-organic frameworks (MOFs) with a large surface area have a total hydrogen uptake of no more than 4.5 mass percent at a temperature of about -200 °C and 2.02 MPa of pressure (Sergey & Andrey, 2021). Certain carbon structures have a storage capacity of up to 8 mass percent at this temperature, but at room temperature, it drops to 0.5 mass percent.

Liquid organic hydrogen carriers **(LOHC)** rely on hydrogenation and dehydrogenation of chemical molecules to store hydrogen (Preuster et al., 2017), as shown in **Figure 18**. The most well-studied LOHCs are methylcyclohexane and toluene (MCH-TOL); dibenzyl toluene and perhydro-dibenzyltoluene (DBT-PDBT); and N-ethylcarbazole and dodecahydro-N-ethylcarbazole (NEC-DNEC), while many more have been proposed. All of these compounds are aromatic in their dehydrogenated form, with gravimetric hydrogen storage densities by weight percentage and volumetric hydrogen densities of 6.1 % and 47 kg/m^3 for MCH-T, 6.2 % and 64 kg/m^3 for DBT-PDBT, and 5.8 % and 54 kg/m^3 for NEC-DNEC, respectively (Bourane et al., 2016).

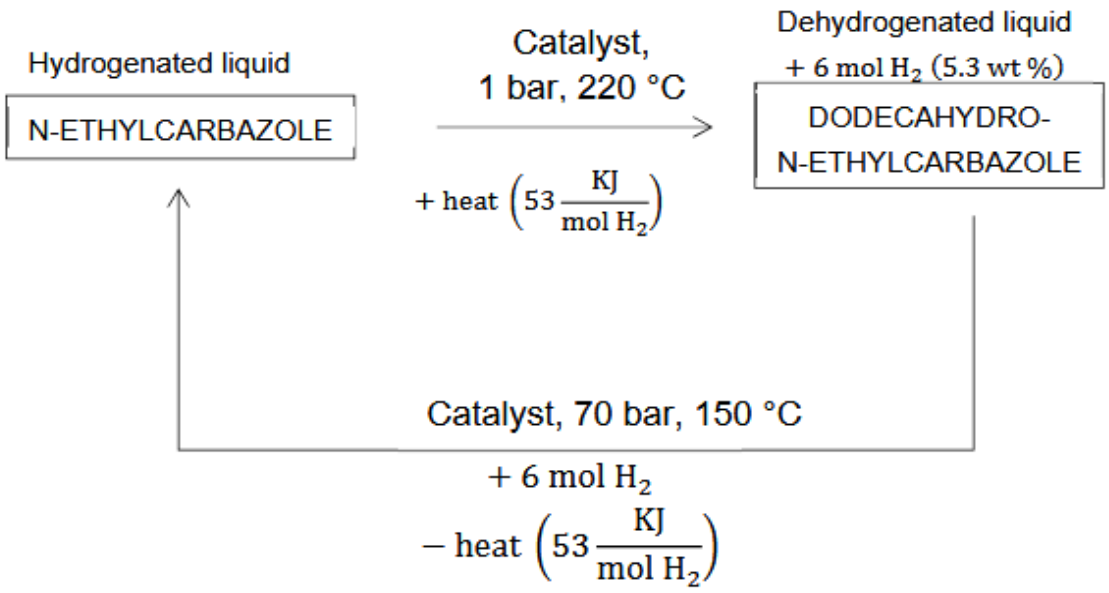

Figure 18. NEC hydrogen uptake and release (adapted from Ref. (Teichmann et al., 2012)).

Dehydrogenation of cyclic hydrocarbons to yield unsaturated or aromatic chemicals is a rather well-established method, particularly in the petroleum sector. The hydrogenation and

dehydrogenation of LOHCs are usually endothermic and exothermic. The dehydrogenation of DNEC yields 22.1 (wt. %) hydrogen, a large quantity of heat, and about 60 % of the gravimetric energy density of diesel fuel. As a result, hydrogenation and dehydrogenation of LOHC are better suited to applications where heat can be conveniently utilized or supplied (Rivard et al., 2019). LOHCs are liquid under atmospheric conditions (20 °C and 1 atm), making them easy to handle, store, and transport. Furthermore, it is robust, secure, and compatible with the current fuel infrastructure.

A cryogenic suspension of combined sub-cooled liquid and solid hydrogen at a triple point (- 259 °C, 7.042 kPa) is known as "**Slush Hydrogen**" (Gursu et al., 1994). Its gravimetric density is about 15-20 % higher than that of liquid hydrogen. In comparison to liquid hydrogen at its boiling point, the gravimetric density and heat capacity of hydrogen slush containing 50 % mass fraction of hydrogen solid are enhanced by 15.5 and 18.3 %, respectively. It is primarily used as a fuel in aerospace rockets and has a greater density and heat capacity than liquid hydrogen (Jin et al., 2017). Furthermore, any repetitive freeze-thaw procedure that brings liquid hydrogen close to its boiling point while lowering pressure can produce slush hydrogen. As a result, liquid hydrogen vaporizes, losing its latent heat and lowering its temperature. When the liquid hydrogen is subsequently cooled down, and its triple point is reached, solid hydrogen is formed on the surface of the vaporizing liquid. When the vacuuming is halted, the pressure rises, causing the solid hydrogen to melt before it sinks and becomes agitated liquid hydrogen. This procedure is repeated (Muhammad Aziz, 2021).

Comparison of liquid storage options based on gravimetric and volumetric energy density.

High hydrogen storage density is required for large-scale hydrogen storage. Liquid hydrogen and ammonia are regarded as viable storage technologies due to their hydrogen storage density and efficiency, as shown in the **Table 7**. When high-purity hydrogen is needed for use, liquid hydrogen is the most economically competitive option (Wijayanta et al., 2019). Furthermore, liquid hydrogen is still quite competitive in many carbon-neutral applications when compared to ammonia. It is anticipated that liquid hydrogen will be useful for cutting-edge applications like aviation and maritime that require high gravimetric energy density. Both options are elaborated below with their characteristics and flexibility:

5.1.4 Ammonia

Ammonia (NH_3) as a hydrogen energy carrier is also an important path for producing electricity from fuel cells. It contains 17.65 % by weight of hydrogen. The production of ammonia in a sustainable way could lead to an excellent hydrogen carrier because it can store and transport

hydrogen efficiently, enabling a potential global hydrogen economy. (Chatterjee et al., 2021) made a brief study on ammonia and other potential substances. NH_3 is currently the second most highly produced chemical in the world, with a global manufacturing capacity of ~230 million tons (Mt) per year. Currently, 180 million tons of NH_3 are produced annually, predominantly through the steam methane reforming (SMR) process to generate the desired H_2, followed by industrial NH_3 synthesis. A schematic diagram of the Haber-Bosch process for ammonia synthesis using hydrogen generated by an electrolyzer powered by a RE source as a feedstock is shown in **Figure 19.** The process of electrolysis yields hydrogen. A renewable energy source, such as solar photovoltaics (PV), wind turbines, or tidal power, produces the necessary electricity. The Haber-Bosch synthesis reactor receives compressed hydrogen and nitrogen from an air separation unit (ASU) at the necessary synthesis pressure. In NH_3 synthesis, 3 mol of H_2 and 1 mol of N_2 react at a medium temperature and high pressure, with the presence of a catalyst to improve the conversion. Ammonia synthesis is an exothermic reaction that requires a large amount of energy input, particularly due to the requirement for the generation of extremely pure N_2. The reaction that occurs during the production of NH_3 is depicted in Eq. 5.1. The electrolyzer capital costs and operating costs are the primary factors influencing the cost of the ammonia and energy input for this approach. According to some estimates, this method uses between 10 and 12 kWh of energy per kg of ammonia (Giddey et al., 2017).

$$N_2 + 3H_2 \rightarrow 2NH_3, \quad \Delta H = -92.4 \ \frac{kJ}{mol} \qquad (5.1)$$

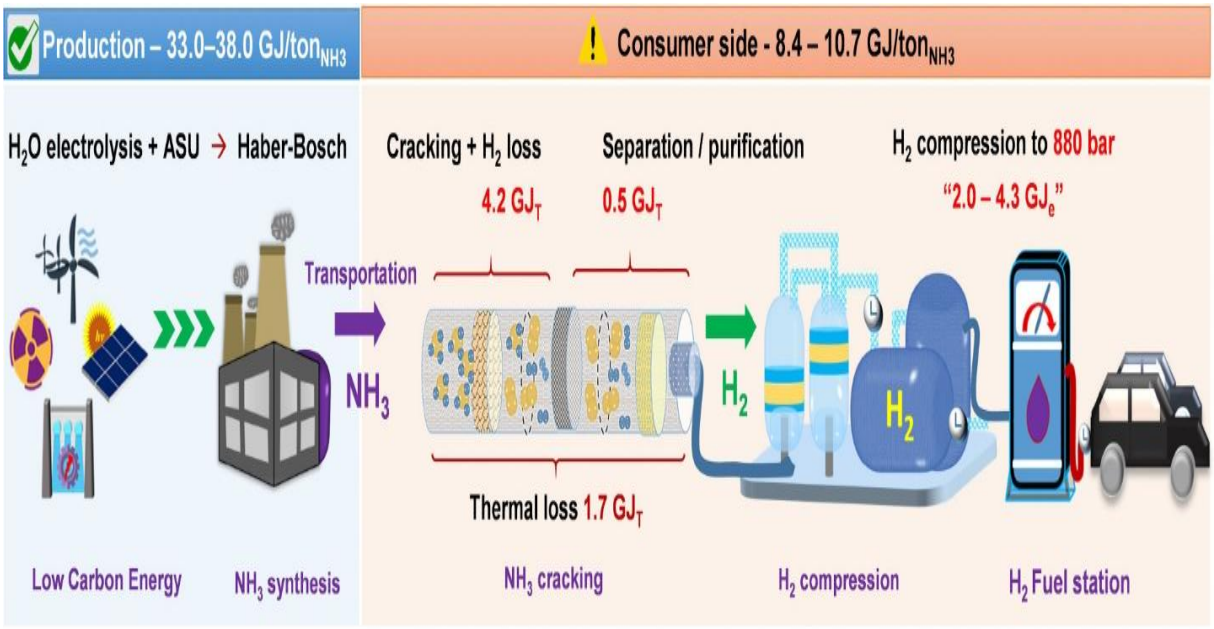

Figure 19. Power-to-power (PTP) energy consumption of NH_3 as a hydrogen energy carrier (adapted from Ref. (Chatterjee et al., 2021)).

Note that the theoretical electrical input will be higher due to resistive losses, polarization, and system losses in the electrolyzer stack component, even though the theoretical electrical input needed to create hydrogen by electrolyzing water is approximately 7 kWh per kilogram of ammonia. An electrolyzer with a net efficiency of 65-70 % requires 48-55 kWh of renewable energy (LHV) to produce 1 kg of hydrogen, similar to natural gas production (45-50 kWh per kg of hydrogen). The net hydrogen energy content of 1 kg of ammonia is equal to 5.88 kWh. Ammonia is a cheaper and more convenient method of storing and transporting than hydrogen gas because it is easier to liquefy. Liquid hydrogen is cooled down to -253 °C for liquefaction, whereas ammonia is cooled down to -33 °C. However, there are some limitations, such as being toxic and corrosive, requiring high energy for cracking (>425 °C), and generating NO_x emissions.

The data illustrated in **Table 7** shows the physical and chemical properties of different hydrogen energy carriers. However, Ammonia has a limited role as a hydrogen carrier due to the large energy requirement for cracking and compressing at the customer end. Importantly, it can lead to significant problems, such as difficult ignition, low speed, and higher compression, in addition to NOx emissions from the combustion of pure NH_3 or ammonia-fuel blends. The leakages in different stages of the supply chain may lead to a wide range of direct and indirect environmental impacts. The combustion of ammonia could also lead to the formation of nitrogen oxides, which have an impact on air quality, and most importantly, N_2O, which is a powerful greenhouse gas (GHG) (Boero et al., 2021).

Table 7. Characteristics comparison of selected chemical fuel (adapted from Ref. (Züttel, 2004)).

Properties	Units	H_2	CH_3OH ($+H_2O$)	MCH	NH_3
Phase		Liquid	Liquid	Liquid	Liquid
Density	kg/m^3	70.8	792	770	610[a]/680[b]
Boiling Point	°C	-253	65 (100)	101	-33
Volumetric H_2 Content	kg/m^3	70.8	99 (95.04)	47.1	107.7/120
Volumetric Energy Density[c]	MJ/L	8.49	11.88 (11.40)	5.66	12.92 /14.4
Gravimetric H_2 Content	Wt. %	100	12.5 (12)	6.1	17.65

Properties	Units	H_2	CH_3OH ($+H_2O$)	MCH	NH_3
Gravimetric Energy Density[d]	MJ/kg	120	15 (14.4)	7.35	21.18
Energy to produce carrier	kWh/kg	6-15[f]	-	-	11.2-22.5[f]
Enthalpy of Dehydrogenation	kJ/mol	0.907	16.3	69.8	30.6
Enthalpy of Evaporation	kJ/mol	-	31.7[e] (13)	10.8	15.1
H_2 Release		Evaporation	Reforming (250 °C)	Dehydrogenation (350 °C)	Cracking (>425°C)
Explosive limit in Air	Vol. %	4-75	6.7-36	1.2-6.7	15-28
Flammability/ Toxicity		Highly flammable	Toxic	Toxic	Toxic

([a]At 20 °C and 10 bar. [b]at -33 °C. [c, d]Values are corresponding hydrogen energy densities, calculated based on the LHV of a stoichiometric amount of hydrogen (LHV_{H_2}= 120 MJ/kg). [e]For steam reforming of methanol, one must evaporate both methanol and water. In a real case, a stoichiometric excess of 50% water is typically used (Chatterjee et al., 2021). [d]Includes current industrial and conceptual hydrogen liquefaction plants capacities, from 5 TPD to ≥ 50 TPD for liquid hydrogen, and for ammonia value calculated from energy requirement for ammonia synthesis only (Al Ghafri et al., 2022)).

Ammonia is a colorless gas characterized by a pungent and distinctive odor, perceptible to humans at low concentrations in the air (20 ppm). However, even a small leak can be easily detected by sensors in concentrations below the harmful limit. Even in low concentrations, inhalation or contact with ammonia can cause cough and irritation, and high levels can be even fatal (2000 and 3000 ppm within an hour of exposure) (Negro et al., 2023).

5.1.5 Liquid Hydrogen

Hydrogen is currently produced in a limited number of plants and transported using various storage systems, including cryogenic tankers, cylinders, and tube trailers. It is then stored either as a liquid or a gas. However, the storage density of the gas is higher compared to that of the liquid. Hence, for widespread hydrogen use in energy applications and especially in

transportation, hydrogen delivery, storage, and even conversion technologies, barriers have to be overcome (Bourane et al., 2016). A cryogenic tank is used to store liquid hydrogen at -251 °C under standard pressure. Since there is no liquid phase above the critical temperature, liquid hydrogen can only be held in open systems due to the low critical temperature of hydrogen. At ambient temperature, the pressure in a closed storage system might reach around 10^4 bar before hydrogen freezes (Züttel et al., 2010). Liquid hydrogen appears more appealing due to its greater mass per container volume of 0.07 g/ml, compared to that of compressed hydrogen at 70 MPa (0.039 g/ml). However, the temperature for hydrogen liquefaction is -253 °C and atmospheric pressure, which necessitates a considerable amount of energy (more than 30% lower heating value of hydrogen).

Due to hydrogen's critical temperature of just -241 °C, boil-off occurs, leading to concerns about liquid losses as well as cost, energy, efficiency, and safety (Bourane et al., 2016). The equipment, such as pipe, tank, vessel, vent, valve, etc., that comes into direct contact with liquid hydrogen must be made to resist extremely low temperatures. Additionally, it is necessary to reduce the amount of ice that forms around the pipes, valves, and vents because this could result in material rupture, particularly when considerable pressure and force are applied. Furthermore, there is no need to use any special material to avoid corrosion because liquid hydrogen is non-corrosive (Muhammad Aziz, 2021). The operating temperature, pressure, and insulation quality are among the design characteristics that are established when constructing the liquid hydrogen tank. When addressing thermal insulation, two distinct structural and material techniques are typically used. Closed-cell foam was used in the initial design and placed between the walls. Additionally, several metallic layers were considered to enhance the foam's functionality. The second method depends on the use of a multilayered, high-reflection, low-emissive system that is divided by fiberglass. It is possible to achieve low radiation heat transfer and poor thermal conductivity due to the partial vacuum between the layers. Liquid hydrogen tanks are typically composed of aluminum and stainless steel. Additionally, a metallic inner has been produced in conjunction with lightweight fiber-reinforced materials. Austenitic stainless steel double-walled jars with a vacuum between the walls are currently the most common type (Hedayat, 2002).

The major challenge for storing liquid hydrogen for a long period of time is to minimize the boil-off gas (BOG) losses. BOG is the term used to describe the phenomenon where liquid hydrogen vaporizes to its gaseous state during storage. There are two distinct losses occurs when hydrogen evaporates during storage: the energy loss for liquefaction and hydrogen loss from purging the evaporated gas to prevent pressure building inside the vessel (Andersson &

Grönkvist, 2019). The O-P hydrogen ratio, tank dimensions and design, and thermal insulation are all related to this BOG. If the vaporized hydrogen is not evacuated from the storage tank and vessel, the internal pressure of the tank and vessel will rise drastically, increasing the risk of cracking or explosion.

The depletion of hydrogen capacity in the tank and vessel is indicated by the release of gaseous hydrogen from the storage tank. Some active and passive strategies, such as accelerating the isomer change from O-P hydrogen during liquefaction, minimizing the surface-to-volume ratio of the vessel (such as by making it spherical), improving the vessel's insulation lessen heat transfer from the surroundings, and using a cryocooler, can reduce BOG (zero boil-off) (Muhammad Aziz, 2021).

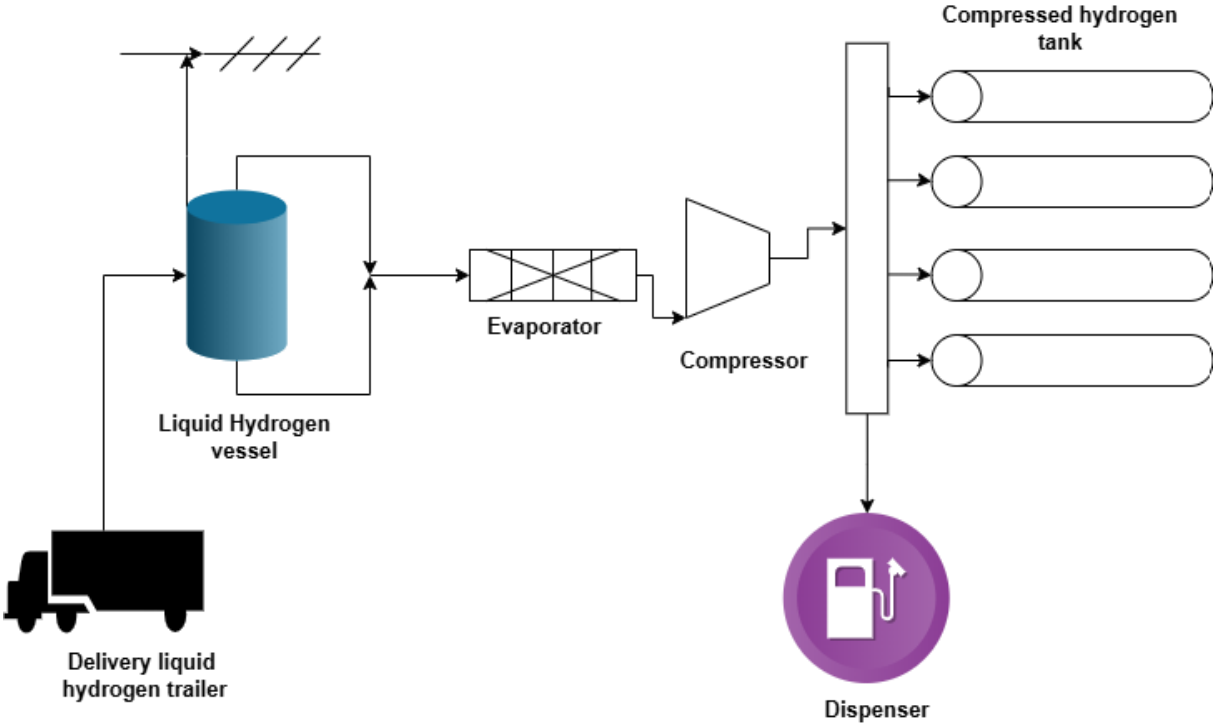

Figure 20. Schematic diagram of a typical hydrogen refueling station with liquid hydrogen delivery (Adapted from Ref. (Muhammad Aziz, 2021)).

A typical refueling station with liquid hydrogen delivery is schematically depicted in the **Figure 20.** Only a limited number of hydrogens refueling stations employ liquid hydrogen, while the predominant configuration relies on compressed gaseous hydrogen for transportation, dispensing, and on-site storage.

A delivery trailer is used to transport liquid hydrogen to the station, where it is then moved to the liquid hydrogen tank. Liquid hydrogen tank and boil-off gas are used simultaneously, evaporated, and compressed before being kept in compressed hydrogen tanks. These compressed hydrogen tanks were connected to the hydrogen dispenser

5.2 Rationale for Selecting Liquid Hydrogen Over Ammonia as an Energy Carrier

Liquid hydrogen and ammonia have drawn a lot of interest as possible large-scale hydrogen carriers for long-distance storage and transportation. However, liquid hydrogen is a more efficient energy carrier than ammonia when hydrogen is needed as the final energy vector. This is mainly because of its lower CO_2 emissions, simpler system, and better hydrogen delivery performance. According to (Wijayanta et al., 2019), they evaluated the three carriers of hydrogen among several candidates, where they have mainly focused on LH_2, NH_3, and MCH (methyl cyclohexane). Liquid hydrogen poses issues due to the high energy consumption during liquefaction and hydrogen loss through boil-off during storage. The primary challenge with MCH is the high energy required for dehydrogenation. Finally, both the synthesis and cracking of ammonia need a significant amount of energy.

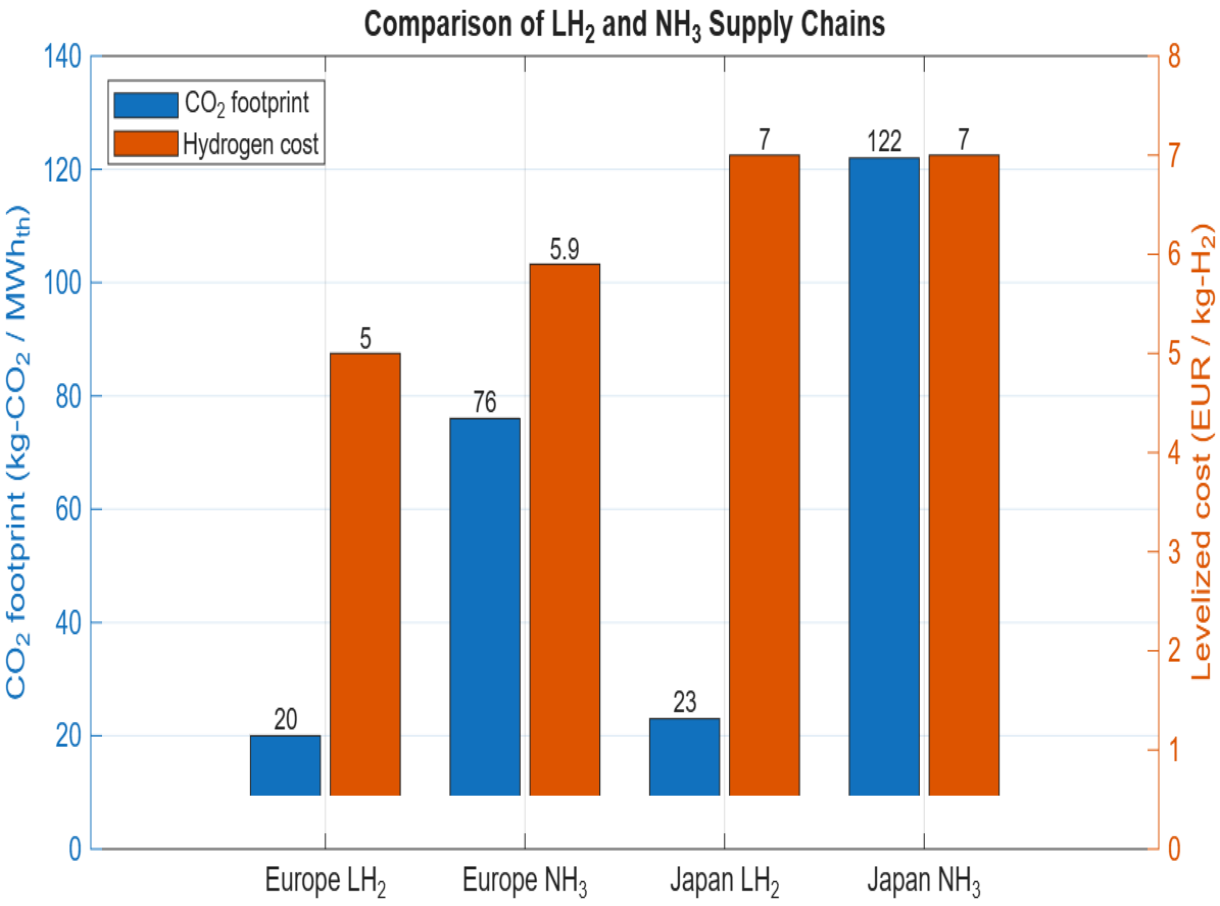

Figure 21. Graphical representation of environment impact and the levelized cost of hydrogen by liquid hydrogen and ammonia energy carriers transporting to Europe and Japan from Norway.

However, a detailed case study was made by Ishimoto et al., for large-scale production and transport of liquid hydrogen and ammonia from Norway to Europe (Rotterdam) and Japan (Tokyo) as a hydrogen energy carrier (Ishimoto et al., 2020). The production of hydrogen is

followed by liquefaction, transport, storage, and regasification in the LH_2 route. The ammonia pathway, on the other hand, necessitates two more energy-intensive steps, namely ammonia synthesis and downstream cracking back to hydrogen. The overall energy efficiency of the liquid hydrogen chain is much higher (about 53-61 %) than that of the ammonia chain (around 42-44 %). Only roughly 69.5 % of the hydrogen content is recovered throughout the cracking and purifying operations, which is the primary cause of decrease in efficiency. This inherent efficiency penalty makes ammonia less appealing when hydrogen, rather than ammonia, is the preferred end-use fuel.

The data illustrated in **Figure 21** shows the CO_2 intensity of both carriers for transportation to Europe and Japan, illustrating the environmental effects of these efficiency disparities. CO_2 emissions from liquid hydrogen are significantly lower in both cases. In the European scenario, LH_2 produces about 20 kg-CO_2/MWh$_{th}$, while ammonia produces 76 kg-CO_2/MWh$_{th}$. The difference is even more noticeable for long-distance transportation to Japan, where ammonia produces 122 kg-CO_2/MWh$_{th}$ while LH_2 releases around 23 kg-CO_2/MWh$_{th}$. The increased energy requirements of synthesis and cracking, as well as higher fuel consumption during transportation, are the main causes of these increased ammonia emissions. The graphical comparison makes it quite evident that low-carbon hydrogen methods and strict decarbonization targets are more compatible with liquid hydrogen.

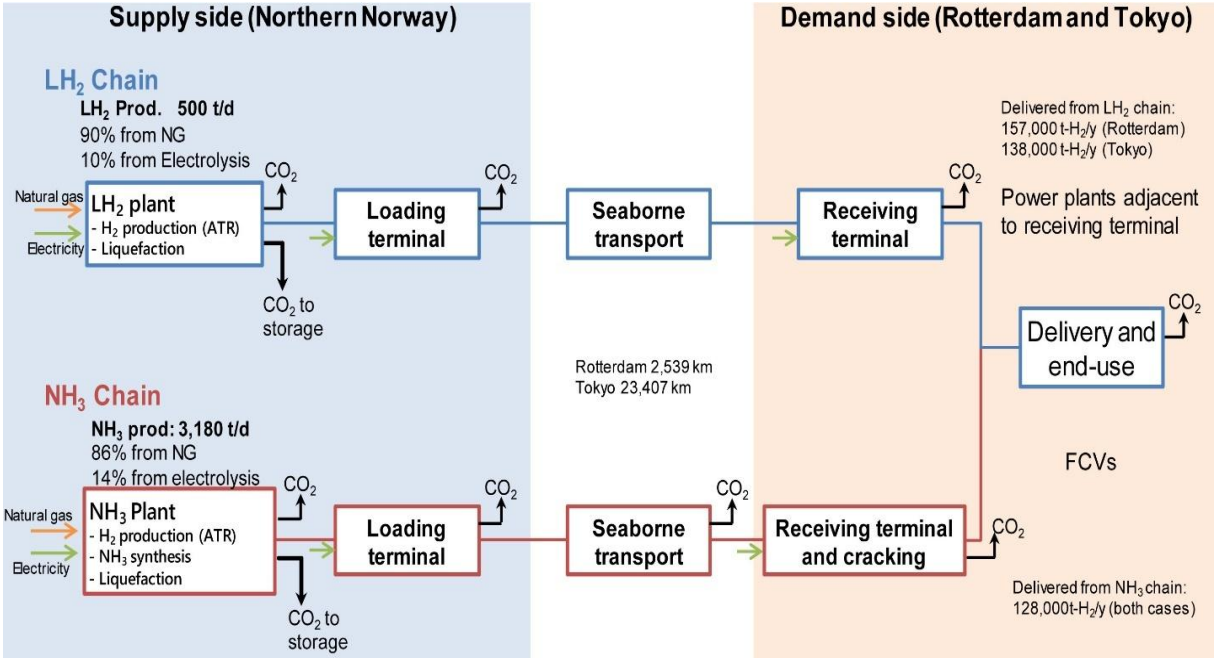

Figure 22. Schematic diagram of the LH_2 and NH_3 chains (adapted from Ref.(Ishimoto et al., 2020)).

The LH_2 chain produces more usable hydrogen since there are no chemical conversion losses, even though ammonia has a larger volumetric energy density, as stated in **Table 7**. For instance,

transportation via seaborne to Rotterdam produces about 157,000 tons H_2, and Tokyo produces about 138,000 tons H_2 annually via LH_2 as opposed to 128,000 tons H_2 annually via ammonia for both cases, as shown in **Figure 22**. This distinction emphasizes how liquid hydrogen allows for direct and effective hydrogen utilization, while ammonia mostly serves as an indirect hydrogen carrier. The graph illustrated in **Figure 21** displays the levelized cost of delivered hydrogen (LCOH), and summarizes the economic implications. Liquid hydrogen is less expensive to ship to Europe (~5.0 €/kg H_2) than ammonia (~5.9 €/kg H_2). For Japan, both pathways exhibit similar costs under conservative assumptions; however, LH_2 has a greater potential for cost reduction. Liquid hydrogen is getting close to long-term hydrogen cost targets of Japan at 3.2 €/kg H_2 under optimistic assumptions about capital cost (CAPEX) reduction and operational improvements. Ammonia's long-term competitiveness is still limited by inevitable efficiency losses and increased infrastructural needs.

Overall, the graphical comparison of energy efficiency, CO_2 emissions, delivered hydrogen quantity, and cost consistently illustrates the advantages of liquid hydrogen over ammonia. LH_2 is the preferred option for large-scale, low-carbon energy transport due to its superior performance and greater compatibility with future hydrogen-based energy systems, while ammonia may be used as a translational or specific in certain applications.

6. Hydrogen Liquefaction

Hydrogen must be liquified by removing heat and rejecting it into the environment using a combination of refrigeration methods that are accessible to the cryogenics sector. A liquefaction work of cryogens depends on both its condensing temperature and the surrounding air temperature. The minimal Carnot cycle effort required to produce refrigeration at different temperatures shows how the theoretical work increases exponentially as the temperature drops. At absolute zero, the theoretical work becomes limitless (Baker, 1978).

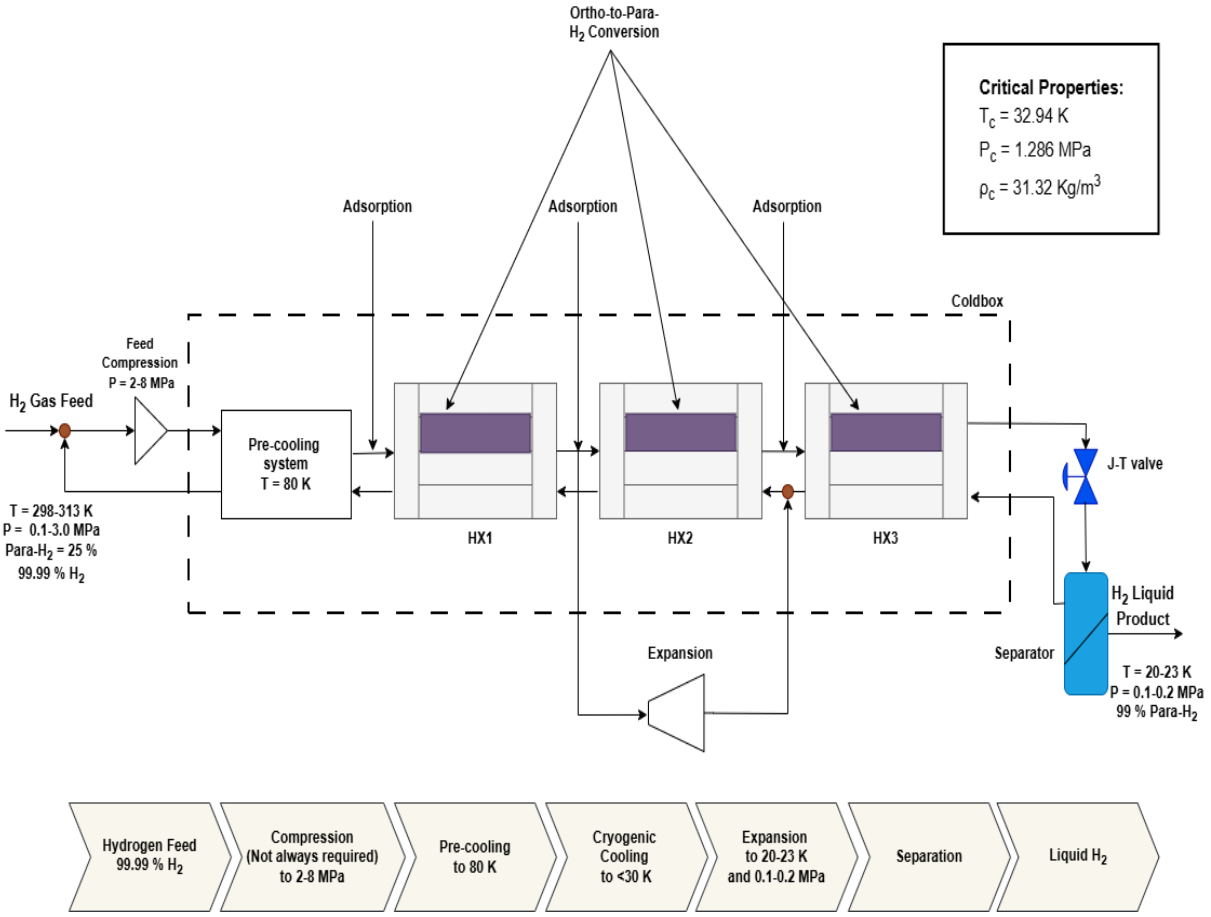

Figure 23. Simplified schematic diagram of the simple Claude cycle for the hydrogen liquefaction process (adapted from (Al Ghafri et al., 2022)).

Hydrogen liquefaction techniques are covered in several recent papers (Rezaie et al., 2016a; Shimko & Gardiner, 2008; Yin & Ju, 2020a; T. Zhang et al., 2023). Thus, just a summary of the principle is given, as shown in **Figure 23**. Feed hydrogen with the following properties is taken into consideration: T = 298 K, P = 0.1-3.0 MPa, Ortho-H_2 = 75 %, Para-H_2 = 25 %, 99.99 % purity. Pre-compression is the initial stage of the process if the hydrogen feed gas is supplied at relatively low pressure. After that, the hydrogen gas goes through an optional pe-cooling step to 80 K with the help of liquid nitrogen or other mixed refrigerants as discussed in section **6.2.2.** An adsorption step is performed after pre-cooling to remove contaminants that

could freeze out during cryogenic liquefaction. A closed-loop cryogenic refrigeration cycle is then used to chill the hydrogen to below 30 K. In this cycle, ortho-H_2 is catalytically converted to para-H_2 either continuously or in batches. Adiabatic expansion, which can be either turbine expansion or J-T expansion. The expanded fluid is a two-phase fluid collected in a separator, where liquid hydrogen (LH_2) is transferred to the liquid hydrogen storage tank, and vapor hydrogen is sent back to the ejector to re-liquefy through expansion (Al Ghafri et al., 2022). LH_2 typically exists with a para-H2 content of more than 98 % at 20-23 K and a pressure of 0.1-0.2 MPa.

(Baker, 1978) evaluated three techniques for large-scale hydrogen liquefaction. The first method is Joule-Thompson expansion, in which compressed hydrogen is throttled via a valve or nozzle to a lower pressure. The throttled gas typically experiences a temperature drop as a result of this adiabatic process. When it comes to hydrogen, which has an inversion temperature of 204 K, temperature drops only if the gas has been precooled below the inversion temperature. The liquefaction cannot be solely responsible for this refrigeration technique. Introducing an auxiliary refrigerating fluid from a source outside of the hydrogen liquefaction process is the second technique. For this purpose, liquid nitrogen is commonly utilized, and the nitrogen's liquefaction process may use an auxiliary refrigerant, such as a halogenated hydrocarbon. The precooling requirement for the hydrogen to liquefy through Joule-Thomson expansion can be supplied by liquid nitrogen. The third method involves using an expansion engine to expand compressed hydrogen to a lower pressure. This is an isentropic process that lowers the enthalpy of the expanding gas in a fully efficient engine. The developed work can be recovered from external use after being rejected from the process through the engine shaft. Expanders can be centrifugal or reciprocating, but in large-scale applications, centrifugal turbines are more cost-effective. Energy can be recovered by connecting an electric generator to the turbine shaft.

6.1 Early Development

The process of converting hydrogen gas into a cryogenic liquid by cooling it to its boiling point, approximately -253 °C, is known as hydrogen liquefaction. Sir James Dewar was the first to liquefy hydrogen successfully in 1898 (Dewar, 1898). This method utilizes pre-cooled compressed hydrogen at 180 bar pressure, combined with liquid air and carbolic acid. Later, the first experimental method for liquefying hydrogen was the Linde-Hampson system. Higher efficiency experimental systems were introduced around 1900, including the Claude system and the precooled Claude system. Later in 1957, the first large-scale hydrogen liquefaction plant for the petrochemical and aerospace sectors in the United States was built using the precooled

Claude method (Rezaie et al., 2016a). The facility used a hydrogen refrigeration system to reach -253 ℃ and was precooled to -193 ℃. (Krasae-in et al., 2010a) proposed a comparative study on the earlier development of the liquefier, which led to the construction of the first liquid hydrogen plant in 1960 to support the Apollo program. There was significant demand from the US space program in the early 1960s. The capacity to meet the entire Apollo program's needs was achieved by 1965 and continued until 1977. Due to reduced space activities of NASA, no further new plants were built during this period. The rise in commercial demand for liquid hydrogen after 1977 mainly drove the development of new facilities. Currently, Europe has 4 plants with capacities of 5-10 TPD, Asia has 11 plants ranging from 0.3-11.3 TPD, and the US operates over 9 hydrogen liquefaction plants with output rates of 5-34 TPD. Today, liquid hydrogen is used to reduce the cost of hydrogen distribution (Drnevich & Praxair, 2003).

Table 8: Hydrogen liquefaction plants constructed within the last 20 years (Adapted from Ref. (Al Ghafri et al., 2022)).

Location	Operator	Capacity (TPD)	Commissioned in
Kimitsu, Japan	Nippon Steel Corporation	0.2	2004
Saggonda, India	Andhra Sugars	1.2	2004
Osaka, Japan	Iwatani (hydro-edge)	10	2006
Leuna, Germany	Linde	5	2008
Chiba, Japan	Iwatani	5[a]	2009
Yamaguchi, Japan	Iwatani and Tokuyama	5[a]	2013
Akashi, Japan	Kawasaki Heavy Industries	5	2014
Yamaguchi, Japan	Iwatani and Tokuyama	10	2017
Port of Hastings, Australia	HESC	0.25	2020
Las Vegas, USA	Air Liquide	27.2[b]	2020[c]
Leuna, Germany	Linde	10	2021
La Porte, USA	Air Products	27.2[b]	2021
La Porte, USA	Praxair	27.2[b]	2021
California, USA	Air Products	*	2021
Ulsan, Korea	Hyosung and Linde	13	2022

(*Sources did not state a value. [a]Production capacity: 3000L/hour per unit. [b]Metric tonne. [c]Construction was set to begin in 2020.)

6.2 Basic Cycles of Hydrogen Liquefaction

Simple Claude, dual-pressure Claude, pre-cooled Linde-Hampson, pre-cooled dual-pressure Linde-Hampson, pre-cooled simple Claude, pre-cooled dual-pressure Claude, helium pre-cooled Claude, pre-cooled mixed refrigerant (MR) cycle, and cascade system are some of the basic hydrogen liquefaction cycles (Rezaie et al., 2016a; Yin & Ju, 2020b).

6.2.1 Simple Claude Cycle

George Claude developed the Claude cycle in 1902 to liquefy air, but it can also be used to liquefy hydrogen, as shown in **Figure 24(a).** The Claude cycle employs an extra isentropic expander, which distinguishes it from Linde-Hampson (Rezaie et al., 2016a). The isentropic process in the expander can lead to a higher reduction in gas temperature and less exergy destruction than the isenthalpic process in the J-T valve. The expanded gas is then combined with the regenerated return gas to provide the cooling load in an isobaric heat exchange (Abdi et al., 2019). The Claude cycle can be applied to hydrogen liquefaction without the need for pre-cooling techniques because of the additional cooling effect from the isentropic expansion. According to reports, the straightforward Claude cycle for producing liquid hydrogen produced a liquefaction yield of 8 %, SEC of 22.1 $\mathrm{kWh/kg_{LH_2}}$, and an exergy efficiency of 18.1 % (Aasadnia & Mehrpooya, 2018).

6.2.2 Pre-Cooled Claude Cycle

To enhance the hydrogen liquefaction performance of the simple Claude cycle, several modifications have been suggested. Among these, integrating pre-cooling is seen as a promising approach (Abdi et al., 2019). A liquid nitrogen pre-cooling process with the Claude cycle could increase the exergy efficiency to 50-70 % (T. Zhang et al., 2023). This is illustrated in **Figure 24(b)**, where the compressed feed hydrogen is initially cooled with liquid nitrogen before cryogenic cooling through a J-T valve. When liquefying gases whose inversion temperature is lower than the ambient, pre-cooling is an essential requirement. Lowering the enthalpy of the high-pressure gas at the warm end of HX-1 can also increase the liquid yield. Furthermore, lowering the working fluid temperature before throttling can lower the high pressure needed in the optimal liquefaction process (Aasadnia & Mehrpooya, 2018).

6.2.2.1 Nitrogen Pre-Cooled Cycles

(Nandi & Sarangi, 1993) examined how the liquid nitrogen pre-cooled Claude cycle for hydrogen liquefaction was affected by the hydrogen pressure following compression. According to their findings, the liquid hydrogen yield, energy consumption, and exergy

efficiency can reach 16-20 %, 28-39.2 kWh/kg_{LH_2}, and 9.2-13 %, respectively, at a hydrogen pressure of 1-3 MPa. (Baker, 1978) suggested using liquid nitrogen as the hydrogen pre-cooling load in a dual-pressure Claude cycle for hydrogen liquefaction. With a planned production capacity of 250 TPD. This pre-cooled dual-pressure Claude cycle can attain an exergy efficiency of 36 % and the SEC of 10.85 kWh/kg_{LH_2}. (Bracha et al., 1994) demonstrated the Linde large-scale nitrogen pre-cooled Claude facility in Ingolstadt. This liquefier had the SEC of 13.58 kWh/kg_{LH_2}, and its liquefaction capacity was 4.4 TPD. Currently, the biggest liquefier in Germany is a liquid nitrogen pre-cooled dual-pressure Claude cycle with the SEC of 11.9 kWh/kg_{LH_2}, exergy efficiency 23.6 %, and its liquefaction capacity of 5 TPD (Rezaie et al., 2016a). (Kuz'menko et al., 2004) developed, estimated, and compared four hydrogen liquefiers with comparable capacities (5.4 TPD). The fourth version employed helium gas as the refrigerant for the liquefaction cycle and delivered LN_2 with an SEC of 0.5 kWh/kg_{LH_2}as the precooling cycle. The SEC and EXE values for version 4 were 12.7 kWh/kg_{LH_2},and 34.6 %, respectively.

(Yu et al., 2024) developed a system that consists of a dual hydrogen refrigeration cycle cryo-cooling process and a closed cycle of nitrogen pre-cooling process that are merged to produce and create the coupled system. An independent system that separates the pre-cooling and cryo-cooling processes is also built for comparison analysis in order to assess the performance of the suggested hydrogen liquefaction technology. A genetic algorithm is used to optimize the parameters for both independent and coupled systems. For both independent and coupled systems, a genetic algorithm is used to optimize the parameters. According to the findings, the coupled system's SEC, Coefficient of performance (COP), and exergy efficiency are 11.41 kWh/kg_{LH_2}, 0.12, and 26.1 %, respectively. (Yin & Ju, 2020a) designed a hydrogen liquefaction plant process based on liquid nitrogen pre-cooling and helium gas turbine expansion refrigeration. Additionally, the SEC of the system is taken into account as the objective function when the genetic algorithm (GA) performs multi-parameter optimization of the system. After optimization, the SEC of the system is 7.1329 kWh/kg_{LH_2}, 19.65 % lower than the base case. The COP and figure of merit (FOM) are 0.1704 and 0.4941, respectively, higher than those of the prior optimization process. (Hammad & Dincer, 2018) suggested and examined an advanced hydrogen liquefaction method using heat exchangers (HXs) infused with a catalyst. The hydrogen gas was liquified using the J-T cycle after being pre-cooled by the running LN_2 and refrigerated by expanding high-pressure hydrogen gas (2 MPa) in three

expanders connected in series. Aspen Plus was implemented to generate the process simulation, and the EXE was 11.58 %.

6.2.2.2 Helium Pre-Cooled Cycles

Helium pre-cooled hydrogen liquefaction is a cryogenic method that uses cold helium gas as a precooling and refrigeration medium to effectively liquefy hydrogen. (Shimko & Gardiner, 2008) assembled and modeled a large capacity (50 TPD) hydrogen liquefaction cycle using four ortho-para catalyst beds that are pre-cooled by helium. The investigation revealed that the SEC of this procedure was 8.73 kWh/kg_{LH_2}, and the EXE was 44.6 %. (Staats, 2008) suggested and employed a helium pre-cooling Claude cycle to numerically investigate a supercritical hydrogen liquefaction cycle. Three ortho-para catalyst beds were required, and the liquefaction capacity was 50 TPD. A MATLAB simulation program was developed to examine how cycle efficiency is affected by component efficiencies and other system characteristics. The outcome demonstrated that the four-stage helium expansion was the most efficient of the two-, three-, and four-stage cycles, with an exergy efficiency of 35.6 %. It was anticipated that the significant increase in capital cost associated with adding a stage to a cycle would not be worthwhile. Additionally, they manually optimized the parameters and reran the simulation at these new operating points to find an efficient strategy to boost performance. Finally, the outcome showed that increasing the HX area might potentially raise the efficiency to 44 %.

(Yuksel et al., 2017) examined and evaluated a new supercritical hydrogen liquefaction process that is thermodynamically based on cycles of helium pre-cooled hydrogen liquefaction. This process is a modified (Staats, 2008) cycle. To pressurize the hydrogen and helium flows to the necessary pressure, the four helium expanders provide electricity that powers the hydrogen and helium compressors. Eight HXs were used in the four stages of helium expansion and refrigeration that liquified hydrogen. It was discovered that the liquefaction capacity, energy, and exergy were 50 TPD, 70.12 %, and 57.13 %, respectively. To investigate the impact of various design variables on the EXE and Exergy destruction rates of the hydrogen liquefaction process, they examined several parameters. The findings showed that the process EXE increased with any increase in the mass flow rate of hydrogen and the inlet pressure of helium expanders. In contrast, increasing the pinch temperature of the catalyst bed by 14 °C increased the exergy destruction rates of the liquefaction process while decreasing the EXE.

6.2.2.3 MR Pre-Cooled Cycles

A mixed refrigerant cycle that utilizes a mixture of refrigerants rather than a single one is typically employed as a pre-cooling procedure for liquid hydrogen liquefaction. (T. Zhang et

al., 2023). This kind of cycle functions similarly to the refrigerant liquefaction cycle. The key difference is that, to produce the cooling effect, isentropic expanders are used in place of expansion valves. (Jacob et al., 2006) suggested a conceptual plant which was built based on the MR cycle method for pre-cooling hydrogen, with a liquid helium bath employed in the cryogenic phase. The planned plant demonstrated that an EXE of 60 % and SEC of 7.0 kWh/kg_{LH_2}were achievable. (Ansarinasab et al., 2019) suggested a two-stage mixed refrigerant cycle system in which hydrogen is cooled to -195 °C in the first stage using a mixture of nine components, and then cooled to -254.55 °C in the second stage using a mixture of 6.19 % hydrogen, 83.61 % helium, and 10.20 % neon. With a particular energy usage of 1.10 kWh/kg_{LH_2}, the overall efficiency of the system is as high as 55.4 %. (Krasae-in et al., 2010b) proposed liquid hydrogen plant employs a multi-component refrigerant (MR) refrigeration technology. A cycle capable of producing 100 TPD of liquid hydrogen is modeled. The MR system can efficiently cool feed normal hydrogen gas from 25 °C to the equilibrium temperature of -193 °C. Furthermore, the new proposed four H_2 Joule-Brayton cascade refrigeration is advised for converting the hydrogen gas equilibrium temperature from -193 °C to -253 °C. The proposed plant's average power usage is 5.35 kWh/kg_{H_2}, with an ideal minimum of 2.89 kWh/kg_{LH_2}.

(Sadaghiani & Mehrpooya, 2017) presented and examined a new configuration for the cryogenic hydrogen liquefaction process. For the pre-cooling cycle, they employed MR with nine components, and for the cryogenic J-B cycle, they used MR with three components (10 % neon, 6.5 % hydrogen, and 83.5 % helium), which could generate 300 TPD of LH_2. They used the Aspen HYSYS program to model the procedure. Additionally, they evaluated the sensitivity of the process outputs versus effective parameters after adjusting the equipment's operating state to the ideal values for process optimization. The SEC and EXE of the system were 4.410 kWh/kg_{LH_2}, and 55.47 %, respectively. According to the energy study, the COP of the process was 0.1797. (Sleiti et al., 2023) introduced a new, effective, and large-scale dual-mixed refrigerant (DMR) method for pre-cooling hydrogen at 2.1 MPa from 25 °C to -192°C. using a newly suggested methodology, new heavyweight-based MR-1 and lightweight-based mixed refrigerant MR-2 are produced for the DMR process. With an SEC of 0.862 kWh/kg_{LH_2}, the suggested DMR process can handle a broad range of hydrogen flow from 100 TPD to 1000 TPD, which is 20.33 % less than the most competitive single-mixed refrigerant (SMR) found in the literature. Further DMR operating parameter tuning lowered the SEC to 0.833 kWh/kg_{LH_2} at an ideal capacity of 500 TPD based on the sensitivity analysis. (Cardella, Decker, Sundberg, et al., 2017) described a new method for developing a large-scale hydrogen

liquefaction process that could yield 100 TPD by using mixed refrigerant as a pre-cooling cycle. In this research, the full hydrogen liquefaction process was calculated using a new process simulation model that was built in the modeling program UniSim Design. Additionally, the gradient-based fmincon solver with the sequence quadratic programming technique optimized the process simulation connected to MATLAB. 22 non-linear inequality constraints were chosen to represent appropriate boundary conditions, 18 variables were optimized, and the SEC was chosen as the objective function. Lastly, two MR pre-cooled hydrogen liquefaction procedures were suggested. One was created using a dual H_2-Ne cycle, while the other used a high-pressure hydrogen Claude cycle for liquefaction and refrigeration. The results showed that the SEC for the two processes was approximately 6.0 $\mathrm{kWh/kg_{LH_2}}$.

6.2.2.4 Liquified Natural Gas (LNG) Pre-Cooled Cycles

LNG is used to pre-cool the hydrogen feed gas flow and the total high-pressure recycle flow of hydrogen and nitrogen to 135 K (Kuendig et al., 2006). LNG is unloaded from tankers as a saturated liquid at ambient pressure before being compressed to 7800 kPa using cold centrifugal pumps. The pumps elevate the temperature of the LNG to 125 K. The pre-cooling heat exchangers are designed to have a temperature difference between 125 K and 135 K at their cold end. Their finding indicated that this integration could greatly reduce the SEC of the cycle to 3.2-8.5 $\mathrm{kWh/kg_{LH_2}}$ with various LNG inputs (43.9-3.2 $\mathrm{kg_{LNG}/kg_{H_2}}$). However, the hydrogen liquefaction plant must co-locate and operate alongside an LNG port, as this integration reduces flexibility.

(Bian et al., 2021b) suggested a hydrogen liquefaction process which reduces energy consumption and investment cost by using a direct expansion cycle of LNG for pre-cooling and a dual-pressure Brayton cascade cycle for cryo-cooling. The proposed hydrogen liquefaction method is evaluated against two reference procedures using different cryo-cooling cycles to determine its performance and cost benefits. The suggested approach offers lower operational and capital expenses, particularly for helium and heat exchangers. Furthermore, the specific energy consumption of the proposed method is 6.60 $\mathrm{kWh/kg_{LH_2}}$. The research illustrated by (Noh et al., 2022) is primarily concerned with establishing the best design for efficiently utilizing LNG cold energy in hydrogen pre-cooling for liquid hydrogen production. They proposed two distinct configurations: (a) adding LNG cold energy to the current hydrogen pre-cooling cycle and (b) replacing the existing hydrogen pre-cooling cycle with LNG cold energy. Bayesian optimization is used to find the ideal operating conditions that minimize energy consumption across all configurations. The configuration, including hydrogen pre-cooling with

only LNG, has a specific energy consumption of 5.513 kWh/kg_{LH_2}, which is 8.13 % and 3.19 % lower than the base case design and the configuration involving hydrogen pre-cooling with both LNG and MR cycle, respectively.

6.2.3 Dual-Pressure Pre-Cooled Claude Cycle

The dual-pressure pre-cooled Claude cycle is an enhanced variant of the simple Claude cycle used for hydrogen liquefaction that improves efficiency, as shown in **Figure 24(c).** Before entering the main cryogenic portion, hydrogen gas is compressed and pre-cooled with liquid nitrogen or a separate refrigeration system. The pre-cooling stage significantly decreases the temperature of hydrogen, reducing the refrigeration load required in the low-temperature region. Unlike the simple Claude cycle, the dual-pressure pre-cooled Claude cycle version uses expansion turbines at two separate pressure levels. The dual-pressure configuration enables improved temperature alignment in heat exchangers, thereby reducing irreversibility and exergy losses. As a result, the cycle obtains deeper cooling before the J-T expansion, which results in final liquefaction.

Table 9. Comparison of basic hydrogen liquefaction cycles (Adapted from Ref. (Yin & Ju, 2020b)).

Basic hydrogen liquefaction cycle	Liquid yield (%)	SEC (kWh/kg_{LH_2})	EXE (%)
Simple Claude	8	22.1	18.1
Pre-cooled Linde-Hampson	12-17	72.8-79.8	4.5-5.0
Pre-cooled dual-pressure Linde-Hampson	41	12.14	27
Pre-cooled simple Claude	16-20	28-39.2	9.2-13
Pre-cooled dual-pressure Claude	-	12.26	-
Helium pre-cooled Claude	100	33.6	6.5-11

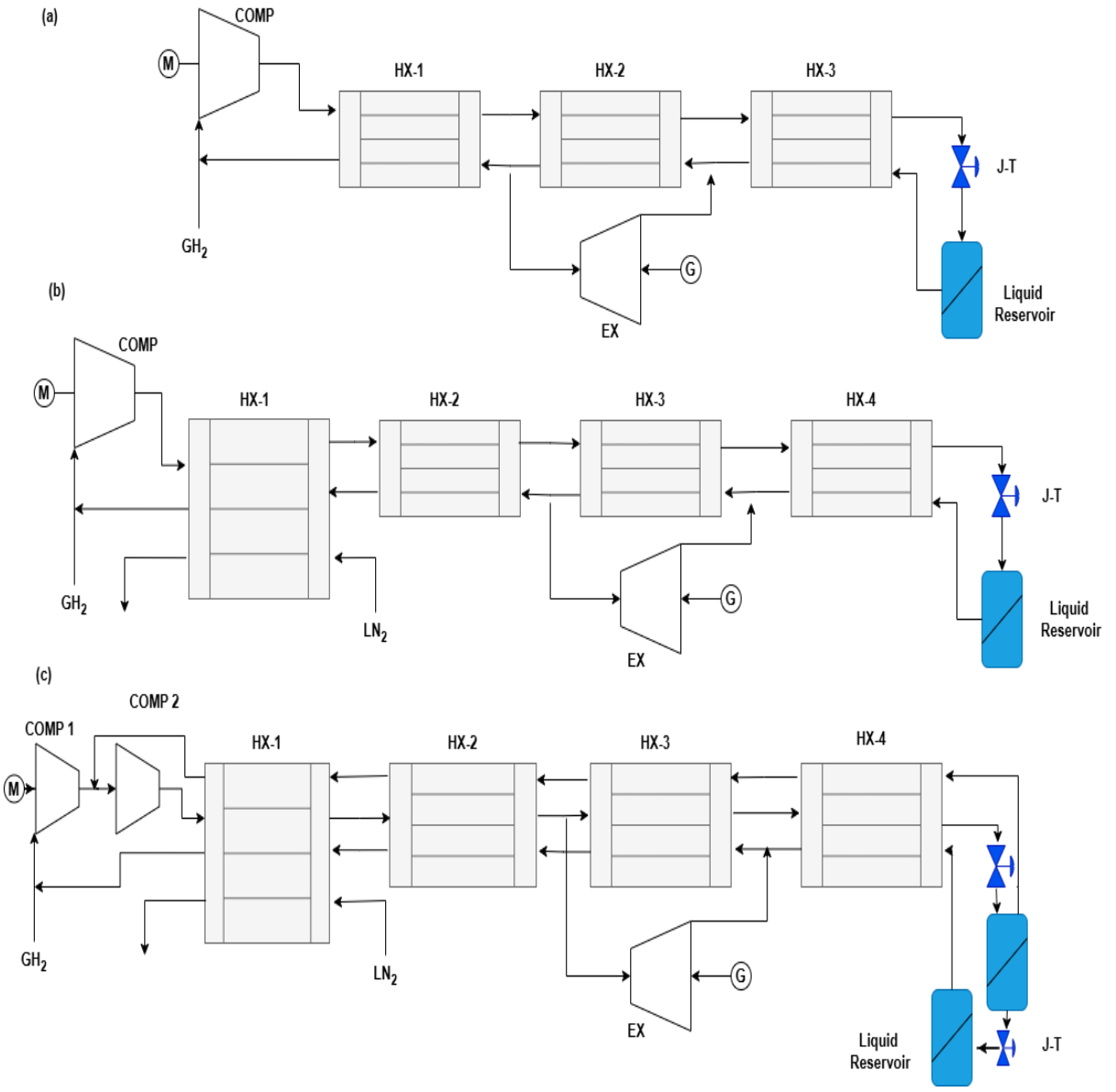

Figure 24. Basic working principle of (a) simple Claude cycle, (b) liquid nitrogen pre-cooled Claude cycle, (c) dual-pressure pre-cooled Claude cycle for hydrogen liquefaction (COMP: compressor, EX: expander, HX: heat exchanger, J-T: Joule-Thompson valve) (adapted from Ref. (Aasadnia & Mehrpooya, 2018)).

6.2.4 Linde-Hampson Cycle

The Linde-Hampson cycle is the most basic and simple gas liquefaction cycle, developed by Carl von Linde and William Hampson in 1895 to liquefy air. **Figure 25(a)** shows a schematic of the Linde Hampson cycle (T. Zhang et al., 2023). In this cycle, the gas is compressed to high pressure and cooled to a low temperature by the cold return gas in the primary heat exchanger. The low-temperature, high-pressure gas is then expanded via a throttling valve (also known as a Joule-Thompson valve or J-T valve) to a low-pressure state. At the same time, the temperature drops throughout this isenthalpic process, resulting in the formation of a liquid phase. After expansion, the leftover gaseous fraction is recirculated to the main heat exchanger to provide

cooling power. Due to its high energy consumption and low efficiency, the simple Linde-Hampson cycle is unsuitable for large-scale gas liquefaction (Abdi et al., 2019). Furthermore, only gases like nitrogen that can be cooled by expansion at room temperature can be liquefied using the Linde-Hampson cycle. Nevertheless, the Linde-Hampson cycle cannot be employed for hydrogen liquefaction unless pre-cooling or other pre-treatment procedures are used because the temperature of hydrogen rises after expansion at room temperature (Rezaie et al., 2016a). A simple Linde-Hampson could not be utilized to liquefy hydrogen due to the usage of a J-T valve and the low inversion temperature of hydrogen. A process occurring in a J-T valve might result in refrigeration if the refrigerant temperature is lower than the inversion temperature.

6.2.5 Pre-Cooled Linde-Hampson Cycle

One typical method to enable the basic Linde-Hampson cycle for hydrogen liquefaction is to pre-cool hydrogen to its inversion temperature (200-205 K) or lower. Adding a liquid nitrogen bath is one way to do the pre-cooling, as shown in **Figure 25(b).** In the pre-cooled Linde-Hampson system, the entering highly compressed H_2 was cooled with an external cooling source before regenerative cooling, such as liquid nitrogen or a vapor-compression cycle with a suitable refrigerant (Abdi et al., 2019), as described in the section from **6.2.2**.

6.2.6 Dual-Pressure Linde-Hampson Cycle

The compression and throttling stages consisted of two stages of compression and expansion. The double-stage compression lowered the compression work, as shown in **Figure 25(c).** Instead of expanding to atmospheric pressure, the compressed gas was expanded to an intermediate pressure through the primary valve before being collected by a receiver. In the receiver, the gas was returned to the high-stage compressor, while the liquid entered the secondary valve and expanded to atmospheric pressure. This resulted in a bigger mass of gas being liquefied than in a single-stage expansion. Another modification to the dual-stage Linde-Hampson cycle was the use of an isentropic expander instead of the Joule-Thompson expansion valve. This resulted in a bigger fraction of the liquefaction flowing from high to intermediate pressure, reducing the amount of work required for compression. To liquefy hydrogen without pre-cooling, an isentropic expander was added to the Linde-Hampson cycle, providing additional cooling along the supply line. This design improvement was known as the Claude cycle (Abdi et al., 2019).

6.2.7 Dual-Pressure Pre-cooled Linde-Hampson Cycle

The pre-cooled dual-pressure Linde-Hampson cycle is the result of combining the pre-cooling and dual-pressure cycles to further increase liquid hydrogen yield and lower usage. **Figure**

25(d) displays a process flow diagram of such a cycle, which consists of a high-pressure compressor, a series of heat exchangers and pre-coolant baths, and a J-T expansion valve. The number of pre-coolant baths (at 77 K and 65 K or at 77 K only), the number of O-P (ortho-para) converters, the splitting of the process stream, and the utilization of boil-off nitrogen vapor can all affect the flow chart, even though the cycle's fundamental concepts remain the same (Nandi & Sarangi, 1993). The dual-pressure pre-cooled Linde-Hampson cycle has an energy efficiency of 27 %, a SEC of 12.14 kWh/kg_{LH_2}, and a liquid hydrogen yield of 41 % (T. Zhang et al., 2023).

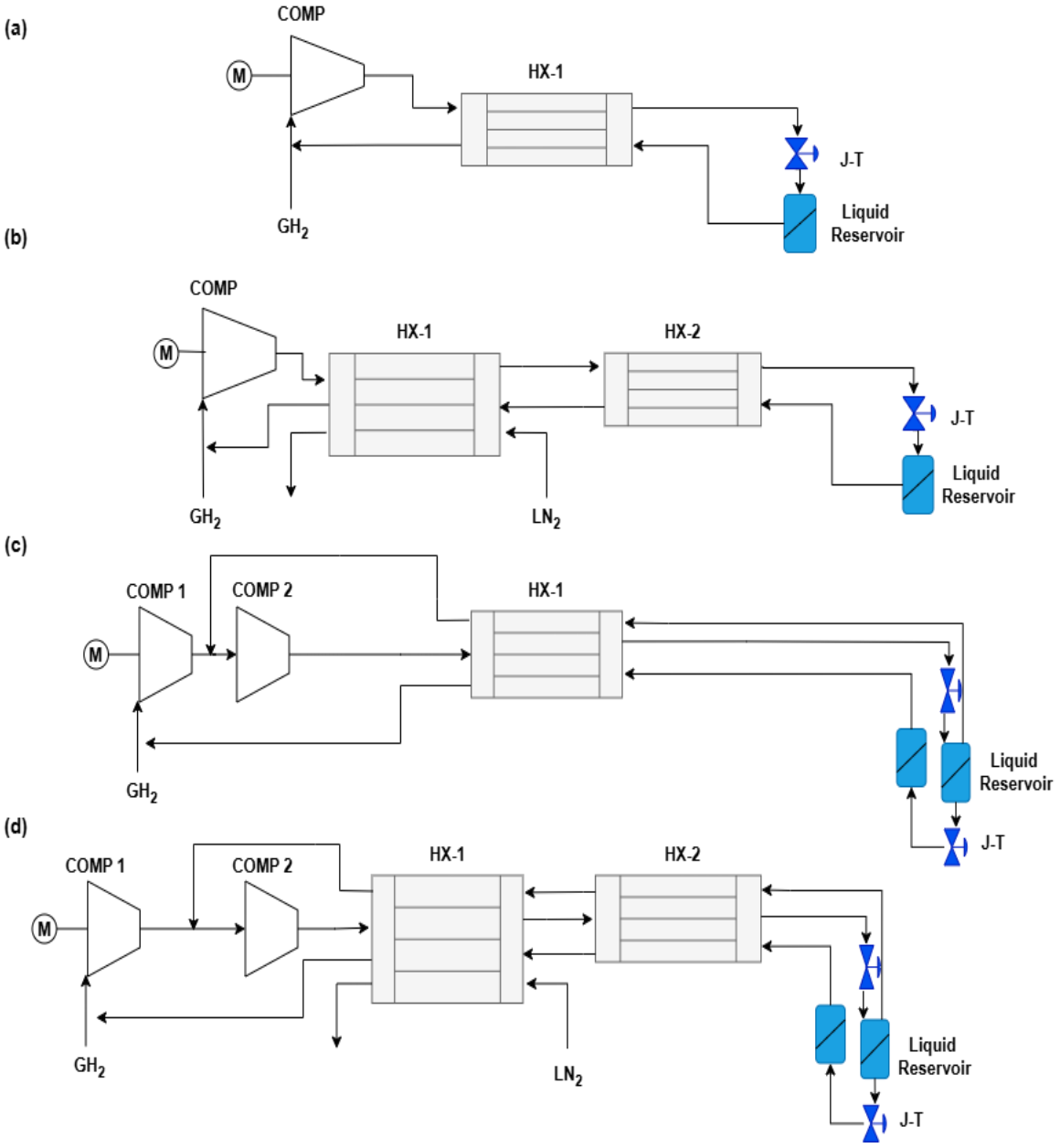

Figure 25. Basic working principle of (a) simple Linde-Hampson cycle, (b) Liquid nitrogen pre-cooled Linde-Hampson cycle, (c) dual-pressure Linde-Hampson, (d) dual-pressure pre-cooled Linde-Hampson cycle for hydrogen liquefaction (COMP: compressor, EX: expander, HX: heat exchanger, J-T: Joule-Thompson valve) (adapted from Ref. (Aasadnia & Mehrpooya, 2018)).

6.3 Existing Industrial Liquefaction Plants

Existing industrial hydrogen liquefiers have a specific energy consumption of 10-15 kWh/kg_{LH_2} or 35-45 % of the lower heating value of hydrogen, with exergy efficiencies varying from 20-30 % (Al Ghafri et al., 2022). This high energy demand is owing in part to the comparatively modest size (capacity) of existing liquefiers, which were designed with an emphasis on low capital cost (CAPEX) rather than high efficiency. This significantly increases the cost and carbon intensity of the end-use hydrogen. As seen in **Table 8** More than 15 industrial hydrogen liquefaction units have been built within the last 20 years.

Air Products is the largest supplier of liquid hydrogen, followed by Praxair in North America. With a daily capacity of 6-35 TPD, Praxair presently operates five liquid hydrogen manufacturing plants in the United States (T. Zhang et al., 2023). A modified Claude cycle with pre-cooling is commonly used in the liquefaction procedures of the Praxair large-scale hydrogen liquefaction plants. According to reports, this system has an exergy efficiency of 19-24 % and a specific energy consumption of 12.5-15 kWh/kg_{LH_2} (Drnevich & Praxair, 2003). A Praxair liquefaction flow sheet is displayed in **Figure 26**. Although it is more complicated for the large-scale system, it resembles the pre-cooled Claude cycle.

Three heat exchangers were employed in this system for better interaction with the feed fluid and refrigerants. Nitrogen gas and the external refrigeration system cool the first heat exchanger. Liquid nitrogen and a portion of the hydrogen supply cool the second heat exchanger (Krasae-in et al., 2010a). A hydrogen refrigeration system that uses some of the feed to expand via turbines and a (J-T) valve cools the third. Currently, Air Products has four hydrogen liquefaction facilities that produce between 30 and 35 TPD of liquid hydrogen in North America. They also have two 5 TPD LH_2 facilities, one in the USA and the other in the Netherlands. Nevertheless, there is no literature regarding the technique of Air Product. Both of Air Liquide's plants, located in Canada and France, have capacities of roughly 10 TPD. There are no publications regarding the Air Liquide cycle, although both of these plants use the Claude cycle with hydrogen as the refrigerant cycle for further cooling of the feed gas (H_2).

Linde operates two hydrogen liquefaction plants in Germany. The first was constructed in Ingolstadt in 1991, while the second was constructed in Leuna in 2008. The largest hydrogen liquefaction plant in Germany was once the Linde hydrogen liquefaction manufacturing plant in Ingolstadt, which uses feed gas from refineries (Rezaie et al., 2016a). The liquefier is based on a modified liquid nitrogen-cooled Claude cycle. The hydrogen is pre-cooled to 80 K using

liquid nitrogen and then cooled to 30 K using a hydrogen expander refrigeration system before being liquified by a throttling process (J-T valve).

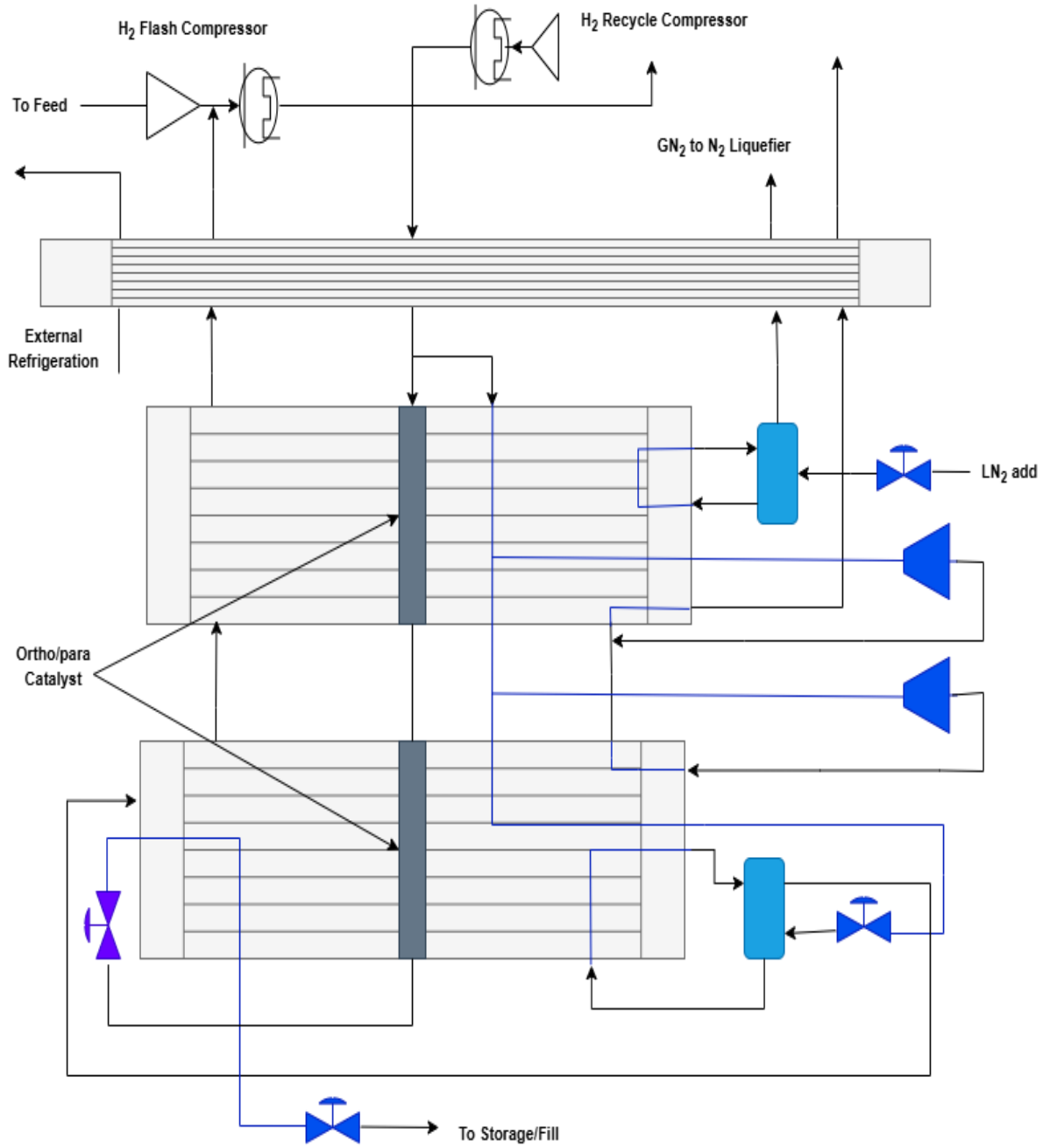

Figure 26. Process flow sheet of Praxair liquefaction plant (adapted from Ref. (Drnevich & Praxair, 2003)).

This liquefier has a specific energy consumption of 13.8 kWh/kg_{LH_2} and a liquefaction capacity of 4.4 TPD (T. Zhang et al., 2023). Linde opened a second hydrogen liquefaction facility at Leuna for 20 million euros. It is the newest and largest hydrogen liquefier facility in Germany, and is also considered the base-case model for this proposed design. The current plan at Ingolstadt is comparable to the system with the new cycle in **Figure 27** (Krasae-in et al., 2010a).

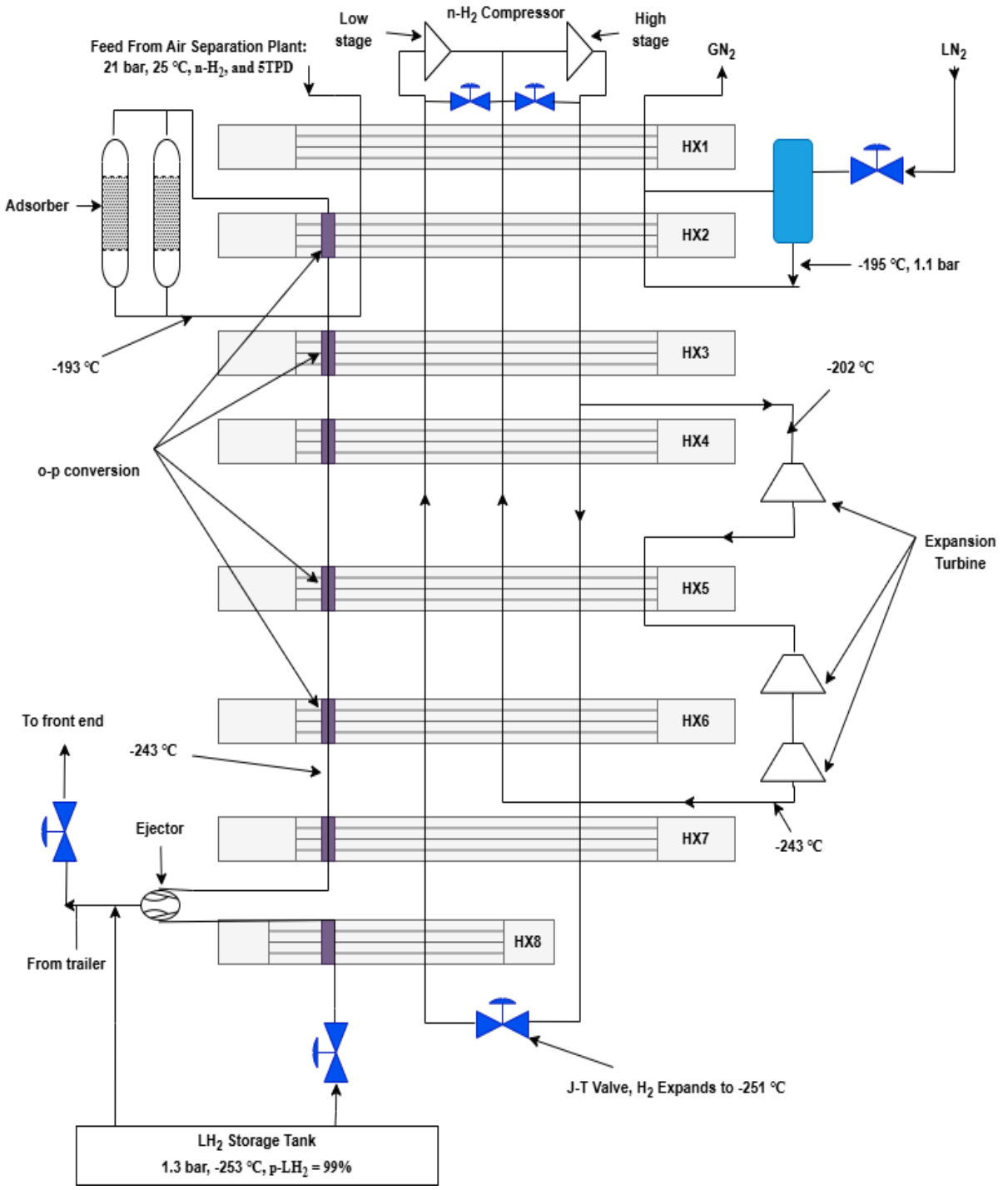

Figure 27. Base case design of hydrogen liquefaction plant in Leuna (adapted from Ref. (Krasae-in et al., 2010a)).

The newly constructed plant at Leuna is more efficient than a similar decommissioned plant in Ingolstadt. Continuous ortho-para conversion, oil-free advanced dynamic gas bearing turbines, and an ejector to re-liquefy boil-off gas and flash gas are the reasons for the advancements. The cryogenic cooling system consists of three turbines connected in series that operate at 102,000 rpm at pressures ranging from 0.52 to 2.0 MPa. The Leuna plant has an exergy efficiency of 23.6 % and a stated SEC of 11.9 kWh/kg_{LH_2} (Al Ghafri et al., 2022).

6.4 Conceptual Hydrogen Liquefaction Cycles

Since 1987, more than 25 theoretical hydrogen liquefaction technologies have been conceptually proposed. These conceptual plants have capacities ranging from 5 to 864 TPD (Al Ghafri et al., 2022). The conceptual hydrogen liquefaction cycle has the SEC range of 4-14 $\mathrm{kWh/kg_{LH_2}}$. These conceptual models aim to show conceptually how the liquefaction process might be maximized. In general, conceptual models do not adequately account for operability, technical readiness, or total cost.

(Quack, 2002) proposed hydrogen liquefaction of 170 TPD and uses a helium-neon mixture as a refrigerant, allowing for the use of the best available compression system. The preliminary design of the plant demonstrates that the overall plant can achieve a thermodynamic efficiency of around 60 %. This leads to an overall power demand ranging from 5 to 7 $\mathrm{kWh/kg_{LH_2}}$, depending on feed pressure and product temperature. These power consumption values are proposed as benchmarks for future investigations on large-scale hydrogen liquefaction.

The process description of the given conceptual cycle is elaborated below with the process flow diagram, as shown in **Figure 28**. For the compression of hydrogen from 0.1 to 8 MPa, a five-stage compression is selected, with an average ratio of about 2.4 per stage. An isentropic efficiency of 85 % per stage is assumed, which includes pressure losses in the pipework, valves, and intercoolers. In addition, an efficiency of 96 % is assumed for the electric motor. The overall power consumption can be reduced by applying intermediate cooling between the compression stages. The compressed hydrogen is first cooled to 300 K using cooling water and then further cooled to 276 K by means of a propane vapor-compression refrigeration system. For compressing the feed hydrogen from 0.1 to 8 MPa, a total energy input of 7.4 MJ/kg is required. Compared with the exergy increase of 5.48 MJ/kg, this corresponds to a compression efficiency of 73 %. This value also includes the electrical power required to operate the propane refrigeration system used for intercooling.

In this study, a helium-neon mixture is selected as a refrigerant for several reasons. First, this option avoids a fixed temperature level at 77 K. Second, it requires a smaller overall number of compressors, which has a beneficial effect on total power consumption. Finally, helium, neon, and their mixtures exhibit superior heat transfer properties compared with nitrogen, leading to improved thermal performance.

For cooling from 77 K to 23 K, neon, hydrogen, and helium are possible choices as refrigerants. A refrigeration mixture with a molecular mass of 7.2 kg/kmol is considered. At a pressure of

0.27 MPa, the corresponding dew point is 25.1 K. The outlet temperature of the final expander is therefore selected as 24.8 K. With this small degree of subcooling, little or no liquid formation is expected at the expander outlet.

The primary process step in this temperature range is the work extracting expansion of the feed hydrogen stream from 8 MPa to 0.1 MPa. The isentropic efficiency of 85 % is assumed for this growth. However, the cooling accomplished in this stage alone is insufficient to attain the storage state, which is saturated liquid.

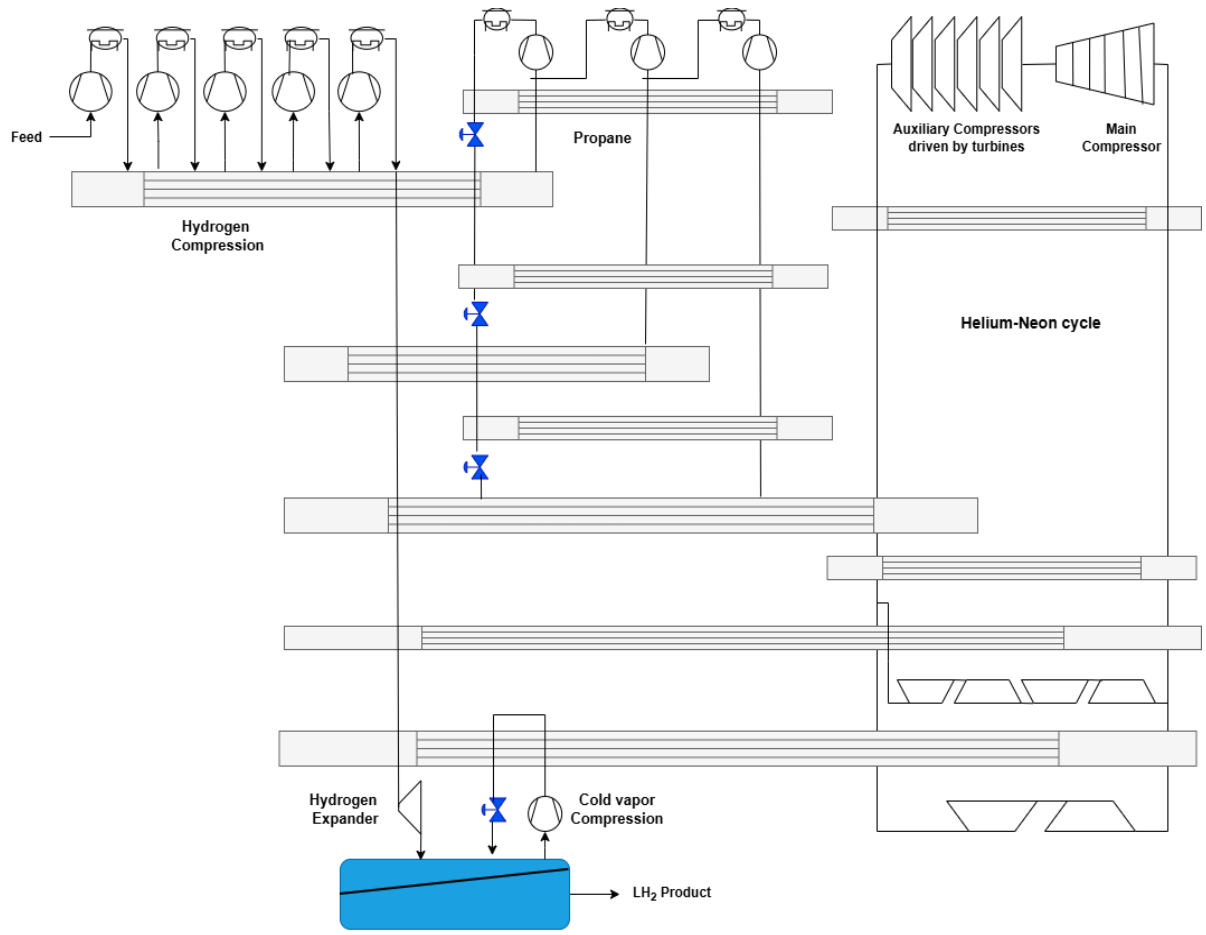

Figure 28. Schematic diagram of the conceptually designed proposal by H. Quack.

The IDEALHY project (Stolzenburg et al., 2013; Stolzenburg & Mubbala, 2013), as shown in **Figure 29**, is a conceptual design for a 50 TPD liquefier that uses MR pre-cooled 'Nelium' mixed refrigerant (75 % helium, 25 % neon) in a dual Brayton refrigeration cycle. The feed is compressed from (2 to 8) MPa using two reciprocating piston compressors. Pre-cooling to 130 K is then accomplished in four heat exchangers utilizing a mixture of nitrogen, methane, ethane, propane, and n-butane. Cryogenic cooling is accomplished through two overlapping Brayton cycles utilizing Nelium. O-P conversion takes place during the pre-cooling stage (130

to 85 K) in four adiabatic converters, followed by continuous conversion in catalyst-packed heat exchangers (<85K). The hydrogen stream is finally expanded to the liquid phase by two expansion turbines with the pressure ranging from 8 to 0.2 MPa. The discharge stream of the final turbine contains hydrogen flash gas. This process has the SEC of 6.7 kWh/kg_{LH_2}, and an exergy efficiency of 32 %. The IDEALHY project discovered that heat integration with an adjacent LNG import and regasification facility could reduce the SEC by 0.62 kWh/kg_{LH_2}. The investment cost for 50 TPD plants was 105 million Euros.

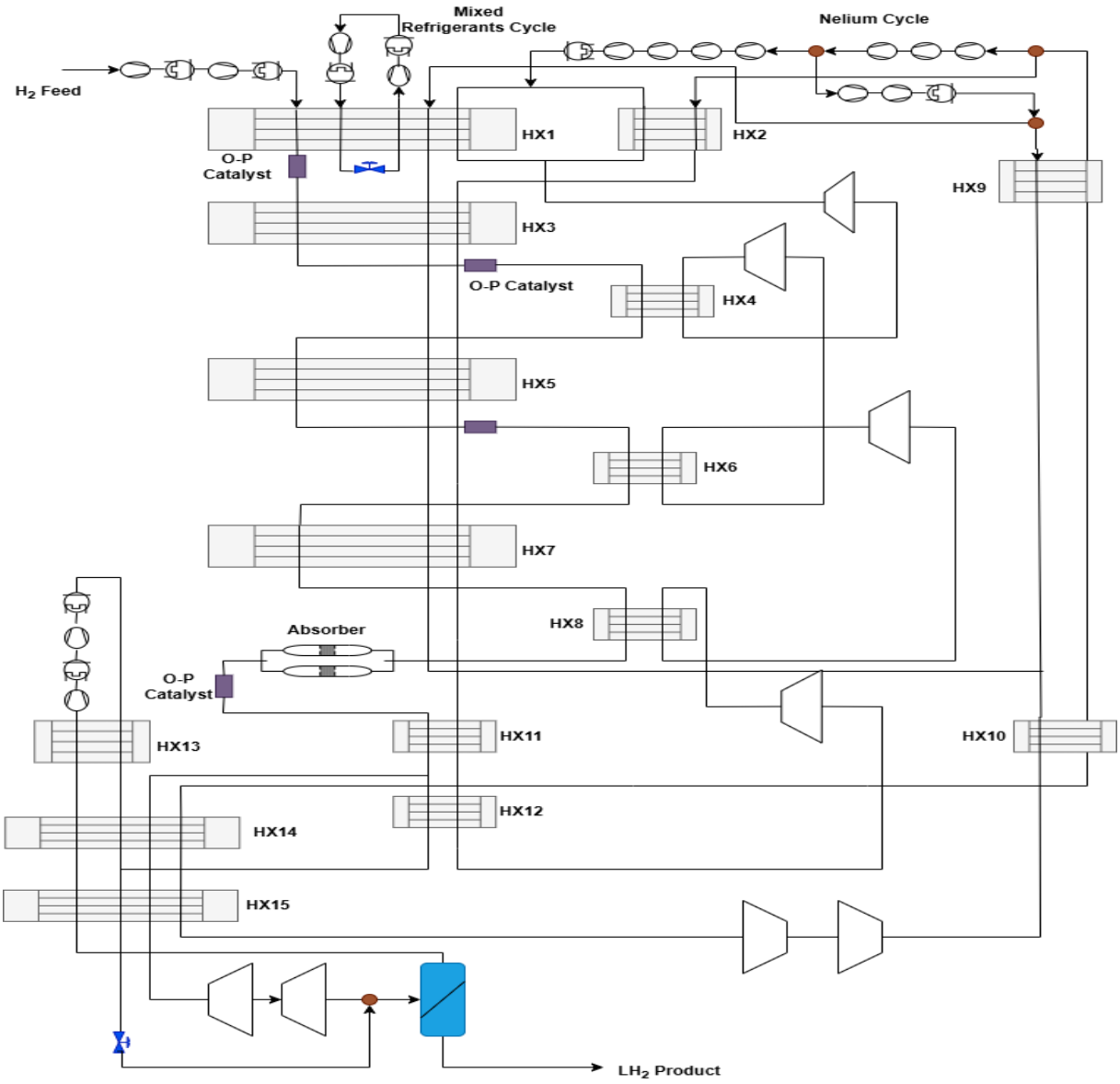

Figure 29. Process flow diagram for IDEALHY project (adapted from Ref. (Stolzenburg et al., 2013)).

(Valenti & Macchi, 2008) proposed a conceptual design for an 864 TPD liquefier based on four cascaded Brayton refrigeration cycles using a helium refrigerant. The primary innovations include the following features. First, the 10 kg/s hydrogen feed stream is cooled in heat

exchangers that catalyze ortho-para conversion. Second, the feed is chilled to a low temperature of 20.5 K while remaining under high pressure of 6 MPa. Third, a liquid-phase turbomachine expands the hydrogen to storage conditions of 0.15 MPa and 20 K. Four helium recuperative J-B cycles provide refrigeration, with the refrigerants following the hydrogen cooling curve. This arrangement produces volume flow rates during compression and expansion, which are ideal for high-efficiency axial-flow turbomachinery. Compression is accomplished with 15 intercooled, 8-stage compressors adapted from gas turbine technology. The necessary surface areas for the heat exchanger are comparable to those of the most advanced hydrogen liquefiers currently available. The projected specific work input of 18 MJ/kg (5 kWh/kg_{LH_2}) is half that of conventional liquefiers, resulting in a second-law efficiency of approximately 48 %.

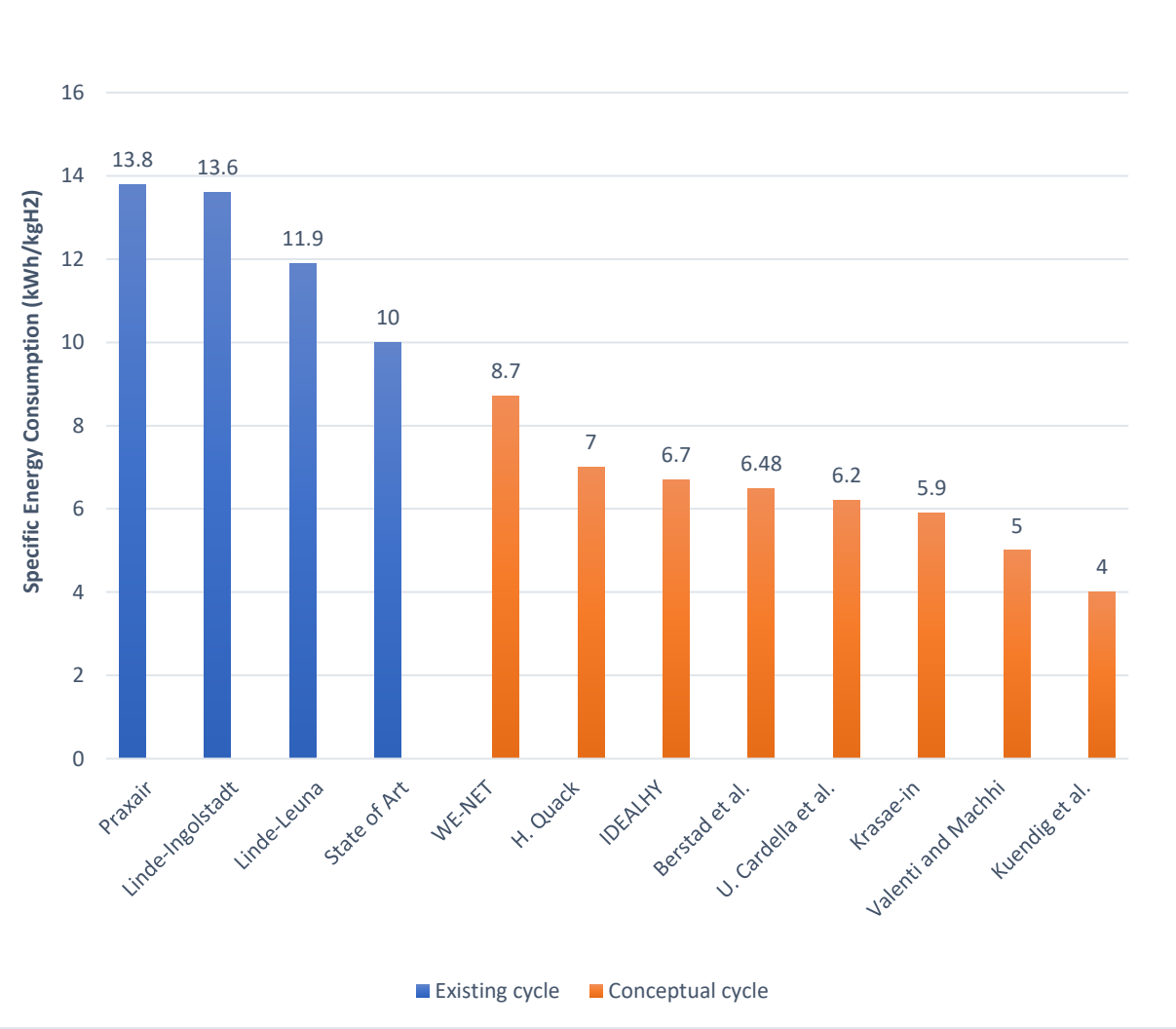

Figure 30. Performance of industrial or existing and conceptual hydrogen liquefiers (Adapted from Ref. (Al Ghafri et al., 2022)).

(Berstad et al., 2010) proposed an innovative large-scale hydrogen liquefaction concept featuring enhanced thermodynamic efficiency. The concept is based on MR pre-cooling,

enabling efficient thermal management in the high-temperature region of the process. In this configuration, MR pre-cooling is applied down to a hydrogen temperature of approximately 75 K, and the required refrigeration is supplied by a reversed Brayton cycle employing helium and neon as working fluids.

Within this framework, two MR-based liquefier configurations have been developed and analyzed. The first configuration utilizes J-T expansion valves for MR throttling, whereas the second replaces these valves with liquid expanders to improve efficiency. For a hydrogen pressure of 2.1 MPa and an ambient temperature of 300 K, the corresponding specific liquefaction power requirements were found to be 6.48 $\mathrm{kWh/kg_{LH_2}}$ and 6.15 $\mathrm{kWh/kg_{LH_2}}$, respectively. Based on current modelling results, these values indicate a potential reduction in specific energy consumption of approximately 45-48 % relative to state-of-the-art hydrogen liquefaction technologies.

The different data illustrated in **Figure 30** demonstrates the SEC of both existing and conceptual hydrogen liquefaction cycles. With Praxair and Linde-Ingolstadt having the highest SEC at 13.8 and 13.6 $\mathrm{kWh/kg_{LH_2}}$, respectively. The data indicate that the existing cycle, shown in blue bars, often consumes more energy than the conceptual cycle, shown in orange bars. This is because the existing plants were designed with limited equipment and optimization, whereas the conceptual cycle is simulated with high-efficiency equipment models and yields a higher optimized result.

7. Simulation Process

A detailed dynamic model for simulation is developed using **Simscape Fluids, MATLAB 2025a**, to assess the thermodynamic performance and SEC of a hydrogen liquefaction process. MATLAB is a computer algebra system that uses its own language to perform complicated computations and data analysis. **MathWorks®** developed MATLAB, which NASA (The National Aeronautics and Space Administration) routinely uses for data processing, analysis, modelling, and simulation (Volle, 2014). Modelling is conducted using MATLAB Simulink, an add-on that includes a graphical user interface and a library of blocks representing mathematical operations that may be put together to visually depict equations and systems. Simscape is a Simulink module that includes blocks for representing physical parts and complete physical systems. Simscape allows you to develop models of entire systems. NE-C1, at Kennedy Space Center (KSC), is also investigating further use of Simscape by the Application & Simulation Software Engineering Branch (Fischer, 2015). Simscape models must be demonstrated to be capable of running in real time, utilizing Trick (a real-time simulation tool), and with an acceptable level of precision.

Simscape® is an acasual method for modelling dynamic systems that uses connected physical components (blocks) with defined equations according to a particular connection design. This acasual methodology varies from the casual one employed in MATLAB Simulink, where the interconnection of blocks reflects the computation procedure rather than the underlying structure of the modeled system (Javier Fernandez de Canete & Jesus Martin-Aguilar, 2020). Every block in Simscape is made up of functional components that communicate with one another by sharing power via their ports, as shown in Figure 31**.**

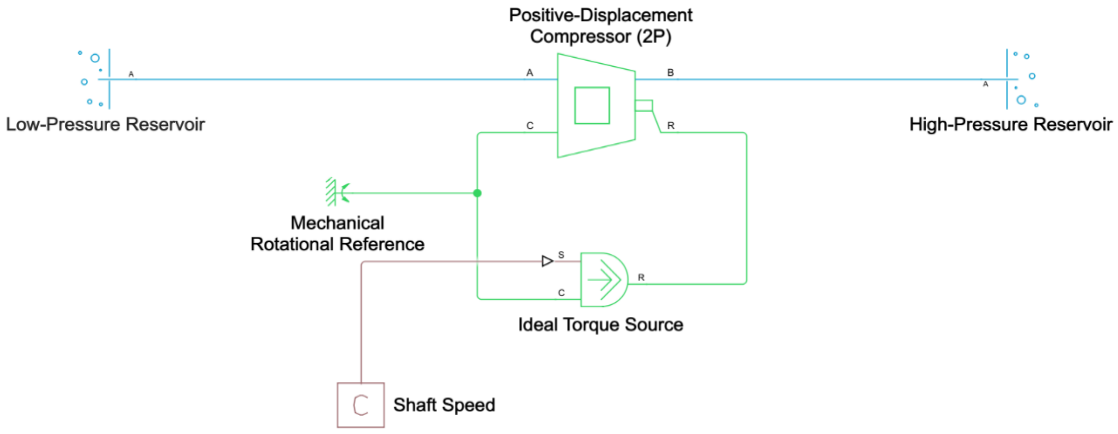

Figure 31. The model shows the energy transfer through ports from the low-pressure region to the high-pressure region.

Only connectors that belong to the same connector classes can be connected to these blocks via precisely defined interfaces (connector ports), where variables used for connection are defined. Simscape Fluids consists of gas, moist air, isothermal liquid, thermal liquid, and two-phase fluid. Simulating the hydrogen liquefaction process primarily uses a two-phase fluid library, as hydrogen is expanded from the feed gas into a two-phase fluid in a separator. When Simscape blocks are connected, information flow does not need to be specified because energy can move in both directions. The various libraries in the Simscape fluids are connected according to their defined phase; the connection between two different phases of fluid cannot be interconnected in their respective ports, as shown in **Figure 32**. The figure demonstrated is just a rough example to showcase the connection between them.

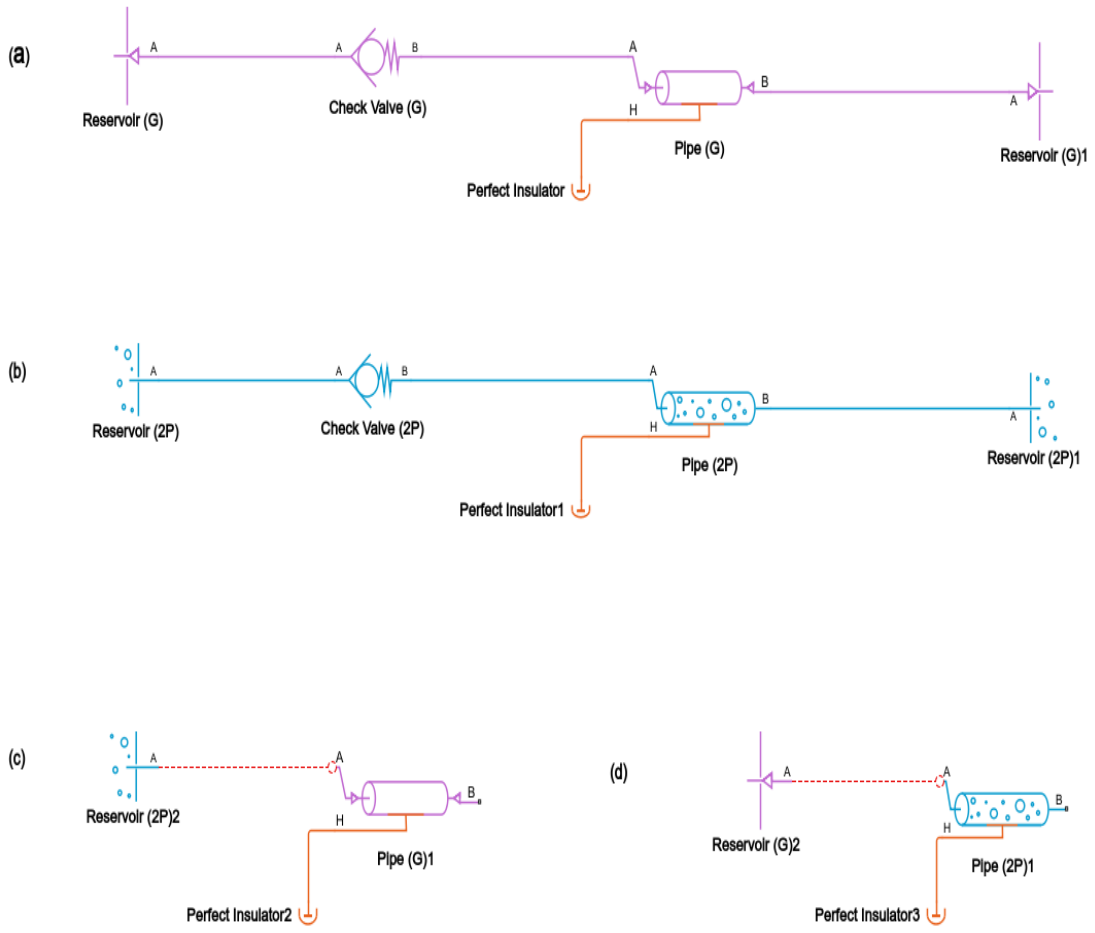

Figure 32. Shows the connection between similar and distinct domains.

The various annotations are made for their respective connection between Gas and Gas domain (G-G), and Two-Phase and Two-Phase domain (2P-2P). Components in Simscape Fluids can only be connected to other components within the same fluid domain because they are arranged

into similar physical domains, as shown in **Figure 32(a) and (b).** Direct connections between the Gas and Two-Phase Fluid domains are not possible through physical conserving ports. Cross-domain connection is physically inconsistent because each fluid domain is subjected to its own set of conservation equations, state variables, and thermodynamic assumptions, as shown in **Figure 32(c) and (d).** In order to ensure that only physically significant fluid networks are simulated, any effort to directly connect components from various fluid domains results in a model configuration error.

7.1 Fluid Properties

Unlike other simulation software, Simscape does not have a predefined fluid property table for hydrogen as a working fluid. External thermophysical property databases were incorporated into the simulation environment to facilitate the creation of fluid property tables for two-phase flow computations in MATLAB. To give precise real-fluid property data, REFPROP and CoolProp were specially utilized. NIST REFPROP utilized the equation of state (EOS) to compute the characteristics of pure nitrogen and hydrogen. The normal-hydrogen fluid characteristics are used to model both the entire hydrogen Claude cycle and the cooling of the hydrogen feed stream from ambient to the pre-cooling temperature (Leachman et al., 2009).

The National Institute of Standards and Technology (NIST) requirements were followed in the installation of REFROP. The syntax below gives the MATLAB command prompt for extracting a two-phase fluid property (Mathworks/twoPhaseFluidTables, 2025).

"fluidTables=twophaseFluidTables(uRange,pRange,mLiquid,mVapor,n,substance,installpath)"

Where,

- uRange = Lower and upper bounds of the specific internal energy range
- pRange = Lower and upper bounds of the absolute pressure range
- mLiquid = Number of rows to include in the liquid tables
- mVapor = Number of rows to include in the vapor tables
- n = Number of columns to include in the fluid tables
- substance = Database name for the fluid whose properties to retrieve.
- Installpath = File path to REFROP installation folder or python package path to CoolProp.
- fluidTables = Name of the structure array in which the fluid tables are stored.

The tables are kept as a structural array in fluidTables. The data for the liquid properties tab is contained in a liquid substructure, and the data for the vapor properties tab is contained in a

vapor substructure. The fluid itself, such as specific volume, specific entropy, kinematic viscosity, thermal conductivity, and others required for simulation, is contained in the fields of the substructures. The tabulated data is represented in a two-dimensional block space. Absolute pressure fluctuates between the columns, and a normalized specific internal energy varies between the rows. These variables are used for generating a pressure-internal energy and temperature diagram, as shown in **Figure 35**.

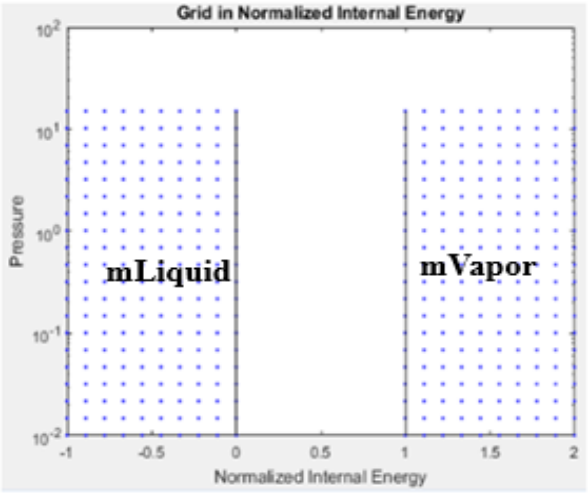

Figure 33. Schematic diagram of pressure versus normalized internal energy grid.

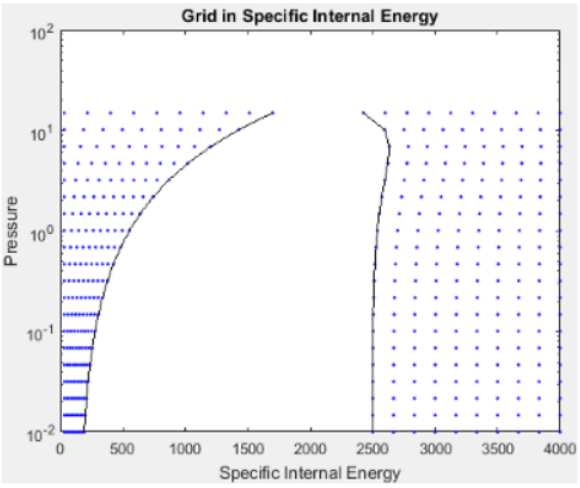

Figure 34. Schematic diagram of pressure versus specific internal energy grid.

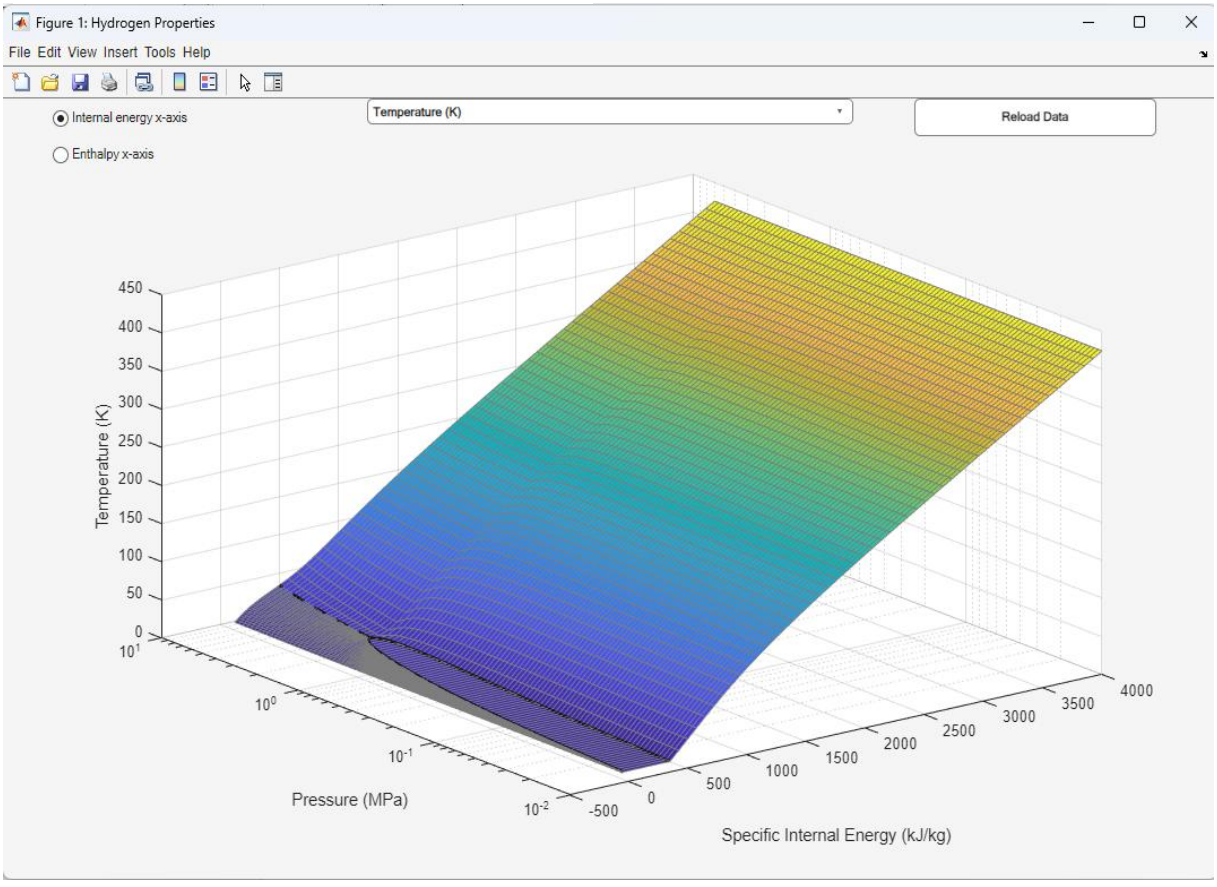

Figure 35. 3-D diagram of hydrogen from the two-phase fluid properties table (adapted from the simulation property table).

For the liquid phase, the normalized specific internal energy spreads between the bounds in uRange across mLiquid rows; for the vapor phase, it spans across mVapor rows, as shown in **Figure 33**. For both liquid and vapor phases, pressure extends over n rows between the constraints in pRange. Interpolation between the pure phases determines the characteristics of liquid-vapor mixtures. After developing a graph between the p-u space and adapting formulas such as $H = U + PV$, which helps in generating a P-H diagram through the physical signal domain (P-H Diagram 2P) in the Simscape two-phase library. The diagram is separated into three regions: liquid, vapor, and liquid-vapor mixture. The saturated liquid (L) and saturated vapor (V) lines form a dome-shaped boundary, enclosing the two-phase region. Inside this dome, the fluid is a mixture of liquid and vapor, with the vapor quality increasing from left to right (0 to 1). Lines of constant temperature, entropy, or specific volume can be drawn on the P-H diagram to demonstrate how the fluid state varies during thermodynamic processes. As the enthalpy directly displays energy content, the P-H diagram is particularly useful to investigate refrigeration systems, where energy transfer and phase shift are important factors.

The sensible setup of operating parameters is required to ensure that the process is rational. To simplify the process simulation, the following assumptions are made based on existing industrial data and available literature.

1. The feed hydrogen gas entering the liquefaction process has been compressed to 2.1 MPa and purified, which consists of only 75% ortho-hydrogen and 25% para-hydrogen.
2. The whole process is handled in accordance with steady state and steady flow, and the influence of kinetic energy and potential energy effects is ignored.
3. The impurities in hydrogen have been removed before the hydrogen enters the liquefaction process.
4. The outlet temperature of the intercoolers is set at 300 K, and the working fluid, which has been used to cool it down, is moist air at atmospheric temperature and pressure.
5. The pressure drop across all heat exchangers and coolers is negligible.
6. The adiabatic efficiencies of the compressors and expanders are both set to 80%.
7. The O-P conversion of hydrogen is done in two stages, preferably at 80K, after pre-cooling and 20K, before J-T expansion.
8. The pressure of the all-incoming stream into the mixing chamber is equal.
9. The pressure ratio of the multi-stage compressors is kept ≤ 3 (Lee et al., 2022).

7.2 Proposed Simulated Design for 5 TPD

The model simulates the entire liquefaction cycle, including compression, heat exchange, O-P conversion using Simscape Language (SSC code), and phase-change processes, allowing for a systematic evaluation of operating conditions and component efficiency.

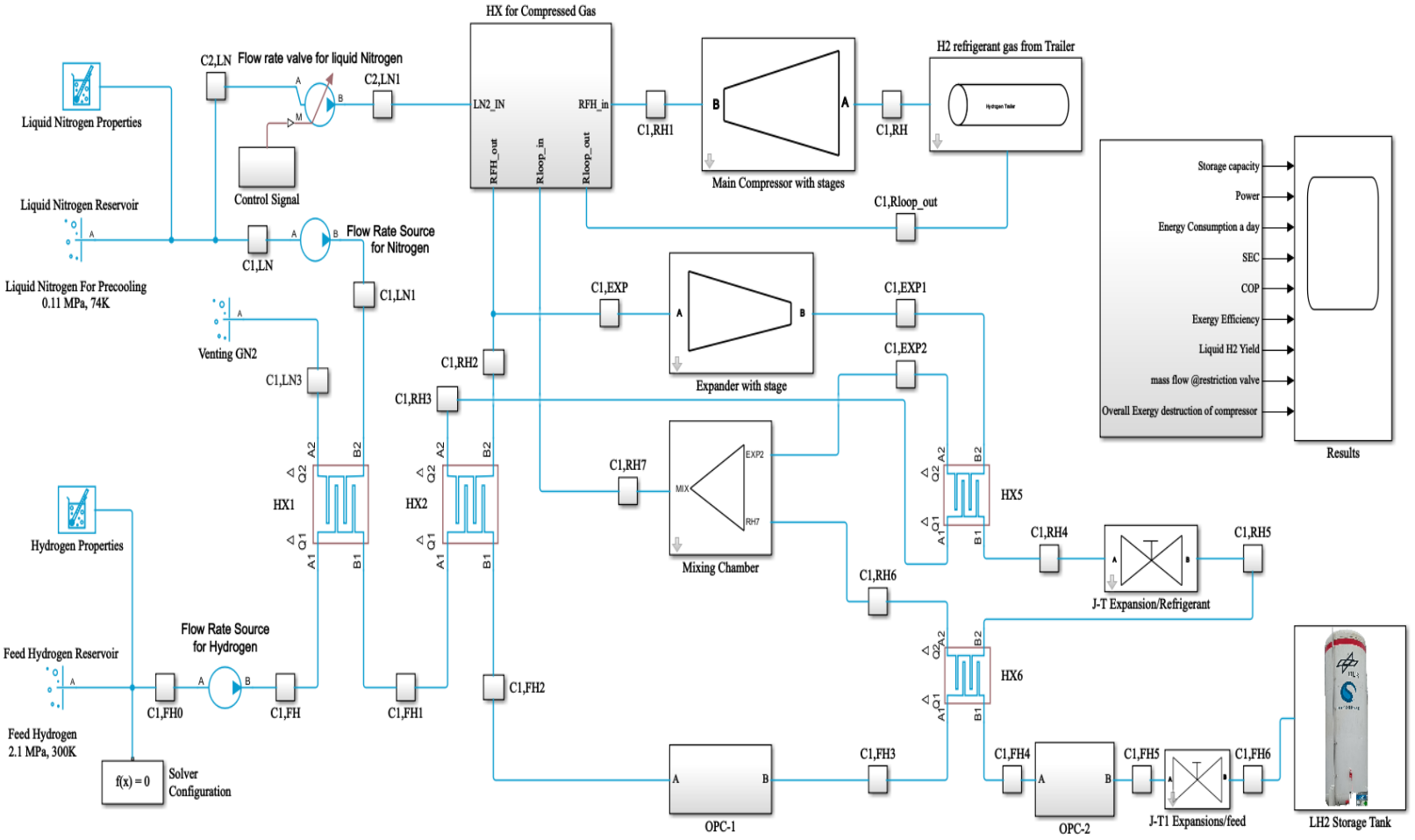

Figure 36. Proposed design of hydrogen liquefaction cycle with 5 TPD capacity.

7.3 Process Description

The proposed design is based on a modified pre-cooled Claude cycle, incorporating an open liquid nitrogen (LN_2) pre-cooling cycle and a closed hydrogen refrigerant loop cycle. Hydrogen gas is supplied at 298 K and 2.1 MPa to the first heat exchanger (HX1), which is responsible for pre-cooling the gas to approximately 80 K. HX1 is a system-level heat exchanger that utilizes (LN_2) as the pre-cooling medium. Hydrogen itself is then used as the refrigerant for subsequent cryogenic cooling for the process stream. The pre-cooled hydrogen stream goes to the first ortho-para converter (OPC-1), which performs a controlled partial conversion. In the downstream cryogenic process, this conversion step is essential for controlling the thermal behavior of hydrogen at storage. According to the model, OPC-1 operates adiabatically, implying no external heat transfer between the converter and its environment. The temperature of the gas rises as a result of the exothermic heat generated during the conversion process, which is retained within the hydrogen stream. This internally generated heat is then carried with the hydrogen to the next heat exchanger, HX2, where it affects the overall heat exchange requirements and temperature profile of the system. The section **8.4** provides a detailed discussion of the conversion extent as a function of the inlet hydrogen temperature and its implications for the thermal management and process efficiency.

The cycle employs a three-stage hydrogen compressor with corresponding intercoolers to cool the compressed gas to 300 K. The refrigerant hydrogen is sourced from a hydrogen gas trailer at standard conditions before entering the compressor. Each intercooler uses moist air as the working fluid, assisted by a fan blower, to remove heat from the refrigerant prior to entering a subsystem referred to as a compressed-gas heat exchanger (HX). This subsystem consists of two heat exchangers, HX3 and HX4. Initially, HX3 precools the refrigerant gas exiting the positive-displacement compressor at 2.1 MPa and 300 K using liquid nitrogen. The liquid nitrogen supply is provided only for a specified duration of 1 s and is regulated by a control valve that shuts off the flow after this period.

After 1 s, the return flow from the mixing chamber is used as the coolant for the refrigerant gas. A directional valve controls the refrigerant flow, directing it to HX3 for the first second and subsequently diverting it entirely to HX4. HX4 facilitates heat transfer between the refrigerant gas and the return flow from the mixing chamber, reducing the refrigerant temperature to approximately 80 K. The cooled refrigerant then enters HX2, where the flow is split and directed to a multistage expansion turbine. The total refrigerant mass flow rate is 0.29 kg/s, which is divided

into two streams. The multistage expander further cools the refrigerant gas to 30 K, and the cold expanded gas transfers heat to the stream exiting HX2 through HX5.

The cooled stream from HX5 then passes through a Joule-Thomson (J-T) expansion valve, where it is expanded to approximately 21.21 K. The cold energy of the fluid exiting the J-T valve is subsequently used to precool the feed hydrogen gas in HX6, after which the refrigerant returns to the mixing chamber. Finally, the feed hydrogen is expanded through a J-T expansion valve (J-T1) to a pressure of 0.13 MPa and a temperature of 21 K. The liquid hydrogen from J-T1 is collected in a liquid hydrogen storage tank at a flow rate of 0.058 kg/s.

7.4 Thermodynamic Analysis

One of the most important performance indicators is specific energy consumption (SEC). In order to improve ***energy efficiency***, the SEC was estimated using energy analysis, and attempts were made to lower its value. This section aims to assess the viability of a base case design process with an SEC value of less than 11.9 kWh/kg_{LH_2} (Rezaie et al., 2016b). Additionally, the impact of design factors and refrigerant choices on total SEC will be quantified through a detailed discussion. In the steady-state processes, ignoring potential and kinetic energy, the mass balance equation for the control volume can be written as (Bian et al., 2021b):

$$\sum \dot{m}_{in} = \sum \dot{m}_{out} \tag{7.1}$$

Where ṁ is the mass flow rate, in and out represent inlet and outlet conditions, respectively. The energy balance equation, defined according to the first law of thermodynamics, can be expressed as:

$$\sum(\dot{m} \cdot h)_{in} + \sum \dot{W}_{in} + \sum \dot{Q}_{in} = \sum(\dot{m} \cdot h)_{out} + \sum \dot{W}_{out} + \sum \dot{Q}_{out} \tag{7.2}$$

Where h represents the mass enthalpy, Ẇ denotes the work rate, and Q̇ indicates the heat transfer rate. The energy of the primary equipment used in the process is determined based on the energy balance equation. The compressors and expanders are devices that consume or produce energy throughout the process. The formulas for calculating energy for them can be stated as follows:

$$\dot{W}_{c-i} = \dot{m}_{c-i}\left(h_{c-i,out} - h_{c-i,in}\right) \tag{7.3}$$

$$\dot{W}_{E-i} = \dot{m}_{E-i}\left(h_{E-i,in} - h_{E-i,out}\right) \tag{7.4}$$

$$\dot{W}_{LN_2} = \dot{m}_{LN_2} \times w_{LN_2} \tag{7.5}$$

Where $\dot{W}$ is the rate of work done, c & E denotes the compressors and expanders, and i denotes component numbers, $\dot{m}$ is the mass flow rate of the various components, w_{LN2} is the energy required for liquid nitrogen production in (kWh/kg), and h denotes the enthalpy of inlet and outlet conditions of the compressor and expander.

The SEC, coefficient of performance (COP), and exergy efficiency (Ex) are commonly used in liquefaction systems to assess system performance. According to the first law of thermodynamics, the SEC is defined as the ratio of total energy consumption in the process to the mass flow rate of production (Yin & Ju, 2020b). That is

$$SEC = \frac{\dot{W}}{\dot{m}_{LH_2}} \tag{7.6}$$

Where, $\dot{W}$ is the total power consumption of the system in kW, as described in equation (28),

$$\dot{W} = \sum \dot{W}_{C-i} - \sum \dot{W}_{E-i} + \dot{W}_{LN2} \tag{7.7}$$

The COP is defined as the ratio of cooling capacity provided by the working fluid to the net input power of the cycle (Aasadnia & Mehrpooya, 2018), given as

$$COP = \frac{\dot{m}_{LH2} \times (h_{feed} - h_{LH2})}{\dot{W}} \tag{7.8}$$

Exergy analysis is used to locate the irreversibilities and thermodynamic inefficiencies of a liquefaction process. This tool has significant importance, especially in cryogenic operations where processes are relatively energy-intensive, and their exergy efficiencies are very low. The proposed study takes into account physical and chemical exergies based on a steady-state system. Equations (29) and (30) were used to calculate the exergy (Szargut, 1989).

$$Ex_{ph,i} = (h_i - h_0) - T_0(s_i - s_0) \tag{7.9}$$

$$Ex_{ch,i} = \sum x_i e_i^{CH} + RT_0 \sum x_i ln x_i \tag{7.10}$$

Equation (29) represents the physical exergy equation, and Equation (30) denotes the chemical exergy. Physical data of each stream were retrieved from MATLAB-based calculations, while chemical exergy was calculated by Eq. (30). Where, x_i represents the mole fraction of the component i, e_i^{CH} is standard chemical exergy, and R denotes the gas constant. However, the Ex for

a liquefaction process is the ratio of the ideal liquefaction work to the actual liquefaction consumption. It can be expressed as

$$Ex(\varepsilon) = \frac{W_{rev}}{W_{act}} = \frac{\dot{m}_{LH2}[(h_{LH2} - h_0) - T_0(s_{LH2} - s_0)]}{\dot{W}} \qquad (7.11)$$

Where T_0 is the ambient temperature, T_0 = 25 °C, W_{rev} is the ideal reversible liquefaction work, W_{act} is the actual liquefaction work, h_0 and s_0 are the hydrogen enthalpy and entropy at ambient temperature, h_{LH2} and s_{LH2} are the enthalpy and entropy of the liquid hydrogen stream (Yin & Ju, 2020b).

Exergy analysis calculates exergy losses and efficiency across equipment and the entire plant. Equipment exergy losses are calculated as the differential between exergy flows entering and exiting the system. The literature contains two types of ways for expressing the exergy efficiency of the equipment. The first is stated as the input-output efficiency, which may be calculated as the ratio of all energy flows entering and exiting from the apparatus. The second is stated as the consumed-produced efficiency, which makes it possible to measure energy quality and deviation from ideality with greater accuracy. Consequently, the exergy efficiency of every component of machinery is determined using the second class (Kori et al., 2024). The overall exergy destruction, exergy losses, and exergy efficiency of the main equipment are given in **Table 10** (Bian et al., 2021b).

Table 10. The formulae of exergy and exergy efficiency for the main equipment.

Equipment	Exergy losses	Exergy efficiency
Compressor	$\Delta E_c = \dot{W}_c - E_{out} + E_{in} = \dot{W}_c - \dot{m}_{c,out} \cdot e_{c,out} + \dot{m}_{c,in} \cdot e_{c,in}$	$\varepsilon_c = \frac{E_{in} - E_{out}}{\dot{W}_c} = \frac{(\dot{m} \cdot e)_{c,out} - (\dot{m} \cdot e)_{c,in}}{\dot{W}_c}$
Expander	$\Delta E_E = -\dot{W}_E - E_{out} + E_{in} = -\dot{W}_E - \dot{m}_{E,out} \cdot e_{E,out} + \dot{m}_{E,in} \cdot e_{E,in}$	$\varepsilon_E = \frac{\dot{W}_E}{E_{in} - E_{out}} = \frac{\dot{W}_E}{(\dot{m} \cdot e)_{E,in} - (\dot{m} \cdot e)_{E,out}}$

Equipment	Exergy losses	Exergy efficiency
Heat Exchanger	$\Delta E_{HX} = E_{in} - E_{out} = \sum_{i=1}^{n} \dot{m}_{streami} \cdot (e_{in} - e_{out})_{streami}$	$\varepsilon_{HX} = \frac{\Delta E_h}{\Delta E_C} = \frac{\sum \dot{m}_h \cdot (e_{out} - e_{in})_h}{\sum \dot{m}_c \cdot (e_{in} - e_{out})_c}$
Mixer	$\Delta E_M = E_{in} - E_{out} = \sum_{i=1}^{n} (\dot{m} \cdot e)_{streami,in} - \dot{m}_{M,out} \cdot e_{M,out}$	$\varepsilon_M = \frac{\Delta E_{inc}}{\Delta E_{re}} = \frac{\sum \dot{m}_{inc} \cdot (e_{out} - e_{inc})}{\sum \dot{m}_{re} \cdot (e_{re} - e_{out})}$

Where $e_{c,in}$ and $e_{c,out}$ is the mass exergy of the compressor inlet and outlet, $\dot{W}_c$ is the total work done by the compressor, respectively. Similarly, $e_{E,in} and\ e_{E,out}$ is the mass exergy of the expander inlet and out, $\dot{W}_E$ is the total work done by the expander. $h\ and\ c$ denotes the hot and cold stream in the heat-exchanger. e_{inc} and e_{re} denotes the stream with increased exergy and reduced exergy in the mixing chamber.

8. Main Component Design

The various design considerations are made to achieve high system efficiency and low energy consumption of the cycle. The focus has been on the handling and parametrization of major equipment. The approach for preliminary sizing, design calculations, and estimating procedures is described in this chapter. The majority of these design processes have been operationalized using MATLAB-derived block equations. Several areas for improvement were identified through the evaluation of existing liquefaction cycles. A cycle that targets the desired improvements is suggested using the concepts and computer simulations of specific system settings. This part covers the primary technical design features of the equipment used in hydrogen liquefaction operations, with an emphasis on capacity and performance constraints.

8.1 Compressor

In the context of compression systems, increasing the feed pressure can reduce the work required in downstream processes. However, the feed conditions are constrained by the maximum allowable operating pressure of the available heat exchangers. Compressors are employed for both feed compression and the refrigeration cycle, and typically account for the largest portion of overall power consumption. Key factors influencing compressor power consumption include stage efficiency, the number of stages, compressor type, intercooling temperature, and pressure losses. The availability of high-pressure feed from hydrogen sources led to the consideration of using a high-pressure product stream. Many water electrolyzers, in particular, function under high pressure. The liquefier could eliminate some compression work if it were coupled to a high-pressure electrolyzer. Instead of using a reciprocating machine, the facility might benefit from the comparatively effective compression process associated with an electrolyzer. Furthermore, less theoretical ideal work input is needed when using high-pressure hydrogen as the inlet condition of feed hydrogen. The same approach is carried out in this simulated design, where the additional compression work for compressing the feed stream was avoided. However, hydrogen reciprocating compressors have been used to pressurize the refrigerant hydrogen from atmospheric pressure 0.101 MPa to 2.1 MPa. The refrigerant hydrogen is used for cryogenic cooling of feed hydrogen through a heat-exchanger and recycled back at atmospheric pressure, and hence the stream works as a loop cycle for producing 5 TPD capacity of hydrogen. This chapter also describes the actual component employed for the simulated design of hydrogen liquefaction.

The Simscape library contains a **positive-displacement compressor 2P** domain as a reciprocating compressor, as shown in **Figure 37**. This block models a positive-displacement compressor in a two-phase network and can be used to model any positive-displacement compressor type, such as reciprocating piston, rotary screw, rotary vane, and scroll. This system works by drawing in a volume of fluid and then reducing its volume to expel the fluid at higher pressure. The compressor used in this design is a vapor compression, which shows errors or warnings when fluid is not fully vaporized.

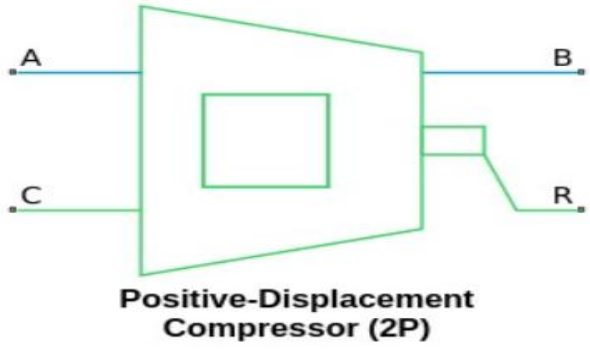

Figure 37. Pictorial diagram of positive-displacement compressor 2P in the Simscape library (adapted from Ref. (Mathworks/positive-displacement compressor 2P, 2025)).

Ports A and B are the two-phase conserving ports associated with the compressor inlet and outlet, respectively. Ports R and C are the mechanical rotational conserving ports associated with the shaft casing, respectively. A positive rotation of port R relative to port C drives fluid flow from port A to port B. The relative velocity of the system is calculated using an Ideal Angular Velocity Source domain from the Simscape library, as shown in Eq. 8.1. This block represents a velocity differential at its terminal proportional to the physical signal (Mathworks/positive-displacement compressor 2P, 2025).

$$Relative\ velocity\ (V) = V_R - V_c \qquad (8.1)$$

The behaviors of the compressor for reversed flow or rotation are undefined. Various assumptions and limitations are considered while setting up the parameters and modeling the compressor, which are given below:

1. The block may not be accurate for the reverse flow from port B to A.
2. The block assumes that the flow is quasi-steady. The compressor does not accumulate mass.

3. The block is designed to operate in superheated vapor. The block may not be accurate in a two-phase mixture or subcooled liquid.

The various parameters used in the positive-displacement compressor are tabulated, as shown in **Table 11**. Different initial conditions are selected to achieve the system objectives. Furthermore, several input values are taken from the existing cycle, such as the mass flow rate or volumetric flow rate, adiabatic efficiency, and Nusselt number, which are used to characterize the flow regime.

Table 11. Design parameters of positive-displacement compressor 2P.

Name	Value	Units
Displacement		
Displacement Specification	Nominal mass flow rate and shaft speed	
Nominal mass flow rate	0.29	kg/s
Nominal shaft speed	800	rpm
Efficiency		
Efficiency specification	Analytical	
Thermodynamic model	Polytropic	
Polytropic exponent	1.4	
Nominal volumetric efficiency	0.95	
Nominal Conditions		
Nominal conditions specifications	Nominal Pressure	
Nominal pressure ratio	20.72 ^ (1/3) = 2.7466	
Nominal inlet pressure	0.101325	MPa
Nominal inlet temperature	273.15	K
Parameters		
Mechanical efficiency	90	%
Inlet area at port A	0.01	m^2
Outlet area at port B	0.01	m^2

Positive displacement units are those in which successive volumes of air are confined within a closed space and elevated to a higher pressure. The capacity of a positive-displacement compressor varies only marginally with the working pressure. A compression cycle is schematically depicted in **Figure 38**. The cylinder is initially filled with gas at conditions (T_a, P_a) at the start of process a-b, and it undergoes compression according to a polytropic process. The discharge valve is then opened, and the gas is released until the piston completes its stroke and the required pressure, P_b, is reached. The dead volume, or V_c, represents the volume currently occupied by the gas, which is approximately at the state (P_b, T_b). Expansion takes place along a different polytropic path with both the entry and discharge valves closed until the pressure drops to approximately P_a at state 'd'. In the d-a process, gas is drawn from the exterior until the stroke is completed at volume V_a. The volume of gas ejected in (c-b) decreases as the compression ratio increases because V_c and V_d get closer. The expansion line (c-d) will coincide with (a-b) if the compression ratio is raised to a point where $V_b = V_c$ and no gas is evacuated when the discharge valve is opened. As a result, no gas will be aspirated in (d-a) (Bin et al., 2013).

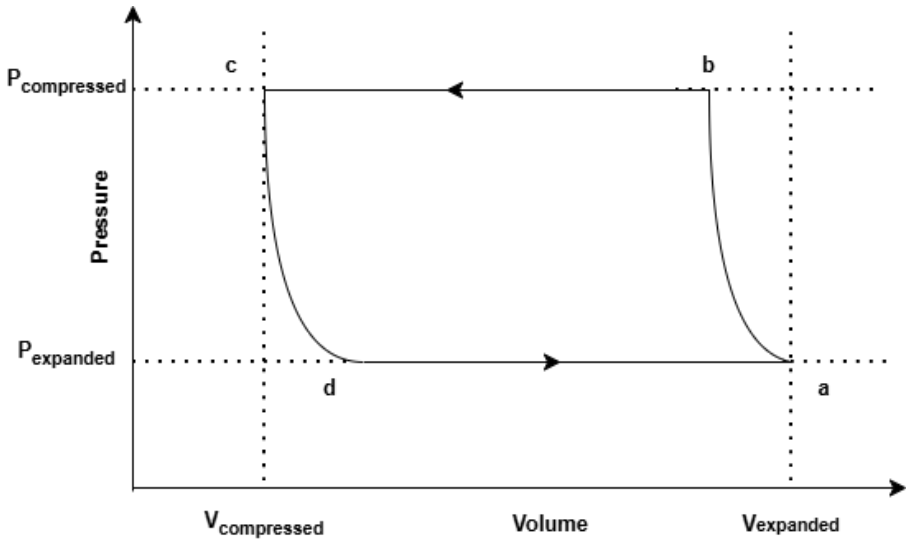

Figure 38. shows the steps of a positive-displacement compressor on the P-V diagram (adapted from Ref. (Mathworks/positive-displacement compressor 2P, 2025)).

Mass flow rate

The block calculates the mass flow rate as, (Mathworks/positive-displacement compressor 2P, 2025).

$$\dot{m} = \eta_v \omega \frac{V_{disp}}{V_s} \tag{8.2}$$

Where,

- $\dot{m}$ is the mass flow rate
- ω is the angular velocity at port R relative to port C.
- V_s is the specific volume at the inlet. The block calculates this value based on the Nominal conditions specification parameters and specified nominal inlet conditions.
- V_{disp} is the displacement volume that the block uses.
- η_v is the volumetric efficiency.

We can parameterize the volumetric efficiency by using analytical values or a lookup table. When we set the efficiency specification to analytical values and the thermodynamic model parameter to polytropic, as shown in **Table 11**. The volumetric efficiency is calculated as,

$$\eta_v = 1 + C - C\left(\frac{p_{out}}{p_{in}}\right)^{1/n} \tag{8.3}$$

Where p_{in} and p_{out} are the inlet and outlet pressure, respectively, and n is the value of the polytropic exponent parameter. The block calculates the clearance volume fraction, C, as,

$$C = \frac{1-\eta_{v_{nominal}}}{p_{ratio}{}^{1/n-1}} \tag{8.4}$$

Where $\eta_{v_{nominal}}$ is the value of the Nominal volumetric efficiency parameter and p_{ratio} is the value of the Nominal pressure ratio parameter.

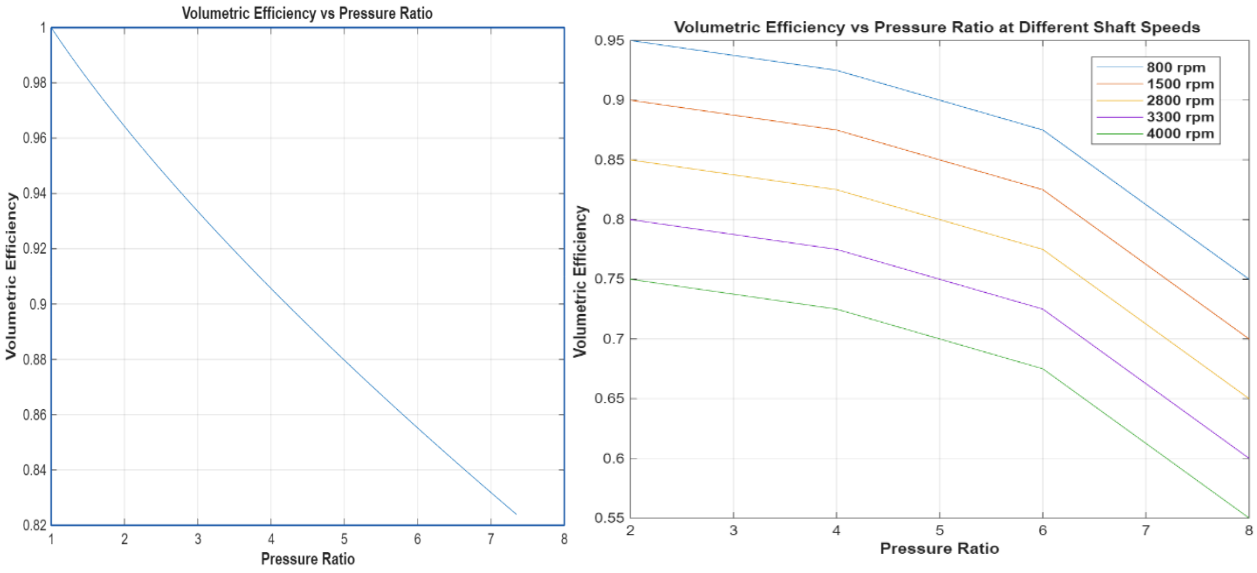

Figure 39. Graphical representation of condition-1 and condition-2, respectively.

The data illustrated in **Figure 39** represents the compressor volumetric efficiency versus pressure ratio when the Efficiency specification is set to Analytical and the Thermodynamic model is set to Polytropic, stated as condition-1. Whereas condition-2 shows the volumetric efficiency versus pressure ratio at different shaft speeds when the Efficiency specification is set to Tabulated.

Continuity Equations

The block conserves mass such that

$$\dot{m}_A + \dot{m}_B = 0 \tag{8.5}$$

Where $\dot{m}_A$ and $\dot{m}_B$ are the mass flow rates at ports A and B, respectively.

The block conserves energy such that,

$$\phi_A + \phi_A + \dot{m}_A \Delta h_t = 0 \tag{8.6}$$

Where Δh_t is the change in specific total enthalpy and $\dot{m}_A \Delta h_t$ is the fluid power, which is equal to the mechanical power, $torque \times \omega$.

When the thermodynamic model parameter is polytropic, fluid power is given as,

$$\dot{W}_c = \omega \frac{n}{n-1} \eta_v p_{in} V_{disp} \left[\left(\frac{p_{in}}{p_{out}} \right)^{\frac{n-1}{n}} - 1 \right] \tag{8.7}$$

Where the block uses the polytropic relationship $pv^n = constant$.

The polytropic compression process is characterized as reversible and non-adiabatic, with a constant ratio of usable compression work to enthalpy change along the polytropic compression path, as shown in **Table 11**. In contrast to an isentropic process, a polytropic process takes into consideration the second rule of thermodynamics, which governs the inevitable degradation of energy. Either the far less accurate, earlier polytropic exponent approaches in a closed form solution, or numerical integration along a specified path can be used to compute polytropic efficiency with high accuracy (Taher & Evans, 2023). Optimizing the interstage pressures in multistage compressors with intercooling reduces the overall compression work. When the compression process is divided into several steps with intermediate cooling, as opposed to

compressing the gas in one step, the temperature rise and, thus, the specific work input needed at each stage are decreased (Méndez et al., 2021).

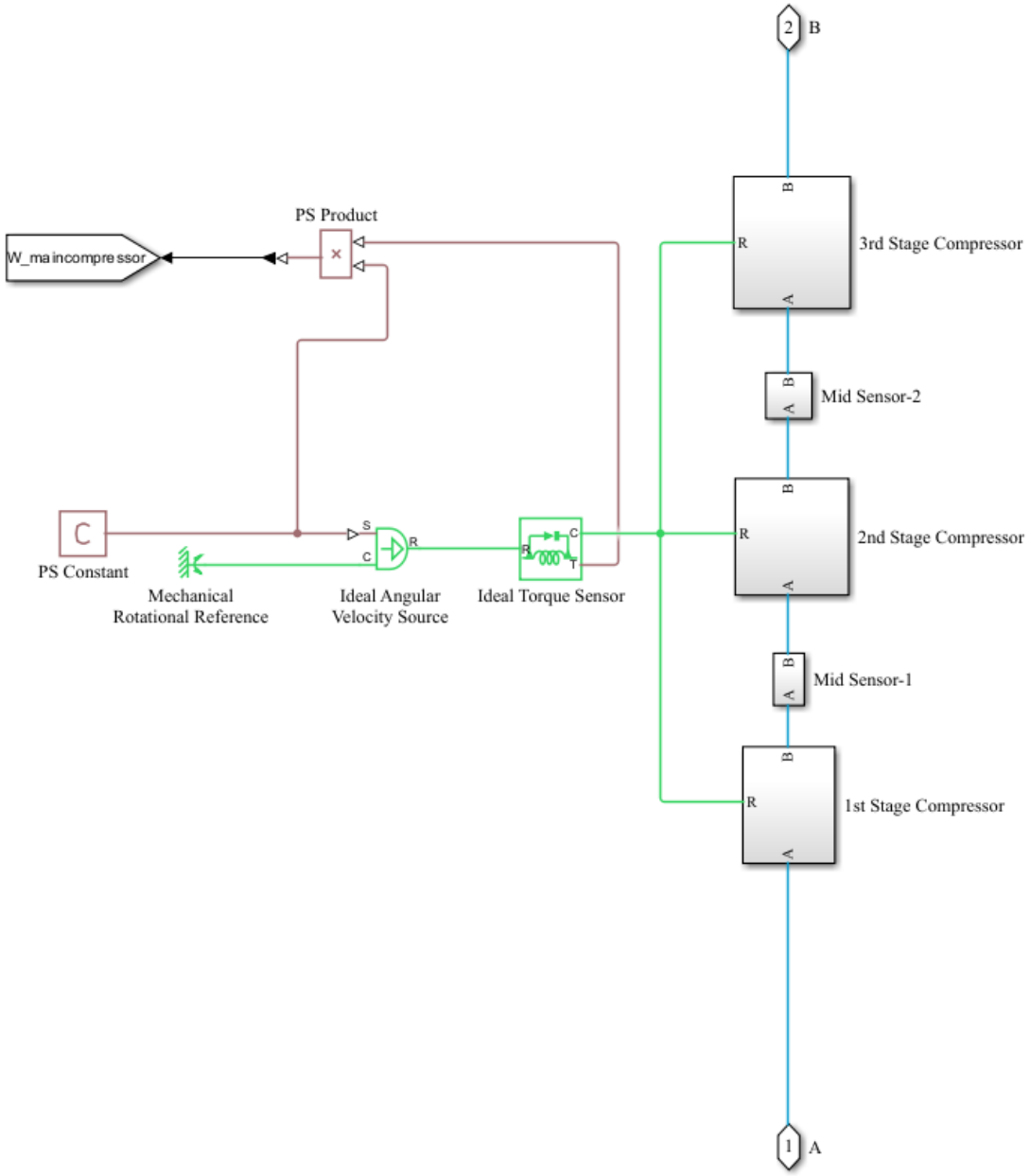

Figure 40. Schematic diagram of a 3-staged compressor connected in a series from the simulated model.

To minimize the overall work input, the three-stage compressor system depicted in **Figure 40** distributes the entire compression process over successive stages. The intercooler structure in **Figure 43** illustrates the intercooling that is applied between each stage. In this setup, refrigerant hydrogen gas is drawn by the first-stage compressor at the initial suction conditions of pressure P1 and temperature T1, and it is compressed via a polytropic path to an intermediate pressure P2 and

temperature T2, as illustrated in **Table 12**. The compressed air is then directed through an intercooler subsystem, which uses a fan-driven airflow to reject heat to the environment by forced convection. This lowers the temperature of the moist air approaching the initial suction temperature while causing a very small pressure loss.

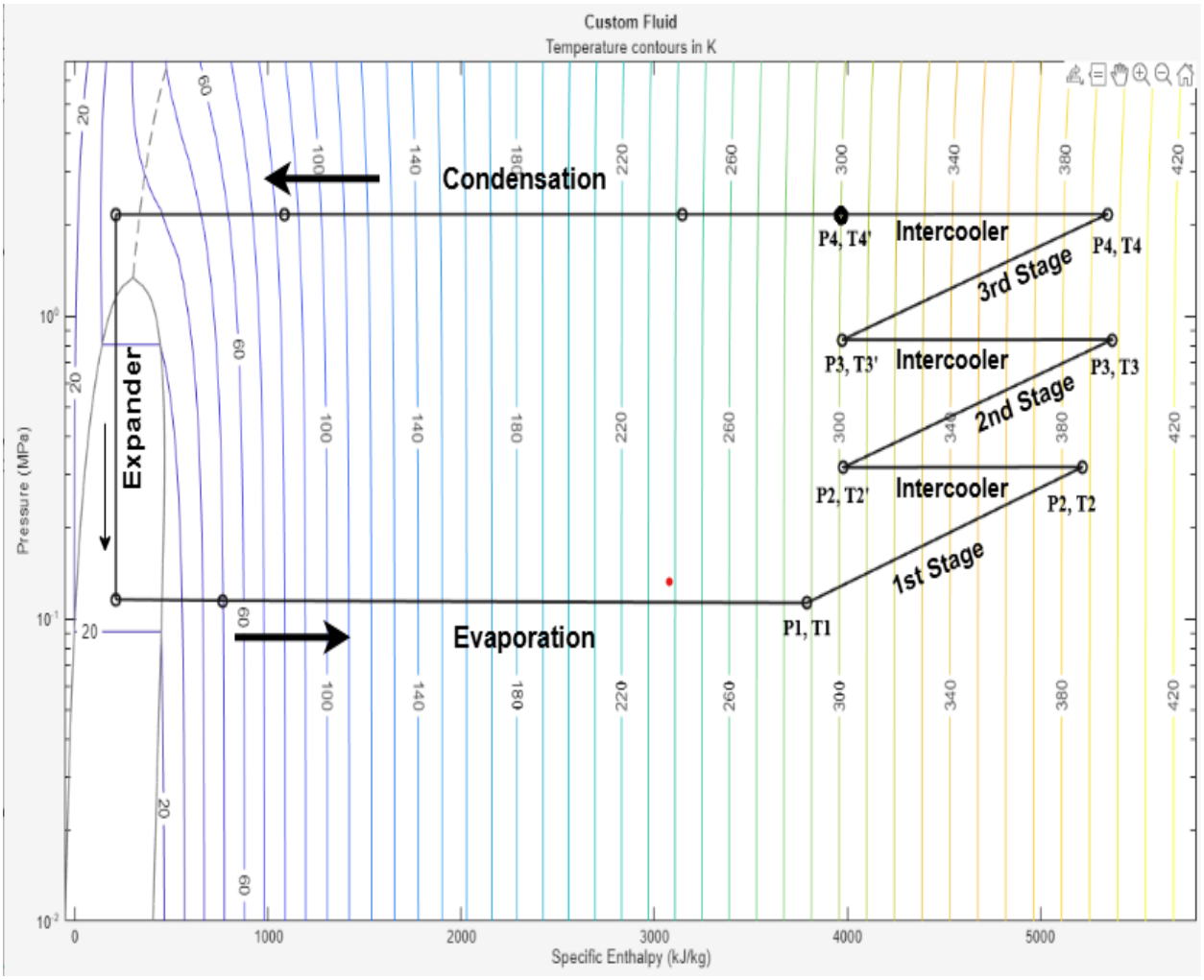

Figure 41. Pressure–enthalpy diagram of the hydrogen refrigeration cycle showing multistage compression, intercooling, condensation, expansion, and evaporation processes with actual operating state points.

The actual operating data points of the compressor-based system are plotted on the pressure–enthalpy (p–h) diagram of the hydrogen refrigerant cycle, which is seen in **Figure 41**. The cycle is a variation of the standard vapor-compression refrigeration process for hydrogen: beginning at state P1–T1, the low-pressure vapor exiting the evaporator is compressed in several steps (P2–T2, P3–T3, and P4–T4), increasing enthalpy and pressure as a result of the compressor's work input. The virtually vertical upward movement on the p-h diagram shows this pressure surge, which coincides

with a large temperature increase, as evidenced by the crossing of higher temperature contours. By changing the state points slightly to the left (enthalpy reduction) and lowering the temperature at roughly constant pressure between compression stages, intercoolers improve compressor efficiency and lower the discharge temperature.

Table 12. Operating condition of the 3-staged compressors and intercoolers having 5 TPD capacity.

Boundary Condition	Suction		Discharge		Intercooling Temperature		Heat Transfer through Intercooler (kW)
	Pressure (MPa)	Temperature (K)	Pressure (MPa)	Temperature (K)	Inlet (K)	Outlet (K)	
1st Stage	0.101325	275.15	0.3175	387.34	387.34	301.25	346
2nd Stage	0.3166	301.25	0.8372	397.78	397.78	288.249	350
3rd Stage	0.8364	288.249	2.17	395.46	395.46	300	350

This intercooler model, shown in **Figure 43**, which includes moist air input and exit boundaries, moist air property evaluation, and a condenser-evaporator heat exchange representation, is repeated for each compression stage to provide uniform thermal treatment throughout the system. The refrigerant gas that has partially cooled after the initial intercooling process enters the second-stage compressor at a temperature and suction pressure that are modified to account for the combined

effects of intercooler performance and compression, which employs a fan for the forced convection of moist air into the condenser-evaporator heat-exchanger. The various parametrization of the fan is made according to **Figure 42**, which shows the working condition and shaft torque on different volumetric flow rates.

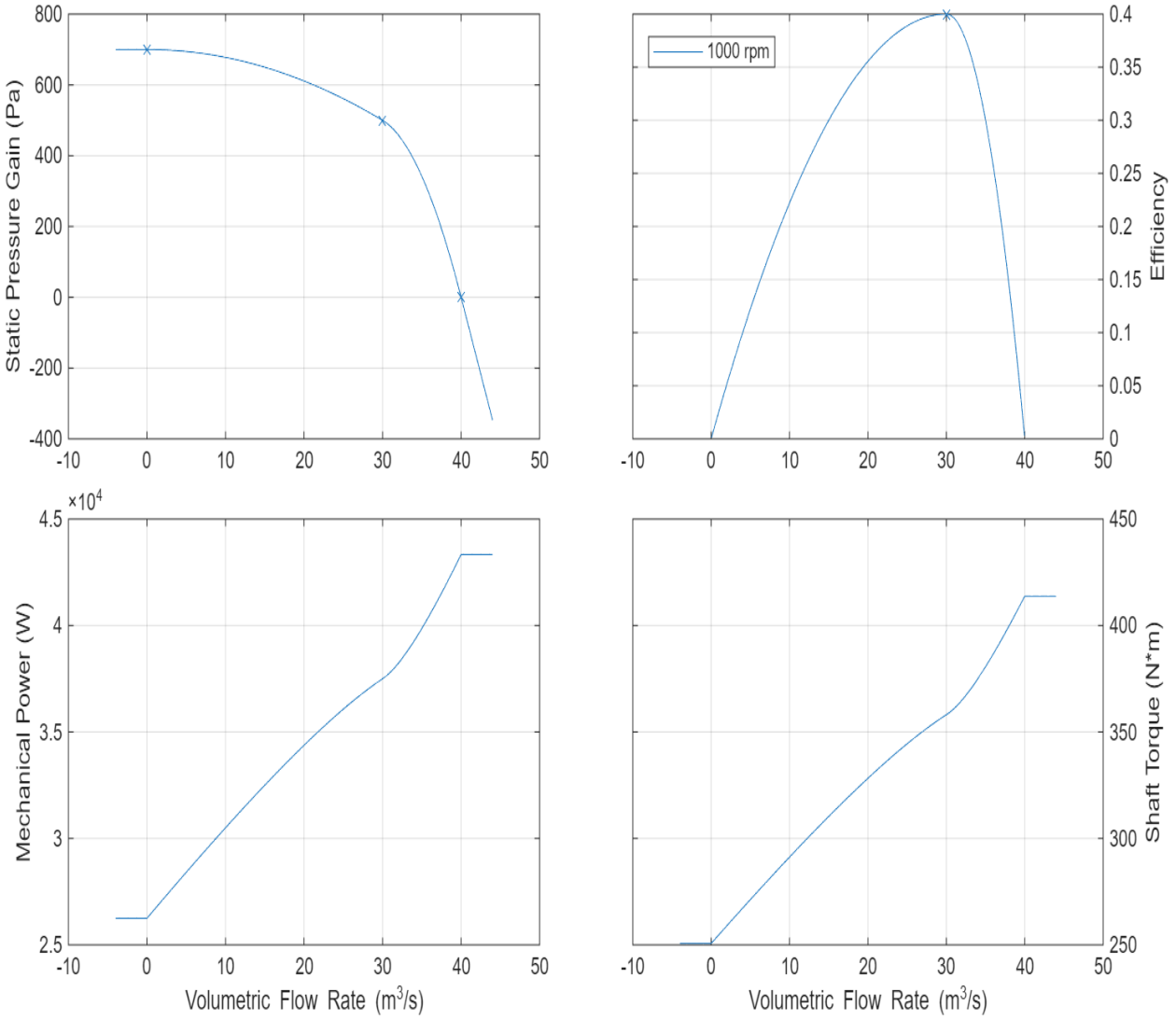

Figure 42. Various characteristics of fan blower versus volumetric flow rate.

An intercooler lowers the discharge temperature before the flow enters the next stage, and the second and third compression stages function similarly. This structured compression-cooling procedure produces intermediate pressures, with corresponding temperature reductions determined by intercooler effectiveness and pressure losses, until the desired ultimate discharge pressure is reached at the third-stage compressor outlet. Direct assessment of compression work is made

possible by the torque and angular velocity sensors built into the drive system, which track the mechanical power transferred to the compressor shaft.

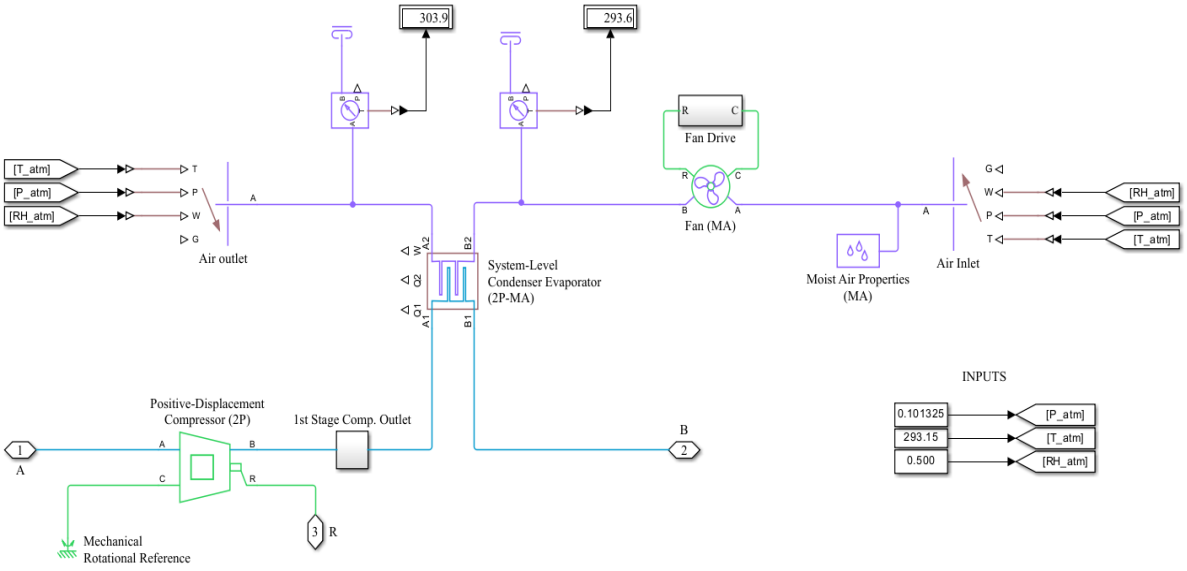

Figure 43. Schematic layout of a compressor stage integrated with an intercooler subsystem.

When adjusted for intercooler pressure drops, non-ideal cooling, and stage-specific polytropic efficiencies, the ideal interstage pressures under these operating conditions are achieved by minimizing the overall polytropic compression work, which results in a roughly geometric distribution of pressure ratios across the stages. **Figure 43** illustrates how the incorporation of realistic intercooler models affects the optimal pressure allocation by highlighting the impact of residual temperature rise and pressure loss on the suction conditions of downstream stages. Therefore, estimating system performance, choosing the right number of compression stages, and achieving a near-minimum-work compression process all depend on an accurate description of the multistage compressor train and the related intercoolers.

8.2 Heat Exchanger

Simscape Fluids is effectively and numerically robust, representing boiling and condensation phenomena by modeling the system-level heat exchanger as an energy-exchange component that functions on thermodynamic state variables rather than intricate geometry. Inlet conditions from the linked fluid network, such as temperature, pressure, mass flow rate, and, if relevant, vapor quality, are continuously sent to each side of the heat exchanger during simulation. These variables

define the instantaneous thermodynamic state of the working fluid, which is computed using the built-in two-phase property tables. The model calculates the rate of heat transfer across the exchanger wall based on the temperature differential between the two sides and the designated heat transfer parameters (e.g., overall heat transfer coefficient or effectiveness). The model determines whether the fluid remains single-phase or transitions to two-phase by updating the fluid enthalpy during heat absorption or rejection. While heat removal during condensation lowers vapor quality until the fluid is completely liquid, additional heat during boiling raises vapor quality at a nearly constant saturation temperature. Energy balance equations manage this phase-change behavior internally, ensuring seamless transitions between subcooled, two-phase, and superheated states without the need for human input. Concurrently, pressure losses are computed according to flow rate and flow regime, allowing for realistic engagement with other hydraulic elements like compressors, pumps, expansion devices, and valves. When thermal mass is activated, the heat exchanger wall stores and releases energy, creating physically significant time delays that affect transient response and startup behavior. Throughout the simulation, the heat exchanger is modeled as part of a coupled physical network, with the solver configuration repeatedly enforcing mass, momentum, and energy conservation across all connected components.

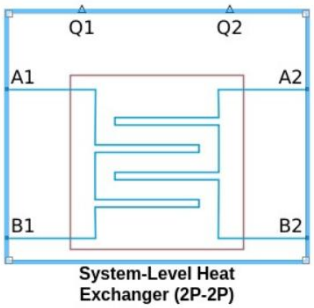

Figure 44. Pictorial diagram of system-level heat exchanger (2P) (adapted from Ref. (Mathworks/System-Level Heat Exchanger 2P, 2025)).

Ports A1 and B1 are the two-phase fluid conserving ports associated with the Two-Phase Fluid 1 inlet and outlet. Ports A2 and B2 are the two-phase fluid conserving ports associated with the Two-Phase Fluid 2 inlet and outlet. Physical signal ports Q1 and Q2 output the rate of heat transfer to Two-Phase Fluid 1 and Two-Phase Fluid 2, respectively, in **Figure 44**.

An internal heat exchanger facilitates more heat exchange between the condenser and evaporator outlets, increasing the efficiency of the refrigeration system. We can use the nominal operating condition to parameterize the block. In a steady state, the heat exchanger is sized to meet the

required performance under nominal operating conditions. Based on the change in enthalpy along the flow path, each side of the heat exchanger represents the liquid, mixed, and vapor zones (Mathworks/System-Level Heat Exchanger 2P, 2025).

Two-phase fluid 1 & 2 mass and energy conservation

The mass conservation equation for the overall two-phase fluid 1&2 flow is (Mathworks/System-Level Heat Exchanger 2P, 2025),

$$\left(\frac{dp_{2P1,2}}{dt}\sum_{Segments}\left(\frac{\partial p_{seg,2P1,2}}{\partial p}\right)+\sum_{Segments}\left(\frac{du_{seg,2P1,2}}{dt}\frac{\partial p_{seg,2P1,2}}{\partial u}\right)\right)\frac{V_{2P1,2}}{N}=\dot{m}_{A,2P1,2}+\dot{m}_{B,2P1,2} \tag{8.7}$$

Where,

- $\frac{\partial p_{seg,2P1,2}}{\partial p}$ is the partial derivative of density with respect to pressure for the segment of two-phase fluid 1 &2.
- $\frac{\partial p_{seg,2P1,2}}{\partial u}$ is the partial derivative of density with respect to specific internal energy for the segment of two-phase fluid 1 & 2.
- $u_{seg,2P1,2}$ is the specific internal energy for the segment of two-phase fluid 1 & 2.
- $V_{2P1,2}$ is the total volume of two-phase fluid 1 &2.
- $N = 3$ is the number of segments.

The energy conservation equation for each segment of the two-phase fluid 1 &2 is

$$\frac{du_{seg,2P1,2}}{dt}\frac{M_{2P1,2}}{N}+u_{seg,2P1,2}\left(\dot{m}_{seg,in,2P1,2}-\dot{m}_{seg,out,2P1,2}\right)=\Phi_{seg,in,2P1,2}-\Phi_{seg,in,2P1,2}+Q_{seg,2P1,2} \tag{8.8}$$

Heat Transfer

The block computes heat transfer between the fluids in each of the three equal-sized segments that it creates from the two-phase fluid 1 flow and the two-phase fluid 2 flow. For the sake of simplicity, the equations in this section apply to only one segment. If you select **Enable wall thermal mass**, then the heat balance in the heat exchanger is

$$Q_{seg,2P1}+Q_{seg,2P1}=-\frac{M_{wall}C_{p_{wall}}}{N}\frac{dT_{seg,wall}}{dt} \tag{8.9}$$

Where,

- $Q_{seg,2P1}$ is the heat flow rate from the wall that is the heat transfer surface to two-phase fluid 1 in the segment.
- $Q_{seg,2P2}$ is the heat flow rate from the wall to the two-phase fluid 2 segment.
- M_{wall} is the mass of the wall.
- $C_{p_{wall}}$ is the specific heat of the wall.
- $T_{seg,wall}$ is the average wall temperature in the segment.
- t is time.

The heat flow rate from the wall to two-phase fluid 1 in the segment is,

$$Q_{seg,2P1} = UA_{seg,2P1}\left(T_{seg,wall} - T_{seg,2P1}\right) \qquad (8.10)$$

Where,

- $UA_{seg,2P1}$ is the weighted-average heat transfer conductance for two-phase fluid 1 in the segment.
- $T_{seg,2P1}$ is the weighted-average fluid temperature for the two-phase fluid 1 in the segment.

The heat flow rate from the wall to two-phase 2 in the segment is,

$$Q_{seg,2P2} = UA_{seg,2P2}\left(T_{seg,wall} - T_{seg,2P2}\right) \qquad (8.11)$$

Where,

- $UA_{seg,2P2}$ is the weighted-average heat transfer conductance for two-phase fluid 2 in the segment.
- $T_{seg,2P2}$ is the weighted-average fluid temperature for the two-phase fluid 2 in the segment.

The fluid properties that the block uses in heat transfer calculations are the average between the value at the inlet and the value in the fluid volume.

Two-Phase Fluid 1& 2 Heat Transfer Correlation

Using the same formulas, the block determines the heat transfer conductance in both two-phase fluids. The heat transfer conductance in the case of a **subcooled liquid (L)** segment is

$$UA_{seg,L,2P1,2} = a_{L,2P1,2}(Re_{seg,L,2P1,2})^{b_{2P1,2}}(Pr_{seg,L,2P1,2})^{c_{2P1,2}}K_{seg,L,2P1,2}\frac{G_{2P1,2}}{N} \quad (8.12)$$

- $a_{L,2P1,2}, b_{2P1,2}, and\ c_{2P1,2}$ are the coefficients of the Nusselt number correlation. These coefficients are block parameters in the Correlation Coefficients section.
- $Re_{seg,L,2P1,2}$ is the average liquid Reynolds number for the segment.
- $Pr_{seg,L,2P1,2}$the average liquid Prandtl number for the segment.
- $K_{seg,L,2P1,2}$ is the average liquid thermal conductivity for the segment.
- $G_{2P1,2}$ is the geometry scale factor for the two-phase fluid 1 & 2 sides of the heat exchanger. The block calculates the geometry scale factor so that the total heat transfer over all segments matches the specified performance at the nominal operating conditions.

The average liquid Reynolds number is

$$Re_{seg,L,2P1,2} = \frac{\dot{m}_{seg,2P1,2}D_{ref,2P1,2}}{\mu_{seg,L,2P1,2}S_{ref,2P1,2}} \quad (8.13)$$

Where,

- $\dot{m}_{seg,2P1,2}$ is the mass flow rate through the segment of two-phase fluid 1 & 2.
- $\mu_{seg,L,2P1,2}$ is the average liquid dynamic viscosity of segment of two-phase fluid 1 & 2.
- $D_{ref,2P1,2}$ is an arbitrary reference diameter of two-phase fluid 1 & 2.
- $S_{ref,2P1,2}$ is an arbitrary reference flow area of two-phase fluid 1 & 2.

Similarly, if the segment is **superheated vapor (V)**, then the heat transfer conductance is,

$$UA_{seg,V,2P1,2} = a_{V,2P1,2}(Re_{seg,V,2P1,2})^{b_{2P1,2}}(Pr_{seg,V,2P1,2})^{c_{2P1,2}}K_{seg,V,2P1,2}\frac{G_{2P1,2}}{N} \quad (8.14)$$

And the average vapor Reynolds number is,

$$Re_{seg,V,2P1,2} = \frac{\dot{m}_{seg,2P1,2}D_{ref,2P1,2}}{\mu_{seg,V,2P1,2}S_{ref,2P1,2}} \quad (8.15)$$

If the segment is a **liquid-vapor mixture (M)**, then the heat transfer conductance of both two-phase fluids is given below,

$$UA_{seg,M,2P1,2} = a_{M,2P1,2}(Re_{seg,SL,2P1,2})^{b_{2P1,2}} CZ (Pr_{seg,SL,2P1,2})^{c_{2P1,2}} K_{seg,SL,2P1,2} \frac{G_{2P1,2}}{N} \quad (8.16)$$

- $Re_{seg,SL,2P1,2}$ is the saturated liquid Reynolds number for the segment of two-phase fluid 1 & 2.
- CZ is the Cavallini and Zecchin term.
- $Pr_{seg,SL,2P1,2}$the saturated liquid Prandtl number for the segment of two-phase fluid 1 & 2.

The saturated liquid Reynolds number is,

$$Re_{seg,SL,2P1,2} = \frac{\dot{m}_{seg,2P1,2} D_{ref,2P1,2}}{\mu_{seg,SL,2P1,2} S_{ref,2P1,2}} \quad (8.17)$$

The Cavallini and Zecchin term is,

$$CZ = \frac{\left(\left(\left(\sqrt{\frac{v_{seg,SV,2P1,2}}{v_{seg,SL,2P1,2}}} - 1\right)(X_{seg,out,2P1,2} + 1)\right)\right)^{1+b_{2P1,2}} - \left(\left(\left(\sqrt{\frac{v_{seg,SV,2P1,2}}{v_{seg,SL,2P1,2}}} - 1\right)(X_{seg,in,2P1,2} + 1)\right)\right)^{1+b_{2P1,2}}}{(1+b_{2P1,2})\left(\sqrt{\frac{v_{seg,SV,2P1,2}}{v_{seg,SL,2P1,2}}} - 1\right)(X_{seg,out,2P1,2} - X_{seg,in,2P1,2})} \quad (8.18)$$

Where,

- $v_{seg,SV,2P1,2}$ is the saturated liquid specific volume for the segment of two-phase fluid 1-2.
- $v_{seg,SL,2P1,2}$ is the saturated vapor specific volume for the segment of two-phase fluid 1-2.
- $X_{seg,in,2P1,2}$ is the vapor quality at the segment inlet of two-phase fluid 1-2.
- $X_{seg,out,2P1,2}$ is the vapor quality at the segment outlet of two-phase fluid 1-2.

Pressure loss

The pressure losses on the two-phase fluid 1 and two-phase fluid 2 sides are given below in equations.

$$P_{A,2P1,2} - P_{2P1,2} = \frac{K_{2P1,2}}{2} \frac{\dot{m}_{A,2P1,2} \sqrt{\dot{m}^2_{A,2P1,2} + \dot{m}^2_{thres,2P1,2}}}{2\rho_{avg,2P1,2}} \quad (8.19)$$

$$P_{B,2P1,2} - P_{2P1,2} = \frac{K_{2P1,2}}{2} \frac{\dot{m}_{B,2P1,2}\sqrt{\dot{m}_{B,2P1,2}^2 + \dot{m}_{thres,2P1,2}^2}}{2\rho_{avg,2P1,2}} \quad (8.20)$$

Where,

- $P_{A,2P1,2}$ *and* $P_{B,2P1,2}$ are the pressures at ports A1, B1, and A2, B2, respectively.
- $P_{2P1,2}$ is the internal two-phase fluid 1 and two-phase 2 pressure at which the heat transfer is calculated.
- $\dot{m}_{A,2P1,2}$ *and* $\dot{m}_{B,2P1,2}$ are the mass flow rates into ports A1, B1, and A2, B2, respectively.
- $\rho_{avg,2P1,2}$ is the average two-phase fluid 1 and two-phase fluid 2 density over all segments.
- $\dot{m}_{thres,2P1,2}$ is the laminar threshold for pressure loss, approximated as 1e-4 of the nominal mass flow rate. The block calculates the pressure loss coefficient, $K_{2P1,2}$, so that $P_{A,2P1,2} - P_{B2P1,2}$ matches the nominal pressure loss at the nominal mass flow rate.

A system-level two-phase (2P) heat exchanger acts as a simplified model of a real heat exchanger, which concentrates on capturing the general fluid and thermal behavior rather than the intricate microscopic flow patterns within it. The system-level model treats the exchanger as a 1D device separated into sections or control volumes and applies conservation of mass, momentum, and energy in an averaged sense rather than simulating bubbles, droplets, or precise flow regimes as in CFD. The model monitors characteristics including vapor quality, saturation temperature, and latent heat to calculate the amount of energy received or released when one or both fluids go through phase change (boiling or condensation) (Collie et al., 1994). The heat transfer on either side is computed using empirical two-phase heat transfer correlations, which yield an effective heat transfer coefficient based on flow parameters, pressure, and phase distribution. The overall heat transfer rate is then calculated by combining these coefficients with the wall thermal resistance, by using Equations 8.10 and 8.11. In order to capture the essential physics of phase-change heat transfer, a system-level 2P heat exchanger model must be computationally efficient and numerically robust. This makes it appropriate for dynamic simulations, performance assessment, and control system development.

For instance, let us consider HX-1 for complete parameterization employed in a pre-cooled Claude cycle having 5 TPD capacity, which uses hydrogen feed as the hot stream and liquid nitrogen as the cold stream to facilitate a more accurate measurement of the overall heat transfer. This heat

exchanger plays a crucial role in the pre-cooling of the hydrogen feed, reducing its temperature from 300 K to 80 K. The values shown in **Table 13** represent the actual operating conditions that have been established for the system setup. These conditions are essential for understanding the performance and efficiency of the heat exchanger during operation.

Table 13. Block parameters: System-Level Heat Exchanger (2P-2P) (HX-1) for liquefier having 5 TPD capacity.

Name	Value	Units
Configuration		
Flow arrangement at nominal condition	Counter flow – Two-Phase fluid 1 flows from A to B and Two-Phase fluid 2 flows from B to A	
Wall mass	50	Kg
Wall specific heat	40	J/(k-kg)
✓ Initialize wall temperature to nominal operating conditions		
Cross-sectional area at port A1	0.01	m^2
Cross-sectional area at port A1	0.01	m^2
Cross-sectional area at port A1	0.01	m^2
Cross-sectional area at port A1	0.01	m^2
Two-Phase fluid 1 (Hydrogen Gas)		
Nominal operating condition	Heat transfer from Two-Phase fluid 1 to Two-Phase fluid 2	
Nominal mass flow rate	0.058	kg/s
Nominal pressure drop	0.001	MPa
Pressure specification	Inlet pressure	
Nominal inlet pressure	2.1	MPa
Inlet condition specification	Specific enthalpy	
Nominal inlet specific enthalpy	3900	kJ/kg
Heat transfer capacity specification	Rate of heat transfer	
Nominal rate of heat transfer	165	kW
Two-Phase fluid 1 volume	0.001	m^3
✓ Initialize Two-Phase fluid 1 to nominal operating conditions		

Two-Phase fluid 2 (Liquid Nitrogen)		
Nominal mass flow rate	0.4	kg/s
Nominal pressure drop	0.001	MPa
Pressure specification	Inlet pressure	
Nominal inlet pressure	0.11	MPa
Inlet condition specification	Specific enthalpy	
Nominal inlet specific enthalpy	-122	kJ/kg
Two-Phase fluid 2 volume	0.001	m^3
✓ Initialize Two-Phase fluid 2 to nominal operating conditions		
Correlation coefficients		
a in $Nu = a \times Re^b \times Pr^c$ two-phase fluid 1liquid	0.023	
a in $Nu = a \times Re^b \times Pr^c$ two-phase fluid 1 mixture	0.005	
a in $Nu = a \times Re^b \times Pr^c$ two-phase fluid 1 vapor	0.023	
b in $Nu = a \times Re^b \times Pr^c$ two-phase fluid 1	0.8	
c in $Nu = a \times Re^b \times Pr^c$ two-phase fluid 1	0.33	
a in $Nu = a \times Re^b \times Pr^c$ two-phase fluid 2 liquid	0.023	
a in $Nu = a \times Re^b \times Pr^c$ two-phase fluid 2 mixture	0.005	
a in $Nu = a \times Re^b \times Pr^c$ two-phase fluid 2 vapor	0.023	
b in $Nu = a \times Re^b \times Pr^c$ two-phase fluid 2	0.8	
c in $Nu = a \times Re^b \times Pr^c$ two-phase fluid 2	0.33	

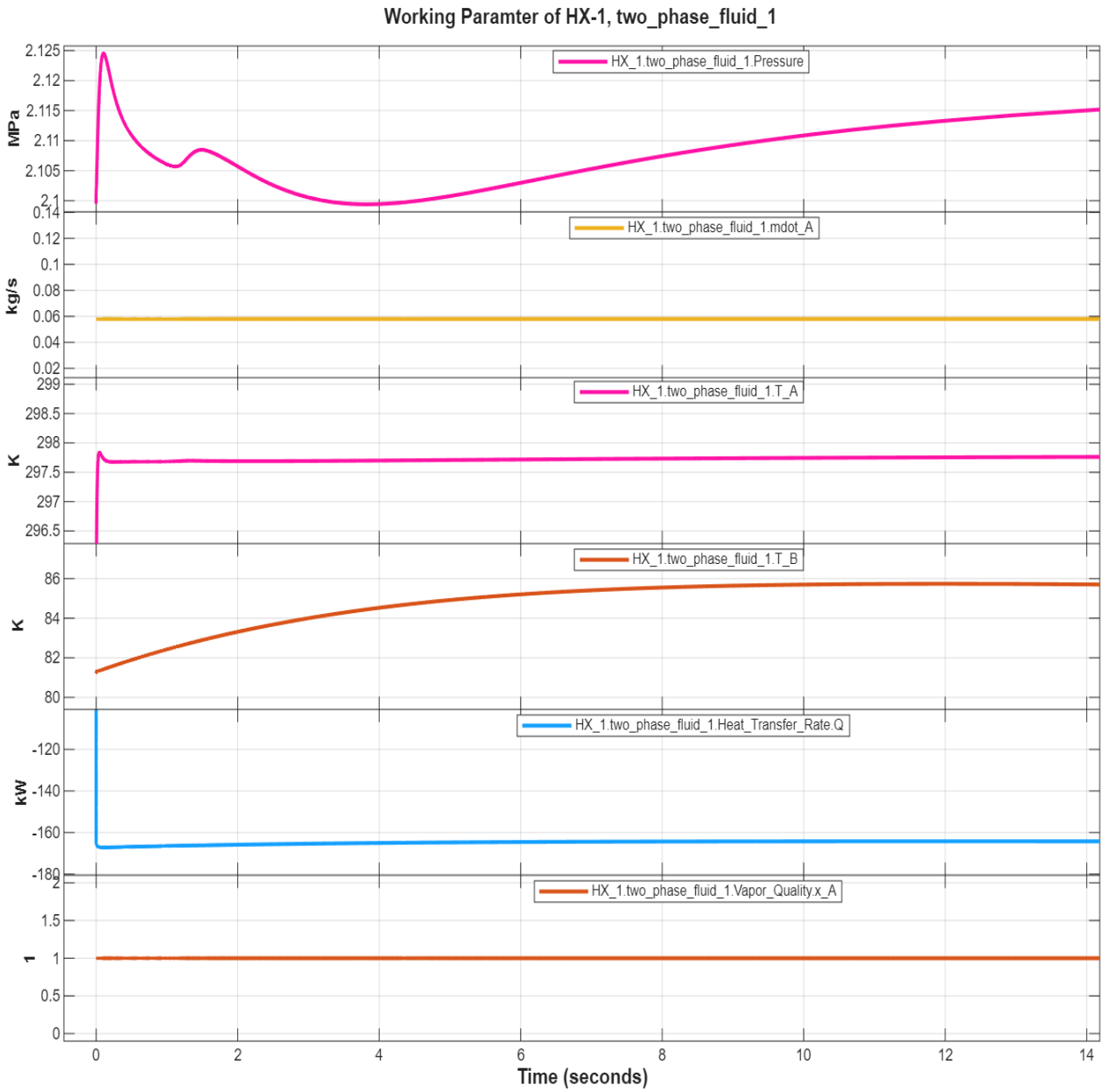

Figure 45. Transient response of thermodynamic parameters in HX-1 for two-phase fluid 1. (Data taken from simulation).

The transient results show how the hydrogen stream (two-phase fluid 1 & two-phase fluid 2) responds dynamically as the model moves closer to steady-state operation after the system-level heat exchanger (HX-1) block has been parameterized and the operating conditions have been applied, as shown in **Figure 45** & **Figure 46**. Small variations in the rate of heat transfer and pressure are initially noted, which is normal during the numerical stabilization stage of a dynamic simulation. The reason for these brief oscillations is that the mass, momentum, and energy

conservation equations are all modifying at the same time to meet the required boundary conditions, fluid characteristics, and heat transfer correlations.

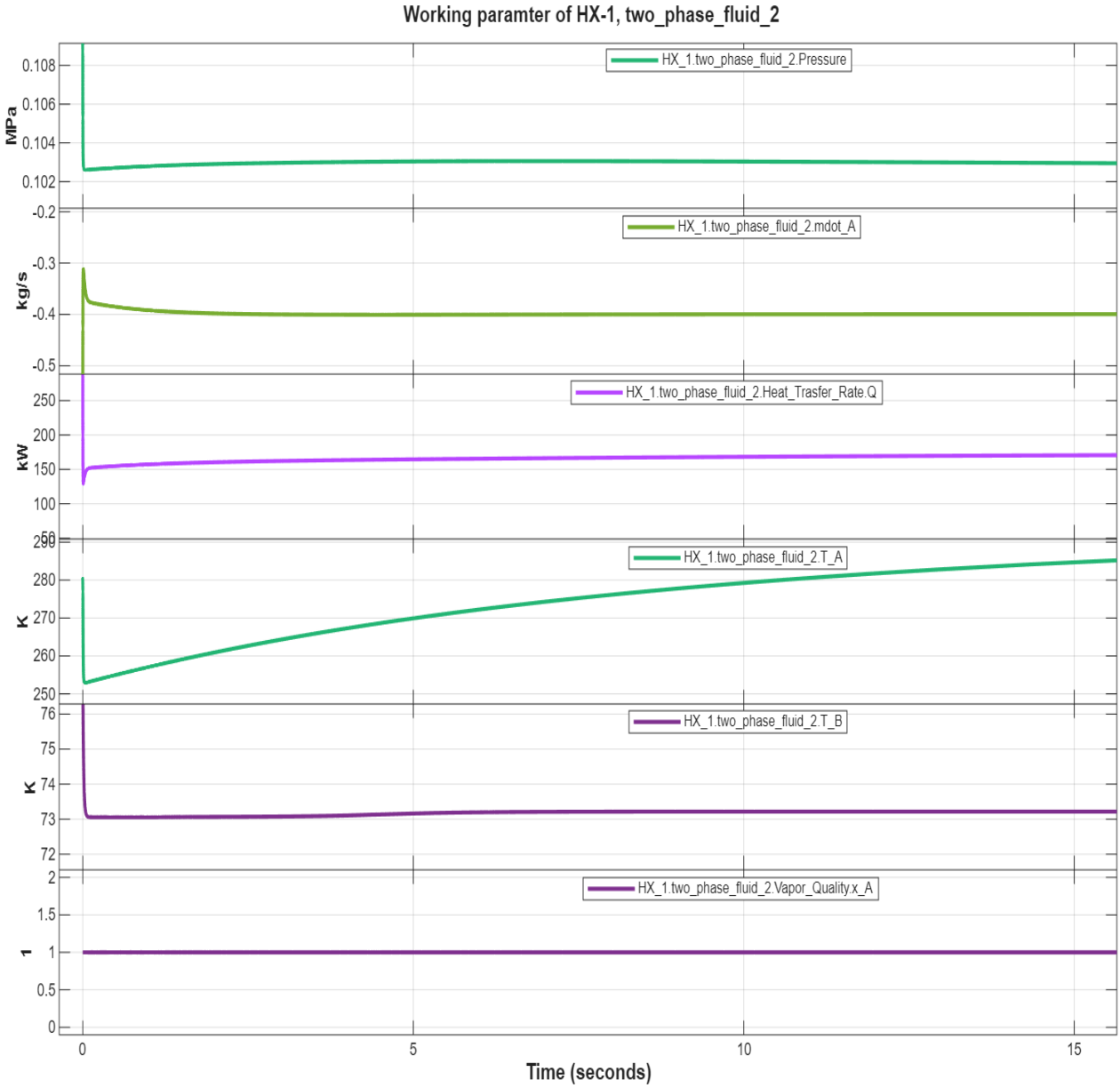

Figure 46. Transient response of thermodynamic parameters in HX-1 for two-phase fluid 2.

A steady stabilization follows the initial peak in the pressure profile for HX-1, two-phase fluid 1 transient diagram. The quick change in density and flow distribution that occurs when the hydrogen stream starts to interact thermally with the cold liquid nitrogen stream is shown in this behavior. Even minor thermal imbalances during startup can result in substantial pressure differences before equilibrium is reached because two-phase systems are extremely sensitive to changes in temperature and pressure. The system is numerically stable and the boundary conditions are

appropriately defined when the mass flow rate stays almost constant. Finally, the vapor quality profile sheds light on the phase condition of the hydrogen stream. A stable vapor quality shows that the model accurately captures the two-phase area and that the chosen correlations are appropriately handling the latent heat effects. Overall, the findings demonstrate that the system-level heat exchanger block is operating as anticipated, preserving numerical stability and computational efficiency while capturing the crucial thermo-fluid behavior.

8.3 Turbo-Expander

In hydrogen liquefaction, a turbo-expander works on the principle of near-isentropic expansion, in which high-pressure hydrogen gas expands through a turbine to a lower pressure, lowering its temperature and converting some of its enthalpy into mechanical work. A turbo-expander recovers useful shaft work during expansion, resulting in a larger temperature drop and higher thermodynamic efficiency than a Joule-Thomson valve, which provides cooling by throttling at constant enthalpy. High-pressure gaseous hydrogen enters the turbine during hydrogen liquefaction cycles, expands through nozzles and revolving blades, and then undergoes a reduction in temperature and pressure as kinetic energy is transformed into rotational energy, which can power a compressor or generator. The expanded hydrogen contributes to the cryogenic cooling needed for liquefaction by leaving at a significantly lower temperature.

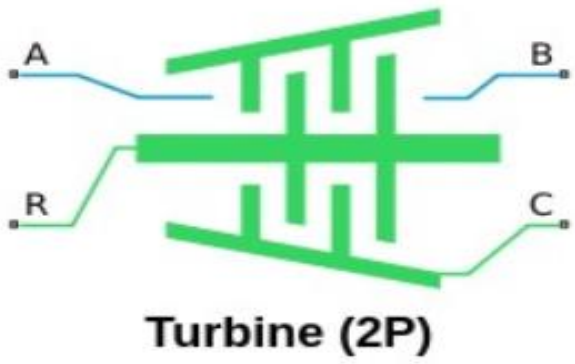

Figure 47. Pictorial diagram of Turbine (2P) in Simscape library (adapted from Ref. (Mathworks/Turbine 2P, 2025)).

The turbine (2P) block models a turbine in a two-phase fluid network. It can be parameterized as a tabulated map that is either a 1-D function of pressure ratio or a 2-D function of pressure ratio and corrected mass flow rate. Fluid flowing from port A to port B generates torque. Port R reports shaft

torque and angular velocity relative to port C, which represents the turbine casing, as shown in **Figure 47**. When enabled, port VN represents the nozzle opening fraction. This value linearly scales the corrected mass flow rate but does not influence the turbine efficiency. A value of 1 corresponds to the data in the turbine map. The turbine (2P) block assumes that superheated fluid enters the inlet. We can use the "**Report when fluid is not fully vapo**r" parameter to choose what the block does when the fluid does not meet superheated conditions. The only limitation of this block is that the shaft does not rotate under reversed flow conditions, and results during reversed flows may not be accurate.

Continuity Equations

Mass is preserved over the block as,

$$\dot{m}_A + \dot{m}_B = 0 \tag{8.21}$$

Where $\dot{m}_A$ is the mass flow rate at port A and $\dot{m}_B$ is the mass flow rate at port B.

The block calculates the energy balance as,

$$\Phi_A + \Phi_A - P_{fluid} = 0 \tag{8.22}$$

Where,

- Φ_A is the energy flow rate at port A.
- Φ_B is the energy flow rate at port B.
- P_{fluid} is the work done by the fluid, which is determined from the total fluid specific enthalpy.

The turbine map depicts performance in terms of the corrected mass flow rate because of the significant variations in temperature and pressure inside a turbine. Using a corrected pressure and temperature, the block modifies the corrected mass flow rate from the inlet mass flow rate.

$$\dot{m}_A \sqrt{\frac{T_A}{T_{corr}}} = \dot{m}_{corr} \frac{P_A}{P_{corr}} \tag{8.23}$$

Where,

- T_A is the temperature at port A.
- T_{corr} is the reference temperature for corrected flow parameter.
- $\dot{m}_{corr}$ is the corrected mass flow rate.
- P_A is the pressure at port A.
- P_{corr} is the reference pressure for corrected flow parameter.

The block also adjusts the shaft speed, ω, According to the reference temperature, the corrected shaft speed is,

$$\omega_{corr} = \frac{\omega}{\sqrt{\frac{T_A}{T_{ref}}}} \tag{8.24}$$

Shaft Torque

The block calculates the shaft torque, τ, as

$$\tau = \frac{\eta_m \dot{m}_A \Delta h_{total}}{\omega} \tag{8.25}$$

Where,

- Δh_{total} is the total change in the fluid specific enthalpy.
- η_m is the value of the mechanical efficiency parameter.
- ω is the relative shaft angular velocity, $\omega_R - \omega_C$.

When the flow is in the opposite direction, from Port B to Port A, the turbine is not functioning within its typical design parameters. The conclusions may not be accurate or physically significant for reverse flow, since the model is based on forward-flow conditions. This is better realistically handled by setting a tiny threshold around zero flow. The model reduces torque output to zero as the flow rate approaches zero or reverses. This ensures the turbine does not produce unrealistic torque in situations where, in real operation, it would not be generating power.

Two distinct graphs are plotted on the turbine map: isentropic efficiency versus pressure ratio, and corrected mass flow rate versus pressure ratio, as shown in **Figure 48**. The plots also depend on the corrected rotor speed, N, when the Turbine map parameterization is set to Tabulated data, which shows flow rate and efficiency versus corrected speed and pressure ratio. The indexing variable β does not need to be the same across the efficiency and mass flow rate tables.

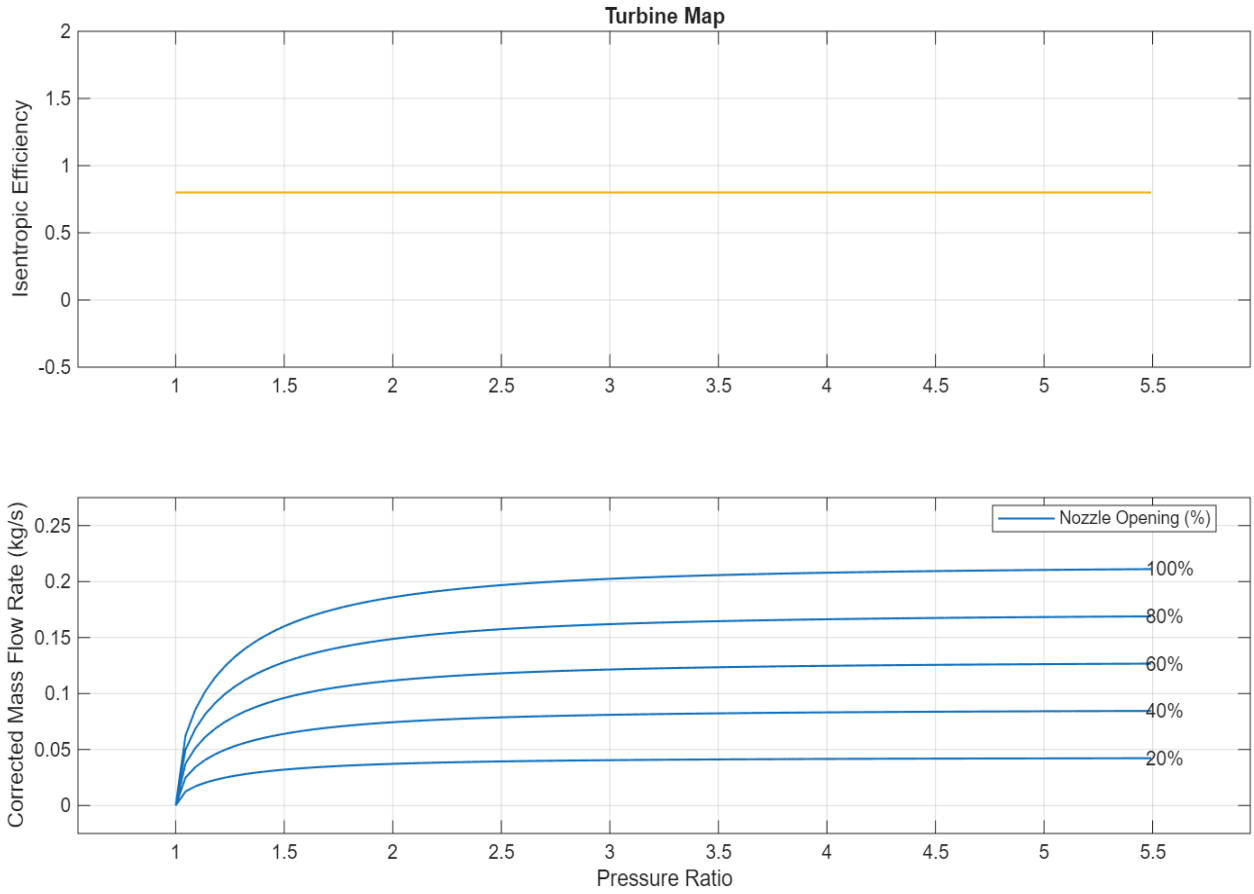

Figure 48. Turbine performance map: isentropic efficiency and corrected mass flow rate versus pressure ratio.

When high-pressure hydrogen passes through two or more turbo-expanders placed in succession, the process is referred to as "hydrogen turbine expansion connected in series." The pressure reduction is spread out throughout the first, second, and third phases rather than occurring in a single expansion step from high pressure to low pressure, as shown in **Figure 49**. This configuration is especially important in hydrogen liquefaction plants, cryogenic processes, and high-pressure energy recovery systems because hydrogen has a low molecular weight, a high specific heat ratio, and a high diffusivity, making single-stage expansion less efficient and difficult to control. A reduced pressure ratio is used for each stage of operation when turbines are coupled

in series. This lowers mechanical and thermal stress, increases isentropic efficiency, and permits more effective temperature control during expansion. In cryogenic hydrogen systems, where an abrupt temperature drop might cause instability or material stress, a gradual temperature drop is crucial. Multi-stage expansion further improves the matching of rotational speed and flow characteristics for each turbo-expander, resulting in higher total power recovery (Niu et al., 2025).

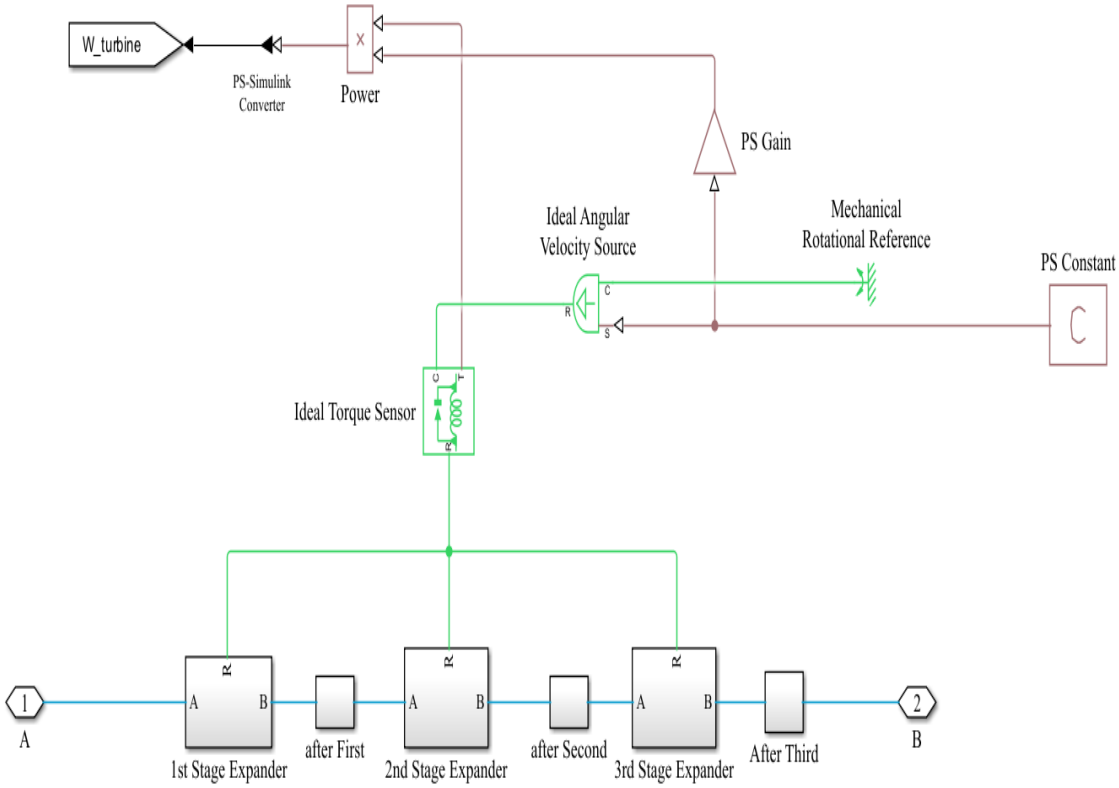

Figure 49. Schematic diagram of a 3-staged turbo-expander connected in a series.

The turbine block is parameterized to replicate the turbine under realistic operating conditions. The data presented in **Table 14** shows the nominal operating conditions of the three-stage turbine, identified as the 1st stage, 2nd stage, and 3rd stage. The work extracted from each stage of the expander is determined by the turbine block equations using the initial condition values, which include inlet and exit pressure, temperature, mass flow rate, and rotational speed. Accurate estimates of power output, efficiency, and temperature changes across the stages are made possible by proper parameterization, which guarantees that the simulation represents true turbine behavior.

Table 14. Design parameter of Turbine (2P) for pre-cooled Claude cycle having 5 TPD capacity.

Name	Value	1st Stage	2nd Stage	3rd Stage	Unit
Turbine map parameterization	Analytical-nominal pressure ratio and corrected mass flow rate				
✓ Model variable nozzle					
Minimum nozzle opening fraction	1e-3				
Maximum nozzle opening fraction	1.				
Flow rate data					
Nominal pressure ratio	20.72^ (1/3) = 2.7466				
Nominal corrected mass flow rate	0.2				kg/s
Efficiency data					
Constant isentropic efficiency	0.8				
Parameters					
Reference pressure for corrected mass flow rate		2.1	0.76	0.276	MPa
Reference temperature for corrected mass flow rate		80	60	40	K
Mechanical efficiency	0.9				
Inlet area at port A	0.01				m^2
Outlet area at port B	0.01				m^2
Report when fluid at inlet is not fully vapor	Warning				

8.4 Ortho-Para Hydrogen Conversion

There are two spin isomeric forms of diatomic hydrogen: ortho-hydrogen, which has its two proton nuclear spins aligned parallel, and para-hydrogen, which has its two proton spins oriented antiparallel, as shown in **Figure 50**. The spin of a proton is connected to its corresponding magnetic moment. These spin isomers have identical chemical characteristics. Nonetheless, the two forms of hydrogen differ slightly in their optical, magnetic, and thermal characteristics. Ortho-hydrogen is at a higher energy state than para-hydrogen. Temperature is the primary determinant of ortho- and para-hydrogen concentrations; refer to **Figure 51**. At normal temperature, hydrogen is made up of 75% ortho-hydrogen and 25% para-hydrogen, whereas liquid hydrogen is made up entirely of para-hydrogen. Ortho-hydrogen is thermodynamically unstable and spontaneously transforms into para-hydrogen in a cryogenic condition. One of the main causes of the boil-off in liquid hydrogen during storage is the exothermic nature of this conversion process. Therefore, when working with liquid hydrogen, it is necessary to take into account the coexistence of two spin isomeric forms (T. Zhang et al., 2023).

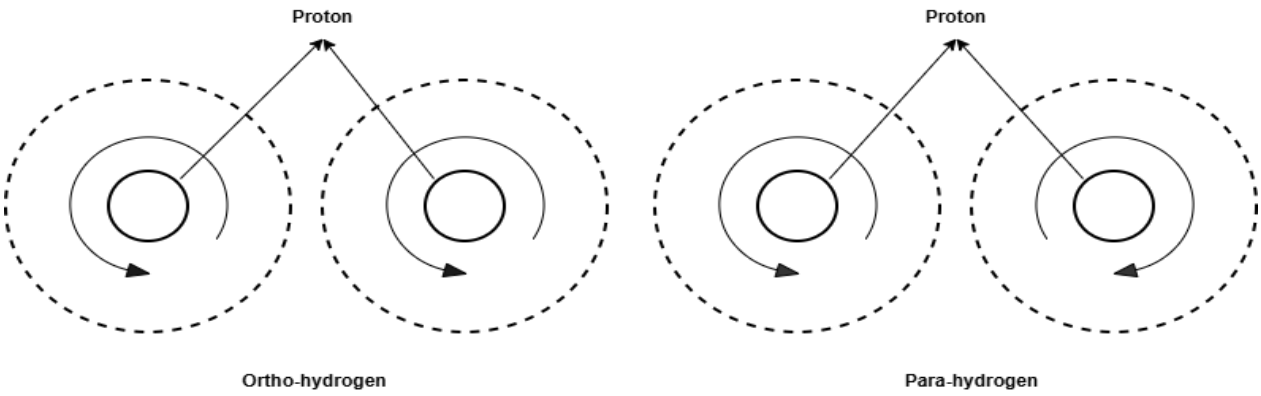

Figure 50. Spin isomers of molecular hydrogen (adapted from Ref. (Yin & Ju, 2020b)).

Ortho-hydrogen has a greater energy level than para-hydrogen. As the temperature drops throughout the hydrogen liquefaction process, the ortho-hydrogen will progressively change into para-hydrogen in order to attain the equilibrium hydrogen. A significant amount of LH_2 will evaporate because the released heat of 670 kJ/kg is more than the latent heat of hydrogen evaporation of 452 kJ/kg (Yin & Ju, 2020b). There is a continual boil-off of liquid hydrogen and a low storage efficiency at this condition because the heat produced by ortho-to-para conversion is greater than the heat absorbed by liquid hydrogen evaporation. Due to the exothermic ortho-to-para conversion, up to 50% of stored hydrogen evaporates after 100 hours, and 65% of stored hydrogen

evaporates after 1000 hours when the gaseous hydrogen containing 75% ortho-hydrogen is liquefied. Therefore, a higher level of para-hydrogen (95–98%) is necessary before hydrogen storage in order to achieve long-term liquid hydrogen storage. In order to decrease the boil-off during storage, methods include using catalysts (such as iron hydroxides and chromium oxides) to speed up the ortho-to-para conversion during hydrogen liquefaction (T. Zhang et al., 2023).

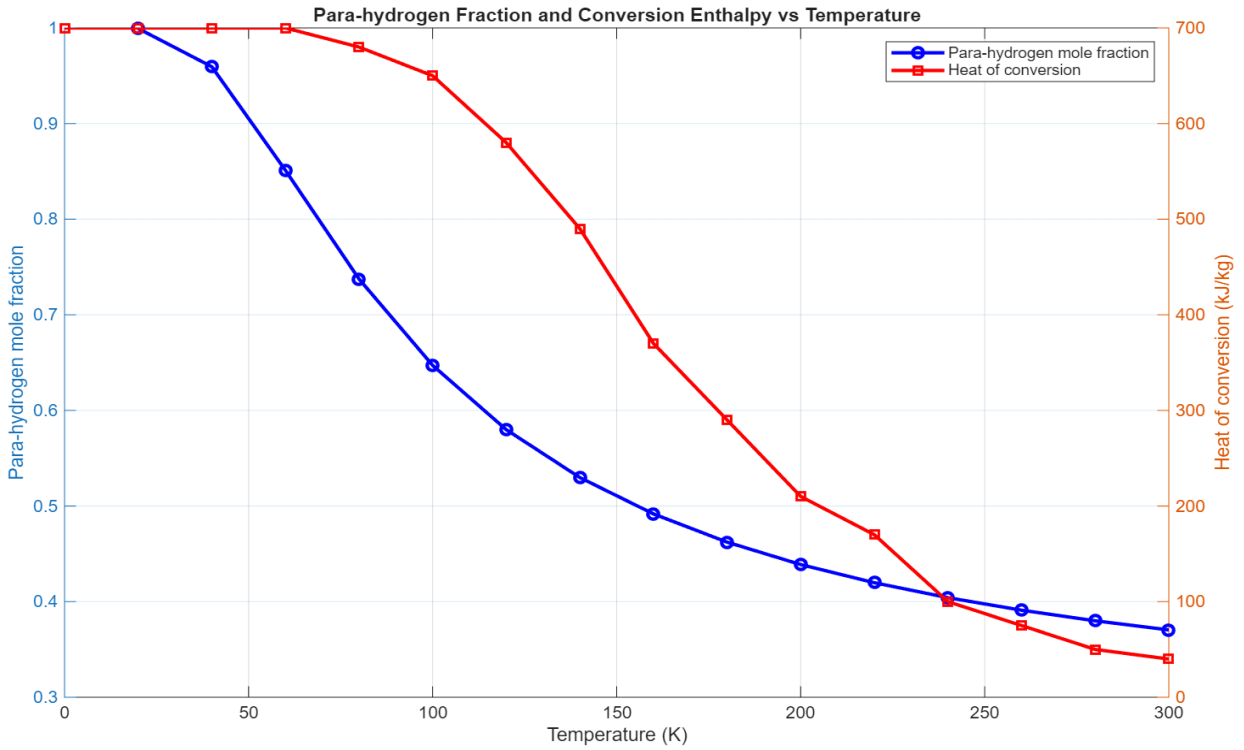

Figure 51. para-hydrogen concentration and heat of conversion at different temperatures (adapted from Ref. (Kanz et al., 2025)).

The graph in **Figure 51** demonstrates that hydrogen exists almost entirely as para-hydrogen at very low temperatures, but as the temperature rises, the fraction of para-hydrogen steadily decreases, reaching about 25 % near room temperature because higher temperatures favor the higher-energy ortho form. At the same time, the heat released during conversion to para-hydrogen is very large at low temperatures and decreases as temperature rises, meaning that converting hydrogen at cryogenic temperatures releases significant heat, while the heat effect is much smaller at higher temperatures.

The equilibrium constant (K_{eq}) for the OPC reaction remains constant regardless of pressure due to the nearly constant ratio of p-H2 to o-H2 at equilibrium conditions. The reason for this is that

the net internal energy of the reaction remains unchanged since the ground energy state for both spin isomers is zero (Al Ghafri et al., 2022).

$$o - H_2 \leftrightarrow p - H_2, \frac{P_{p-H_2}}{P_{O-H_2}} = \left(\frac{p-H_2}{o-H_2}\right) = K_{eq} \qquad (8.26)$$

The correlation for the temperature-dependent equilibrium constant $K_{eq}(T)$ using the Boltzmann distribution (Kanz et al., 2025):

$$K_{eq}(T) = \frac{y_{para}}{y_{ortho}} = \frac{1+5e^{-6x}+9e^{-20x}+13e^{-42x}+\cdots}{9e^{-2x}+21e^{-12x}+48e^{-30x}+\cdots} \qquad (8.27)$$

Thereby, x is defined as:

$$x = {h^2}/{8\pi^2 JkT} = \frac{84.977}{T}$$

With the Planck constant $h = 6.547 \times 10^{-34}$ J s, the Boltzmann constant $k = 1.371 \times 10^{-23}$ J/K and the moment of inertia of the hydrogen molecule $J = 4.66 \times 10^{-48}$ kg m^2. The terms shown in equation 8.27 are already sufficient to calculate the ortho-para ratio.

The equilibrium para molar fraction y_{para} is calculated in equation 8.28:

$$y_{para} = \frac{K_{eq}(T)}{1+K_{eq}(T)} \qquad (8.28)$$

The heat generated from ortho-para conversion is given as,

$$\dot{Q} = \dot{m}_{in} \times (y_{ortho} - y_{para}) \times \Delta h_c \qquad (8.29)$$

Where,

- y_{ortho} is the liquid inflow ortho-isomer mass fraction.
- $\dot{m}_{in}$ is the mass flow rate at inlet.
- y_{para} is the equilibrium para mass fraction
- Δh_c is the heat of conversion.

In hydrogen liquefaction systems, ortho-para hydrogen conversion can be achieved using three methods: isothermal conversion, adiabatic conversion, and continuous conversion. **Figure 52** shows a drawing of several approaches. The feed hydrogen passes through isothermal converters with catalysts positioned within for the isothermal conversion. To maintain the isothermal

condition, the converters are often tubes or containers submerged in a bath of liquid hydrogen (LH_2) or liquid nitrogen (LN_2). The adiabatic conversion occurs in an adiabatic environment, and the heat generated by the conversion builds up in the hydrogen feed, increasing its temperature. Catalysts are inserted into heat exchanger channels to facilitate continuous conversion, which transfers heat to the refrigerant, a cold fluid, and continually removes it during cooling (Teng et al., 2023). Existing liquefaction plants and conceptual processes have incorporated these various conversion techniques. The simplicity of its structure allows for the observation of the isothermal conversion in certain studies of hydrogen liquefaction and early hydrogen liquefaction plants. Since most hydrogen liquefaction plants utilize LN_2 for precooling and produce LH_2, it is simple to achieve the isothermal state by immersing the converters in LN_2 and LH_2 baths.

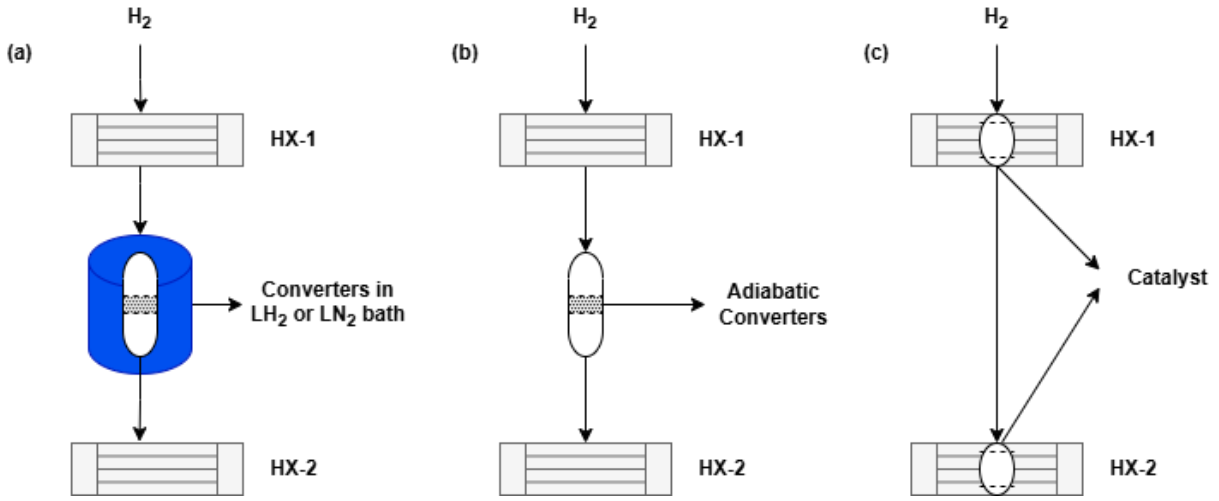

Figure 52. Sketch of different ortho-para hydrogen conversion methods: (a) isothermal conversion, (b) adiabatic conversion, (c) continuous conversion (adapted from Ref.(Teng et al., 2023)).

Simscape Fluids does not provide a predefined block for ortho–para converters. Therefore, to model the OPC block, a Simscape Component block from the Utilities library is used, as shown in **Figure 53**. The Simscape Component block enables you to generate a Simscape block directly from a textual component file, bypassing the need to build a custom library.

This block uses the Simscape language to generate the equations for the component. It enables you to use the Simscape language to directly describe domain parameters, variables, equations, and component structure. For complex processes like ortho-para hydrogen conversion, where reaction kinetics, energy balance, and thermodynamic relationships need to be adjusted for particular operating circumstances, this method is especially helpful. It also makes rapid prototyping and

iterative development easier because changes to the component file may be instantly updated in the model without having to rebuild the complete library.

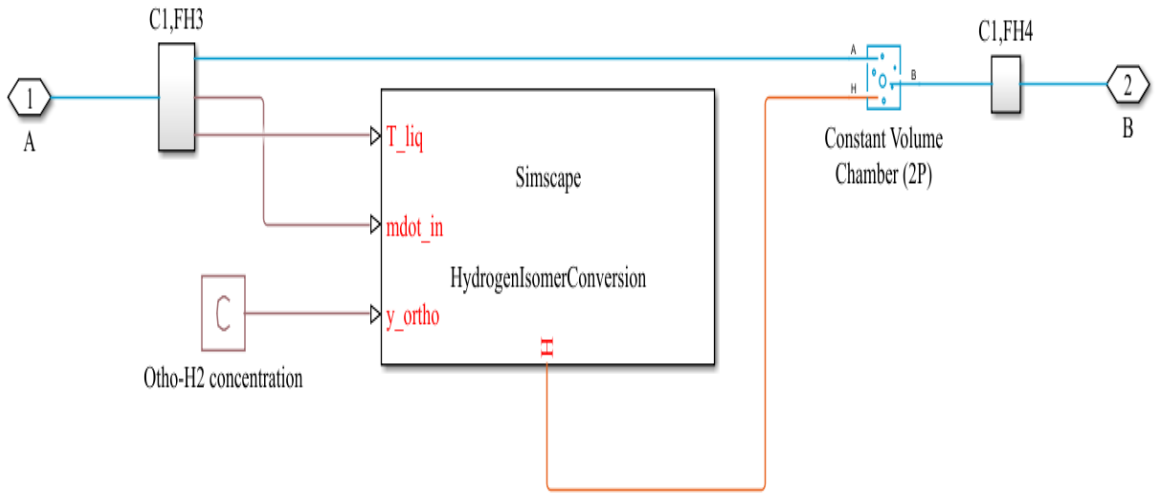

Figure 53. Schematic diagram of the Simscape custom component for hydrogen ortho-para conversion integrated with a two-phase constant volume chamber.

The Simscape custom "HydrogenIsomerConversion" block models the catalytic conversion between ortho- and para-hydrogen within a thermofluid network. The two-phase hydrogen flow is coupled through conserving ports A (inlet) and B (outlet). Physical signal inputs include the inlet liquid temperature T_{liq}, mass flow rate $\dot{m}_{in}$, and inlet ortho-hydrogen fraction y_{ortho}. This process employs the adiabatic conversion method for ortho-para conversion, which circulates heat from the system to the constant-volume chamber via thermal port H, raising the feed temperature even more. Heat production is calculated using Equation 8.29, and temperature-dependent equilibrium relations and conversion kinetics are utilized to get the isomerization rate. This heat release or absorption alters the thermodynamic state, and the energy exchange is transferred to the chamber, ensuring consistent mass and energy conservation. As a result, the block dynamically simulates changes in composition, temperature, and pressure caused by ortho–para conversion in hydrogen storage or transfer systems.

9. Proposed Simulated Design for 50 TPD

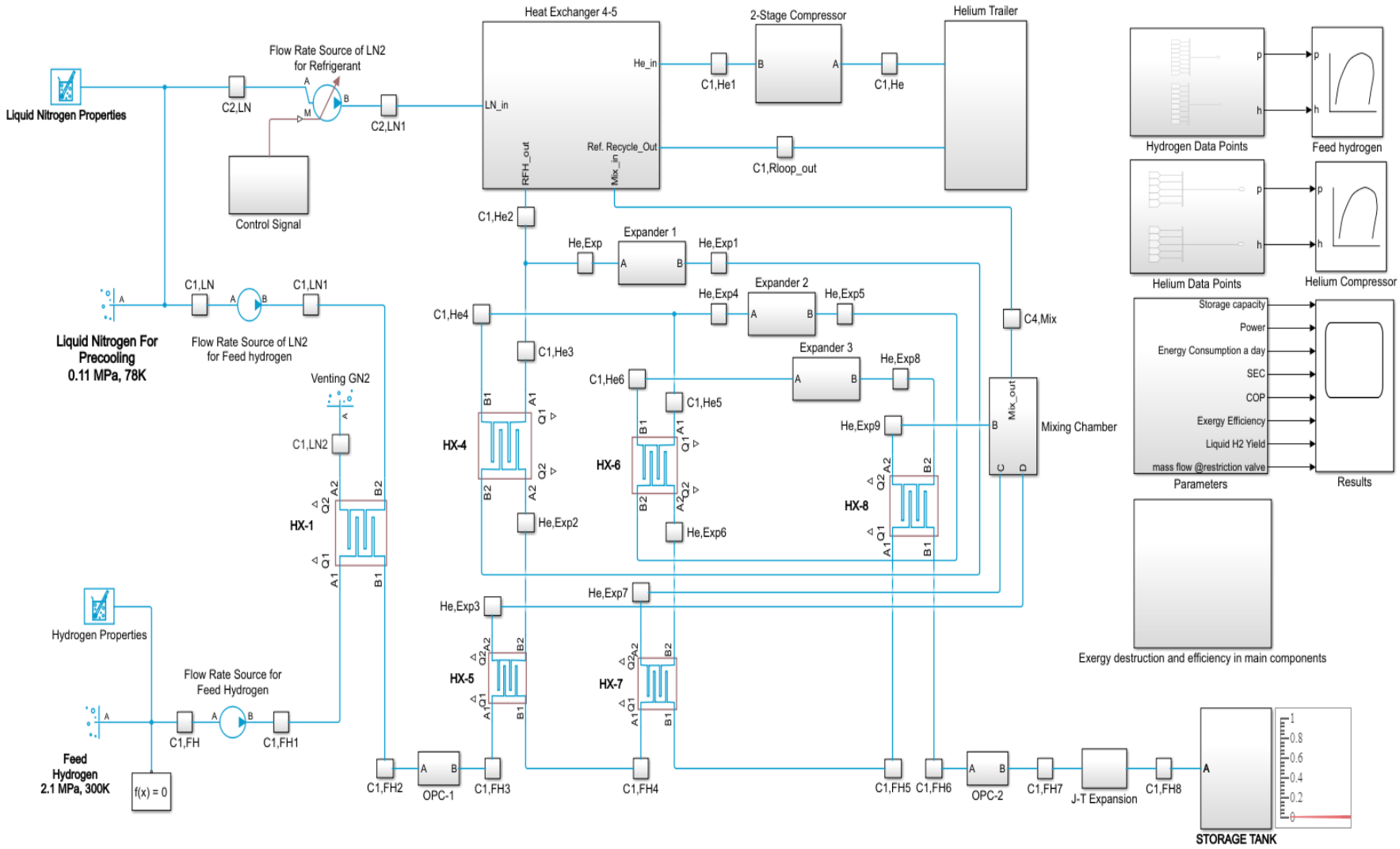

Figure 54. Proposed design of hydrogen liquefaction cycle with 50 TPD capacity.

9.1 Process Description

The proposed design is based on a Joule–Brayton cycle for hydrogen liquefaction, incorporating an open liquid nitrogen (LN_2) pre-cooling cycle and a closed helium refrigerant loop. This process employs a Joule–Brayton cycle with three turbo expanders, and helium is used as the refrigerant instead of hydrogen. The total helium refrigerant mass flow rate is 6 kg/s. Hydrogen gas is supplied at 298 K and 2.1 MPa to the first heat exchanger (HX-1), where it is pre-cooled to approximately 80 K using LN_2 as the cooling medium.

After pre-cooling, the hydrogen process stream enters the first ortho–para converter (OPC-1), where controlled partial conversion takes place. This step is essential for managing the thermal behavior of hydrogen during storage. OPC-1 operates adiabatically, meaning there is no heat exchange with the surroundings. The exothermic nature of the conversion increases the hydrogen temperature, and this internally generated heat is carried forward to the subsequent cryogenic heat exchangers, influencing the overall heat transfer requirements and temperature profile of the system. Section **8.4** provides a detailed discussion of the conversion extent as a function of inlet hydrogen temperature and its impact on thermal management and process efficiency. The refrigeration system employs a three-stage helium compressor with intercoolers to reduce the temperature of compressed helium to 300 K before it enters the cryogenic heat exchanger network. Helium is supplied from a helium trailer at 0.11 MPa and pressurized to 1.6 MPa. Each intercooler uses ambient air, assisted by a fan blower, to remove the heat of compression. The compressed helium then flows through the Heat Exchanger 4-5 subsection, where it is pre-cooled before entering the expansion stages.

After the pre-cooled helium refrigerant stream exits the Heat Exchanger 4–5 subsection, the flow is divided into two parts. The first stream enters Expander-1, while the second stream proceeds to HX-4. The cold stream exiting Expander-1 undergoes heat transfer in HX-4. Simultaneously, stream He, Exp2 flows into HX-5 to further cool the feed hydrogen gas. After this cooling process, stream He, Exp4 enters Expander-2, while the remaining portion flows through HX-6. In addition, stream He, Exp6 passes through HX-7 to further reduce the temperature of the feed hydrogen gas. The stream leaving HX-6 (stream C1, He6) then enters Expander-3, where it expands to a final pressure of 0.11 MPa. This expanded stream subsequently flows directly to HX-8, where the feed hydrogen is further cooled to the cryogenic temperature of 21 K before entering OPC-2. In OPC-2, the final ortho–para conversion takes place. The low-pressure helium streams from He, Exp3,

He, Exp7, and He, Exp9 from the HX-5, HX-7, and HX-8, respectively, are collected in a mixing chamber and routed back through the recuperative heat exchangers, where they pre-cool the incoming high-pressure helium. The combined return stream is then directed back to the compressor, completing the closed-loop helium refrigeration cycle.

Table 15. Boundary condition of the hydrogen liquefaction process.

Parameter	Value	Unit
Feed Hydrogen		
Inlet temperature	300	K
Inlet pressure	2.1	MPa
Mass flow rate	0.579	kg/s
Para-hydrogen	25	%
Ortho-hydrogen	75	%
Liquid Hydrogen		
Outlet temperature	21	K
Outlet pressure	0.13	MPa
Para-hydrogen	99	%
Refrigerant mass flow rate	6	kg/s
Compressor work	6926	kW
Exapnder-1 work	326.3	kW
Expander-2 work	249.4	kW
Expander-3 work	145.4	kW

Meanwhile, the hydrogen process stream, after passing through the final cryogenic heat exchanger and the second ortho-para converter (OPC-2), is expanded through a Joule–Thomson (J-T) expansion valve to a pressure of 0.13 MPa, reaching a temperature of approximately 21 K. The resulting two-phase mixture is separated in the storage tank, where liquid hydrogen is collected as a flow rate of 0.579 kg/s.

10. Proposed Simulated Design for 120 TPD

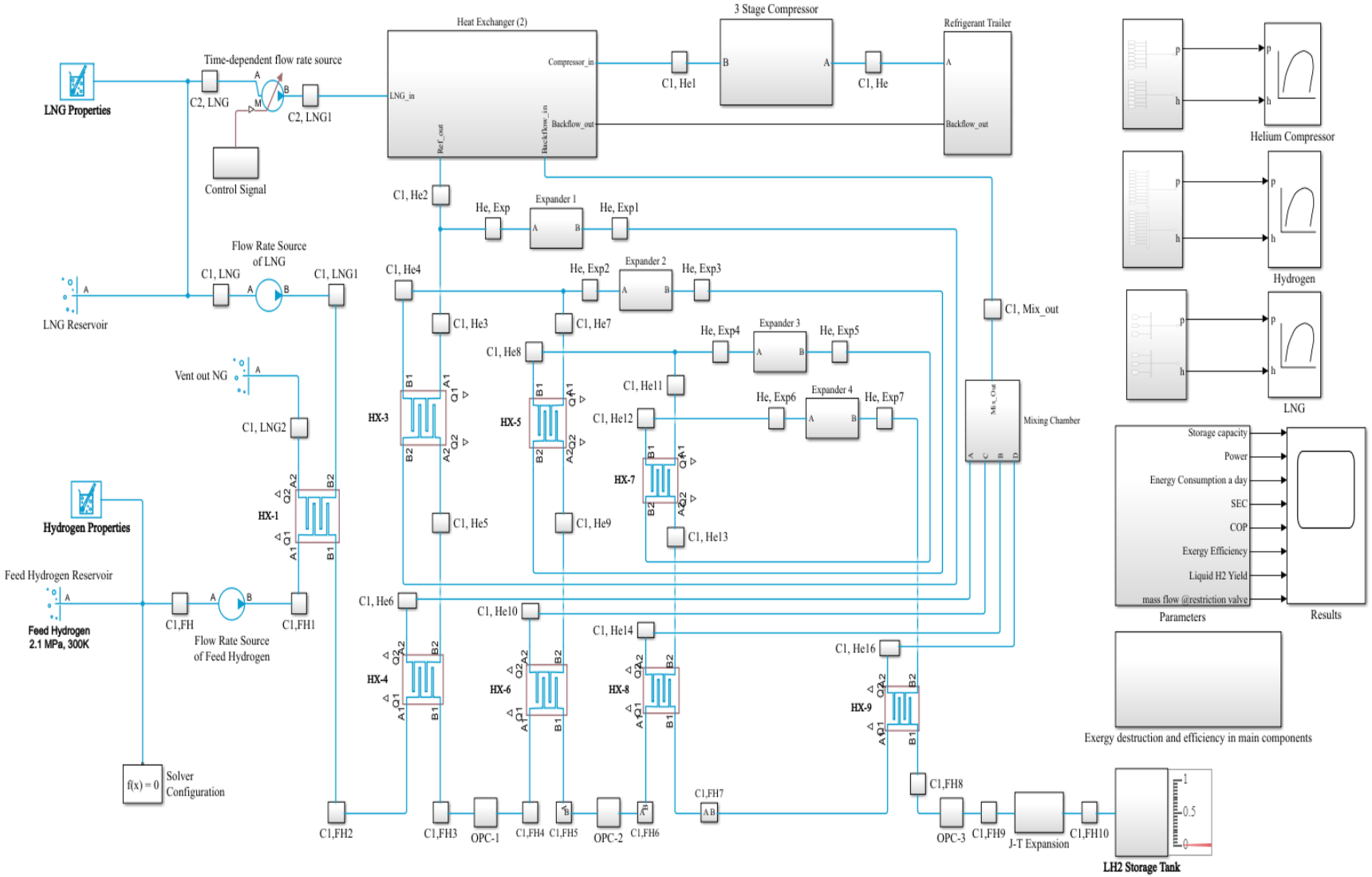

Figure 55. Proposed design of hydrogen liquefaction cycle with 120 TPD.

10.1 Process description

The hydrogen liquefaction process depicted in the **Figure 55** is based on a cascade Joule-Brayton refrigeration cycle, which achieves the cryogenic temperatures required for the production of liquid hydrogen by combining liquified natural gas (LNG) pre-cooling with a closed helium refrigeration loop. This arrangement uses helium as the main refrigerant in the cryogenic refrigeration cycle and LNG as an external pre-cooling medium. For the pre-cooling stage, the process regulates an LNG flow rate of 0.4 kg/s, a helium refrigerant circulation rate of 20 kg/s, and a feed hydrogen flow rate of 1.39 kg/s. The LNG composition for extracting its fluid properties are methane: 91.3 mol. %, nitrogen: 0.2 mol. %, ethane: 5.4 mol. %, propane: 2.1 mol. %, i-butane: 0.5 mol. %, n-butane: 0.5 mol. % (Bian et al., 2021c).

The first heat exchanger (HX-1) receives hydrogen gas from the feed reservoir, which enters the process at 300 K and 2.1 MPa, and LNG at 0.12 MPa and 114 K. LNG is used to pre-cool the hydrogen stream before it enters the main helium refrigeration section. The pre-cooling heat exchanger (Heat Exchanger 2) receives the LNG stream from the LNG reservoir via a regulated flow source and absorbs heat from the entering high pressure helium refrigeration stream. The hydrogen temperature is reduced from 300 K to around 114 K by this heat exchange mechanism, considerably reducing the refrigeration strain imposed on the downstream helium cycle. The heated natural gas is released from the system after serving as cooling.

The hydrogen stream enters the first ortho-para converter (OPC-1) after LNG pre-cooling. Ortho-hydrogen is partially catalytically converted to para-hydrogen in this reactor. Due to the exothermic nature of the conversion process, the temperature of the hydrogen stream increases. Since the reactor runs in an adiabatic environment, the heat that is released stays in the stream and needs to be extracted in the subsequent cryogenic heat exchangers. The excessive heat emission during the final liquefaction stage is avoided and thermodynamic efficiency is increased by using a partial conversion approach.

A closed cascade Joule-Brayton cycle operates the helium refrigeration subsystem. A three-stage helium compressor compresses helium refrigerant that is delivered at low pressure from a helium storage trailer. To eliminate the heat of compression and keep the helium temperature close to 300 K before it enters the cryogenic heat exchanger network, intercooling is used after each compression stage. After entering the first segment of the heat exchanger network, the compressed helium is gradually cooled via counter-flow heat exchange with returning low-temperature helium

streams. The high-pressure helium stream enters the cascade refrigeration network, which consists of four turbo-expanders and several heat exchangers (HX-3 to HX-9), following initial cooling. The helium stream that exits the upstream heat exchanger portion is split into multiple branches to serve as several expansion stages. The first part expands in Expander 1, generating a cold helium stream that passes through HX-4 and absorbs heat from other helium streams and the hydrogen process stream. Concurrently, a portion of the helium refrigerant travels through HX-5 and then enters Expander 2, providing a second low-temperature stream that helps cool the hydrogen stream in the intermediate heat exchangers. A portion of the helium stream exiting HX-6 expands through Expander 3 in the subsequent stage, further lowering its temperature and pressure. This stage produces cold helium, which passes through HX-7 and helps further pre-cool the hydrogen stream and other helium branches. Expander 4 produces the lowest temperature helium stream in the cycle by expanding a last branch of helium. After passing through the last cryogenic heat exchangers (HX-8 and HX-9), this incredibly cold stream eliminates any sensible heat from the hydrogen process stream, bringing the temperature of the hydrogen closer to the liquefaction point.

After leaving the heat exchangers HX-4, HX-6, HX-8, and HX-9, respectively, the low-pressure helium streams from C1, He6, C1, He10, C1, He14, and C1, He16 are collected in a mixing chamber to produce a single return stream. The entering high-pressure helium streams receive the cold energy from this mixed helium stream as it passes back through the recuperative heat exchanger network. This regenerative heat exchange maximizes the refrigeration capacity of the helium cycle before returning the helium to the compressor, completing the closed-loop refrigeration cycle.

Meanwhile, after passing through the final cryogenic heat exchanger (HX-9), the hydrogen process stream is expanded through a Joule–Thomson (J-T) expansion valve, where the pressure is reduced to approximately 0.13 MPa, resulting in a temperature close to 21 K. This expansion produces a two-phase hydrogen mixture consisting of liquid and vapor fractions. The mixture then enters the liquid hydrogen storage tank, where phase separation takes place and the liquid hydrogen at flow rate of 1.39 kg/s is collected as the final product.

11. Results and Discussion

Hydrogen demand is expected to rise from 75 million tons in 2019 to 621 million tons in 2050. The expansion of hydrogen transport and storage required to satisfy anticipated worldwide demand is probably going to be made possible by hydrogen liquefaction. However, hydrogen liquefaction requires a significant amount of energy. To optimize energy consumption and develop a more energy-efficient cycle, three different hydrogen liquefaction processes were simulated. The simulated cycles were designed for capacities ranging from small to large scale. This thesis study was conducted as part of the **EXACT2; HAP5** project, whose primary aim is to eliminate carbon emissions by transitioning aviation fuels to liquid hydrogen while also developing an energy-efficient system. The results obtained from three different liquefaction cycles are illustrated as;

The first model simulated has a capacity of ***5 TPD*** and employs a pre-cooled Claude cycle. The boundary conditions were taken from an existing cycle operated by Linde in Leuna, Germany. **Table 16** presents the model verification, including the key parameters obtained from the proposed simulation and their comparison with the reference data. This comparison helps validate the accuracy and reliability of the developed model.

Table 16. Verification of the 5 TPD pre-cooled Claude cycle model using reference data from the Linde hydrogen liquefaction plant in Leuna, and the decommissioned plant in Ingolstadt, Germany.

Parameters	Unit	Ingolstadt (Bracha et al., 1994)	Leuna (2008) Base Model	Proposed Model
Capacity	TPD	4.4	5	5
H_2 Feed				
Pressure	MPa	2.1	2.4	2.1
Temperature	K	<308	<313	<302
Normal Hydrogen Isomers	%	75-25	75-25	75-25
LH_2 Product				
Pressure	MPa	0.13	0.13	0.13
Temperature	K	21	21	21.23
Para Fraction	%	>95	>95	>95

Parameters	Unit	Ingolstadt (Bracha et al., 1994)	Leuna (2008) Base Model	Proposed Model
Efficiency of Compressor	%	-	65-70	80
Efficiency of Expander	%	-	>85	>80
Ortho-Para Conversion	-	4 Stage	Continuous	2 Stage
Specific Energy Consumption	kWh/kg_{LH_2}	13.6	11.9	9.69
Exergy Efficiency	%	21	23.6	54.2
Coefficient of Performance	%	-	-	0.118
Mass flow rate of Refrigerant	kg/s	-	-	0.3
Mass flow rate of LN_2	kg/s	-	-	0.4

The efficiency of the compression process is one of the main enhancements in the suggested approach. Compared to 65-70 % in the Leuna plant, the compressor efficiency rises to almost 80 %. This enhancement makes a substantial contribution to the overall decrease in energy consumption. The refrigeration cycle performance is also improved by the expander efficiency, which stays over 80 %. The specific energy consumption (SEC) is a key performance parameter. The suggested model achieves 9.69 kWh/kg_{LH_2} while the Leuna plant claims an SEC of 11.9 kWh/kg_{LH_2}. Comparing this to the Leuna process, the energy consumption is around 18.6 % lower. The suggested model exhibits an even greater improvement of almost 28.8 % when compared to the earlier Ingolstadt plant, which has an SEC of 13.6 kWh/kg_{LH_2}. These findings show that the energy required for hydrogen liquefaction can be considerably reduced by the suggested cycle architecture. Furthermore, compared to the data published for the Ingolstadt (21 %) and Leuna (23.6 %) plants, the exergy efficiency of the suggested model rises to 54.2 %. This suggests reduced thermodynamic losses and a more efficient use of energy inside the system. The simulated feasibility for practical applications is further supported by its coefficient of performance (COP) of 0.118.

11.1 Exergy Analysis of 5 TPD Cycle

In addition to performance parameters, the data illustrated in **Table 17** shows the exergy destruction and exergy efficiency of the suggested hydrogen liquefaction cycle in addition to the

performance parameters. The irreversibilities resulted in by thermodynamic losses in system components like compressors, heat exchangers, and expanders are represented by exergy destruction. A more efficient utilization of the available energy is indicated by a lower exergy destruction. The efficiency of the cycle in transforming the input work into functional hydrogen liquefaction is reflected in the exergy efficiency presented in **Table 17**. The suggested model is a viable and energy-efficient configuration for hydrogen liquefaction because of its comparatively higher exergy efficiency, which demonstrates improved thermodynamic performance and shows that the cycle operates at lower internal losses.

Table 17. Exergy analysis results showing exergy destruction and efficiency of system components for 5 TPD capacity.

Components	Electrical Power (kW)	Exergy Destruction (kW)	Exergy Efficiency (%)
Compressor-1	486	49.42	89.84
Compressor-2	474.24	48.28	59.83
Compressor-3	465.63	46.46	90.04
Expander-1	41.062	176.4	33.63
Expander-2	27.79		
Expander-3	20.49		
HX-1	-	183.6	41.59
HX-2	-	0.14	61
HX-3	-	146.3	81.1
HX-4	-	114.2	78.25
HX-5	-	245.3	58.4

The electrical power consumption of the main components in the hydrogen liquefaction process shows that compressors consume most energy in the system, as shown in **Figure 56**. About 32.1 % of the overall power usage, or 486 kW, is used by Compressor-1. Compressor-3 consumes

465.63 kW (30.8 %) of the total electrical power, while Compressor-2 uses 474.24 kW (31.3 %). The expanders, on the other hand, extract low work output. Expander-1 provides work output of 41.06 kW (2.7 %), Expander-2 of 27.79 kW (1.8 %), and Expander-3 of 20.49 kW (1.4 %). Approximately 1515.21 kW of electrical power is used by all system components.

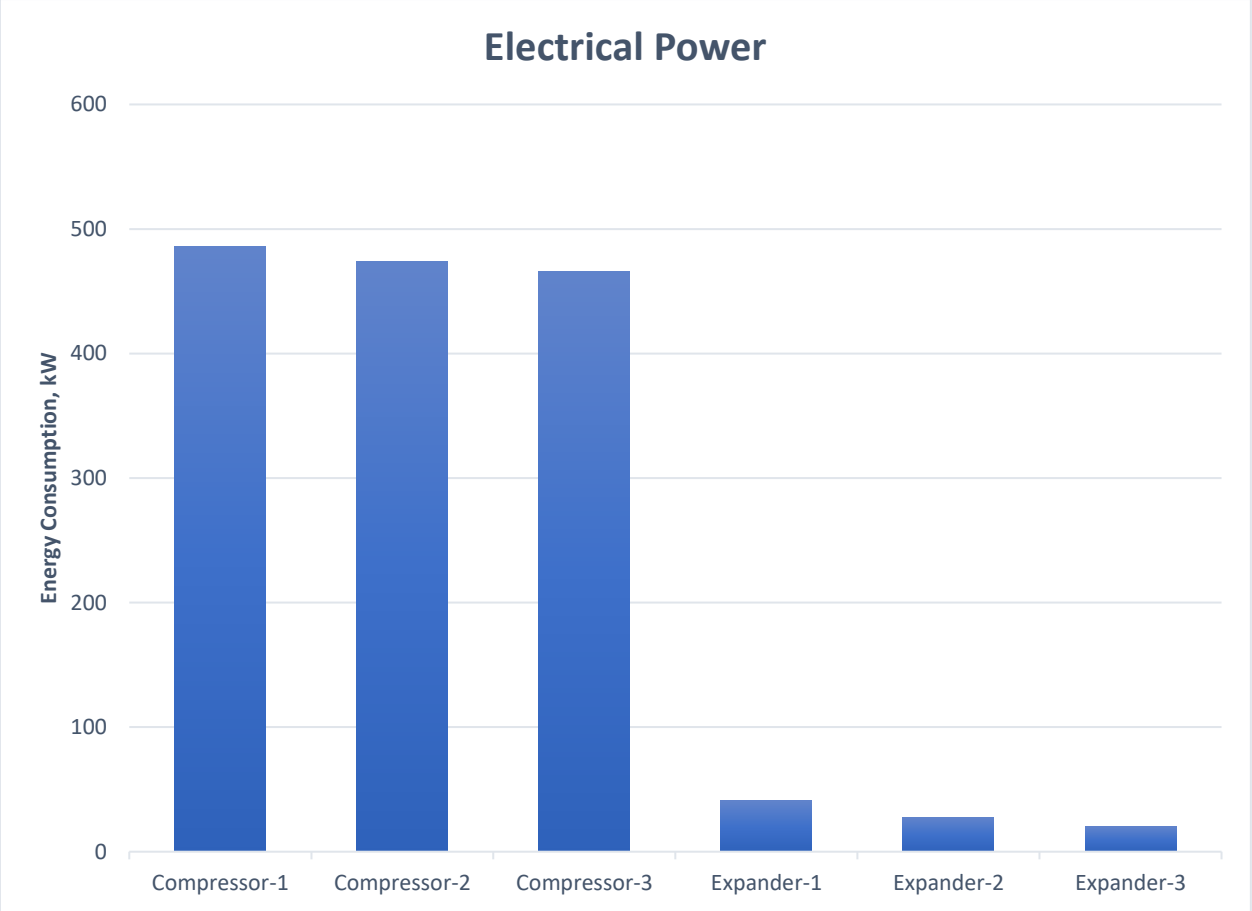

Figure 56. Energy consumption of the main part of the liquefaction system for 5 TPD.

This comparison makes it clear that the expansion stages only provide roughly 5.9 % of the total electrical power, while the compression stages account for roughly 94.2 % of the entire energy usage. Expanders obtain mechanical power from the system as high-pressure fluid expands through them, in contrast to compressors, which require electrical input to increase the pressure of hydrogen gas. A portion of the internal energy of the fluid is transformed into mechanical work during this expansion phase, which helps with cooling and may be partially recovered inside the system.

The data illustrated in **Figure 57** shows exergy destruction and exergy efficiency for the entire day of producing hydrogen and shows that the thermodynamic performance of the compressor

improves as the system operates. Due to increased irreversibilities such as friction, turbulence, heat transfer losses, and unstable flow conditions, exergy destruction is usually higher at the start of operation. The compressor gradually approaches a steady operating condition with more consistent temperature, pressure, and flow. Exergy destruction steadily decreases as a result of this stability, which lowers internal losses and irreversibilities. A decrease in exergy destruction eventually results in a greater exergy efficiency since exergy efficiency gauges how well the input work is transformed into usable exergy of the compressed fluid.

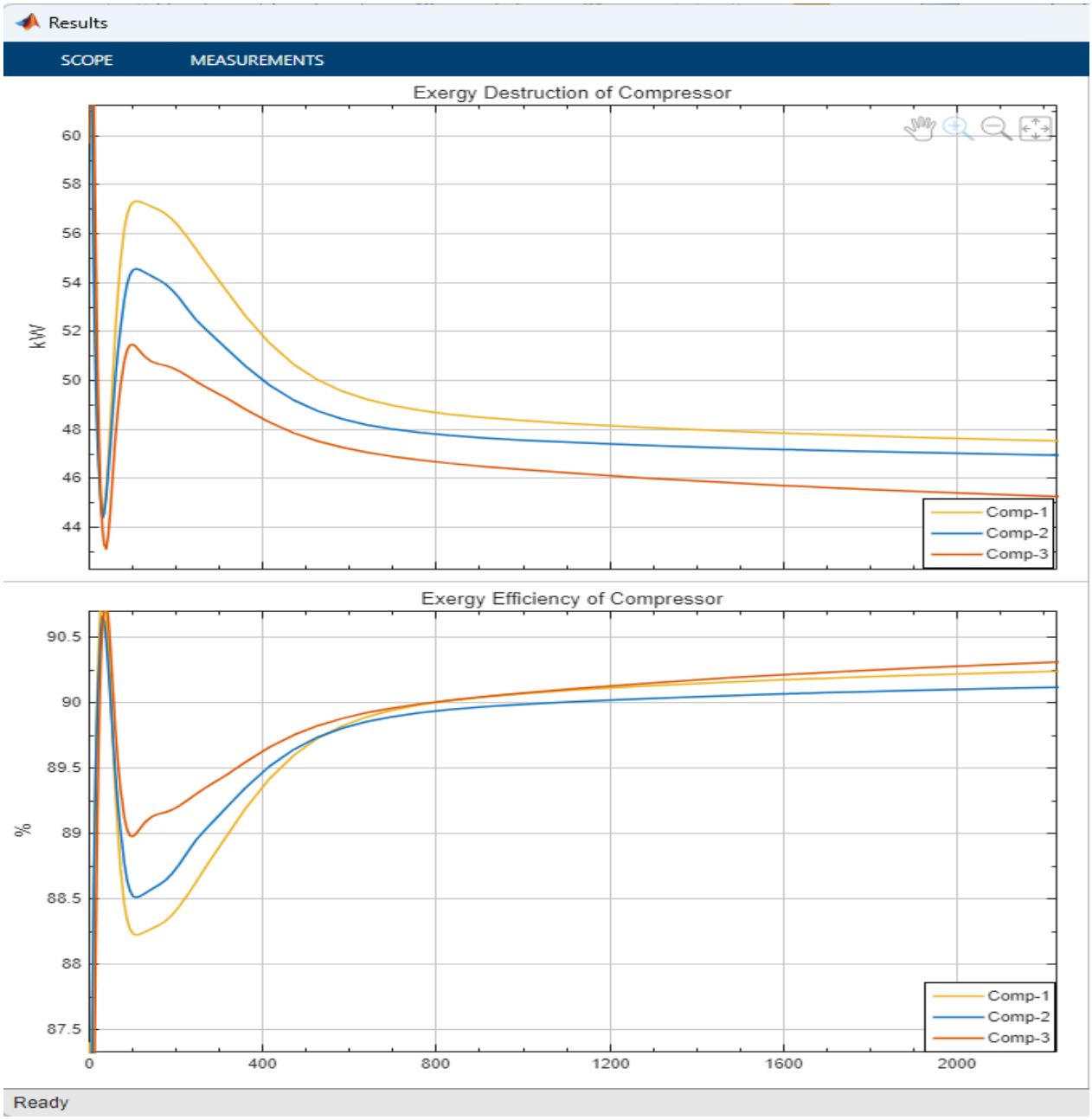

Figure 57. Time-dependent behavior of exergy destruction and exergy efficiency in the compressor.

Consequently, the compressor gets closer to steady-state operation with more effective energy use and less thermodynamic losses, as shown by the decreased trend of exergy destruction and the upward trend of exergy efficiency.

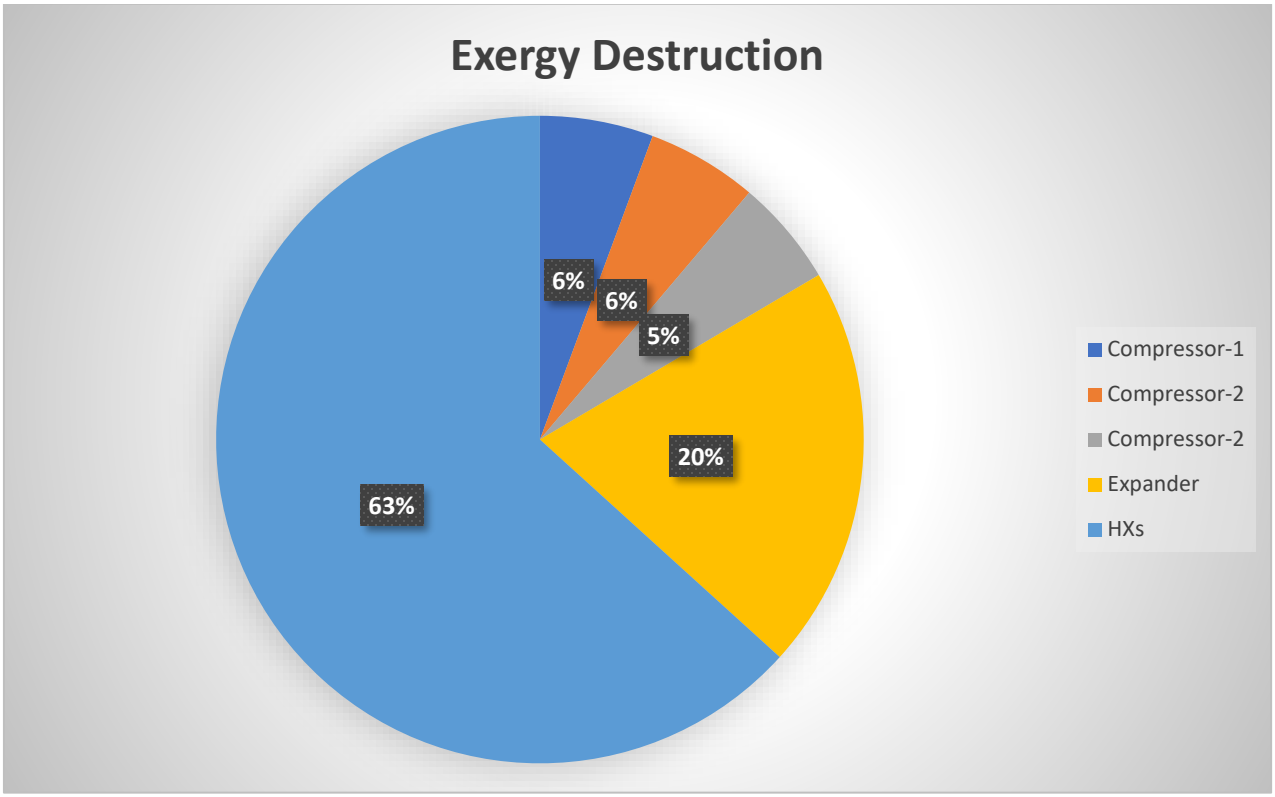

Figure 58. Exergy destruction of the main components of the hydrogen liquefaction cycle with 5 TPD capacity.

The exergy loss of the primary components of the liquefaction system is depicted in **Figure 58**. Actually, it shows the overall results of **Table 17**, which gives a summary of the irreversibility throughout the whole equipment. Heat exchanger, compressor, and expander exergy losses were 552.27, 144.16, and 176.4 kW, respectively. The total energy losses for the compressor, expander, and heat exchanger were quantitative. In particular, compressors showed a loss of 17 %, expanders 20 %, and heat exchangers 63 %, respectively.

Interestingly, compressors accounted for the lower portion of exergy loss, followed by heat exchangers and expanders, which were the solution for Song's findings (Song et al., 2025). Therefore, there was a great deal of potential to increase energy efficiency and reduce energy consumption by optimizing these three main components, especially compressors. Furthermore,

major optimization is made in the compressor in order to reduce the irreversible work and reduce the exergy destruction of the compressor to 17 %.

The second model has been designed for ***50 TPD***. An arrangement similar to that suggested by Song et al. was used as a reference for the current investigation (Song et al., 2025). They used a MATLAB-based tool in conjunction with REFPROP to simulate a hydrogen liquefaction system that included LN_2 pre-cooling and a helium Joule-Brayton cryogenic cycle. The compressor contributed to the higher exergy loss in their base scenario, which took into account a 0.5 TPD liquefaction capacity and reported an exergy efficiency of 28.82 % and a specific energy consumption (SEC) of 9.82 kWh/kg_{LH_2}. The same boundary conditions and process design were used in the current work, which was then scaled up to a 50 TPD capacity, as shown in **Table 18**. Energy performance significantly improved as a result of the scale-up, with a lower SEC of 6.5 kWh/kg_{LH_2}. This reduction is mostly due to enhanced thermodynamic performance and lower relative losses associated with larger-scale operation, illustrating the benefits of process scaling in increasing the efficiency of hydrogen liquefaction systems.

Table 18. Comparison of operating parameters and performance between the reference system by Song et al. and the proposed 50 TPD hydrogen liquefaction model.

Parameters	Unit	Song et al. (2025)	Proposed Model
Capacity	TPD	0.5	50
H_2 Feed			
Pressure	MPa	2.1	2.1
Temperature	K	300	<300
Normal Hydrogen Isomers	%	75-25	75-25
LH_2 Product			
Pressure	MPa	0.1	0.13
Temperature	K	20.2	21.12
Para Fraction	%	>95	>95
Efficiency of Compressor	%	70	75
Efficiency of Expander	%	75	80
Ortho-Para Conversion	-	5 Stage	2 Stage
Specific Energy Consumption	kWh/kg_{LH_2}	9.82	5.75

Parameters	Unit	Song et al. (2025)	Proposed Model
Exergy Efficiency	%	28.82	57.49
Coefficient of Performance	-		0.1932
Mass flow rate of Refrigerant	kg/s	0.1073	6
Mass flow rate of LN_2	kg/s	0.0745	3.8

The increased production capacity is supported by the higher refrigerant flow rate (6 kg/s) and liquid nitrogen flow rate (3.8 kg/s) in the suggested model, which further improves heat transfer and cooling efficiency within the liquefaction cycle. The comparison shows that the suggested design significantly enhances system efficiency, especially in terms of lower SEC and improved exergy efficiency, making it a more energy-efficient configuration for large-scale hydrogen liquefaction.

11.2 Exergy Analysis of 50 TPD Cycle

According to the formula described in the section **7.4,** the exergy destruction and exergy efficiency are calculated in **Figure 60**:

Table 19. Exergy analysis results showing exergy destruction and efficiency of system components for 50 TPD capacity.

Components	Electrical Power (kW)	Exergy Destruction (kW)	Exergy Efficiency (%)
Compressor-1	2897.5	99.46	96.57
Compressor-2	4028.01	475.1	88.21
Expander-1	326.3	457.4	41.64
Expander-2	249.4	561.6	30.75
Expander-3	145.4	531.5	21.49
HX-1	-	1582	44.4
HX-2	-	-	-
HX-3	-	245.4	82.9
HX-4	-	24.64	94.2
HX-5	-	30.52	87.6
HX-6	-	998.9	29.7

The data illustrated in **Figure 59** displays the energy consumption of the compressor, LN_2, and expander output power based on the energy analysis of the liquefaction cycle. Three expanders and two compressors constitute the system. The compressor consumed 6925.51 kW, which was contributed by Compressor-1 (2897.5 kW) and Compressor-2 (4028.01 kW). Expander-1 (326.3 kW), Expander-2 (249.4 kW), and Expander-3 (145.4 kW) produced the expander output work of 721.10 kW. The system used 7689.76 kW of electricity overall. Notably, the expanders helped recover energy by the work they performed throughout the expansion process, but the compressors were the primary sources of energy consumption, making up about 90.06 % of the overall energy consumption.

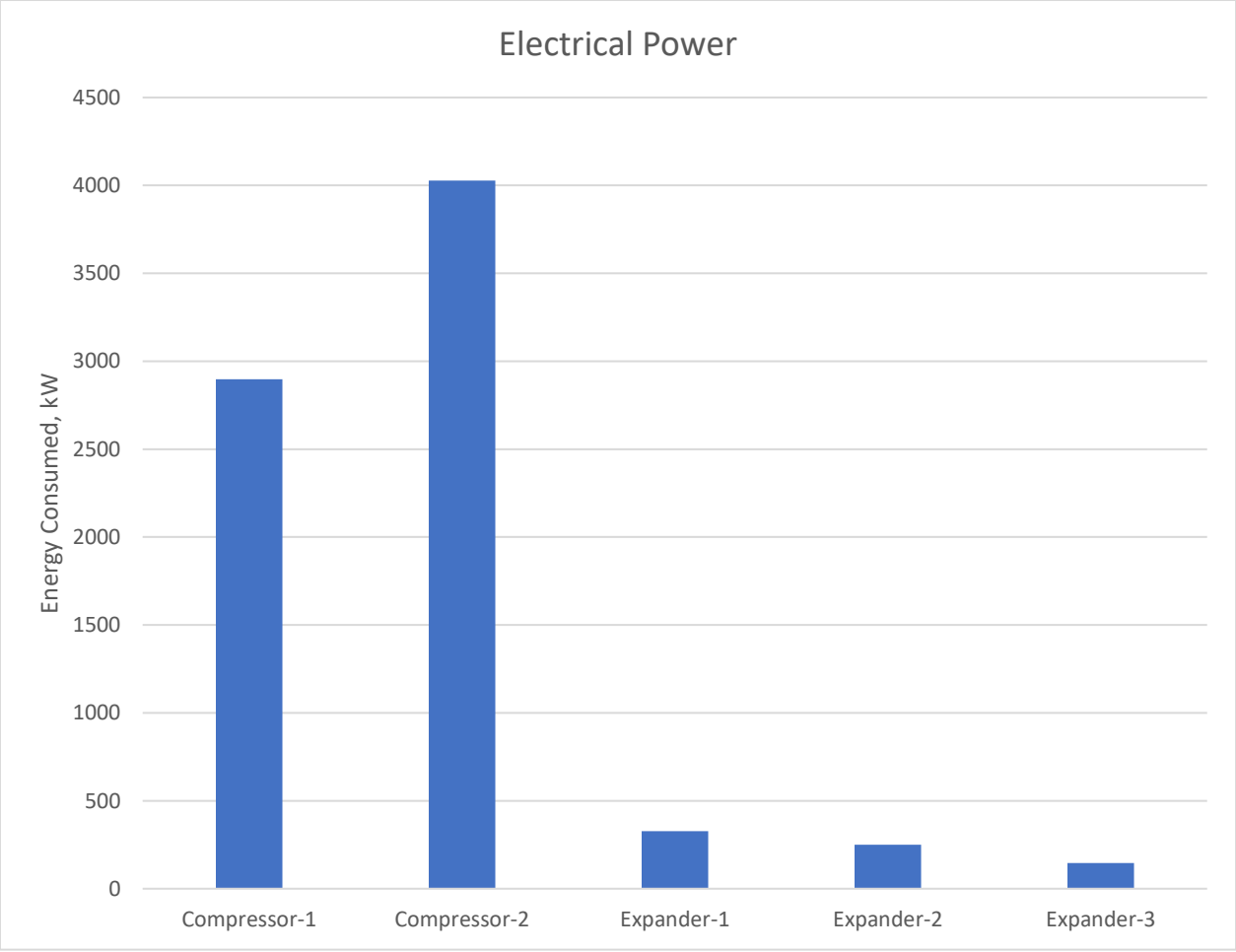

Figure 59. Energy consumption of the main part of the liquefaction system for 50 TPD.

Based on exergy analysis, **Table 19** demonstrates exergy efficiency and destruction of various system components. Among the compressors, Compressor-1 exhibits a high exergy efficiency of 96.57 % and a comparatively low exergy destruction of 99.46 kW, indicating extremely effective

operation with low thermodynamic losses. Compressor-2, on the other hand, has an impoverished exergy efficiency of 88.21 % due to a larger exergy destruction of 475.1 kW; it still operates effectively in comparison to other components. The expanders show lower efficiency and significantly more exergy destruction. Expander-2 and Expander-3 have even higher irreversibilities with 561.6 kW and 531.5 kW of exergy destruction and efficiencies of 30.75 % and 21.49 %, respectively, indicating poor thermodynamic performance. Expander-1 has 457.4 kW of exergy destruction with an efficiency of 41.64 %. Among the heat exchangers, HX-1 has the highest exergy destruction of 1582 kW with a 44.4 % efficiency, indicating severe losses. With exergy destructions of 245.4 kW and 24.64 kW and efficiencies of 82.9 % and 94.2 %, respectively, HX-3 and HX-4 exhibit superior performance. However, HX-6 exhibits a poor efficiency of 29.7 % and a rather high exergy destruction of 998.9 kW, suggesting significant irreversibility in that component. Overall, the findings show that compressors often have higher exergy efficiency, whereas expanders and some heat exchangers have worse thermodynamic performance and more exergy destruction.

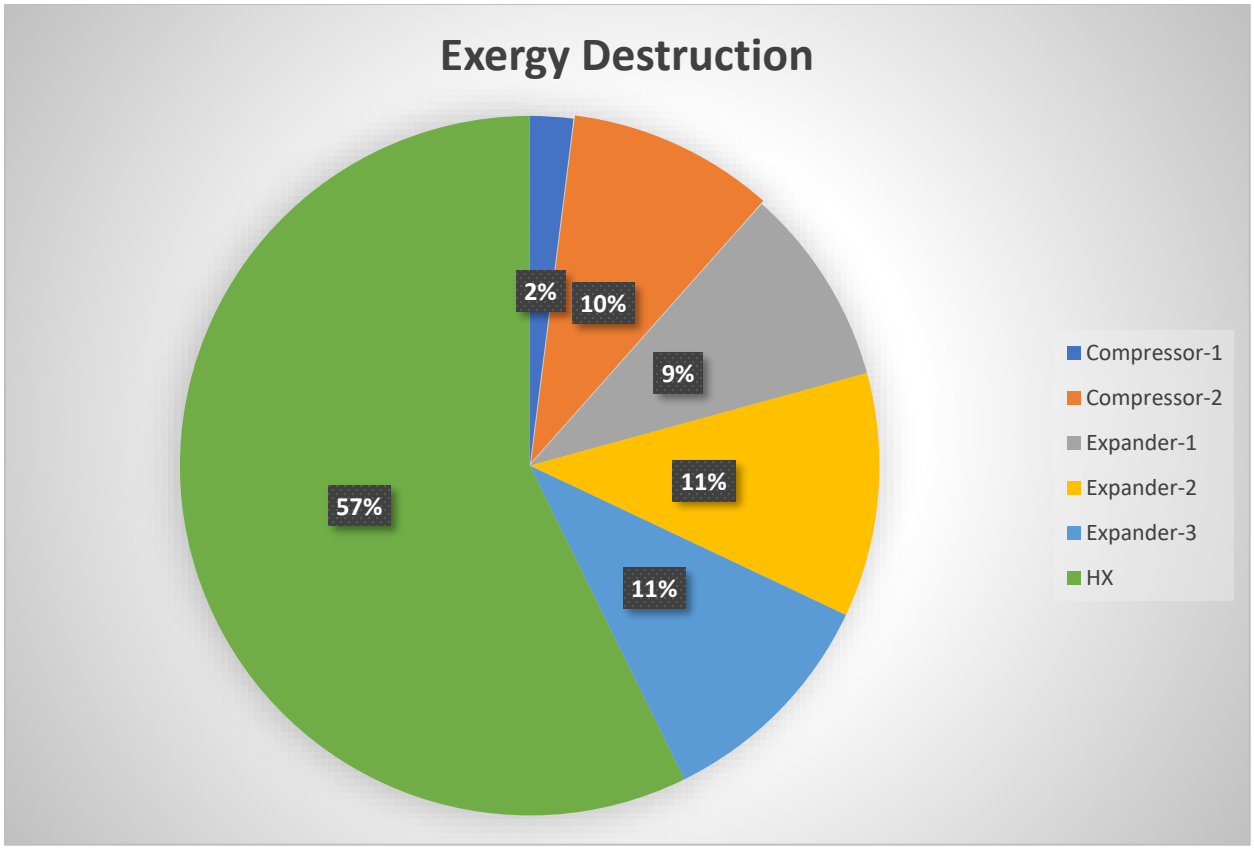

Figure 60. Exergy loss of the main equipment in the liquefaction system for 50 TPD.

The third proposed model is intended for a hydrogen liquefaction capability of **120 TPD**. A cascade Joule-Brayton refrigeration cycle, which incorporates several expansion stages to reach the necessary cryogenic temperatures for hydrogen liquefaction, is the base of the process configuration. An arrangement similar to that proposed by Bian et al. was used as a framework for the current study (Bian et al., 2021c). This study uses operational boundary conditions and base case design parameters that were taken from the reference study, as shown in **Table 20**.

Table 20. Comparison of operating parameters and performance between the reference system by Bian et al. and the proposed 120 TPD hydrogen liquefaction model.

Parameters	Unit	(Bian et al., 2021c)	Proposed Model
Capacity	TPD	120	120
H_2 Feed			
Pressure	MPa	2.1	2.1
Temperature	K	300	<300
Normal Hydrogen Isomers	%	75-25	75-25
LH_2 Product			
Pressure	MPa	0.1	0.14
Temperature	K	20.2	21.54
Para Fraction	%	>95	>95
Efficiency of Compressor	%	80	80
Efficiency of Expander	%	85	80
Ortho-Para Conversion	-	5 Stage	3 Stage
Specific Energy Consumption	kWh/kg_{LH_2}	6.60	7.54
Exergy Efficiency	%	47	43.32
Coefficient of Performance	-		0.144
Mass flow rate of Refrigerant	kg/s	16.54	20
Mass flow rate of LNG	kg/s	3.67	4

In both systems, the hydrogen feed conditions are similar. At a temperature of about 300 K and a pressure of 2.1 MPa, hydrogen enters the liquefaction process with a typical hydrogen isomer composition of 75 % ortho-hydrogen and 25 % para-hydrogen. This composition is commonly used for hydrogen at room temperature prior to ortho-para conversion during the cryogenic phases

of the liquefaction process. The suggested model produces liquid hydrogen at 0.14 MPa and 21.54 K, while the reference example operates at 0.1 MPa and 20.2 K for the liquid hydrogen product. Both methods achieve a para-hydrogen proportion larger than 95%, which is necessary for stable long-term storage of liquid hydrogen by reducing the heat loss associated with ortho-para conversion, even if the product temperature in the suggested system is somewhat higher. Additionally, both models assume similar turbomachinery efficiency. While the expander efficiency is 85 % in the reference model and 80 % in the suggested design, the compressor efficiency is assumed to be 80 % for both operations.

When compared to the reference case, the proposed model shows a higher specific energy consumption (SEC). The primary cause of this discrepancy is several modelling restrictions related to the Simscape Fluids simulation environment. Some common components used in hydrogen liquefaction processes, such as liquid expanders or two-phase expansion turbines, are neither generally available nor simple to design in the existing simulation framework. Liquid expanders are frequently employed in realistic liquefaction systems to recoup expansion work and lower the total energy consumption of the system. However, Joule-Thomson valves, which do not produce mechanical energy, is the main tool used in the current model to depict the liquid expansion process.

11.3 Exergy Analysis of 120 TPD Cycle

In addition to performance parameters, the data illustrated in **Table 21** shows the exergy destruction and exergy efficiency of the suggested hydrogen liquefaction cycle in addition to the performance parameters. The irreversibilities resulted in by thermodynamic losses in system components like compressors, heat exchangers, and expanders are represented by energy destruction.

Approximately 91.6 % of the power used in the hydrogen liquefaction system is consumed by the compressors. Among these, Compressor-1 provides roughly 28.6 %, while Compressor-3 and Compressor-2 contribute roughly 31.6 % and 31.5 %, respectively. Conversely, only around 8.5 % of the total power is extracted by the expanders. Among expanders, Expander-1 makes the largest contribution (3.1 %), while Expander-4 makes the least contribution (0.85 %).

Table 21. Exergy analysis results showing exergy destruction and efficiency of system components for 120 TPD capacity.

Components	Electrical Power (kW)	Exergy Destruction (kW)	Exergy Efficiency (%)
Compressor-1	12874	1404	89.03
Compressor-2	14174.8	1824	87.06
Compressor-3	14228	1847	87
Expander-1	1414.11	2663	34.69
Expander-2	1160.76	2620	30.7
Expander-3	856.47	2563	25.05
Expander-4	381.88	3193	10.68
HX-1	-	2247	43.34
HX-2	-	4497	70.16
HX-3	-	1305	68.15
HX-4	-	24.38	85.67
HX-5	-	1042	76.53
HX-6	-	78.56	89.52
HX-7	-	40.62	99.16
HX-8	-	188.1	86.87
HX-9	-	1016	89.12

The exergy efficiency profile of the hydrogen liquefaction system clearly distinguishes between compressors, expanders, and heat exchangers, as shown in **Figure 61**. The compressors are the most effective at converting input energy into useful output because of their continuously high efficiency, which ranges from 87 to 89 %. The expanders, on the other hand, have significantly lower efficiencies, which gradually decline from Expander-1 to Expander-4, with values ranging from roughly 35 % to just 11 %, indicating substantial exergy losses during the expansion process. The heat exchangers show a wide range of efficiency: HX-7 achieves almost whole efficiency at over 99 %, while HX-1 and HX-in these phases. 5 show more moderate efficiencies between 43

and 76 %. High efficiencies exceeding 85 % are maintained by a number of heat exchangers, such as HX-4, HX-6, and HX-8, indicating successful thermal energy recovery.

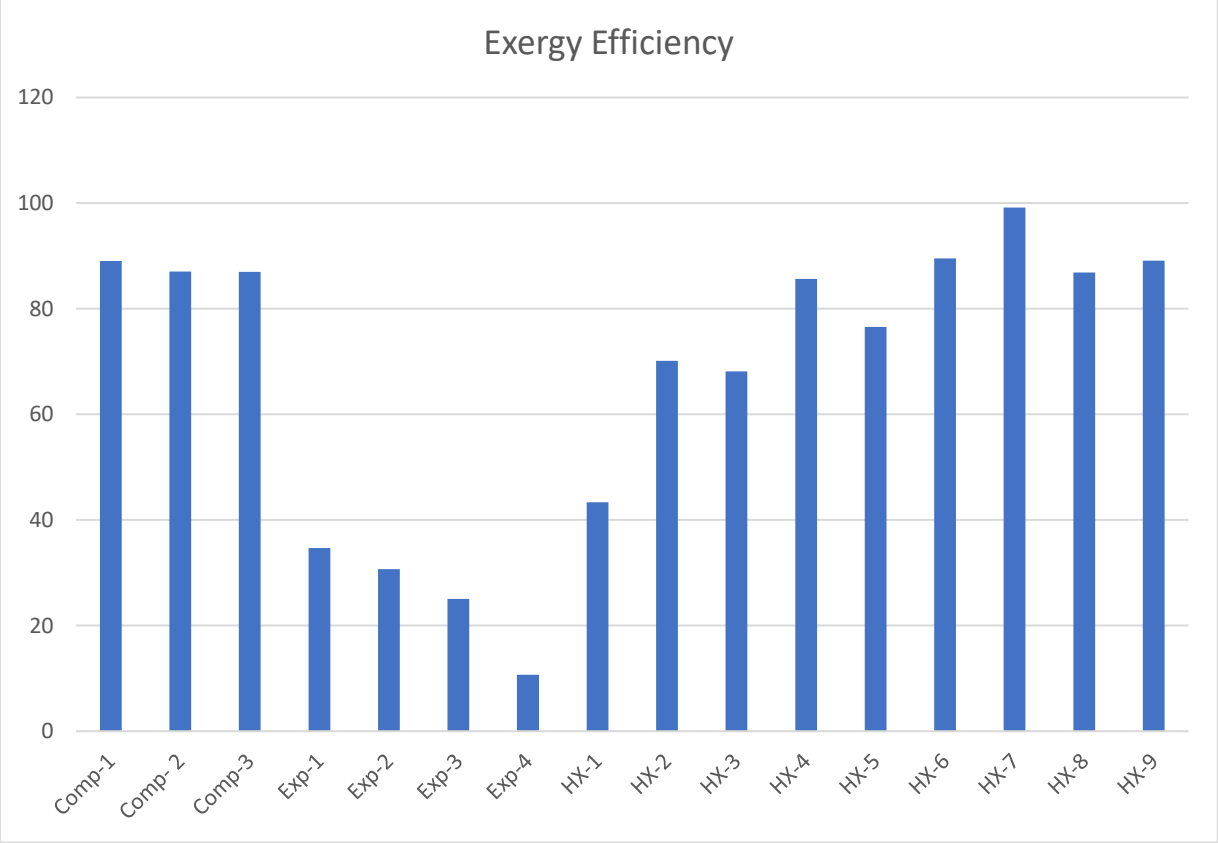

Figure 61. Exergy efficiency of the main components in the hydrogen liquefaction system.

Exergy destruction offers crucial insight into the thermodynamic inefficiencies of the process from the standpoint of irreversibility. According to the reference study, the overall exergy destruction is roughly 12.36 MW, with the compressors and expanders accounting for the majority of losses, which combined account for nearly 10 MW of exergy destruction (Bian et al., 2021c). Heat exchangers contribute a lesser part of the total exergy loss, around 2.29 MW, because of their relatively high thermodynamic efficiency.

Similarly, the proposed design demonstrates that the turbomachinery components, especially the expanders, are the main contributors to exergy destruction. For example, Expander-1, Expander-2, Expander-3, and Expander-4 have exergy destruction values of 2663 kW, 2620 kW, 2563 kW, and 3193 kW, respectively. Expansion devices with large temperature gradients and pressure dips at extremely low cryogenic temperatures are the primary cause of comparatively high energy losses. As a result, exergy efficiencies of the expander, which range from 10.68 % to 34.69 %, are much

lower than those of the compressors. This supports the findings in the reference study that the exergy performance of cryogenic expansion stages is relatively low.

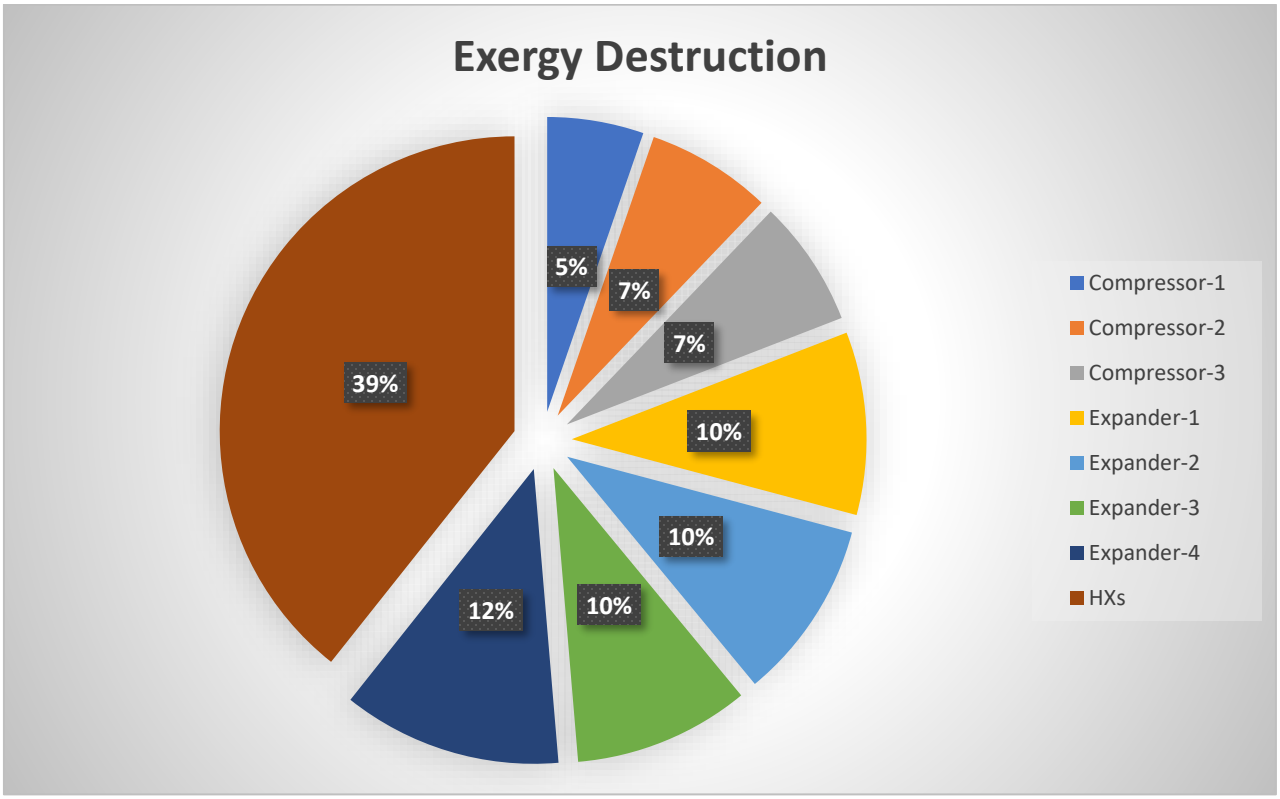

Figure 62. Exergy loss of the main equipment in the liquefaction system for 50 TPD.

The heat exchangers in the suggested design have comparatively high exergy efficiencies exceeding 70 % for the majority of units and considerably reduced exergy destruction, with values ranging from 24 kW to 4497 kW. This shows that the heat exchanger network maintains good thermodynamic performance while efficiently transferring thermal energy across process streams. Heat transfer processes are not the main causes of irreversibility in hydrogen liquefaction systems, as demonstrated by similar behaviour observed in the reference process, where the exergy efficiency of cryogenic heat exchangers approached 90 %.

Overall, the comparison demonstrates that the reference process and the suggested design have comparable thermodynamic behaviour, with heat exchangers operating with comparatively high efficiency and compression and expansion processes dominating both power consumption and energy destruction. However, the thorough component analysis of the suggested system reveals areas that could use more development, especially in the stages of cryogenic expansion when substantial exergy losses take place.

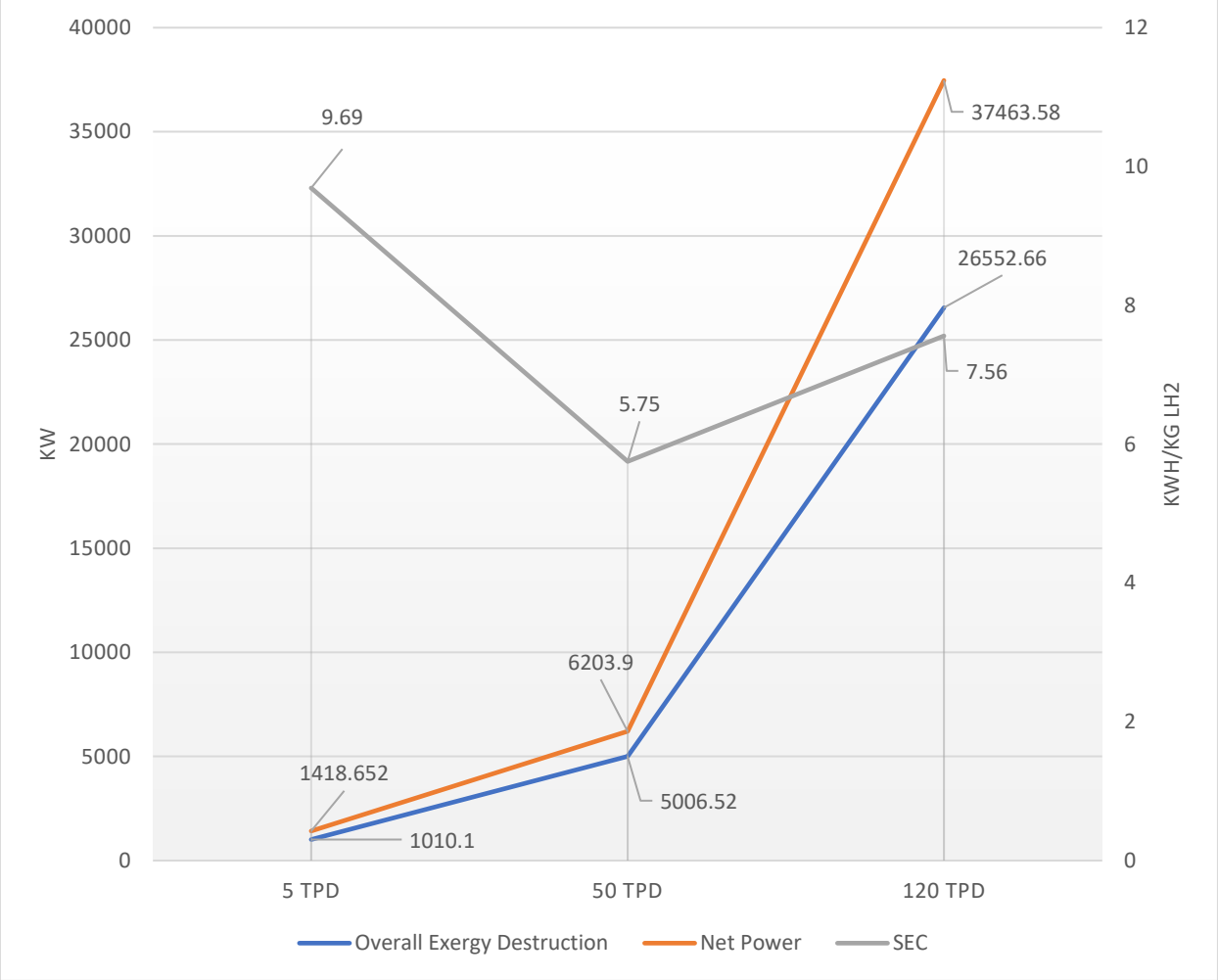

Figure 63. Comparative performance analysis of exergy destruction, net power consumption, and specific energy consumption (SEC) for hydrogen liquefaction plants at different production capacities (5, 50, and 120 TPD).

An exergy study was performed on hydrogen liquefaction plants with capacities of 5 TPD, 50 TPD, and 120 TPD. The findings in **Figure 63** demonstrate that total energy destruction rises dramatically with plant capacity, from roughly 1010 kW for the 5 TPD system to 5006 kW for the 50 TPD plant and 26,553 kW for the 120 TPD system. Higher mass flow rates and greater heat transfer responsibilities in larger facilities are the primary causes of this rise. Compressors show comparatively high exergy efficiencies across all capacities, indicating effective compression operations. Exergy destruction, on the other hand, is mostly caused by expanders and some heat exchangers, especially in bigger systems with larger temperature and pressure reductions. These findings imply that the total thermodynamic efficiency of hydrogen liquefaction facilities might be greatly increased by enhancing the performance of expansion turbines and crucial heat exchangers.

The major changes in energy-efficient hydrogen liquefaction are carried out in **Table 22,** which shows the relative decrement of SEC according to the reference cases.

Table 22. Comparison of specific energy consumption (SEC) between the proposed hydrogen liquefaction model and reference cycle configurations at different plant capacities.

Cycle Configuration	Capacity TPD	Reference Case SEC	Proposed Model SEC	Relative Change in SEC (%)
Pre-cooled Claude	5	11.9	9.69	-18.57
Pre-cooled Joule-Brayton	50	9.82	5.75	-41.44
LNG pre-cooled Cascade Joule-Brayton	120	6.60	7.56	+14.54

(Note: Negative values of relative change indicate a reduction in SEC compared to the reference case, while positive values indicate an increase.)

As shown in **Table 22** the specific energy consumption (SEC) of the suggested hydrogen liquefaction model was contrasted with a number of reference cycle configurations documented in the literature. When compared to the pre-cooled Claude and pre-cooled Joule-Brayton cycles, the results demonstrate that the suggested system achieves SEC reductions of **18.57 %** and **41.44 %** for the 5 TPD and 50 TPD capacities, respectively. This indicates that the suggested arrangement performs better in terms of energy at small and medium production scales. Nevertheless, compared to the LNG pre-cooled cascade Joule-Brayton cycle, the SEC of the suggested model is **14.54 %** greater for the 120 TPD capacity. Since Simscape Fluids lacks a designated block or adjustable component for liquid expanders, which are commonly employed in large-scale hydrogen liquefaction systems to recover expansion work, this increase is mostly attributable to modelling constraints within the simulation framework. Consequently, a higher estimated SEC for the 120 TPD configuration results is calculated because of liquid expansion work recovery.

Outlook

Future research will focus on enhancing the thermodynamic performance and modelling accuracy of the proposed hydrogen liquefaction plant. One alternative route is to optimize the refrigerant mass flow rate into the compressors, which will help decrease compression work and reduce the total specific energy consumption (SEC) of the operation. Further research will examine the use of plate-fin heat exchangers for continuous catalytic conversion of isomers, which will improve thermal integration within the liquefaction process and enable multi-stream heat exchange with multiple inlet and outlet ports.

Additionally, the Joule-Thomson (J-T) expansion used in the current model does not recover mechanical work from the system. To facilitate work recovery during the expansion process, future research will investigate the use of liquid expanders rather than J-T expansion. The SEC may be further reduced by using liquid expanders, especially for large-scale systems like the 120 TPD arrangement. Furthermore, future research will focus on enhanced process optimization and improved component-level modelling to increase the overall efficiency and performance of hydrogen liquefaction systems.

Bibliography

Aasadnia, M., & Mehrpooya, M. (2018). Large-scale liquid hydrogen production methods and approaches: A review. Applied Energy, 212, 57–83. https://doi.org/10.1016/j.apenergy.2017.12.033

Abbas, H. F., & Wan Daud, W. M. A. (2010). Hydrogen production by methane decomposition: A review. International Journal of Hydrogen Energy, 35(3), 1160–1190. https://doi.org/10.1016/j.ijhydene.2009.11.036

Abdi, A., Chiu, J., & Martin, V. (2019). State of the Art in Hydrogen Liquefaction. Proceedings of the ISES Solar World Congress 2019, 1–10. https://doi.org/10.18086/swc.2019.23.01

Al Ghafri, S. Zs., Munro, S., Cardella, U., Funke, T., Notardonato, W., Trusler, J. P. M., Leachman, J., Span, R., Kamiya, S., Pearce, G., Swanger, A., Rodriguez, E. D., Bajada, P., Jiao, F., Peng, K., Siahvashi, A., Johns, M. L., & May, E. F. (2022). Hydrogen liquefaction: A review of the fundamental physics, engineering practice and future opportunities. Energy & Environmental Science, 15(7), 2690–2731. https://doi.org/10.1039/D2EE00099G

Andersson, J., & Grönkvist, S. (2019). Large-scale storage of hydrogen. International Journal of Hydrogen Energy, 44(23), 11901–11919. https://doi.org/10.1016/j.ijhydene.2019.03.063

Andreas Züttel, Arndt Remhof, Andreas Borgschulte, & Oliver Friedrichs. (2010). Hydrogen: The future energy carrier. https://doi.org/doi:10.1098/rsta.2010.0113

Ansarinasab, H., Mehrpooya, M., & Sadeghzadeh, M. (2019). An exergy-based investigation on hydrogen liquefaction plant-exergy, exergoeconomic, and exergoenvironmental analyses. Journal of Cleaner Production, 210, 530–541. https://doi.org/10.1016/j.jclepro.2018.11.090

Baker, C. (1978). A study of the efficiency of hydrogen liquefaction. International Journal of Hydrogen Energy, 3(3), 321–334. https://doi.org/10.1016/0360-3199(78)90037-X

Ball, M., & Wietschel, M. (Eds.). (2009). The Hydrogen Economy: Opportunities and Challenges. Cambridge University Press. https://doi.org/10.1017/CBO9780511635359

Balthasar, W. (1984). Hydrogen production and technology: Today, tomorrow and beyond. International Journal of Hydrogen Energy, 9(8), 649–668. https://doi.org/10.1016/0360-3199(84)90263-5

Berstad, D. O., Stang, J. H., & Nekså, P. (2010). Large-scale hydrogen liquefier utilising mixed-refrigerant pre-cooling. International Journal of Hydrogen Energy, 35(10), 4512–4523. https://doi.org/10.1016/j.ijhydene.2010.02.001

Bhandari, R., Trudewind, C. A., & Zapp, P. (2014). Life cycle assessment of hydrogen production via electrolysis – a review. Journal of Cleaner Production, 85, 151–163. https://doi.org/10.1016/j.jclepro.2013.07.048

Bian, J., Yang, J., Li, Y., Chen, Z., Liang, F., & Cao, X. (2021a). Thermodynamic and economic analysis of a novel hydrogen liquefaction process with LNG precooling and dual-pressure Brayton cycle. Energy Conversion and Management, 250, 114904. https://doi.org/10.1016/j.enconman.2021.114904

Bian, J., Yang, J., Li, Y., Chen, Z., Liang, F., & Cao, X. (2021b). Thermodynamic and economic analysis of a novel hydrogen liquefaction process with LNG precooling and dual-pressure Brayton cycle. Energy Conversion and Management, 250, 114904. https://doi.org/10.1016/j.enconman.2021.114904

Bian, J., Yang, J., Li, Y., Chen, Z., Liang, F., & Cao, X. (2021c). Thermodynamic and economic analysis of a novel hydrogen liquefaction process with LNG precooling and dual-pressure

Brayton cycle. Energy Conversion and Management, 250, 114904. https://doi.org/10.1016/j.enconman.2021.114904

Bin, T., Yuanyang, Z., Liansheng, L., Guangbin, L., Le, W., Qichao, Y., Haiping, X., Feng, Z., & Wenhui, M. (2013). Thermal performance analysis of reciprocating compressor with stepless capacity control system. Applied Thermal Engineering, 54(2), 380–386. https://doi.org/10.1016/j.applthermaleng.2013.01.036

Boero, A. J., Kardux, K., Kovaleva, M., Salas, D. A., Mooijer, J., Mashruk, S., Townsend, M., Rouwenhorst, K., Valera-Medina, A., & Ramirez, A. D. (2021). Environmental Life Cycle Assessment of Ammonia-Based Electricity. Energies, 14(20), 6721. https://doi.org/10.3390/en14206721

Bourane, A., Elanany, M., Pham, T. V., & Katikaneni, S. P. (2016). An overview of organic liquid phase hydrogen carriers. International Journal of Hydrogen Energy, 41(48), 23075–23091. https://doi.org/10.1016/j.ijhydene.2016.07.167

Bracha, M., Lorenz, G., Patzelt, A., & Wanner, M. (1994). Large-scale hydrogen liquefaction in Germany. International Journal of Hydrogen Energy, 19(1), 53–59. https://doi.org/10.1016/0360-3199(94)90177-5

Cardella, U., Decker, L., & Klein, H. (2017). Roadmap to economically viable hydrogen liquefaction. International Journal of Hydrogen Energy, Special Issue on The 21st World Hydrogen Energy Conference (WHEC 2016), 13-16 June 2016, Zaragoza, Spain, 42(19), 13329–13338. https://doi.org/10.1016/j.ijhydene.2017.01.068

Cardella, U., Decker, L., Sundberg, J., & Klein, H. (2017). Process optimization for large-scale hydrogen liquefaction. International Journal of Hydrogen Energy, 42(17), 12339–12354. https://doi.org/10.1016/j.ijhydene.2017.03.167

Chatterjee, S., Parsapur, R. K., & Huang, K.-W. (2021). Limitations of Ammonia as a Hydrogen Energy Carrier for the Transportation Sector. ACS Energy Letters, 6(12), 4390–4394. https://doi.org/10.1021/acsenergylett.1c02189

Chen, H. L., Lee, H. M., Chen, S. H., Chao, Y., & Chang, M. B. (2008). Review of plasma catalysis on hydrocarbon reforming for hydrogen production—Interaction, integration, and prospects. Applied Catalysis B: Environmental, 85(1–2), 1–9. https://doi.org/10.1016/j.apcatb.2008.06.021

Chi, J., & Yu, H. (2018). Water electrolysis based on renewable energy for hydrogen production. Chinese Journal of Catalysis, 39(3), 390–394. https://doi.org/10.1016/S1872-2067(17)62949-8

Collie, J. G., Eng, F. R. S. F., John, R., & Phil, T. D. (1994). Conditions Influencing The Performance Of Boiling And Condensing Systems. In J. G. Collie, F. R. S. F. Eng, R. John, & T. D. Phil (Eds.), Convective Boiling and Condensation (p. 0). Oxford University Press. https://doi.org/10.1093/oso/9780198562825.003.0011

Das, A., & Datta Peu, S. (2022). A Comprehensive Review on Recent Advancements in Thermochemical Processes for Clean Hydrogen Production to Decarbonize the Energy Sector. Sustainability, 14, 11206. https://doi.org/10.3390/su141811206

Dell, R. M., & Bridger, N. J. (1975). Hydrogen—The ultimate fuel. Applied Energy, 1(4), 279–292. https://doi.org/10.1016/0306-2619(75)90029-X

Demirbaş, A. (2001a). Biomass resource facilities and biomass conversion processing for fuels and chemicals. Energy Conversion and Management, 42(11), 1357–1378. https://doi.org/10.1016/S0196-8904(00)00137-0

Demirbaş, A. (2001b). Biomass resource facilities and biomass conversion processing for fuels and chemicals. Energy Conversion and Management, 42(11), 1357–1378. https://doi.org/10.1016/S0196-8904(00)00137-0

Dewar, J. (1898). Liquid Hydrogen. Nature, 58(1501), 319–319. https://doi.org/10.1038/058319c0

DOE/EE-1552. (2017). Hydrogen Storage. https://www.energy.gov/sites/prod/files/2017/03/f34/fcto-h2-storage-fact-sheet.pdf

Drnevich & Praxair. (2003). Hydrogen Delivery Liquefaction & Compression. https://www1.eere.energy.gov/hydrogenandfuelcells/pdfs/liquefaction_comp_pres_praxair.pdf

El-Shafie, M. (2023). Hydrogen production by water electrolysis technologies: A review. Results in Engineering, 20, 101426. https://doi.org/10.1016/j.rineng.2023.101426

Fischer, N. P. (2015). Simscape Modeling of a Custom Closed-Volume Tank.

Giddey, S., Badwal, S. P. S., Munnings, C., & Dolan, M. (2017). Ammonia as a Renewable Energy Transportation Media. ACS Sustainable Chemistry & Engineering, 5(11), 10231–10239. https://doi.org/10.1021/acssuschemeng.7b02219

Gursu, S., Sheriff, S., Vezirocglu, T., & Sheffield, J. (1994). Review of slush hydrogen production and utilization technologies. International Journal of Hydrogen Energy, 19(6), 491–496. https://doi.org/10.1016/0360-3199(94)90002-7

Hallenbeck, P. (2002). Biological hydrogen production; fundamentals and limiting processes. International Journal of Hydrogen Energy, 27(11–12), 1185–1193. https://doi.org/10.1016/S0360-3199(02)00131-3

Hammad, A., & Dincer, I. (2018). Analysis and assessment of an advanced hydrogen liquefaction system. International Journal of Hydrogen Energy, 43(2), 1139–1151. https://doi.org/10.1016/j.ijhydene.2017.10.158

He, T., Cao, H., & Chen, P. (2019). Complex Hydrides for Energy Storage, Conversion, and Utilization. Advanced Materials, 31(50), 1902757. https://doi.org/10.1002/adma.201902757

Hedayat, A. (2002). Analytical modeling of variable density multilayer insulation for cryogenic storage. AIP Conference Proceedings, 613, 1557–1564. https://doi.org/10.1063/1.1472190

Holladay, J. D., Hu, J., King, D. L., & Wang, Y. (2009). An overview of hydrogen production technologies. Catalysis Today, 139(4), 244–260. https://doi.org/10.1016/j.cattod.2008.08.039

Hydrogen | Properties, Uses, & Facts | Britannica. (2025, October 17). https://www.britannica.com/science/hydrogen

Hydrogen | Properties, Uses, & Facts | Britannica. (2026, February 27). https://www.britannica.com/science/hydrogen

Hydrogen—Thermophysical Properties. (2025). https://www.engineeringtoolbox.com/hydrogen-d_1419.html

Iribarren, D., Susmozas, A., Petrakopoulou, F., & Dufour, J. (2014). Environmental and exergetic evaluation of hydrogen production via lignocellulosic biomass gasification. Journal of Cleaner Production, 69, 165–175. https://doi.org/10.1016/j.jclepro.2014.01.068

Ishimoto, Y., Voldsund, M., Nekså, P., Roussanaly, S., Berstad, D., & Gardarsdottir, S. O. (2020). Large-scale production and transport of hydrogen from Norway to Europe and Japan: Value chain analysis and comparison of liquid hydrogen and ammonia as energy

carriers. International Journal of Hydrogen Energy, 45(58), 32865–32883. https://doi.org/10.1016/j.ijhydene.2020.09.017

Jacob, Neksa, & Brendeng. (2006). On the design of an efficient hydrogen liquefaction process. https://www.researchgate.net/publication/288472069_On_the_design_of_an_effient_hydrogen_liquefaction_process/link/5b227341aca272277fab4867/download?_tp=eyJjb250ZXh0Ijp7InBhZ2UiOiJwdWJsaWNhdGlvbiIsInByZXZpb3VzUGFnZSI6bnVsbH19

Jakobsen, D., & Åtland, V. (2016). Concepts for Large Scale Hydrogen Production [Master thesis, NTNU]. In 143. https://ntnuopen.ntnu.no/ntnu-xmlui/handle/11250/2402554

Javier Fernandez de Canete & Jesus Martin-Aguilar. (2020). Ship-course modeling and control using the SIMSCAPE physical modeling environment. https://doi.org/10.1177/0037549720974751

Jin, T., Li, Y. J., Liang, Z. B., Lan, Y. Q., Lei, G., & Gao, X. (2017). Numerical prediction of flow characteristics of slush hydrogen in a horizontal pipe. International Journal of Hydrogen Energy, 42(6), 3778–3789. https://doi.org/10.1016/j.ijhydene.2016.09.054

Juste, G. L. (2006). Hydrogen injection as additional fuel in gas turbine combustor. Evaluation of effects. International Journal of Hydrogen Energy, 31(14), 2112–2121. https://doi.org/10.1016/j.ijhydene.2006.02.006

Kalinci, Y., Hepbasli, A., & Dincer, I. (2009). Biomass-based hydrogen production: A review and analysis. International Journal of Hydrogen Energy, 34(21), 8799–8817. https://doi.org/10.1016/j.ijhydene.2009.08.078

Kanz, B., Tafone, A., Stops, L., Massier, T., & Klein, H. (2025). A novel approach to simulate ortho-para conversion in hydrogen liquefaction based on the van’t Hoff equation. International Journal of Hydrogen Energy, 140, 870–880. https://doi.org/10.1016/j.ijhydene.2025.02.304

Kapdan, I. K., & Kargi, F. (2006). Bio-hydrogen production from waste materials. Enzyme and Microbial Technology, 38(5), 569–582. https://doi.org/10.1016/j.enzmictec.2005.09.015

Kori, N. A. E., Blanco-Marigorta, A. M., & Martel, N. M. (2024). Definition of Exergetic Efficiency in the Main and Emerging Thermal Desalination Technologies: A Proposal. Water, 16(9). https://doi.org/10.3390/w16091254

Krasae-in, S., Stang, J. H., & Neksa, P. (2010a). Development of large-scale hydrogen liquefaction processes from 1898 to 2009. International Journal of Hydrogen Energy, 35(10), 4524–4533. https://doi.org/10.1016/j.ijhydene.2010.02.109

Krasae-in, S., Stang, J. H., & Neksa, P. (2010b). Simulation on a proposed large-scale liquid hydrogen plant using a multi-component refrigerant refrigeration system. International Journal of Hydrogen Energy, 35(22), 12531–12544. https://doi.org/10.1016/j.ijhydene.2010.08.062

Kuendig, A., Loehlein, K., Kramer, G. J., & Huijsmans, J. (2006). Large scale hydrogen liquefaction in combination with LNG re-gasification.

Kuz'menko, I. F., Morkovkin, I. M., & Gurov, E. I. (2004). Concept of Building Medium-Capacity Hydrogen Liquefiers with Helium Refrigeration Cycle. Chemical and Petroleum Engineering, 40(1), 94–98. https://doi.org/10.1023/B:CAPE.0000024144.92081.aa

Leachman, J. W., Jacobsen, R. T., Penoncello, S. G., & Lemmon, E. W. (2009). Fundamental Equations of State for Parahydrogen, Normal Hydrogen, and Orthohydrogen. 721–748.

Lee, H., Haider, J., Abdul Qyyum, M., Choe, C., & Lim, H. (2022). An innovative high energy efficiency–based process enhancement of hydrogen liquefaction: Energy, exergy, and economic perspectives. Fuel, 320, 123964. https://doi.org/10.1016/j.fuel.2022.123964

Mann, M., & Spath, P. (2004). Life Cycle Assessment of Renewable Hydrogen Production via Wind/Electrolysis: Milestone Completion Report (NREL/MP-560-35404, 15006927; p. NREL/MP-560-35404, 15006927). https://doi.org/10.2172/15006927

Martino, M., Ruocco, C., Meloni, E., Pullumbi, P., & Palma, V. (2021). Main Hydrogen Production Processes: An Overview. Catalysts, 11(5), 547. https://doi.org/10.3390/catal11050547

Mathworks/positive-displacement compressor 2P. (2025). Positive-Displacement Compressor (2P)—Positive displacement compressor in a two-phase fluid network—MATLAB. https://de.mathworks.com/help/hydro/ref/positivedisplacementcompressor2p.html

Mathworks/System-Level Heat Exchanger 2P. (2025). System-Level Heat Exchanger (2P-2P)—Heat exchanger based on performance data between two two-phase fluid networks—MATLAB. https://de.mathworks.com/help/hydro/ref/systemlevelheatexchanger2p2p.html

Mathworks/Turbine 2P. (2025). Turbine (2P)—Two-phase turbine in a thermodynamic cycle—MATLAB. https://de.mathworks.com/help/hydro/ref/turbine2p.html

Mathworks/twoPhaseFluidTables. (2025). twoPhaseFluidTables—Generate fluid property tables from REFPROP or CoolProp database—MATLAB. https://de.mathworks.com/help/simscape/ref/twophasefluidtables.html

Mazloomi, K., & Gomes, C. (2012). Hydrogen as an energy carrier: Prospects and challenges. Renewable and Sustainable Energy Reviews, 16(5), 3024–3033. https://doi.org/10.1016/j.rser.2012.02.028

Megía, P. J., Vizcaíno, A. J., Calles, J. A., & Carrero, A. (2021). Hydrogen Production Technologies: From Fossil Fuels toward Renewable Sources. A Mini Review. Energy & Fuels, 35(20), 16403–16415. https://doi.org/10.1021/acs.energyfuels.1c02501

Méndez, H. L., Arenas, T. L., Aldaco, A. T., González, E. V. T., & Cruz, M. S. (2021). Interstage Pressures of a Multistage Compressor with Intercooling. https://doi.org/10.3390/e23030351

Muhammad Aziz. (2021). Liquid Hydrogen: A Review on Liquefaction, Storage, Transportation, and Safety.

Nandi, T., & Sarangi, S. (1993). Performance and optimization of hydrogen liquefaction cycles. International Journal of Hydrogen Energy, 18(2), 131–139. https://doi.org/10.1016/0360-3199(93)90199-K

Negro, V., Noussan, M., & Chiaramonti, D. (2023). The Potential Role of Ammonia for Hydrogen Storage and Transport: A Critical Review of Challenges and Opportunities. Energies, 16(17), 6192. https://doi.org/10.3390/en16176192

Ni, M., Leung, D. Y. C., Leung, M. K. H., & Sumathy, K. (2006). An overview of hydrogen production from biomass. Fuel Processing Technology, 87(5), 461–472. https://doi.org/10.1016/j.fuproc.2005.11.003

Nikolaidis, P., & Poullikkas, A. (2017). A comparative overview of hydrogen production processes. Renewable and Sustainable Energy Reviews, 67, 597–611. https://doi.org/10.1016/j.rser.2016.09.044

Niu, B., Chen, L., Deng, K., Wang, H., Qu, J., Li, S., Zhang, Z., Chen, S., & Hou, Y. (2025). Genetic algorithm based optimization design and coupling performance analysis of multi-stage series hydrogen turbo-expanders. Energy, 335, 138128. https://doi.org/10.1016/j.energy.2025.138128

Nnabuife, S. G., Darko, C. K., Obiako, P. C., Kuang, B., Sun, X., & Jenkins, K. (2023). A Comparative Analysis of Different Hydrogen Production Methods and Their

Environmental Impact. Clean Technologies, 5(4), 1344–1380. https://doi.org/10.3390/cleantechnol5040067

Noh, W., Park, S., Kim, J., & Lee, I. (2022). Comparative design, thermodynamic and techno-economic analysis of utilizing liquefied natural gas cold energy for hydrogen liquefaction processes. International Journal of Energy Research, 46(9), 12926–12947. https://doi.org/10.1002/er.8064

Osman, A. I., Mehta, N., Elgarahy, A. M., Hefny, M., Al-Hinai, A., Al-Muhtaseb, A. H., & Rooney, D. W. (2022). Hydrogen production, storage, utilisation and environmental impacts: A review. Environmental Chemistry Letters, 20(1), 153–188. https://doi.org/10.1007/s10311-021-01322-8

Patlolla, S. R., Katsu, K., Sharafian, A., Wei, K., Herrera, O. E., & Mérida, W. (2023). A review of methane pyrolysis technologies for hydrogen production. Renewable and Sustainable Energy Reviews, 181, 113323. https://doi.org/10.1016/j.rser.2023.113323

Preuster, P., Papp, C., & Wasserscheid, P. (2017). Liquid Organic Hydrogen Carriers (LOHCs): Toward a Hydrogen-free Hydrogen Economy. Accounts of Chemical Research, 50(1), 74–85. https://doi.org/10.1021/acs.accounts.6b00474

Quack, H. (2002). Conceptual design of a high efficiency large capacity hydrogen liquefier. AIP Conference Proceedings, 613, 255–263. https://doi.org/10.1063/1.1472029

Rafique, M., Mubashar, R., Irshad, M., Gillani, S. S. A., Tahir, M. B., Khalid, N. R., Yasmin, A., & Shehzad, M. A. (2020). A Comprehensive Study on Methods and Materials for Photocatalytic Water Splitting and Hydrogen Production as a Renewable Energy Resource. Journal of Inorganic and Organometallic Polymers and Materials, 30(10), 3837–3861. https://doi.org/10.1007/s10904-020-01611-9

Rezaie, H., Ziabasharhagh, M., & Mafi, M. (2016a). A review of hydrogen liquefaction, current situation and its future.

Rezaie, H., Ziabasharhagh, M., & Mafi, M. (2016b). A review of hydrogen liquefaction, current situation and its future.

Rivard, E., Trudeau, M., Zaghib, K., Rivard, E., Trudeau, M., & Zaghib, K. (2019). Hydrogen Storage for Mobility: A Review. Materials, 12(12). https://doi.org/10.3390/ma12121973

Rosen, M. A., & Koohi-Fayegh, S. (2016). The prospects for hydrogen as an energy carrier: An overview of hydrogen energy and hydrogen energy systems. Energy, Ecology and Environment, 1(1), 10–29. https://doi.org/10.1007/s40974-016-0005-z

Sadaghiani, M. S., & Mehrpooya, M. (2017). Introducing and energy analysis of a novel cryogenic hydrogen liquefaction process configuration. International Journal of Hydrogen Energy, 42(9), 6033–6050. https://doi.org/10.1016/j.ijhydene.2017.01.136

Sakintuna, B., Lamaridarkrim, F., & Hirscher, M. (2007). Metal hydride materials for solid hydrogen storage: A review☆. International Journal of Hydrogen Energy, 32(9), 1121–1140. https://doi.org/10.1016/j.ijhydene.2006.11.022

Sánchez-Bastardo, N., Schlögl, R., & Ruland, H. (2021). Methane Pyrolysis for Zero-Emission Hydrogen Production: A Potential Bridge Technology from Fossil Fuels to a Renewable and Sustainable Hydrogen Economy. Industrial & Engineering Chemistry Research, 60(32), 11855–11881. https://doi.org/10.1021/acs.iecr.1c01679

Sergey & Andrey. (2021). Hydrogen energy: Development prospects and materials. https://doi.org/10.1070/rcr5014

Shafiee, S., & McCay, M. H. (2016). Different reactor and heat exchanger configurations for metal hydride hydrogen storage systems – A review. International Journal of Hydrogen Energy, 41(22), 9462–9470. https://doi.org/10.1016/j.ijhydene.2016.03.133

Shimko & Gardiner. (2008). Innovative Hydrogen Liquefaction Cycle. https://www.hydrogen.energy.gov/docs/hydrogenprogramlibraries/pdfs/progress08/iii_7_shimko.pdf

Sleiti, A. K., Al-Ammari, W. A., & Ghani, S. (2023). Novel dual-mixed refrigerant precooling process for high capacity hydrogen liquefaction plants with superior performance. Journal of Energy Storage, 66, 107471. https://doi.org/10.1016/j.est.2023.107471

Song, W., Liu, K., Zhao, Z., Zhang, L., Dong, X., Yang, X., Tian, C., Liu, S., & Cao, S. (2025). Simulation and Analysis of a Novel Hydrogen Liquefaction Process Based on the Liquid Nitrogen and Helium Joule–Brayton Cycle. ACS Omega, 10(8), 8089–8102. https://doi.org/10.1021/acsomega.4c09299

Spath, P. L., & Mann, M. K. (2000). Life Cycle Assessment of Hydrogen Production via Natural Gas Steam Reforming (NREL/TP-570-27637, 764485; p. NREL/TP-570-27637, 764485). https://doi.org/10.2172/764485

Staats, W. L. (2008). Analysis of a Supercritical Hydrogen Liquefaction Cycle.

Stolzenburg, K., Berstad, D., Decker, L., Elliott, A., Haberstroh, C., Hatto, C., Klaus, M., Mortimer, N., Mubbala, R., Mwabonje, O., Nekså, P., Quack, H., Rix, J., Seemann, I., & Walnum, H. (2013). Efficient Liquefaction of Hydrogen: Results of the IDEALHY Project.

Stolzenburg, K., & Mubbala, R. (2013). Fuel Cells and Hydrogen Joint Undertaking (FCH JU).

Szargut, J. (1989). Chemical exergies of the elements. Applied Energy, 32(4), 269–286. https://doi.org/10.1016/0306-2619(89)90016-0

Taher, M., & Evans, B. F. (2023, June 26). Centrifugal Compressor Polytropic Performance Evaluation: Taher-Evans Methods. GT2023. https://doi.org/10.1115/GT2023-104213

Teichmann, D., Arlt, W., & Wasserscheid, P. (2012). Liquid Organic Hydrogen Carriers as an efficient vector for the transport and storage of renewable energy. International Journal of Hydrogen Energy, 37(23), 18118–18132. https://doi.org/10.1016/j.ijhydene.2012.08.066

Teng, J., Wang, K., Zhu, S., Bao, S., Zhi, X., Zhang, X., & Qiu, L. (2023). Comparative study on thermodynamic performance of hydrogen liquefaction processes with various ortho-para hydrogen conversion methods. Energy, 271, 127016. https://doi.org/10.1016/j.energy.2023.127016

Umberto Federico Cardella. (2018). Large-scale hydrogen liquefaction under the aspect of economic viability.

Umegaki, T., Yan, J.-M., Zhang, X.-B., Shioyama, H., Kuriyama, N., & Xu, Q. (2009). Boron- and nitrogen-based chemical hydrogen storage materials. International Journal of Hydrogen Energy, 34(5), 2303–2311. https://doi.org/10.1016/j.ijhydene.2009.01.002

Ursua, A., Gandia, L. M., & Sanchis, P. (2012). Hydrogen Production From Water Electrolysis: Current Status and Future Trends. Proceedings of the IEEE, 100(2), 410–426. https://doi.org/10.1109/JPROC.2011.2156750

Usman, M., & Yamada, T. (2025). Methanol Reforming for Hydrogen Production: Advances in Catalysts, Nanomaterials, Reactor Design, and Fuel Cell Integration. ACS Engineering Au, 5(4), 314–346. https://doi.org/10.1021/acsengineeringau.5c00031

Valenti, G., & Macchi, E. (2008). Proposal of an innovative, high-efficiency, large-scale hydrogen liquefier. International Journal of Hydrogen Energy, 33(12), 3116–3121. https://doi.org/10.1016/j.ijhydene.2008.03.044

Verhelst, S., & Wallner, T. (2009). Hydrogen-fueled internal combustion engines. Progress in Energy and Combustion Science, 35(6), 490–527. https://doi.org/10.1016/j.pecs.2009.08.001

Volle, C. E. E. (2014). Simscape Modeling Verification in the Simulink Development Environment.

Wijayanta, A. T., Oda, T., Purnomo, C. W., Kashiwagi, T., & Aziz, M. (2019). Liquid hydrogen, methylcyclohexane, and ammonia as potential hydrogen storage: Comparison review. International Journal of Hydrogen Energy, 44(29), 15026–15044. https://doi.org/10.1016/j.ijhydene.2019.04.112

Worku, A. K., Ayele, D. W., Deepak, D. B., Gebreyohannes, A. Y., Agegnehu, S. D., & Kolhe, M. L. (2024). Recent Advances and Challenges of Hydrogen Production Technologies via Renewable Energy Sources. Advanced Energy and Sustainability Research, 5(5), 2300273. https://doi.org/10.1002/aesr.202300273

Wulf, C., & Kaltschmitt, M. (2012). Life cycle assessment of hydrogen supply chain with special attention on hydrogen refuelling stations. International Journal of Hydrogen Energy, 37(21), 16711–16721. https://doi.org/10.1016/j.ijhydene.2012.03.028

Yin, L., & Ju, Y. (2020a). Process optimization and analysis of a novel hydrogen liquefaction cycle. International Journal of Refrigeration, 110, 219–230. https://doi.org/10.1016/j.ijrefrig.2019.11.004

Yin, L., & Ju, Y. (2020b). Review on the design and optimization of hydrogen liquefaction processes. Frontiers in Energy, 14(3), 530–544. https://doi.org/10.1007/s11708-019-0657-4

Yu, S., Wang, Z., Qiu, G., Che, X., Chen, J., Li, Q., & Cai, W. (2024). Optimization and analysis of a novel hydrogen liquefaction coupled system with dual path hydrogen refrigeration cycle and the closed nitrogen cycle pre-cooling. Journal of Cleaner Production, 470, 143281. https://doi.org/10.1016/j.jclepro.2024.143281

Yuksel, Y. E., Ozturk, M., & Dincer, I. (2017). Analysis and assessment of a novel hydrogen liquefaction process. International Journal of Hydrogen Energy, 42(16), 11429–11438. https://doi.org/10.1016/j.ijhydene.2017.03.064

Zhang, H., Lin, G., & Chen, J. (2010). Evaluation and calculation on the efficiency of a water electrolysis system for hydrogen production. International Journal of Hydrogen Energy, 35(20), 10851–10858. https://doi.org/10.1016/j.ijhydene.2010.07.088

Zhang, S., & Liu, G. (2022). Design and performance analysis of a hydrogen liquefaction process. Clean Technologies and Environmental Policy, 24(1), 51–65. https://doi.org/10.1007/s10098-021-02078-z

Zhang, T., Uratani, J., Huang, Y., Xu, L., Griffiths, S., & Ding, Y. (2023). Hydrogen liquefaction and storage: Recent progress and perspectives. Renewable and Sustainable Energy Reviews, 176, 113204. https://doi.org/10.1016/j.rser.2023.113204

Züttel, A. (2004). Hydrogen storage methods. Naturwissenschaften, 91(4), 157–172. https://doi.org/10.1007/s00114-004-0516-x

Züttel, A., Remhof, A., Borgschulte, A., & Friedrichs, O. (2010). Hydrogen: The future energy carrier. Philosophical Transactions of the Royal Society A: Mathematical, Physical and Engineering Sciences, 368(1923), 3329–3342. https://doi.org/10.1098/rsta.2010.0113

Declaration

I herewith declare that I have composed the thesis myself and without the use of any other medium than the cited sources and aids. Every source of information, data, and materials utilized to prepare this thesis has been properly cited and acknowledged. I further declare that I have secured the required permits for the use of data, experimental work, or any third-party resources, and that this research has been carried out in compliance with the ethical standards and rules of Hochschule University of Applied Sciences, Nordhausen.

The thesis in the same or similar form has not been submitted to any examination board and has not been published. This thesis was not yet, even in part, used in another examination or as a course performance, either in Germany or abroad.

Shekh Mojamil

Lampoldshausen, 19/03/2026